UNIVERSITY OF CALIFORNIA,
IRVINE

Breakup and Disruption of Drops in Shearing and Extensional Particulate Flows

DISSERTATION

Submitted in partial satisfaction of the requirements
for the degree of

DOCTOR OF PHILOSOPHY

in Mechanical and Aerospace Engineering

by

Franz H. Hernández Gaitán

Dissertation Committee:
Professor Roger H. Rangel Chair
Professor Marc Madou
Professor Manuel Gamero-Castaño

2016

DEDICATION

To

my parents, Ana and Roncesval, and friends

in recognition of their worth

an aphorism

"For we are like tree trunks in the snow. In appearance they lie sleekly and a little push should be enough to set them rolling. No, it can't be done, for they are firmly wedded to the ground. But see, even that is only appearance"

Franz Kafka, The Trees

and hope

"The one who gets tired loses"

Leopoldo López

LIST OF CONTENTS

LIST OF FIGURES

Page

LIST OF TABLES

Page

LIST OF SYMBOLS

$\mathbf{A}$	First Rivlin-Ericksen stress tensor
B	Blockage
a, R	Particle/drop radius
Ca	Capillary number
De	Deborah Number
E	Elasticity Number, also Young modulus
F	Volume fraction
$\mathbf{F}$	External force
$\mathbf{f}$	Force per unit volume or per unit surface
L	Characteristic length
La	Laplace Number
M	Viscoelastic Mach number
p	Pressure
$\mathbf{r}$	Position vector
Re	Reynolds number
$\mathbf{S}$	Piola-Kirchhoff stress tensor, or surface vector
Stk	Stokes number
$\mathbf{u}$	Linear velocity of the fluid
$\tilde{\mathbf{u}}$	Displacement vector of the solid
u, v, w	Cartesian components of $\mathbf{u}$ velocity
U	Double of maximum u velocity
U_i	Displacement component
$\mathbf{v}$	Linear velocity of the particle

$\tilde{\mathbf{v}}$	Linear velocity of the solid
x, y, z	Position, Cartesian
W	Separation between the walls
We_p	Particle Weber
Wi	Weissenberg number
β	Blockage ratio
γ	Density ratio
$\dot{\gamma}$	Shear strain rate
κ	Curvature
$\boldsymbol{\lambda}$	Lagrange Multipliers
λ	Viscosity ratio
λ_1	Relaxation time
λ_2	Retardation time
η	Fluid viscosity
η_0	Zero strain rate fluid viscosity
ρ	Density of the mixture
σ	Surface tension coefficient
$\boldsymbol{\sigma}$	Total stress tensor
τ	Extra-stress tensor (Viscoelastic)
$\boldsymbol{\omega}$	Angular velocity of the particle

LIST OF ABBREVIATIONS

BDR Basic donating region

DDR Defined donating region

DR Donating region

DEM Discrete element method

FENE Finitely extensible nonlinear elastic model

CSF Continuum surface force model

HF Height Function (method or discrete function)

LS Level-Set method

PLIC Piecewise linear interface construction

SIMPLE Semi-Implicit Method for Pressure Linked Equations

VOF Volume-of-fluid method

ACKNOWLEDGMENTS

I want to thank the department of Mechanical and Aerospace and Professor Roger Rangel for the financial support and academic assistance.

CURRICULUM VITAE

Franz H. Hernández Gaitán

- 2002-2008 Mechanical Engineering, Simón Bolívar University, Caracas, Venezuela
- 2008-2010 Master in Mechanical Engineering, Simón Bolívar University, Caracas, Venezuela
- 2016 Ph.D. in Mechanical an Aerospace Engineering, University of California, Irvine

EXPERIENCE: TEACHING AND RESEARCH

Teaching

Guest lecturer at the University of California Irvine (UCI):

· MAE130A "Introduction to Fluid Mechanics" (Winter-2015), (Fall-2012)

· MAE230B "Viscous Incompressible Fluid Mechanics" (Winter-2015)

Lecturer at the University of California Irvine (UCI):

· MAE91 "Introduction to Thermodynamics Online": (Summer II 2015, Summer 10wk 2016).

· MAE130A "Introduction to Fluid Mechanics" (Summer I 2014), (Summer II 2013).

Teaching Assistant at the University of California Irvine (UCI) (2011-Present):

· MAE130A "Introduction to Fluid Mechanics" (Winter-2016) (Winter-2015) (Winter-2014) (Fall-2013) (Fall-2012) (Fall-2011).

· MAE91 "Introduction to Thermodynamics" (Fall-2014), (Spring-2014), (Fall-2013), (Summer I-2013), (Spring-2013), (Spring-2012).

· MAE130B "Viscous/Compressible Flows" (Winter-2013)

Research

· University of California Irvine (UCI) (2010-2016): "Breakup and Disruption of Drops in Shearing and Extensional Particulate Flows".

· Central University of Venezuela (UCV) (2009-2010): - Experimental validation of a numerical to characterize torrential landslides using the Discrete Element Method (DEM-Solids) and Finite Volumes (FVM-Liquid).

· Simón Bolívar University (USB - FONACIT) (2008-2009): - Formulation and development of a model in MATLAB to characterize torrential landslides using the Discrete Element Method (DEM-Solids) and Finite Volumes (FVM-Liquid).

· Short Internship at Simón Bolívar University: Rheology of torrential landslides and CFD simulation using a rotational viscometer to measure rheological parameters. Summer 2006 (FONACIT).

ACADEMIC PUBLICATION AND PRESENTATION

Preprint submitted to the Journal of Computers and Fluids (May-2016): "Breakup of Drops in Simple Shear Flows with High-Confinement Geometry".

Preprint submitted to the Journal of Computational Physics (Dec-2014): "Interfacial Models for Drop Dynamics in Volume-Tracking Frameworks".

MAE-UCI Seminar (Spring-2014): "Deformation of particles in a simple shear flow using a volume-tracking framework".

SoCal Fluids IX Symposium (2015): "Numerical instabilities of a drop in a capillary tube".

SoCal Fluids VIII Symposium (2014): "Deformation of liquid and solid particles in shearing flows".

SoCal Fluids VII Symposium (2013): "Effect of the curvature models on the motion of an interface using the Volume-of-Fluid method".

CIMENIECS 2010 (Merida-Venezuela) (Numerical Methods): "Optimizing the calculation times for the discrete Element Method".

ASME FEDSM2009 (CFD): "Eulerian-Eulerian Modeling of non-Newtonian Slurries Flow in Horizontal Pipes".

ASME FEDSM2008 (CFD): "CFD Modeling of Slurry Flows in Horizontal Pipes". A 3D numerical simulation with CFX^{TM} using particle kinetic theory studied the viability of simulating liquid-sand transport in horizontal pipes.

ABSTRACT OF THE DISSERTATION

Breakup and Disruption of Drops in Shearing and Extensional Particulate Flows

By

Franz H. Hernández Gaitán

Doctor of Philosophy in Mechanical and Aerospace Engineering

University of California, Irvine, 2016

Professor Roger H. Rangel, Chair

When biological cells approach regions with high strain-rates, the membrane deformation can surpass the yielding point, leading to cell lysis. In the interest of enhancing such effects, drop dynamics is studied. Here, bending stiffness and viscoelastic area compression of the membrane are not considered. Surface-tension force is used to model planar tensile stresses instead. Breakup of drops has been shown to depend on the type of flow, the Reynolds number, Re, the capillary number, Ca, the viscosity ratio, λ, the density ratio, γ, and the Stokes number (particulate flows). In simple shear flows at low Re and low Ca, breakup is not possible. The main purpose of this work is to find conditions that enhance drop disruption under such flows. While the deformation of drops and elastic capsules in simple shear flows and particulate flows have been subject of research, less attention has been given to the deformation of drops in particulate simple shear flows that are initially quiescent. The effects of rigid particles on drops are studied numerically for several flow conditions and the deformation is analyzed using the particle-particle distance. It is observed a decrease in deformation as Re (moderate regime) increases for different initial position of the particles. Drop deformation increases with Ca, meanwhile larger and denser particles are preferred to induce drop puncturing. Without particles, the conditions for drop breakup are found when the walls are closely located. Similarly, a gravity-driven particulate flow is studied and the dependence on the Bond number is shown. The problem of drop splitting in sudden expansions is also analyzed, showing dependence on the expansion ratio. The conservation laws are solved numerically using finite volumes and the Crank-Nicolson scheme. Velocities are corrected with SIMPLEC. The interface is tracked using the volume-of-fluid method, reconstructed with the piecewise linear interface calculation algorithm (PLIC), and fluxed based on the defined donating region (DDR). A High-Resolution technique (SMART) is employed to discretize advection terms. A continuum surface force (CSF) models surface tension. Rigid particles are introduced in the domain with the Lagrange multiplier method.

Chapter 1

Introduction

1.1 Problem Description and Motivation

The problems of particle deformation, disruption, fragmentation and breakup, and particle-particle repulsion and attraction (agglomeration) are phenomena commonly observed in many industrial applications and natural processes, leading to vigorous research activity in a variety of fields due to its multiphase nature and the complexity of the dynamics of drops, bubbles and rigid/elastic/viscoelastic particles: oil recovery and emulsions; dust control in the mining industry (drops); spraying and mixing in combustion systems and propulsion; drug delivery and cell transport, analysis and manipulation (biology); locomotion of small organism, among many others. Some of these processes involve the breakup of a jet to produce drops, or the transport of drops/particles in micro-channels, or the disruption of a free surface due to instabilities. In the case of liquids, the analysis of single drops, i.e. transport, orientation, deformation and breakup mechanisms, provides useful information about the phenomena. One scenario where drop-drop interactions are limited is in dilute emulsions. When drops do interact with each other in a given flow, coalescence and/or fragmentation could take place and such dynamics is complex. In the case of drop-wall or drop-particle interactions, the flow field can produce conditions of instability leading to breakup. In that sense, studying drop deformation in shear and extensional flows may improve the understanding of cell lysis happening naturally or mechanically from a fundamental point of view.

Micro-channel flow lysis, bead-beaten lysis and osmotic lysis are common methods used to break up cell membranes (Abmayr et al., 1995). When cells are transported in capillary regions, or close to walls, shear stresses are capable of deforming the membrane beyond the yield strength limit, where structural failure takes place. This mechanism can be enhanced by the interaction and collision of glass beads in a microfabricated lysis chamber. Another mechanism is the osmotic lysis, where changes in pressure jump

across the interface modify the tensional stresses at the interface. This can be accomplished by creating an extensional flow with important variations in pressure, by injecting mass inside the cell, or by placing the cell in a press. The objective of mechanical cell lysis is to extract DNA or proteins for further applications and the amount of sample is normally a limiting factor. Therefore, any mechanism capable of enhancing the rupture of the membrane is relevant.

If the cell membrane is relatively thick, or if its ultimate stress is considerable large, modeling the membrane is justified. Such membrane can behave as a viscoelastic solid, not only in tension or compression, but also in bending. In the case of weak membranes, thin-membrane theory can be used, or even simpler, the cell can be modeled as a droplet subject to surface tension.

Liposomes are vesicles composed of a lipid bilayer that can be modeled as a membrane. These vesicles are commonly used to transport drugs and therefore subject to numerous research. The deformation of liposomes was studied by Foo et al. (2006) to understand the effect of membrane biomechanical properties on the shape. It was found that membrane tension contributes significantly to the resistance during the deformation, justifying the use of drop dynamics as a simplified model. Cell membranes are semi-permeable structures that resist tension, flow under shearing and are capable of reducing the osmotic pressure by transporting solvent in/out of the cell, characteristic that clearly differentiates a drop from a biological cell.

Other interesting problems are the magnetophoresis of nanoparticles (Lim et al., 2011) and nuclear targeting of nanoparticles (Kang et al., 2010), used for imaging and drug delivery. Brownian motion and electrochemical potential are of extreme relevance in these problems because the scale of the nanoparticles is $\sim 10nm$. In that sense, our work is incapable of studying those flows (nanoscale), but some qualitative descriptions can be captured.

The fundamental study of the interaction between particles in Newtonian, or viscoelastic fluids, and the breakup of the interface has an impact on the mentioned problems.

1.2 Dynamic scales

Common eukaryotic cell have lengths ranging $10 - 100\,\mu$m, with a nucleus of the size $3 - 10\,\mu$m. Diameters of capillaries, veins, and micropipettes range from $10\,\mu\text{m} - 1\,mm$ with velocities around $0.3 - 100\,$mm/s, leading to shear strain-rates of $\dot{\gamma} = 30 - 100 s^{-1}$. Considering plasma or blood as the working fluid, dynamic and kinematic viscosities are $\eta_{blood} \sim 3 \cdot 10^{-3}\,$Pa-s, $\nu_{blood} \sim 3 \cdot 10^{-6}\,\text{m}^2/s$ (Cho and Kensey, 1991). The surface-tension coefficient of common liquids is in the order of $\sigma = 2 - 60\,$dyne/cm. Then, the flow obeys a small to moderate Reynolds number flow, $Re_{flow} = 0.001 - 30$, a moderate Reynolds number of the interface, $Re_{osc} = 1.5 - 25$ and very small to small capillary number, $Ca = 1 \cdot 10^{-5} - 0.015$. The definition of these

dimensionless number will be explained in the sections involving the dynamics of drops.

Deformable particles in low Re flows will exhibit two types of interfacial motion: nonlinear oscillatory and monotonically damped. The former is likely to happen for $Re_{osc} \gtrsim 10$, but requires a given initial deformation. For low-to-moderate Re regimes and low Ca, shearing itself is incapable of producing disruption because surface tension is sufficiently strong. In that sense, any perturbation on the shape will produce restructuring forces that recover the steady-state shape. For that reason, one way to produce lysis is by changing hydrodynamic forces with the presence of particles and therefore the importance of studying this problem.

In order to study the effect of rigid particles on a deformable particle in viscoelastic fluids, a previous understanding of how particles interact is very important. For instance, spheres in a simple shear flow might experience particle chaining or particle-particle repulsion. In the case of drops in a viscoelastic fluids, the matrix effect is to stabilize the drop.

Plasma and whole blood are viscoelastic, with relaxation times $\lambda = 1.5 - 2.6ms$ and $\lambda = 7.8ms$ respectively. Additionally, whole blood fluid is shear thinning with $\eta_0 = 0.0169$Pa-s, specially for $\dot{\gamma} < 40\text{s}^{-1}$, while plasma is a Boger fluid with zero shear viscosity $\eta_0 = 1.34$mPa-s (Brust et al., 2013). Deborah number is used to characterize viscoelasticity by relating the relaxation time of the flow with the time scale of the experiment. For the same range of shear-strain-rate previously stated, the Deborah number is $De = \lambda\dot{\gamma} = 0.04 - 0.8$, which reveals an important effect of viscoelasticity in biological system flows. Low values of De can be modeled numerically, but De numbers approaching the unity or above require very fine mesh resolutions and convergence is normally lost or numerical breakdown could appear, typically around $De \sim 1$, depending on the fluid model employed. Considering that only the most complex viscoelastic models are capable of representing viscoelastic fluids, and up to some extent in accuracy, the study of viscoelastic effects is limited in this work.

Analyzing the relationship between Re, Ca, De, the viscoelastic elasticity $E_{viscoelastic}$, the elastic elasticity, $E_{elastic}$ and the conditions that lead to over-extension and breakup will allow for a complete understanding of the influence of a membrane, particles and the flow itself. This could produce cost reductions or improve safety by knowing how to induce breakup or how to avoid it.

1.3 Outline of the Research Project

The overall progress of this PhD research is summarized in the following sections:

1. Development of an incompressible viscous fluid solver with the following additions and validations:

   (a) We have incorporated a high-resolution technique for advective terms: Sharp and Monotonic Algorithm for Realistic Transport (SMART) scheme. SMART provides third order accuracy on uniform meshes. This approach is required to solve viscoelastic flows.

   (b) The rigidifying force of the distributed Lagrange multiplier method (DLM) was provided with sub-grid velocity resolution at the interface, to set a real non-slip boundary condition. This method produced incorrect drag forces, but smooth stresses. The appropriate approach is to perform a multi-level discretization around the interface (multigrid). This is one of the reasons for the low convergence of the DLM.

   (c) The volume of fluid method together with the Flux Corrected Transport algorithm (FCT-VOF) has been incorporated. The advection of the color function is computed using SMART, instead of the conventional unbounded n^{th} order polynomials, and advanced in time with a second order finite difference scheme, achieving a sharp interface and volume conservation.

   (d) Validation of the code for different flows: Planar Poiseuille flow (transient scheme), lid-driven cavity flow (advection and diffusion), flow past a cylinder (viscoelastic drag) and settling of a sphere (DLM for transient problems). Section 6.

2. We have found that recent investigations use the hybrid level-set volume-of-fluid method, giving better results than level-set or VOF alone. Advances with VOF are the following:

   (a) Our implementation of the FCT-VOF method shows dependence on the continuous surface force model chosen (staggered, p-centered, cell averaged, density based, volume fraction based) and the method used to compute the curvature (height functions, interface normal divergence). A staggered-surface tension force without weighting (i.e. by density) produces a sharp interface, compared to other methods, even for high density ratios. The curvature computed from the divergence of the interface normal using a smoothed color function is the best method to compute transient phenomena.

   (b) The implementation of the PLIC algorithm using two levels of complexity for the calculation of the donating zone. First, a simple and fast method denoted as BDR is shown to converge with zero-to-first order in time and space. By changing the fluxing from area based to volume based and

incorporating a volume redistribution algorithm, the BDR method shows a minimal apparition of wisps and voids, but is not necessarily volume conserving. The second level of complexity is the DDR scheme, which was implemented in 3D from the description of a 2D algorithm found in the literature. This method solved the voids and is one of the most accurate methods that conserves mass exactly, and converges with at least first order.

(c) Validation of the VOF code:

i. Static drop problem: we obtained the right pressure jump across the interface and an approximate curvature. Section 6.4.1.

ii. Oscillation of a viscous drop: frequency and amplitude of the oscillation was reproduced. Section 6.4.2.

iii. Drop deformation in a tube.

iv. Simple shear flow problem.

(d) Using the height method allows for an accurate prediction of the curvature. We found that such method is not accurate for advected-type VOF methods (no clear or sharp interface), but it is sufficiently accurate for methods that resolves the interface with high accuracy (PLIC). Our implementation of the HF method to compute curvatures is almost second order.

3. Drops deforming in simple shear flows showed Taylor deformation parameters, angles of orientation and drop half-lengths in good agreement with other studies. This study considered subcritical and supercritical flows for weak wall effects and strong wall effects. We found that bringing the walls closer to the drops increase their stability slightly. We also found that for drops with close walls, the critical capillary number increases for viscosity ratio 1.9, contrary to the results in the literature for weak walls.

4. The phenomena of drop deformation in the presence of two particles in a simple shear flow was studied under moderate Reynolds number, Re, and Capillary number, Ca. For a sufficiently large Ca, the drop shows large deformation and even hollowing, that is, the creation of a hole in the drop when two particles approach each other in collision trajectory. We have introduced the particle Weber number which indicates the degree of acceleration in the vertical direction of the particles, but such number does not correlate with the deformations of drops. Instead, better correlation is found with the Laplace parameter $La = Re/Ca$. A phenomoenological model is obtained for uniform properties and a fixed initial condition. More work is required to obtain a general phenomenological model that includes density ratio, viscosity ratio, particle-to-drop radius ratio and initial position. Larger particles are

required to produce puncturing at low Ca and the density ratio has a minimal but positive effect on the deformation.

5. Breakup of a viscoelastic membrane by two shearing particles is a problem that has not been addressed, even though the shearing of a membrane has been studied extensively in the literature. We implemented a model to characterize the deformation of elastic solids and used it in the fluid solver as an immerse boundary. We found a relationship between drop deformation and the deformation of a solid. However, the main difference is the oscillatory behavior of the elastic solid. More work is required on the fluid-solid coupling and in the hyperelastic/viscoelastic models.

6. Particle Chaining: we have conducted many simulations to validate the viscoelastic model in order to characterize the motion of interacting particles. Two particular problems we addressed are the sedimentation and shearing of particles in viscoelastic fluids. Our main limitation is the radical difference between viscous time and relaxation time, that set up an upper bound on the maximum resolution we can afford, where accuracy is the trade-off. The problem is fairly well understood for simple shear flows (recently), but there are multiple opinions about the conditions that produce attraction in side-by-side sedimentation, since the effect of elasticity and shear-thinning is not known clearly. The problem of the sedimentation of a sphere is selected in order to decide the required minimal resolution for future simulations (i.e. $R/\Delta r > 10$). We had good agreement in former simulations with Oldroyd-B fluid, but present simulations with Oldroyd-B, Giesekus and the extension to FENE-type fluids are required. A simulation with a Giesekus fluid shows drafting of two particles settling side by side when $De < 1$. This project was dropped because we found that models in the literature are in general incapable of describing the experimental results with sufficient accuracy, only qualitatively at most.

1.4 Present and Future Work

We have developed several models to address the transport of interfaces using VOF. We started with the FCT model and SLIC, advanced to PLIC with a primitive form of BDR and then resolved the undesired problems of mass conservation and wisps with the DDR-PLIC method. This final method coupled with the height function model to compute curvatures and the fluid flow solver allow us to analyze the process of drop disruption, fragmentation and breakup in an accurate manner. Our understanding is that these methods are already available in the literature. Even though the DDR method is presented theoretically to describe more complex schemes, or to solve 2D problems, it is not commonly used in literature. We found that such method complies with accuracy (up to second order), robustness (no wisps), consistency and is not as computationally expensive as more advanced models. This code allowed for the study of sheared drops under high confinement, which gave us a better understanding of the mechanisms related to drop breakup. To the best of our understanding, this problem has not been addressed numerically for very small Ca and large Re, mainly due to numerical reasons: accuracy degrades with Re which enhances spurious currents.

To study the breakup of drops under the presence of rigid particles, we tested a wide range of capillary number: $Ca = 0.1 - 30$. Our results indicate that rigid particles do not produce drop breakup, but they can create other phenomena: drop puncturing and large deformations. For large capillary numbers, $Ca > 1$, drop puncturing can be achieved with uniform properties, however it is a challenge for small capillary numbers. In order to observe large deformations under low capillary numbers, the rigid particles were required to be considerably more dense and larger than the drop. We then introduced the particle weber number to determine if such parameter correlated with the observations. It was found that considerably large values of We_p were required to induce drop puncturing. By performing several simulations, we could generate a map of Re against Ca that consider the limiting regions of different regimes.

We wanted to study the effect of the flow on membrane disruption of deformable particles as a closer model to biological cells. The difference between the models when puncturing takes place is that a drop recovers its shape and the elastic membrane may fracture. An actual cell may present a different rupture than the simplistic models. However, it allows us to understand the phenomena of simpler problems. The model for the solid was observed to be unstable under rotations. A viscoelastic model for the stress tensor was not fully included. A biological membrane can be modeled mathematically as a 2D thin membrane. Our model is 3D and the required transformations were not performed. In order to characterize large deformations, the nonlinear term of the strain must be computed following a gauss quadrature as done with the linear terms. The actual coupling between the solid and the fluid is still unstable. One possible solution is the use of adaptive multilevel methods, but due the complexity of such method, the code could not be completed on

time. To model the membrane, a mapping of a capsule and the particle-membrane collisional model are also required. Preliminary simulations with the coupled model showed how solids deform in a damped-oscillatory manner. More studies in this field will let understand the requirements on Re and particle size and location to produce mechanic failure. The parameters for this study are the membrane elasticity, relaxation time and ultimate strength. The extension of the work in simple shear flow is the incorporation of particles, as it is done with the drop.

The interaction of particles in viscoelastic fluids was studied. The DLM method requires several iterations in order to converge. Our effort to reduce the amount of iterations and prescription of the boundary condition was not successful. In order to obtain the right Lagrange multipliers, the rigidization force must be cleared every iteration. This method imposes a relevant constraint on the computational time. One of the possible solutions is the immerse boundary method, but the surface-force/stress model is not sufficiently accurate. Literature shows that such method may have problems under supergrid and subgrid resolutions between the interface and the medium mesh. This could be a relevant future work.

Viscoelastic fluids have a known numerical limitation when the Deborah number exceeds the unity, which limits the amount of cases that can be studied. By increasing De, the mesh size is required to be decreased exponentially to remain within a given accuracy. Two problems were studied, side-by-side sedimentation, using Oldroyd-B and Giesekus fluids and end-to-end sedimentation. Because it is not possible to prescribe the particles boundary conditions using DLM, the stress tensor around a cylinder or sphere shows large fluctuations, fact that affects the results if the mesh is too coarse. This imposed another limiting problem, the amount of cells required to achieve a given accuracy were excessively high. We also worked with the FENE-P viscoelastic model, but the literature review indicated that in order to be able to predict natural phenomena, even more advanced models were required. For these reasons, the study of these problems were abandoned. What could be done in these type of problems is to compare different cases for several Re and De, and study shear-thinning effects in order to produce a criteria for attracting and repelling spheres.

Chapter 2

Literature Survey

2.1 Interface dynamics

The dynamics of drops and bubbles in different flows has been subject to extensive research. Analytical solutions have been obtained, from potential flows and Stokesian flows, to small deformation-perturbation approximations, in order to establish the fundamentals that govern different phenomena, where interface breakup and instabilities are among them. Studying these problems may require balancing forces at the interface, which are typically the following: surface tension, dependent on the surface-tension coefficient and local curvature; pressure gradients and viscous stresses in the neighborhood of the interface (hydrodynamic forces acting); jump in pressure and viscous stresses across the interface; and inertia.

The simplest case is a droplet in a quiescent fluid for which the pressure jump across the interface can be found with the Young-Laplace equation. A bubble can be studied with the Rayleigh-Plesset equation where the pressure is obtained as a function of time. The settling velocity of a viscous drop in an infinite domain can be computed from the drag force developed by Hadamard and Rybczynski. The problem of the rising bubble has been shown to be dependent on the Reynolds number, Re, and Eotvos number, Eo, which categorizes the shapes as follows: spherical, spherical cap, skirted, dimpled ellipsoidal cap, wobbling; the extension of this studies include non-Newtonian fluids and the phenomena has been reproduced numerically. A very common problem is the Raleigh-Taylor instability and the shear layer instability. The oscillating viscous drop due to an initial deformation is another example; the oscillation can be oscillatory-linear for large Re and nonlinear oscillatory or dampened for low Re. Droplet dynamics in a simple shear flow is governed by Re, Ca, viscosity ratio λ and confinement R/H; the deformation, orientation and possibility of breakup into smaller drops is very well documented in the literature.

2.1.1 Drop Oscillation

The interface of a drop is initially deformed and placed in a quiescent flow evolves as a nonlinear oscillator with a position proportional to $e^{-\beta_n t}$. A dimensional analysis performed on the region inside the drop shows a dimensionless length and time of $r^* = r/a$ and $t^* = t/\sqrt{\rho_d a^3/\sigma}$, respectively, and a dimensionless velocity of $u^* = u/\sqrt{\sigma/(\rho_d a)}$, where a is the radius of equilibrium of the drop. Thereby, this flow is governed by Reynolds number $Re_{osc} = \sqrt{\rho_d \sigma a}/\eta_d$ and Weber number $We = 1$ or capillary number $Ca = \eta_d/\sqrt{\sigma \rho_d a}$. A point of the interface could manifest an oscillatory, damped oscillatory, or aperiodic motion depending on the real and imaginary values of β_n, given by $\beta_n = b \pm \sqrt{b^2 - \omega^2}$, where ω is the frequency of the oscillation of an inviscid liquid drop, $\omega = [n(n-1)(n+2)]^{1/2}$ (Rayleigh, 1879), and b is the damping constant for relatively small viscosity ($Re \gg 1$), that in terms of the mode of the oscillation, n, is $b = (n-1)(2n+1)/Re_{osc}$ (Lamb, 1932, Prosperetti 1980). Viscous effects dampen the oscillation at low Re, while under moderate-high Re and small deformations, the motion is described by linear oscillations. For a damped oscillatory motion, the position of the interface as a function of time can be predicted as $x = a + \delta x_0 e^{-bt} \cos\left(\sqrt{\omega^2 - b^2}t\right)$, where δx_0 is the initial deformation.

2.1.2 A Drop in Shearing and General Flows

The deformation of an isolated drop in simple shear flow has been subject of numerous research in multiphase flow. One important phenomena is the deformation and breakup of an initially spherical drop. Depending on the flow conditions and the location of the boundaries, a drop can deform to a steady-state shape or deform until it undergoes a pinching process. The flow conditions are dependent on the Reynolds number $Re = \frac{\rho_m \dot{\gamma} a^2}{\eta_m}$, the capillary number $Ca = \frac{We}{Re} = \frac{\eta_m \dot{\gamma} a}{\sigma}$ or the Weber number $We = \rho \dot{\gamma}^2 a^3/\sigma$, and the ratio of the drop-medium properties, $\lambda = \frac{\eta_d}{\eta_m}$, for a drop with undeformed radius a, viscosity η_d, density ρ_d, within a liquid matrix or medium of viscosity η_m and density ρ_m. The end pinching process takes place as an "elongative end pinching" or "retractive end pinching"; another terminology for both mechanisms are fracture and tipstreaming, respectively. For low Re, when λ is less than four, there is a "critical capillary number", Ca_c, above which the drop continues to deform without reaching a steady shape. When $\lambda = 1$ and $Re = 0$, breakup is observed after $Ca_c \approx 0.41$ Li et al. (2000). In the other hand, when surface tension is relatively important, a drop could evolve into a steady shape and it can be analyzed using the angle of orientation, θ, measured with respect to the horizontal, or using the Taylor deformation parameter, $D = (l-b)/(l+b)$, where l and b are the half-length and half-breadth of the drop, respectively. A small perturbation deformation procedure to second order in Ca, gives the following equation for the orientation angle (Barthès-Biesel and Acrivos, 1973),

$$\theta = \frac{\pi}{4} - Ca\frac{(16+19\lambda)(3+2\lambda)}{80(1+\lambda)}$$

While the Taylor deformation parameter for a confined droplet has been found to be Shapira and Haber (1990),

$$D = \frac{19\lambda+16}{8(\lambda+1)}Ca\left[1+C_s\frac{2.5\lambda+1}{\lambda+1}\left(\frac{R}{H}\right)^3\right]\sin\theta\cos\theta$$

where C_s is a numerical factor that depends on the relative distance between the particle and the wall ($C_s = 5.6996$ when the particle is halfway), and H is the separation of the plates.

Numerous research has been done numerically and experimentally for different types of flow (α) and blockage ratios, as summarized in figure 2.1. The parameter α is $\alpha = 0$ in simple shear flows and $\alpha = 1$ in plane hyperbolic flows (irrotational and elongational). More information can be found in Stone (1994). A conclusion from Clift et al. (1978) is that for equal shear rates, irrotational shear appears to produce more effective breakup and dispersion than rotational shear, even at low viscosity ratios. Blockage ratio, R/h, affects the critical capillary number and is dependent on the viscosity ratio, as shown.

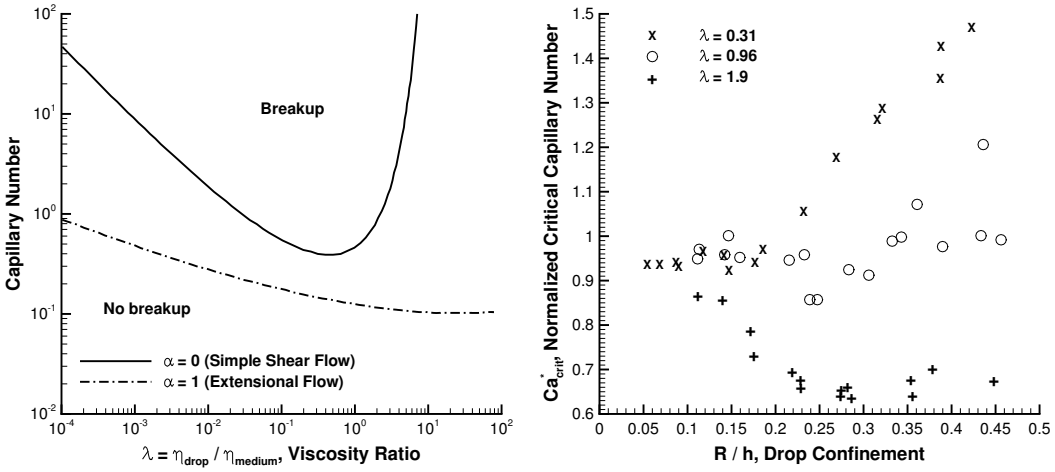

(a) (b)

Figure 2.1: Breakup of a droplet and critical capillary number: (a) Stability regions as a function of viscosity ratio, λ, and flow parameter α (b) Effect of confinement for several λ, where the critical capillary number is normalized with the critical value estimated by de Bruijn (1993). Reproduced from Almeida-Rivera and Bongers (2012) and Minale (2008).

2.1.3 Numerical Methods in Interface Dynamics

Challenges in the tracking moving interfaces brought the development several numerical approaches: boundary integral method (BIM), level set (LS) (Sussman et al., 1994), volume of fluid (VOF), front tracking (FT) (Unverdi and Tryggvason, 1992), smoothed particle hydrodynamics (SPH), lattice Boltzmann (LB) and hybrid methods like the coupled level-set and VOF (CLSVOF) (Sussman, 2003), and the particle-level-set (P-LS) (Enright et al., 2002), among others. Each method has its own limitations and improvements, normally related to implementation time, accuracy of the solution, mass conservation capabilities and minimal resolution of subgrid structures. Rider et al. (1995) concluded that a level-set methodology does not guarantee volume conservation in highly distorted flows, giving rise to unacceptable errors. Front-tracking methods are very accurate, but they exhibit loss of mass due to non-solenoidal velocity projections; accurate advection of the front points tends to minimize the error produced by changes in the total mass. Furthermore, changes in mass were found to be unacceptably high for long-term simulations involving many bubbles or drops where the resolution of each particle is relatively low (Tryggvason et al., 2001). Additional techniques aimed at improving computational performance have been successfully applied to compute the surface-tension force and other properties across the interface, like the multi-level methods, formulations based on adapted grids, and the use of unstructured meshes. This work is limited to VOF.

Despite all the advances in volume-tracking methods (VOF), there are several disadvantages. For example, traditional and high-order/high-resolution techniques used to solve the advection equation have been shown to degrade the interface thickness and shape, regardless of the order of the scheme (Rider et al., 1995; Kothe et al., 1996; Kothe, 1998), unless special downwinding schemes or interface reconstructions are employed, like in the flux-corrected transport algorithm (FCT-VOF) of Rudman (1997) or the piecewise parabolic method (PPM) of Miller and Colella (2002). First-order VOF methods suffer from the so-called "flotsams" or "wisps", which are lumps of dispersed or matrix fluid not fluxed properly. This problem has been mitigated by using redistribution algorithms (Harvie and Fletcher, 2000).

The surface-tension force acting on an interface has been successfully implemented with the continuum surface force model (CSF) of Brackbill et al. (1992), where the interfacial force is expressed as a force per unit volume. The extent of this force is determined by a discrete delta function which smooths the jump conditions ideally present across an interface. An alternative technique based on the ghost fluid method (GFM) and LS imposes a sharp boundary condition where surface-tension forces are present, but it was shown to develop serious spurious currents and lack of mass conservation (Liu et al., 2000). A sharp surface-tension force (SSF) was also implemented on a VOF method by using the reconstructed distance function (Francois et al., 2006). Within a volume-tracking framework, the CSF method yields a continuous pressure

distribution across the interface characterized by a first-order convergence in space, meanwhile the SSF method yields a sharp jump which shows second-order convergence in space. However, both methods show the same error of the spurious currents, which are artificial vortex-like structures created by a large body force that leads to an increase in flow acceleration, especially critical on the region with lower density, that may disrupt the interface and conduce to a failure of convergence, even on grid refinement. Additionally, for the static-drop problem, it was shown how the magnitude of the spurious currents at the interface depends on fluid properties, according to $u \simeq C\sigma/\eta$, and the curvature model, but not on the surface-tension model (CSF or SSF), meanwhile the error in pressure depends primarily on the surface-tension model. In the static drop problem, the constant of proportionality C adopts values of 0.01 in the VOF method of Lafaurie et al. (1994), 10^{-4} in the parabolic reconstruction method of Renardy and Renardy (2002) (both with uniform properties), and 10^{-5} in the the connected marker method of Tryggvason and coworkers (Scardovelli and Zaleski, 1999). The spurious currents also depend on other parameters, as it was shown to be slightly smaller when the time step Δt was reduced; they tended to increase slightly when the density ratio ρ_{out}/ρ_{in} was increased (the converse test was not performed); and they were reduced considerably by increasing the internal fluid density, following $u \sim \sigma \Delta t E \left(\kappa\right)^2 / \rho_{in}$, where E is the error in curvature (Francois et al., 2006). A simple analysis can show that the numerical imbalance between the surface-tension force and the pressure gradients is the cause of the spurious currents. It was argued that these parasitic currents appear due to the existence of nonparallel terms between the gradient of the curvature and the gradient of the volume fraction, as shown from the nonzero curl components of the surface tension force, $\mathbf{F}_s$, given by $\nabla \times \mathbf{F}_s = \sigma \nabla \kappa \times \nabla F$ (Kothe, 1998). If further reduction is desired, the gradient of the curvature must be parallel to the gradient of volume fraction.

The effect of a surface-tension force dominating over inertial or viscous forces was discussed by Tong and Wang (2007) for the relaxation dynamics of an elongated ligament and the droplet pinch-off mechanism. For a CSF approach, the spurious currents grew initially and then disappeared after inertia took place as a dominant force. However, for the pressure boundary method (PBM), no spurious currents were observed at any stage. Based on a different approach, energy conservation, a method capable of eliminating the spurious currents completely was developed by Jamet et al. (2002).

A comparison between several advection/transport techniques using VOF was performed by Rudman (1997): the simplified line interface calculation (SLIC, piecewise constant) method of Noh and Woodward (1976), the VOF method of Hirt and Nichols (1981) (piecewise constant), the piecewise linear interface construction method (PLIC) of Youngs (1982) and the flux-corrected transport algorithm (FCT). The FCT-VOF does not require approximate interface reconstructions and maintains sharp interfaces. Different test problems, like the linear advections, rigid-body rotations and shear flows, show how the method originally

proposed by Youngs was superior, while the FCT-VOF performed slightly better than SLIC and the method of Hirt and Nichols.

Several multi-dimensional fluxing schemes have been proposed. The first-order defined donating region (DDR) method of Harvie and Fletcher (2001) is a piecewise linear scheme that integrates cell boundary fluxes geometrically and provides exact mass conservation. The second-order methods of Puckett et al. (1997) and Rider and Kothe (1998) increases the complexity by extending the donating region to adjacent cells. Another fluxing strategy is the Stream scheme of Harvie and Fletcher (2000), which is a fully multidimensional boundary flux integration technique based on the calculation of the volume of several streamtubes at a control surface. The Stream scheme shows first to second-order convergence on mesh refinement in the single-vortex test, depending on the reconstruction method used. Several multidimensional schemes require volume redistribution to conserve mass. High-order multidimensional fluxing schemes have been achieved, like the fourth-order DRACS (donating region approximation by cubic splines) method of Zhang (2013).

Among various methods that reconstruct an interface following a case-by-case procedure in 2D are the linear method of FLAIR Ashgriz and Poo (1991) and the second-order method of Kim and No (1998). Second-order case-by-case reconstructions are in general avoided because of the excessive amount of cases. In 3D and considering second-order reconstructions, the parabolic reconstruction of surface tension (PROST) method of Renardy and Renardy (2002) was capable of predicting deformation and breakup of drops accurately.

When comparing PLIC-based methods, the accuracy is determined by the error incurred in the reconstruction (calculation of the interface normal vector) and the fluxing. A sufficient condition to reconstruct smooth interfaces with second-order accuracy is for the algorithm to reproduce linear/planar interfaces exactly (Pilliod and Puckett, 2004). The method of Youngs computes the normal vector explicitly from the volume fractions and is first-order accurate, while the full least-squares minimization or Swartz's method is second-order (Rider and Kothe, 1998). Other methods that achieve second-order accuracy on smooth interfaces are the minimization methods of LVIRA (Puckett, 1991) and ELVIRA (Pilliod, 1992). When the interface presents sharp corners, second-order methods like ELVIRA reduce their accuracy to first order (Zhang, 2013).

An important quantity that determines the accuracy of the solutions in multiphase flows involving surface-tension forces is the the curvature. Among different techniques used to compute the curvature, the height function (HF) method offers second-order convergence on mesh refinement (Sussman, 2003; Francois et al., 2006; Ferdowsi and Bussmann, 2008; Liovic et al., 2010). Despite the advances in the field with the HF method since the work of Helmsen et al. (1997), hybrid methods, like the "best candidate" method of Liovic et al. (2010) that selects the curvature from different stencils/methods, seem to be the solution to overcome the errors incurred when using the traditional HF methods. The largest error in curvature using the HF

method was reported to occur in regions where the components of the normal vector at the interface are of similar magnitude and when the radius of curvature is comparable or smaller than the grid size Cummins et al. (2005). By advecting the normal vector, Raessi et al. (2007) introduces another approach that produces curvatures with second-order convergence. In comparison, traditional level-set methods show no convergence.

Here, VOF methods are compared using classical problems involving viscous flows. A simplified method to transport the volume fraction, denoted as BDR, is compared with the DDR method. The semi-analytical DDR method here developed was tested for different problems in 3D. The use of multi-step methods is discussed. The static-drop problem is included to conclude on the accuracy of the pressure jump and the curvature. The nonlinear oscillation of an initially-deformed drop is studied to determine the accuracy, robustness and long-term stability when different transport models are employed. Finally, the deformation and breakup of a drop in a simple shear flow is considered, for strong-wall effects.

2.1.4 Typical difficulties in VOF simulations

The principal concern in VOF is the methodology or set of models needed to transport different phases in a given flow. Starting with the number of phases, the mixture model or the n-fluid model can be adopted. For more than two phases, the complexity of the problem increases and certain simplifications must be made in the submodels, which are expected to increase the numerical error. For instance, if advective-diffusive schemes are employed, the subgrid location of each interface is not know, or if sharp schemes are used (i.e. SLIC, PLIC, PROST), only an approximation of the interface is known. In the case of PLIC-like schemes, the method used for the interface reconstruction plays a relevant role in the final error.

One typical problem in VOF is the wisp generation. Several techniques have been made to mitigate the wisp generation, like volume redistributions, volume limiters, among others, but they could introduce other problems, for instance, more computational effort and issues with mass conservation. Some of these techniques are described in this work.

When surface-tension forces are considered, there are four main concerns: the undesired effects of the parasitic currents which are velocities that appear due to numerical imbalances (not fully resolved, but can be mitigated), the sharpness of the interface, that is, the number of cells associated with the jump in pressure or volume fraction, the numerical diffusion or smearing of the volume fraction F, and the accuracy of the force or the interface curvature. Another problem associated with the interface sharpness and accuracy is the creation of stairs, which is common in low-order methods when the interfaces are inclined with respect to the grid.

Spurious Currents are small as long as the Ohnesorge number is sufficiently large,

$$Oh = \sqrt{Ca/Re}$$

where Ca is the capillary number, typically written as $Ca = \mu U/\sigma$, and Re is the Reynolds number, defined as $Re = \rho UR/\mu$. The spurious currents do not disappear with mesh refinement, leading to non convergence of the method (Renardy, 2002). For low Re and moderate to large Ca, the spurious currents are small, but they become a problem when Ca is small and large Re. Their growth is explained in section 2.1.3.

2.2 Particle Interaction and Viscoelastic Fluids

2.2.1 Viscoelastic fluids and Dimensionless Numbers

A viscoelastic fluid exhibits a combination of both elastic and diffusive properties which are time dependent. Several models have been proposed to characterize this type of fluids, where their success is limited to the complexity of the molecules in question. Because the elastic component is always present, it serves as a reference among several models. The dimensionless numbers that scales with Maxwellian models are the Deborah number De, Weissemberg number Wi, particle Reynolds number Re_p, elasticity number E, and viscoelastic Mach number M (Huang and Joseph, 2000), commonly defined as,

$De_p = \frac{\lambda_1 U_o}{a} \qquad De_w = \frac{2\lambda_1 U_o}{W} \qquad Wi = \lambda_1 \dot{\gamma}$

$Re_p = \frac{2\rho_f U_o a}{\eta_o}$

$E = \frac{\text{Elastic Stress}}{\text{Inertial Stresses}} = \frac{Wi}{Re} = \frac{\lambda_1 \eta_0}{2a^2 \rho_f}$

$M = \frac{U}{c}$

where λ_1 is the relaxation time, a is the radius of a sphere, U_o is the characteristic velocity, c is the viscoelastic wave speed, η_o is the zero shear viscosity and ρ is the density.

For $M \ll 1$ the dynamics of linearized Maxwell models is determined by Re and De, and for supercritical conditions $M \gg 1$ it is useful to use M and E. For transcritical flow the important dimensionless parameters are Mach number M and elasticity E (Joseph, 1990). For the Jeffreys-like models, another set of parameters should be added based on retardation to relaxation time ratio (λ_2/λ_1) and mobility factor (α).

2.2.2 Particle Migration

When a particle is let free in a viscoelastic fluid flow the inertia of the particle during the start-up process has the strong effect of changing normal stresses with respect to Newtonian case, producing particle migration and agglomeration. In previous years, understanding the effect of the polymer stress was carried out with the analysis of flows around bodies in second order fluids(Joseph et al., 2007), using asymptotic analysis and

constitutive equations, local similarity solution (Zheng et al., 1990), and numerical simulations in 2D (planar and axisymmetric).

Numerical simulations of cylinders in viscoelastic shear flow (D'Avino et al., 2010a) show how the migration of a particle always tend towards the closest wall; with a linear Maxwellian liquid the conclusion is that normal stresses are the only responsible that causes the migration, irrespectively of any thinning of the rheological properties. It was compared with a Newtonian case, where the absence of inertia produce no migration while its presence could generate migration towards the channel center plane (Halow and Wills, 1970; Ho and Leal, 1974). The angular velocity of the particle decreases as the particle approaches the wall and as the Deborah number increases (D'Avino et al., 2010b).

The same research group use numerical simulations of cylinders in Poiseuille flow (Villone et al., 2011) of viscoelastic fluid (Giesekus Model), showing a cross-streamline particle migration, where large Deborah number and shear thinning speed up the migration velocity. If the particle is small compared to the gap (small confinement), then the particle migrates towards the channel centerline or the wall, depending on its initial position. A critical value of confinement for larger particles is reported (in agreement with (Huang et al., 1997)), above which the channel centerline is no longer attracting and the particle is predicted to migrate towards the closest wall when its initial position is not on the channel centerline. As the particle approaches the wall, the translational velocity in the flow direction is found to become equal to the linear velocity corresponding to the rolling motion over the wall without slip.

Numerical simulations of particle migration in Couette, Poiseuille and settling flows (2D) was performed (Huang et al., 1997) and are in agreement with recent research. For a shear flow it is shown that below certain critical conditions given by a relationship between Deborah De and Reynolds Re numbers, the particle reaches an equilibrium position at the centerline of the channel, regardless of its initial position and velocity. If the Reynolds number is increased, the particle is pushed away from the sidewall and moves toward the centerline, very fast when inertia is strong. If the convective term is neglected (Stokes flow) then the particle stays very close to the wall. When De is increased, the particle tendency is to migrate towards the wall and the motion is enhanced with shear thinning. This behavior is explained as a balance of lubrication forces at the side near the wall and normal compressive stresses generated on the other side. This effect is strengthened when the blockage is increased, while for small blockage, the wall attraction becomes minimal and the normal stress generates a lift force that equilibrates at the centerline where the shear rate is zero.

More on the particle equilibrium can be found (Ko et al., 2006), where diagrams for unstable and stable positions are show.

2.2.3 Particle Chaining

Another branch of investigations are focused on demonstrating the chaining behavior of multi-particle-shape systems. Experimental (Wang et al., 2004) and numerical results (Hao et al., 2009) show a particular behavior of solid bodies within a non-Newtonian fluid when compared with a Newtonian one. For example, long bodies settling in a viscoelastic fluid align the long side parallel to the stream, contrary to a Newtonian fluid where they put their broadside perpendicular to the stream. A system of particles in a Newtonian fluid exhibit the principal iterations described by the process of drafting, touching, tumbling and separation, and in a viscoelastic fluids it is possible to have reorientation followed by particle chaining instead of separation, since tensile forces keep the particles in contact (Joseph et al., 2007).

This behavior of a progressive draft combined with rotation that leads to the final end-to-end sedimentation of two particles has been reproduced numerically using an Oldroyd-B fluid (Boger fluid) Hao et al. (2009). When two spheres are released from rest in a Boger fluid, the spheres achieve a unique stable final distance, independent of the initial separation distance, but determined by the point where the velocities of the two sphere become the same. This stable arrangement is a result of the effect of an upper sphere with an increased velocity, compared to a single sphere, which is more or less independent of the position of the lower sphere, and the velocity of a lower sphere which is dependent on the actual separation distance, i.e. the velocity is similar to that of a single sphere for large distances and it increases for small distances, where the development of a wake is inhibited (tension is reduced on the backside region of the particle). The stable separation distance increases with the Deborah number, De, and decreases with a/R Bot et al. (1998). When the fluid is shear-thinning instead of Boger, spheres attract each other within a critical distance.

When a system of particles initially dispersed are subject to a shear flow in a Boger fluid they keep dispersed, but when shear thinning is considered, they form chains, showing how shear thinning should play a key role in chaining even though the first normal stress difference may be responsible for the movement across the main flow direction Won and Kim (2004).

Numerical simulations were performed to analyze the interaction of particles in a viscoelastic Oldroyd-B fluid (Boger fluid) subject to shear flow, and it was found how two particles close enough shows a behavior that can be described as a kissing-tumbling-tumbling phenomena: a continuous rotation around each other (confirmed in 2D and 3D) (Hwang et al. (2004), Yoon et al. (2012)). There are three mechanism found depending on the initial separation and We: pass, tumbling and return, being tumbling in between a pass and a return. The same group studied the alignment of particles in a confined shear flow using a Giesekus fluid (shear-thinning fluid) Choi and Hulsen (2012), and it was shown how particles form a string-like structure, where the final state is independent of the initial particle distribution or the histories to reach the steady-state.

As the Weissenberg number increases, particles can form longer strings, but the maximum obtainable length of a string of particles is limited by the fluid rheology. Moderate wall confinement promotes the alignment of particles, however, too strong confinement hinders the alignment by enhancing repulsive interaction between particles (wall migration). The steady-state angular velocities of particles were compared with respect to the length of strings. The the two end-particles shows larger angular velocity than those in between, and the non end-particles share the same angular velocity. If the string length increases, for a string with more than 3 particles, the steady-state angular velocities of the two end-particles do not change significantly, while those of the non end-particles increase. Also, as the string length increases, the inter-particle distance increases.

The trajectory of particles in shear flow could create close orbits, if the initial separation is not large, for given Wi number. This might suggest that in a system of many particles, concentration of particles will determine the level of chaining.

In the work of Yoon et al. (2012) two particles in a simple shear flow have three mechanism of interaction depending on the initial location of the particles: passing, tumbling and returning. The particles return when they are relatively close to the centerline. As the vertical distance is increased, for a given horizontal separation, there is a critical value for which the particles do no longer return. For Newtonian fluids, the particles pass over each other after this critical point. For viscoelastic fluids, there is a range where the particles exhibit tumbling. Increasing the vertical separation in viscoelastic fluids creates a second critical point where tumbling changes to passing. The range between the initiation and ending of tumbling for increasing initial separations is proportional to Weissenber number. These mechanisms can be the explanation for the statistical creation of doublet, triplets and larger conglomeration of particles in shearing flows. The initial concentration will then determine the possibilities for any two particles to enter in tumbling trajectories based on current trajectories and similarly for larger systems of particles.

The mechanisms described for two particles interacting in simple shear flows of Newtonian fluids play an essential role in describing their behavior when a drop is included.

2.2.4 Particulate Flows

In the case of numerical simulation of planar flows and many particles under pressure driven planar flows (Huang and Joseph, 2000), it was observed that shear thinning has a large effect when the inertia or elasticity is large, but only a small effect when they are small. At moderate Reynolds numbers, shear thinning causes particles to migrate away from the centerline, creating a disk particle-free zone in the core of the channel. In a viscoelastic fluid with shear thinning, particles migrate either toward the centerline or toward the walls, creating an annular particle-free zone. With $Re = 0.156$, $De = 2.5$ and $M = 0.625$ and without shear thinning it was shown that the particles move toward the centerline of the channel by the effect of forces

arising from viscoelastic normal stresses. Since the particles are small, that is in agreement with the results for one particle, where it should migrate toward the centerline.

2.2.5 Numerical Methods and Benchmarks

For an area of study with only a few numerical works in certain flows it is important to rely on accurate benchmarks and analytical solutions. For a Jeffreys' like constitutive model, the proper set up of the boundary conditions is an issue, commonly resolved with periodic boundaries, or by placing boundaries (inconsistent with the viscoelastic model) away of the area if interest.

Available numerical solutions are the flow past a cylinder, flow past a sphere in a pipe with obstruction $\beta = 0.5$, a flow in a channel with a sudden contraction $4:1$, the unbounded rotation of a sphere, settling of a particle. The flow over a sudden contraction is commonly the selected benchmark to study spatial accuracy. It also possible to use the analytical solution of the starting flow in a channel or a cylinder, where the transient and spatial scheme can be compared. When studying particles, the common benchmarks are flow past a sphere (Lunsmann et al., 1993) and sedimentation of a sphere in a cylinder (Becker et al., 1994).

The breakdown of the numerical methods after a certain De has been related to the lack of positive definiteness preserving property of the conformation tensor at the discrete level during the entire time integration (Hao et al., 2009). There are many techniques used to increase the breakdown Deborah number De_b: the streamwise upwinding scheme (Crochet et al., 1984); streamline upwind Petrov-Galerkin (SUPG) method; the Explicitly Elliptic Momentum Equation (EEME) method for Upper Convected Maxwell models (UCM) with no solvent viscosity; the Elastic Viscous Split Stress formulation (EVSS) using differential models or using integral methods (INT) (Rajagopalan et al., 1993, 1996) for fluids with Newtonian solvent, like Oldroyd-B, Giesekus and Phan-Thien models.

2.2.6 Drop puncturing in shearing flows

A numerical simulation using a finite-volume algorithm simulated the deformation and breakup of a drops in particulate shear flows (Ardekani et al., 2008). The results show that the presence of particles leads to larger droplet deformation. In some cases a perforation occurs in the center of the droplet as particles approach toward each other. The perforation is shown to depend on the Stokes number. The critical value of the Stokes number correlates linearly with with the inverse of the capillary number and viscosity ratio. Large values of the capillary number are needed to have puncturing.

Chapter 3

Objectives

General Objective:

Study the breakup and interaction of rigid and deformable particles in shearing flows for Newtonian and viscoelastic fluids using numerical simulations.

Specific objectives:

- Development of a numerical code to simulate transient multiphase and multi-physic phenomena of non-Newtonian fluids and rigid/elastic/viscoelastic solids.
- Analyze the accuracy of the sub-models employed.
- Study the effects of Reynolds number, Capillary number, viscosity ratio, elasticity, viscoelasticity and blockage ratio on the breakup of deformable particles surrounded by rigid particles after applying a simple shear flow (cell lysis).
- Study the viability of breaking up drops in abrupt expansions and gravity driven flows.
- Study the effect of membrane elasticity and fracture strength on the deformation and breakup of a punctured deformable particle due to a rigid particle (not completed).
- Study the effect of shear thinning and viscoelasticity on the motion of two particles settling side-by-side in a viscoelastic Oldroyd-B or FENE-type fluids: drafting or separation (dropped objective).

Hypothesis

- Rigid particles that are large enough and critically localized can deform and break drops under low Reynolds number, Re, and low Capillary number, Ca, for a simple shear flow (Solved). Also, viscoelastic membranes can deform and break up for low dimensionless shear rate number, G, when relatively large particles are included (Partially solved).

- Two particles sedimenting side by side can experience attraction only for a range of Re and De, or E and M (Not solved).

- Shear-thinning effects speed up the drafting process between two particles settling side-by-side (Not solved).

Chapter 4

Problem formulation

The problem of an isothermal incompressible, immiscible and viscous drop and rigid particles is modeled with a classical two-fluid mixture model, where an interface divides the dispersed phase, denoted by "d", from the medium "m". In this model, the velocity field is a mixture-averaged velocity, instead of the velocity for each phase. Fluid properties are functions of the volume fraction, F, defined as $F = \mathcal{V}_d/\mathcal{V}_{cv}$, where $\mathcal{V}$ is the volume of the dispersed phase or the control volume. The domain Ω is union of the domain of the medium, Ω_m, with the domain of the drop, Ω_d, the rigid particles, Ω_p, and/or the membrane, Ω_M, depending on the case. The motion of the drop interface is obtained by solving the conservation laws, together with the advection equation of the volume fraction. The motion of the rigid particles is determined after balancing the rigidifying forces that complies with the rigid body motion constrain and the hydrodynamic forces. In the case of the membrane, the dynamics of an elastic solid is coupled with the fluid motion using natural boundary conditions.

4.1 Governing equations

In general, conservation of mass is given by,

$$\frac{\partial \rho}{\partial t} + \nabla \cdot (\rho \mathbf{u}) = 0$$

which reduces to the continuity equation for incompressible fluids,

$$\nabla \cdot \mathbf{u} = 0 \qquad \text{on } \Omega \tag{4.1}$$

In the case of a two fluid mixture, density is given by $\rho = \rho_1 + (\rho_2 - \rho_1) F$. The volume fraction or color

function, F, is transported by the advection equation, written in conservative form as,

$$\frac{\partial F}{\partial t} + \nabla \cdot (F\mathbf{u}) = F \nabla \cdot \mathbf{u} \qquad \text{on } \Omega \tag{4.2}$$

Conservation of linear momentum can be written in conservative form as,

$$\frac{\partial (\rho \mathbf{u})}{\partial t} = \nabla \cdot (-\rho \mathbf{u}\mathbf{u} + \boldsymbol{\tau}) - \nabla p + \mathbf{f}^{CSF} + \mathbf{f}_{DLM} + \rho \mathbf{g} \qquad \text{on } \Omega \tag{4.3}$$

where $\mathbf{u}$, $\boldsymbol{\tau}$, p, $\mathbf{f}^{CSF}$ and $\mathbf{f}_{DLM}$ are the mixture velocity, viscous-stress tensor, pressure, surface-tension force per unit volume and rigidifying force per unit volume, respectively. For a Newtonian fluid the viscous stress or extra stress tensor is given by $\tau_{ij} = 2\eta\dot{\gamma}_{ij}$, where the strain-rate tensor is given by $\dot{\dot{\gamma}}_{ij} = \frac{1}{2}\left(\frac{\partial u_i}{\partial u_j} + \frac{\partial u_j}{\partial u_i}\right)$. For a mixture, the viscosity can be weighted using a linear profile or the arithmetic mean as $\eta = \eta_m + (\eta_d - \eta_m) F$, or using the harmonic mean as $\eta = \left(\frac{F}{\eta_d} + \frac{1-F}{\eta_m}\right)^{-1}$. For a non-Newtonian fluid, the extra stress tensor can be decoupled into the polymer, $\boldsymbol{\tau}_p$, and the solvent, $\boldsymbol{\tau}_s$, contribution (Bird et al., 1977) as $\boldsymbol{\tau} = \boldsymbol{\tau}_s + \boldsymbol{\tau}_p$, where the solvent stress behaves like a Newtonian fluid and the polymer extra-stress depends on the viscoelastic fluid in consideration.

In the case of an incompressible solid, a material or Lagrangian frame of reference is employed and the equations of motion are,

$$\frac{\partial (\tilde{\mathbf{u}})}{\partial t} = \tilde{\mathbf{v}} \qquad \rho_o \frac{\partial (\tilde{\mathbf{v}})}{\partial t} = \nabla \cdot \mathbf{S} + \mathbf{f}_{ext\,o} + \rho_o \mathbf{g} \qquad \text{on } \Omega_M \tag{4.4}$$

where $\tilde{\mathbf{u}}$ is the displacement, $\tilde{\mathbf{v}}$ is the material velocity, $\mathbf{S}$ is the second Piola-Kirchhoff stress tensor, which reduces to the Cauchy stress tensor, $\boldsymbol{\sigma}$, for infinitesimal deformations, the subindex o indicates the reference configuration and $\mathbf{f}_{ext}$ includes any external force like the hydrodynamic forces. Body forces per unit volume are included as $\rho\mathbf{g}$ for the solid and the fluid.

The boundary conditions are prescribed velocity,

$$u_i = U_i(\mathbf{x}) \qquad \text{on } \partial\Omega \tag{4.5}$$

prescribed pressure with normal velocities,

$$\begin{aligned} \frac{\partial u_i}{\partial x_n} &= 0 \\ p &= P(\mathbf{x}) \end{aligned} \qquad \text{on } \partial\Omega \tag{4.6}$$

and symmetry,

$$
\begin{aligned}
u_n &= 0 \\
\tfrac{\partial u_t}{\partial x_n} &= 0 \qquad \text{on } \partial\Omega \\
\tfrac{\partial p}{\partial x_n} &= 0
\end{aligned}
\tag{4.7}
$$

where n and t denote normal and tangential direction, respectively.

4.1.1 Surface-Tension Force

The surface-tension force exerted on two immiscible fluids divided by interface was formulated by Brackbill et al. (1992) in terms of a force per unit volume as $\mathbf{F}^{CSF} = \int \sigma\kappa\left(\mathbf{x}_s\right)\hat{\mathbf{n}}\left(\mathbf{x}_s\right)\delta\left(\mathbf{x}-\mathbf{x}_s\right)d\mathcal{V}$, where σ is the surface-tension coefficient, κ is the local curvature, $\hat{\mathbf{n}}$ is the unit-normal vector at the interface, $\mathbf{x}_s$ is the location of the interface, $\mathbf{x}$ is the position, and δ is the distance function related to the jump condition $[F] = 1$. Following the continuum surface force model (CSF), the force per unit volume at the interface is Francois et al. (2006),

$$
\mathbf{f}^{CSF} = \sigma\kappa\frac{\nabla F}{[F]} \tag{4.8}
$$

Two typical methodologies to mollify the CSF force include the scaling by density or volume fraction. The density-scaled CSF can be used for high density ratios and is given by,

$$
\bar{\mathbf{f}}^{CSF} = \frac{\rho}{\bar{\rho}}\mathbf{f}^{CSF}
$$

while the volume-fraction-scaled model can be used to treat the spurious currents and is given by van Sint Annaland et al. (2005),

$$
\mathbf{f}^{CSF} = 2F\sigma\kappa\nabla F
$$

4.1.2 The Distributed Lagrange Multiplier Method

Rigid particles are introduced into the domain with the Distributed Lagrange Multipliers method (DLM). In this method, a rigidifying force is added as an external force in such a way that the local domain, Ω_p, moves as a rigid body. The benefit of this method is that it avoids the necessity of re-meshing every time step and the calculation of the hydrodynamic forces acting on boundary of the solid. The penalty for simplicity is the accuracy of the velocity field and therefore, the viscous stress acting on the solid region. The particle is considered to be rigid or non-deformable and it shares the velocity field of the fluid $\mathbf{u}$ (Eulerian framework) by means of the particulate volume-fraction field, ϕ_s, which permits the calculation of the particle position

and velocity. Hydrodynamic forces and torques that determine the motion of the particle cancel with its reaction when the weak formulation for the combined fluid-particle system is formulated (Yu et al., 2002). For simplicity, the stress tensor and pressure field are unified in the whole field. The method of the distributed Lagrange multipliers (Ardekani et al., 2008) is used to rigidify the particle i. The new stress for the body is,

$$\sigma_{S\,i} = -p\mathbf{I} + \mathbf{D}\left(\boldsymbol{\lambda}\right) \tag{4.9}$$

This model for the particles gives rise to a stress field in $\Omega_{p\,i}$ that is a function of the Lagrange Multipliers $\boldsymbol{\lambda}_i$. The problem is constrained in such that each particle i satisfies a rigid body motion in a body-fixed frame of reference that is located at the center of mass. The velocity of the particle "i" is given by,

$$\mathbf{u}_{p\,i} = \mathbf{u}_{cm\,i} + \boldsymbol{\omega}_i \times \left(\mathbf{r}_{\Omega_p} - \mathbf{r}_{cm\,i}\right) \tag{4.10}$$

that is $\mathbf{u}_{cm} = \mathbf{u}_{cm}\left(t\right)$ and $\boldsymbol{\omega} = \boldsymbol{\omega}\left(t\right)$. On the interface, the non slip conditions between the surrounding fluid and the particle defines the constrain,

$\mathbf{v}_i\left(\mathbf{r}_{\mathcal{S}_{p\,i}}\right) = \mathbf{u}$

where $\mathbf{r}_{\Omega_p}$ denotes any material position of the domain Ω_p seen from the main system and is bounded by the interface $\mathcal{S}_{p\,i} = \partial\Omega_{p\,i}$.

The rigidifying force converts subspace Ω_m into Ω_p. This force is given by,

$$\mathbf{f}_{DLM}^{m} = \sum_{j=1}^{m} \delta\mathbf{f}_{DLM\,j} \tag{4.11}$$

$$\delta\mathbf{f}_{DLM} = \begin{cases} C\left(\mathbf{u} - \mathbf{u}_R\right) & \text{on } \Omega_p \\ 0 & \text{on } \Omega_m \end{cases} \tag{4.12}$$

where m is the last corrected sub-step, C is a constant, $\mathbf{u}$ is the velocity field and $\mathbf{u}_R$ is the relative velocity between the fluid and the particle,

$$\mathbf{u}_R = \left(1 - \phi_s\right)\mathbf{u} + \phi_s\mathbf{u}_p \tag{4.13}$$

Notice how $\mathbf{f}_{DLM}$ vanishes for $\mathbf{u} = \mathbf{u}_R = \mathbf{u}_p$ regardless of ϕ_s. The position $\mathbf{r}_{cm}$, the velocity $\mathbf{u}_{cm}$, the angular velocity $\boldsymbol{\omega}_{cm}$ and moment of inertia $\mathbf{I}_{cm}$ of the center of mass are expressed as,

$$\mathbf{r}_{cm} = \frac{1}{m_p}\int_\Omega \rho\phi_s \mathbf{r} d\mathcal{V}$$
$$\mathbf{u}_{cm} = \frac{1}{m_p}\int_\Omega \rho\phi_s \mathbf{u} d\mathcal{V}$$
$$\mathbf{I}_{cm}\cdot\boldsymbol{\omega}_{cm} = \int_\Omega \rho\phi_s \mathbf{r}_p \times \mathbf{u} d\mathcal{V}$$
$$\mathbf{I}_{cm} = \frac{1}{m_p}\int_\Omega \rho\phi_s \left[\mathbf{r}_p\cdot\mathbf{r}_p\,\mathbf{1} - \mathbf{r}_p^T\mathbf{r}_p\right] d\mathcal{V}$$

The mass of each particle is obtained by the integration $m_p = \int_{\Omega_p} \rho\phi_s d\mathcal{V}$. Then, motion of the particle "i" is given by,

$$m_{p\,i}\mathbf{a}_i = \mathbf{F}_{h\,i} + \mathbf{F}_{DLM\,i} + \sum_j \left(\mathbf{F}_{c\,ij} + \mathbf{F}_{l\,ij}\right) \tag{4.14}$$

where $\mathbf{a}$ is the acceleration of the unified domain, $\mathbf{F}_h$ is the hydrodynamic force, $\mathbf{F}_{DLM} = \int_\Omega \mathbf{f}_{DLM} d\mathcal{V}$ is the rigidifying force, $\mathbf{F}_c$ is the collisional force and $\mathbf{F}_l$ is the lubrication force between particles i and j.

Collision and lubrication force

In lubrication theory, two smooth interfaces moving towards each other will never touch. As the distance diminishes, the force on the objects increases and physical contact is avoided. When this phenomena is modeled numerically, the discretization in time and space introduces error. The surface also presents a rugosity, which can deform and trap fluids as the interfaces get closer. To overcome the complexity of this problem, two typical forces are included: collisional forces, where a region of overlapping geometry is considered, and the lubrication force.

Using a discrete element method (DEM), the collision force is given by a linear mass-spring-dashpot model (Cundall and Strack, 1979). Considering that we encountered sufficient elastic reduction just from the transformation from DEM to DLM when the gap between particles is relatively small (less than 4 cells), only the elastic contribution is used,

$$\mathbf{F}_{c\,ij} = \begin{cases} k\delta\mathbf{r}_{ij} & \text{for } i \neq j \\ 0 & \text{for } i = j \end{cases} \tag{4.15}$$

where $\delta\mathbf{r}_{ij} = \left(R_{p\,i} + R_{p\,j} + \epsilon - |\mathbf{r}_{cm\,i} - \mathbf{r}_{cm\,j}|\right)\hat{\mathbf{r}}_c$ is the overlapping displacement between two solids, $\hat{\mathbf{r}}_c = \left(\mathbf{r}_{cm\,i} - \mathbf{r}_{cm\,j}\right)/|\mathbf{r}_{cm\,i} - \mathbf{r}_{cm\,j}|$ and k is the rigidity that determines the degree of deformation. Large overlapping regions are present for relatively small values of k. In the other hand, the stability of the numerical method is compromised when k is relatively large. The constant k is estimated as $K\langle\rho\rangle U_{ij}^2\langle R_p\rangle$, where $K = 1 - 100$.

When two interfaces are approaching each other and the separation between them is around or less than the size of a cell, the pressure is in large error. To compensate for a such problem, a lubrication force can be added to compensate for the errors in pressure.

$$\mathbf{F}_{l\,ij} = \begin{cases} -\frac{3}{2}\pi\eta R_p^2 \left[(\mathbf{u}_i - \mathbf{u}_j)\cdot\hat{\mathbf{r}}_c\right]\left(\frac{1}{\delta h_{l\,ij}} - \frac{1}{\epsilon_l}\right)\hat{\mathbf{r}}_c & \delta h_{l\,ij} < \epsilon_l \\ 0 & \delta h_{l\,ij} \geq \epsilon_l \end{cases} \tag{4.16}$$

where $\epsilon_l = \frac{2}{3}\Delta x$ and $\delta h_{l\,ij} = |\mathbf{r}_{cm\,i} - \mathbf{r}_{cm\,j}| - (R_{p\,i} + R_{p\,j})$.

Boundary conditions

The boundary conditions are not automatically satisfied by the Equation (4.12) because the cell velocity is given by the contributions of the fluid and the solid and those velocities are not necessarily the same, only for special cases. This problem introduces considerable errors that affect the stress at the interface. Our early attempts to included interface interpolating techniques showed lack of mass conservation and were avoided. A simple solution is then adopted, the fluid and the particle share the same velocity in a mixed region. Thereby, Equation (4.12) can be used. A better solution for this problem should be based on geometric fluxing, but it was not researched (only partially employed on the drops).

The constant K determines the stability and convergence of the method. The convergence increases for larger values of C, but convergence is lost if K is too large.

4.1.3 Viscoelastic Models

Oldroyd-B is the viscoelastic model used to describe Boger fluids, which is characterized by a rheology where shear-thinning effects are absent. It is preferred in shear flows, since its elongational viscosity is unbounded, thus not suitable for extensional flows when $De \gtrsim 1$. The mathematical model of the solvent and polymer extra-stress of an incompressible solution are Bird et al. (1977),

$$\boldsymbol{\tau}_s = \eta_s \mathbf{A} \tag{4.17}$$

$$\boldsymbol{\tau}_p + \lambda_1 \overset{\triangledown}{\boldsymbol{\tau}}_p = \eta_p \mathbf{A} \tag{4.18}$$

where $\lambda_1$is the relaxation time and λ_2 is the retardation time; η_0, η_s,η_p are the zero shear, solvent and polymer viscosities, respectively, following the relations $\eta_0 = \eta_s + \eta_p$, $\eta_s = \eta_0\lambda_2/\lambda_1$, $\eta_p = \eta_0\,(1 - \lambda_2/\lambda_1)$ and $\lambda_2 = \frac{\lambda_1\eta_s}{\eta_p+\eta_s}$; $\mathbf{A}$ is the first Rivlin-Ericksen tensor, $\mathbf{A} = 2\mathbf{D} = \mathbf{L} + \mathbf{L}^{\mathrm{T}}$ and $\mathbf{L}$ is the velocity gradient

$\mathbf{L} = (\nabla \mathbf{u})^{\mathrm{T}}$; the lower triangle represents the upper convected time derivative,

$$\overset{\triangledown}{\boldsymbol{\tau}} = \frac{\mathrm{d}\boldsymbol{\tau}}{\mathrm{d}t} - \mathbf{L} \cdot \boldsymbol{\tau} - \boldsymbol{\tau} \cdot \mathbf{L}^{\mathrm{T}} \tag{4.19}$$

Giesekus model can be applied to extensional flows, since its elongational viscosity is bounded, contrary to Oldroyd-B model, but one must retain the solvent effect, that is, some retardation λ_2 is required. The difference with Oldroyd-B fluid is the shear-thinning term, determined by the mobility factor α. Following the definitions from Oldroyd-B constitutive model, the polymer extra-stress for the Giesekus model is Bird et al. (1977),

$$\boldsymbol{\tau}_p + \lambda_1 \overset{\triangledown}{\boldsymbol{\tau}}_p + \alpha \frac{\lambda_1}{\eta_p} \left[\boldsymbol{\tau}_p \cdot \boldsymbol{\tau}_p\right] = \eta_p \mathbf{A} \tag{4.20}$$

FENE-P A constitutive differential equation for dilute polymer mixtures that considers the interaction of dumbbells molecules (bead-spring) is given by the finite extension nonlinear elastic model, provided with the Peterlin's closure (FENE-P) Bird et al. (1977),

$Z\boldsymbol{\tau}_p + \lambda_1 \overset{\triangledown}{\boldsymbol{\tau}}_p - \lambda_1 \left(\boldsymbol{\tau}_p + (1 - \varepsilon b)\, \frac{\eta_p \mathbf{I}}{\lambda_1}\right) \frac{D \ln Z}{Dt} = (1 + \varepsilon b)\, \eta_p \mathbf{A}$
where $Z = 1 + \left(\frac{3}{b}\right)\left(1 + \lambda_1 \frac{tr\boldsymbol{\tau}_p}{3\eta_p}\right)$ and $\varepsilon = \frac{2}{b(b+2)}$.

4.1.4 Elastic and viscoelastic solid

The simplest model for the stress tensor of a solid is the elastic model, which is isotropic and linear with respect to the Eulerian-Almansi elastic strain $\boldsymbol{\epsilon}^{(e)}$,

$$\boldsymbol{\sigma} = \mathbf{D}\boldsymbol{\epsilon}^{(e)} \tag{4.21}$$

where $\mathbf{D}$ for an elastic material is given by the Lamé equations (3D),

$$\mathbf{D} = \frac{E}{(1+\nu)\,(1-2\nu)} \begin{bmatrix} 1-\nu & \nu & \nu & & & \\ \nu & 1-\nu & \nu & & \mathbf{0} & \\ \nu & \nu & 1-\nu & & & \\ & & & 1-2\nu & & \\ & \mathbf{0} & & & 1-2\nu & \\ & & & & & 1-2\nu \end{bmatrix}$$

where E and ν are the Young modulus and Poisson ratio, respectively. If plasticity takes place,

$\boldsymbol{\epsilon}^{(e)} = \boldsymbol{\epsilon}^{(T)} - \boldsymbol{\epsilon}^{(P)} \qquad \boldsymbol{\epsilon}^{(T)} = \frac{1}{2}\left(\frac{\partial \tilde{u}_i}{\partial x_j} + \frac{\partial \tilde{u}_j}{\partial x_i}\right)$

where $\boldsymbol{\epsilon}^{(T)}$ is the total infinitesimal strain, $\boldsymbol{\epsilon}^{(P)}$ is the plastic strain and x_i is the actual configuration, in contrast with the initial configuration X_i.

For finite strain deformations, it is required to use the appropriate transformation between the undeformed or reference configuration with respect to the deformed or actual configuration. The total Green-Lagrangian strain given in terms of the displacement is,

$$E_{ij}^{(T)} = \frac{1}{2}\left(\frac{\partial \tilde{u}_i}{\partial X_j} + \frac{\partial \tilde{u}_j}{\partial X_i} + \frac{\partial \tilde{u}_k}{\partial X_i}\frac{\partial \tilde{u}_k}{\partial X_j}\right) \tag{4.22}$$

Now, the elastic strain is $\boldsymbol{E}^{(e)} = \boldsymbol{E}^{(T)} - \boldsymbol{E}^{(P)}$. The constitutive equation for an elastic solid reduces to,

$$\boldsymbol{S} = \frac{E}{(1+\nu)}\left[\frac{\nu}{1-2\nu}\varrho\mathbf{I} + \mathbf{E}^{(e)}\right] \qquad \varrho = \nabla \cdot \tilde{\mathbf{u}} = \mathrm{tr}\,(\mathbf{E}) \tag{4.23}$$

If plasticity is neglected, then equation 4.23 reduces to 4.21, but the strain is given by equation 4.22.

Hyperelastic solid A biological cell membrane is capable of sustaining tension, and it flows under shear. On thicker membranes, or non-homogeneous membranes like lipid bilayer, bending effects and shear elasticity must be considered. Many constitutive equations have been used to model viscoelasticity of the membrane: neo-Hookean, Mooney-Rivlin, SK (Skalak et al., 1973), ES (Evans and Skalak, 1980). For capsules with thin membranes SK and ES laws could be used to fit the experimental compression data with good precision, whereas the commonly used neo-Hookean law could not (Barthès-Biesel, 2011). The Mooney-Rivlin model does not predict the relative behavior in uniaxial tension and isotropic tension observed in red cell membranes (Skalak et al. 1973). The SK model for an incompressible, plane isotropic and hyperelastic thin membrane can be expressed in terms of the strain energy function W as (2D),

$$\mathbf{S} = \frac{\partial W}{\partial \mathbf{E}} \qquad W = \frac{B}{4}\left(\frac{1}{2}I_1^2 + I_1 - I_2\right) + \frac{C}{8}I_2^2 \tag{4.24}$$

where B and C are material properties, the invariants given in alternate form are $I_1 = 2\,(E_{11} + E_{22})$ and $I_2 = 4E_{11}E_{22} + 2\,(E_{11} + E_{22})$ for a plane with a normal in the directions 3. Then, the second Piola-Kirchhoff stress tensor in the plane reduces to,

$S_{11} = BE_{11} + \frac{C}{2}\,(1 + 2E_{22})\,I_2$

$S_{22} = BE_{22} + \frac{C}{2}\,(1 + 2E_{11})\,I_2$

Viscoelastic solid The investigation of Evans et al. (1976) used the problem of micropipette aspiration of cells to show how the relaxation is dominated by the membrane viscosity and that the cytoplasmic and extracellular fluid flow have negligible influence on the relaxation time. The membrane viscosity, which was

not considered before, makes the membrane viscoelastic. The stress for a viscoelastic solid is also given by the elastic and the viscous terms as,

$$\mathbf{S} = \mathbf{S}^{(e)} + \mathbf{S}^{(v)} \tag{4.25}$$

where $\mathbf{S}^{(e)}$ and $\mathbf{S}^{(v)}$ are the elastic and viscous Piola-Kirchhoff stress tensors. If the Kelvin-Voigt model is used, then,

$\mathbf{S}^{(v)} = \eta_e \tilde{\mathbf{A}}$

where η_e is the membrane viscosity, $\tilde{\mathbf{A}} = \tilde{\mathbf{L}} + \tilde{\mathbf{L}}^{\mathrm{T}}$ and $\tilde{\mathbf{L}}$ is the velocity gradient, $\tilde{\mathbf{L}} = (\nabla_{\mathbf{X}} \tilde{\mathbf{v}})^T$.

Chapter 5

Numerical Method

5.1 Conservation of Mass and Linear Momentum

The Finite Volume Method (FVM) is used to integrate the governing equations in space for a Cartesian, staggered and rigid grid. The integration in time is performed following semi-implicit (Crank and Nicolson, 1996), splitting and unsplitting schemes to advance from the step n to $n+1$. The last corrected step is represented by a subscript m. The pressure p, normal stresses τ_{ii} and volume fraction F are cell centered, while the velocities u, v, w and density ρ (ρ_u, ρ_v, ρ_w) are staggered componentwise by a half cell. The shear stresses τ_{xy}, τ_{yz}, τ_{xz} and the respective dynamic viscosity η are staggered to the common face between the velocity components of the respective shear strain rate.

For the linear momentum, the local acceleration term is discretized following a central second-order scheme. The trapezium rule is applied to integrate most of the forces, based on the information at time n and the last corrected step m. That procedure converts a semi-implicit scheme evaluated at $t+1/2$ into a pseudo-Crank-Nicolson scheme, which is still semi-implicit, but evaluated at t and $t+\Delta t$. Pressure forces are evaluated implicitly. The viscous and surface-tension forces discretizations follow the mentioned semi-implicit scheme. The non-linear convective acceleration term is linearized following either the Picard's successive approximation (M. and DeBlois, 1997), i.e. $(\rho u)^n u^m$, or the pseudo semi-implicit approach, as shown in 5.1. The justification of this selection is shown in section 6.1.1. The momentum fluxes at the control surfaces are computed following the sharp and monotonic algorithm for realistic transport (SMART) high-resolution scheme introduced by Gaskell and Lau (1988). The strain-rate tensor required to compute the stress tensor is discretized following a non-uniform second-order central-difference scheme for the first derivative (Ferziger and Peric, 1999). The stress and advective terms at time n are obtained from the previous iteration, while only the coefficients related to $\mathbf{u}$ and deferred terms of the linear system are computed at

time m. The crossed component of the Newtonian viscous stress is deferred. Our latests implementation approximated the zero shear viscosity at the cell face using harmonic mean.

$$\begin{aligned}\tfrac{1}{\Delta t}\int_\Omega\left[(\rho\mathbf{u})^{n+1}-(\rho\mathbf{u})^{n}\right]d\mathcal{V}= \quad & \tfrac{1}{2}\int_{\partial\Omega}\mathbf{n}\cdot\left\{-(\rho\mathbf{u})^{n}\mathbf{u}^{n}-(\rho\mathbf{u})^{m}\mathbf{u}^{m}+(\boldsymbol{\tau}^{n}+\boldsymbol{\tau}^{m})\right\}d\mathcal{A}\\ & +\int_\Omega\left[-\nabla p^{m}+\tfrac{1}{2}\left(\mathbf{f}^{n}+\mathbf{f}^{m}\right)\right]d\mathcal{V}\end{aligned} \tag{5.1}$$

Here, $\mathbf{f}$ stands for all the forces mentioned in 4.3. The accuracy of the interface for problems involving deforming drops improves when $\mathbf{f}^{CSF}$ is discretized following a pseudo semi-implicit scheme, in comparison to an implicit scheme, and by staggering the volume-fraction gradient, $\partial F/\partial x_i$, which is only defined in u_i cell.

For a high-resolution scheme, the flow of the conservative quantity ϕ^c is given by

$$\int_{\partial\Omega_i}\mathbf{n}\cdot\mathbf{u}\phi^{c}d\mathcal{A}=\sum_{f}\left(\mathbf{n}\cdot\mathbf{u}\right)_{f}HR\left(\phi^{c}_{i-2},\ldots,\phi^{c}_{i+2}\right)\mathcal{A}_{f\,i}$$

where the subscript f denotes that the evaluation is being made at a face (interpolated when the value is not directly available), HR is the high-resolution limiting function Gaskell and Lau (1988), and $\mathcal{A}$ is the area of the control surface. In the case of the linear momentum equation in the x direction, $\phi^c=\rho u$.

Performing surface/volume integrations without any curvature conduces to the following set of linear algebraic equations,

$$\left(C^{n}_{p}+D^{m}_{p}+S^{m}_{t}\right)u^{n+1}_{p}=S^{n}_{t}u^{n}_{p}+\sum\left(C^{n}_{nb}+D^{m}_{nb}\right)u^{n+1}_{nb}+\sum\left(C^{n}_{nb}+D^{n}_{nb}\right)u^{n}_{nb}+S_{p}+D^{m}v_{nb}+S_{\text{others}} \tag{5.2}$$

where C D S_t S_p represents advective, Newtonian diffusive, temporal and pressure gradient terms respectively, while v represents crossed velocity terms and S_{others} stands for remaining source terms, like the non-Newtonian extra-stress, particle rigidifying force, old and new surface-tension and gravity terms. The term u_{nb} includes the extended grid region, i.e. $i+2$ or $i-1$ for evaluations at i.

Then, the discretized equations reduce to a linear system, $A\boldsymbol{\phi}=\mathbf{b}$, or $A^{n}_{p}\phi^{n+1}_{p}=\sum\left(A^{m}_{nb}\right)\phi^{n+1}_{nb}+S$, where A represents the coefficients of the linear system and S stands for the all source terms, i.e. in x direction, $S=S^{n}_{t}u^{n}_{p}+\sum\left(C^{n}_{nb}+D^{n}_{nb}\right)u^{n}_{nb}+S_{px}+D^{m}v_{nb}+D^{m}w_{nb}+S_{\text{x others}}$. In the case of $\phi=u$, the implicit terms involving the other velocity components v, w, and some nonlinear terms (advection) are deferred, that is, they are treated as source terms. Because the deferred terms contain implicit variables or nonlinear expression, the terms are updated every local iteration. After the system is assembled, further under-relaxation is applied. The solution is considered converged once the changes in ϕ between local iterations

are below a certain tolerance, typically 10^{-7}, together with small value of the normalized residuals, defined as $RES = \frac{1}{RES_o} \sum_{i=1}^{N} |A_p\phi_p + \sum A_{nb}\phi_{nb} - b|_i \lesssim 10^{-8}$.

In order to solve the system of algebraic equations, the tridiagonal matrix algorithm (TDMA) (Anderson, 1994) is used. By deferring the crossed terms, the system becomes pentadiagonal, and the solver for a tridiagonal system is finally used because it is computationally fast and several local iterations are needed in general. An iterative Gauss-Seidel method is employed after each TDMA sweeping in order to propagate the information along the other two directions. The extra terms of the pentadiagonal system are also deferred and updated every local iteration of the solver. After each iteration, a residual is computed and the degree of convergence is determined. Normally, additional loops are required when using an implicit or semi-implicit HR scheme, for non-Newtonian fluids, for flows with rigid particles and for starting simulations.

The SIMPLE algorithm (Patankar, 1980) together with under-relaxation factors are implemented to satisfy continuity on each time step. The iterative process corrects the pressure and velocity field and permits the convergence of non-linear forces on each cell like the extra-stress tensor, rigidifying, collisional and surface-tension forces. Incompressibility is enforced every time step by correcting the velocity and pressure fields according to $\mathbf{u}_i^* = \mathbf{u}_i^m + \mathbf{u}'$ and $p^* = p^m + \alpha_p p'$, where u^*, $p*$ are the corrected velocity and pressure; u^m, p^m are the last velocity and pressure updates; α is the under-relaxation factor for the pressure correction equation; $\mathcal{A}$ is the control surface; A_p is the "p" coefficient of the linear system; and u', p' are the velocity and pressure corrections. The velocity correction is given by $\mathbf{u}' = -\alpha_u \frac{\mathcal{A}_u}{A} \nabla p'$. When following the SIMPLEC algorithm (van Doormaal and Raithby, 1984), the pressure correction is solved from,

$$\frac{\delta}{\delta x_i}\left(\frac{\mathcal{V}_{u_i}}{A_{p\,u_i}}\frac{\delta p'}{\delta x_i}\right) \approx \frac{\delta u_i^m}{\delta x_i} + \alpha_{pp}\frac{\delta u_i^{'}}{\delta x_i} \tag{5.3}$$

where density variations are accounted for in the $A_{p\,u_i}$ term, which is the A_p coefficient associated with the u_i cell of volume $\mathcal{V}_{u_i}$, and $\alpha_{pp} \in [0,\, 1]$. The velocity correction u' is predicted from 5.3 by making $\alpha_{pp} = 0$ and solving for p' (SIMPLE step). Then, a corrected p' is computed for $0 < \alpha_{pp} \leq 1$. An iterative process (per time step) corrects the pressure and the velocity field while permitting the convergence of the non-linear terms on each control volume.

For the solid, the method of discretization of Bailey and Cross (1995) is followed: a Lagrangian finite volume formulation based on interpolating functions. The equations of motion extended to a dynamic case and large deformation reduce to,

$$\tilde{\mathbf{v}}^{n+1} = \frac{\tilde{\mathbf{u}}^{n+1} - \tilde{\mathbf{u}}^n}{\Delta t} \qquad \int_{\Omega_o} \rho_o \frac{\tilde{\mathbf{v}}^{n+1} - \tilde{\mathbf{v}}^n}{\Delta t} d\mathcal{V} = \int_{\Omega_o} \left(\nabla \cdot \boldsymbol{S}^n + \mathbf{f}^m\right) d\mathcal{V} \tag{5.4}$$

The code is implemented in Fortran and parallelized using OpenMP directives. The load is typically

between $80-98\%$ when the code is running in $16-4$ threads.

5.1.1 High-Resolution scheme: SMART

Numerical fluxes computed using a low order scheme generally create numerical dissipation. In the other hand, if a high order scheme is used, spurious oscillations are created, leading to numerical instability. When a high-resolution scheme is used to compute the numerical flux, a limiter function selects or weights between a low order and a high order scheme in order to reduce numerical diffusion, improve accuracy and maintain numerical stability. Between HR schemes, there are total variation diminishing (TVD) schemes and non-TVD schemes, bounded and not bounded schemes like QUICK. One scheme used in viscoelastic models is the sharp and monotonic algorithm for realistic transport (SMART) due to Gaskell and Lau (1988), which is based on the normalized variable diagram, third-order accurate for equally spaced meshes, bounded and non-TVD. The normalized variables are,

$\hat{\phi}_f = \frac{\phi_f - \phi_u}{\phi_d - \phi_u}$, $\hat{\phi}_p = \frac{\phi_p - \phi_u}{\phi_d - \phi_u}$

$\hat{\xi}_f = \frac{\xi_f - \xi_u}{\xi_d - \xi_u}$, $\hat{\xi}_p = \frac{\xi_p - \xi_u}{\xi_d - \xi_u}$

where ϕ is the transported variable, ξ is the coordinate and u, p, f and d represent the location of the upwind cell (upwind of p), the actual cell (upwind of f), the face and downwind cell, respectively. The variable computed at the face is then,

$$\hat{\phi}_f = \begin{cases} \frac{\hat{\xi}_f\left(1-3\hat{\xi}_p+2\hat{\xi}_f\right)}{\hat{\xi}_p\left(1-\hat{\xi}_p\right)}\hat{\phi}_p & 0 < \hat{\phi}_p < \frac{\hat{\xi}_p}{3} \\ \frac{\hat{\xi}_f\left(1-\hat{\xi}_f\right)}{\hat{\xi}_p\left(1-\hat{\xi}_p\right)}\hat{\phi}_p + \frac{\hat{\xi}_f\left(\hat{\xi}_f-\hat{\xi}_p\right)}{1-\hat{\xi}_p} & \frac{\hat{\xi}_p}{3} \leqslant \hat{\phi}_p \leqslant \frac{\hat{\xi}_f}{\hat{\xi}_p}\left(1+\hat{\xi}_f-\hat{\xi}_p\right) \\ 1 & \frac{\hat{\xi}_f}{\hat{\xi}_p}\left(1+\hat{\xi}_f-\hat{\xi}_p\right) < \hat{\phi}_p < 1 \\ \hat{\phi}_p & elsewhere \end{cases}$$

5.1.2 Time step and stability

The stability of the numerical method is determined by the local velocity, or referential velocity u_o, and the remaining force-related velocities. When dealing with surface-tension forces, the phase velocity of the capillary wave, v_{CSF}, is required to constrain the timestep to avoid catastrophic failure. A semi-implicit method allows for relatively large viscous diffusion velocities, $v_{\boldsymbol{\tau}} \sim 2\eta/(\rho\Delta x)$, but in order to capture transient effects of the viscous stresses, the time step it limited by $v_{\boldsymbol{\tau}}$. The maximum capillary-wave phase velocity v_{CSF} for the wave number $k = \pi/\Delta x$ is given by $v_{CSF} \sim \sqrt{\frac{2\pi\sigma}{\Delta x\langle\rho\rangle}}$ (Brackbill et al., 1992). When including viscoelastic forces, the shear wave speed, $v^{VE} = \sqrt{\nu_0/\lambda_1}$, is the referential velocity for stability. Then, for a given minimum length of the volume, Δx, a flow conditions, the time step is limited by the

Courant-Friedrichs-Lewy condition, CFL, as,

$$\Delta t = \frac{\Delta x \, CFL}{\max\left(u_o,\, v_{\boldsymbol{\tau}},\, v_{VE},\, v_{CSF}\right)}$$

The PLIC method is expected to be stable for $CFL_u < 0.5$ Harvie and Fletcher (2001) when the velocity field is sufficiently solenoidal. Depending on the donating-region method used, smaller CFL numbers would increase the convergence on mesh refinement. Additionally, the fluxing method is required to satisfy $1 \geq F - \frac{\Delta t}{\Delta \mathcal{V}} \sum_{l=1}^{6} (\mathbf{u} \cdot \mathbf{A})_l \geq 0$, which is enforced through a redistribution strategy when necessary. The DDR method does not need redistribution because the wisps are only generated by machine-precision errors. The BDR method requires a redistribution algorithm. The minimum volumetric fluxing criterion is limited to $\epsilon < 10^{-6}$.

The mesh spacing is also restricted by the maximum curvature of the interface as $\Delta x \lesssim 1/\kappa$ because the HF method tends to increase the error when the curvature is relatively large, that is, when the interface becomes trans-grid or sub-grid. This criterion is normally violated when the drop breaks up. It may also be violated in large deformations, but it is hard to determine a priori, or because of numerical limitations, such violation must be accepted.

5.2 The Volume-of-Fluid Method

Among various VOF fluxing strategies, special attention is given to Eulerian unsplit PLIC methods. Two formulations are considered: a basic fluxing strategy, denoted as BDR, and the defined donating region (DDR) method of Harvie and Fletcher (2001) extended for 3D domains. In the first formulation, the donation region (DR) is a rectangular extrusion of the control surface. For example, if a control surface is a rectangle of sides a and b, and the flow is in the x direction, then the DR is a parallelepiped of volume $\int\int \mathbf{u} \cdot d\mathbf{A} dt \approx uab\Delta t$. The edgewise volumetric flow is given by the intersection between the extruded "wet area" at the control surface in the direction of the flow and the DR. The flow reassembles an extruded triangle, quadrilateral or pentagon depending on how the reconstructed plane intersects with the control surface. Because a method of this type is low-order, a temporal multi-scale strategy could be adopted. Meanwhile the linear momentum equation advances one time step Δt, the local time step is $\Delta t^* = \Delta t / N$. The discretization of Equation 4.2 in time follows an Euler-forward scheme,

$$\int_\Omega \frac{F^{l+1} - F^l}{\Delta t^*} d\mathcal{V} + \int_{\partial\Omega} \left(\mathbf{n} \cdot \mathbf{u}F\right)^l d\mathcal{A} = \int_\Omega F^l \left(\nabla \cdot \mathbf{u}^l\right) d\mathcal{V} \tag{5.5}$$

where the step l is the Eulerian-forward intermediate step between n and $n+1$ ($l = n$ for the single-step

approach), the flow term is evaluated using a simplified unsplit strategy, and the source term is computed at the center of the cell. In general, the net volumetric flow of the dispersed phase is given by,

$$\int_t^{t+\Delta t} \int_{\partial\Omega_i} (\mathbf{n} \cdot \mathbf{u}F)\, d\mathcal{A}dt \approx (\mathcal{F}_e + \mathcal{F}_w + \mathcal{F}_n + \mathcal{F}_s + \mathcal{F}_t + \mathcal{F}_b) \tag{5.6}$$

where the flow in any direction is limited by the upwind contribution. For instance, in the positive x direction, the volumetric flow is,

$$\mathcal{F}_{i,e} = \begin{cases} \mathcal{V}_{i,E} & \text{if } u_{i,e} > 0 \\ -\mathcal{V}_{i,W} & \text{if } u_{i,e} < 0 \\ 0 & \text{if } u_{i,e} = 0 \end{cases} \tag{5.7}$$

The solution to Equation 5.5 is direct once all the fluxes are computed. In order to determine the fluxes, a plane is reconstructed on each cell where an interface is present. The parameters of the plane are then used to find the points that generate the "wet area". This area can be expressed in terms of the parameters of the plane, the reconstructed case and the face direction, as summarized in the Appendix, Table 5.2. An upwind flux is chosen because the "wet areas" are discontinuous across contiguous cells. In this manner, the topology of the volumetric flow remains inside the DR. For example, the flow in the "x" direction is given by $\mathcal{V}_{i,E} = u_{i,e}\mathcal{A}_{i,E}\Delta t$, or $\mathcal{V}_{i,E} = u_{i,e}\mathcal{A}_{i+1,W}\Delta t$, according to Equation 5.7. This type of fluxing is based on a basic donating region (BDR).

In the defined donating region (DDR) method, the DR is reconstructed from the streamtube formed by approximated streamlines at the corners of a given control surface of the cell. These streamlines are based on the normal velocities at the center of the adjacent faces. For instance, the velocity at the origin (corner) of the cell ijk is $\mathbf{u}_o = (u_{ijk}, v_{ijk}, w_{ijk})$, which determines the direction of the associated line as $\mathbf{u}_o / |\mathbf{u}_o|$. If any component of the line is pointing outwards of the cell, then the DR, or part of it, is inside the cell. With the direction of the four lines at the corners of a given control surface known, the volume of the DR depends only on one parameter, α, which is found after matching the BDR and DDR volumes (see Figure 5.2.1 for more details). In this way, eight vertices of the hexahedra are known and the defined donating region is reconstructed. More advanced DR reconstruction methods consider variations of the velocity in time and space, and mixed influx/outflux regions to reconstruct the streamtube(s).

The DR represents the maximum flow of the dispersed phase at a given face. These DRs are then intersected with the plane of the interface to approximate the actual net flow, as discussed in the appendix. In the DDR method, the net flow is also given by Equation 5.7, but the volume $\mathcal{V}_{i,j}$ is now computed using

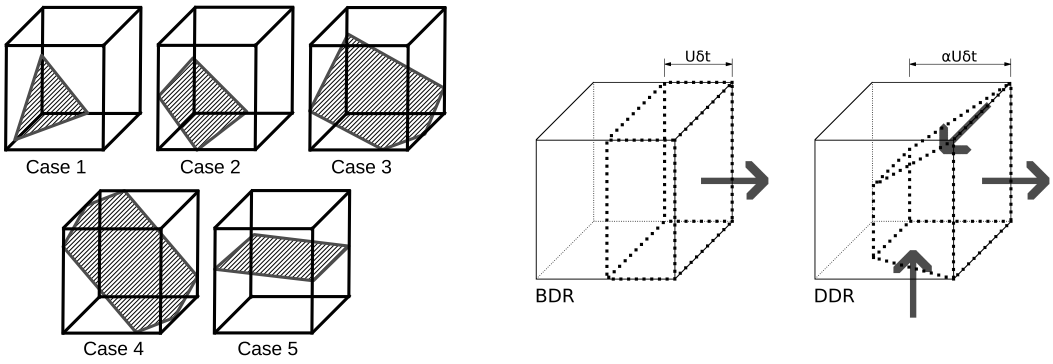

(a) Different cases of plane reconstructions in the normalized and oriented cell

(b) Donating Region of the east flow

Figure 5.1: The PLIC method

a combination of tetrahedra, truncated frustums, pyramids, prisms and hexahedra.

Treatment to Wisp Generation

Depending on the strategy used to flux the volume, there is tradeoff between volume conservation and accuracy. For incompressible flows, when the volumetric outflow is larger than the inflow, a void in the dispersed fluid is created. Similarly, when the inflow is larger than the outflow, an overflow is produced. Voids and overflows are indicatives of errors in mass conservation, and several VOF-PLIC methods are prone to produce them. Possible strategies to reduce wisp generation include lowering the CFL number, flux limiting, wisp redistribution and exact fluxing (not necessarily mass conserving, but volume conserving). The BDR method here employed generates wisps and are eliminated by using the upstream redistribution algorithm suggested by Harvie and Fletcher (2000). This method consists on the following procedure:

- Reducing the overflow by distributing it on the upstream neighbor first and then to the remaining neighbors if the upstream cell is full.
- Increase the underflow by subtracting from the downstream neighbor first and then to the remaining ones if downstream is full.

The DDR method does not need this treatment because the fluxing is exact and does not produce wisps, but it is employed to correct roundoff errors.

5.2.1 The Piecewise Linear Interface Calculation (PLIC)

The piecewise linear interface calculation (PLIC) is a technique used to reconstruct a plane inside a cell containing one or more interfaces from the knowledge of the volume-fraction field, F. Here, only one interface

within a cell is considered, which is represented by a plane that is reconstructed when $\epsilon < F < 1 - \epsilon$, where $\epsilon \in \left(10^{-3}, 10^{-12}\right)$. A large value of ϵ may reduce the apparition of flotsams, but accuracy is reduced as well, meanwhile a lower limit is dependent upon machine-precision error. For very small values of ϵ, quad precision is necessary in the reconstruction algorithm. The minimum fluxing value is set to $\epsilon = 10^{-6}$.

A case-by-case model for plane reconstruction is selected, as described by van Sint Annaland et al. (2005). In order to find a plane, the normal vector of the equivalent planar interface is required, which is given by,

$$\hat{\mathbf{n}} = -\nabla F / |\nabla F| \tag{5.8}$$

Because F is a discrete non-smooth function, Equation 5.8 cannot be applied directly. Different strategies can be chosen to approximate $\hat{\mathbf{n}}$. The normal vector can be computed using different techniques to produce second-order reconstruction accuracy, as explained by Rider and Kothe (1998). Here, a combination of the height-function method and the central-difference scheme is considered to compute $\hat{\mathbf{n}}$. For cases in which the height function cannot produce a normal, the central difference is used, which was shown to offers super-linear order of convergence in the case of average reconstruction of circles (the translation achieves order $1.7 - 2.0$ on fine-coarse meshes), and linear to sub-linear order of convergence when lines are reconstructed (order $1.5 - 0.6$ on fine-coarse meshes) according to Pilliod and Puckett (2004). The HF method for the normal is discussed in the next section. On coarse meshes, the central-difference scheme produces lower error than other second-order methods, characteristic that is helpful when resolving small structures.

Once the normal, $\hat{\mathbf{n}}$, is obtained, a transformation is performed, which allows for the reconstruction of a plane in terms of the local coordinates, ζ_i, the plane constant, d, and the oriented normal, n_i, as,

$$n_1\zeta_1 + n_2\zeta_2 + n_3\zeta_3 = d \quad \zeta_i = \frac{x_i - x_{i\,ref}}{\Delta x_i} \tag{5.9}$$

Markers are used to determine whether a cell has an interface, is the neighbor of a cell with an interface, or is a single-fluid cell. If an interface is present, the number of cases in three dimensions can be reduced to six after these transformations:

1. Change of coordinate directions, such that $n_i > 0$.
2. Mutual interchange of coordinate directions to satisfy $n_3 > n_2 > n_1$.
3. Interchange between the phases, such that if $F > 0.5$, then $F^* < 0.5$.

The 3D cases can degenerate to 2D cases, when $n_1 < \epsilon_n$ or $n_2 < \epsilon_n$, or to 1D cases, when $n_1 < \epsilon_n$ and $n_2 < \epsilon_n$. By performing a volume integral of the cases presented in Figure 5.1a, different equations for the

plane constant d can be found, as summarized in Table 5.1 (van Sint Annaland et al., 2005). A valid solution for d can be encountered for $\epsilon_n < 1 \times 10^{-10}$, or as limited by machine-precision error. The plane function of each cell is determined independently from the neighbors once the normal vector is known. As a consequence of the linear reconstruction, highly curved interfaces are flattened, incurring in large reconstruction errors. A traditional method to solve this issue is the multi-grid approach, but it was not implemented here.

Table 5.1: Cases and equations of the reconstructed planes

Case	Plane	Root finding method
I	$d^3 = 6n_1n_2n_3F^*$	Explicit
II	$d^3 = 6n_1n_2n_3F^* + (d-n_1)^3$	Fixed-point iteration
III	$d^3 = 6n_1n_2n_3F^* + (d-n_1)^3 + (d-n_2)^3$	As case 2 and secant method
IV	$d^3 = 6n_1n_2n_3F^* + (d-n_1)^3 + (d-n_2)^3 + (d-n_3)^3$	Brent's method
V	$d^3 = 6n_1n_2n_3F^* + (d-n_1)^3 + (d-n_1)^3 - (d-n_1-n_2)^3$	Combination of methods

A robust implementation depends on the degree of convergence of the plane constant, d. The secant method, the fixed-point iteration and the Brent's method are used to find d, depending on the case being considered. Case I has an explicit solution. Case II is solved with the fixed-point iteration method. Case III is solved as case II, while complemented with the secant method to accelerate convergence. The Brent's method cannot determine the root of a function if the function does not change signs within an interval. There is no change of signs for case III, therefore, the Brent's method cannot be employed. Case IV is solved using the Brent's method. A combination of the aforementioned methods is used to solve for d in case V, where a change of sings of the function must be checked when using the Brent's method. It is important to give an appropriate initial condition when seeking the value of d, and proper bounds, since it is possible to have multiple roots, or divergence, within the interval $[0, 1]$ due to the cubic nature of the equations.

Another two cases arise if the interface is a closed surface that is contained within a cell, or shared between two cells, like a droplet or a small filament. These cases were not implemented because they require more than one plane inside a cell. This problem can be solved by means of a Lagrangian transport, which requires a sub-grid model for the drag force, or by using a multi-grid approach, which could require several levels if the droplet is small.

5.2.2 Curvature Model and Normal Vector

Different strategies can be used to find the curvature of an interface. In general, the curvature is given by the normal vector at the interface, $\hat{\mathbf{n}}$, as (Brackbill et al., 1992),

$$\kappa = -\nabla \cdot \hat{\mathbf{n}} \tag{5.10}$$

In VOF methods, the curvature is normally computed from the volume fraction, F, on a given stencil. Because of the discontinuous nature of F, strategies employed on smooth functions tend to produce large errors. Common approaches use either the smoothed volume fraction, a convolution technique or the height function method.

The curvature then can be obtained from the knowledge of the normal vector, which can be computed from the volume fraction as $\hat{\mathbf{n}} = \nabla F / |\nabla F|$. This approach involves the numerical differentiation of a discontinuous function, fact that introduces errors in the calculation. To overcome this difficulty, a smoothed volume fraction function $\tilde{F}$ can be computed to estimate the unit normal to the interface. This method computes the curvature from the divergence of a smoothed interfacial normal vector, therefore it is denoted as DINV. A common method in 2D is based on weighting the information of F at the cell with the values of the neighbors Dupont and Legendre (2010),

$$\tilde{F}_{ij} = \frac{3}{4} F_{ij} + \frac{1}{16} \sum F_{nb}$$

In 3D, the weighted averaged of F among the surrounding cells is Yabe et al. (2007),

$$\tilde{F}_{ijk} = \frac{1}{2} \left\{ F_{ijk} + \frac{1}{1 + 6a + 12b + 8c} \left[F_{ijk} + a \left(\sum F_{1axis} \right) + b \left(\sum F_{2axis} \right) + c \left(\sum F_{3axis} \right) \right] \right\}$$

where the constants are, $a = \frac{1}{6+12\sqrt{2}+8\sqrt{3}}$, $b = a/\sqrt{2}$ and $c = a/\sqrt{3}$, while the summation terms are

$$\sum F_{1axis} = F_{i-1,j,k} + F_{i+1,j,k} + F_{i,j-1,k} + F_{i,j+1,k} + F_{i,j,k-1} + F_{i,j,k+1}$$

$$\begin{aligned} \sum F_{2axis} = \quad & F_{i-1,j-1,k} + F_{i-1,j+1,k} + F_{i+1,j-1,k} + F_{i+1,j+1,k} \\ & + F_{i-1,j,k-1} + F_{i+1,j,k-1} + F_{i-1,j,k+1} + F_{i+1,j,k+1} \\ & + F_{i,j-1,k-1} + F_{i,j+1,k-1} + F_{i,j-1,k+1} + F_{i,j+1,k+1} \end{aligned}$$

$$\begin{aligned} \sum F_{3axis} = \quad & F_{i-1,j-1,k-1} + F_{i-1,j-1,k+1} + F_{i-1,j+1,k-1} + F_{i-1,j+1,k+1} \\ & + F_{i+1,j-1,k-1} + F_{i+1,j-1,k+1} + F_{i+1,j+1,k-1} + F_{i+1,j+1,k+1} \end{aligned}$$

Another technique based on smoothening functions is,

$$\tilde{F}_{ijk}(x,y,z) = \sum_{i',j',k'=-1}^{+1} D(x - x_{i+i'}) D(y - y_{j+j'}) D(z - z_{k+k'}) F(x_{i+i'}, y_{j+j'}, z_{k+k'}) h^3$$

where the smoothening function D is given by the function proposed by Peskin (1977),

$$D(x) = \frac{1}{2h}\left(1 + \cos\left(\pi x/h\right)\right)$$

where h represents the smoothened width, i.e. $h = 2\Delta x$, which has to be selected carefully, because if the width is too small then numerical instabilities may arise, especially for large surface tension coefficients, or if the stencil is too large, excessive smoothening is obtained. Then, the computation of ∇F is simplified. For example, the variation of F in the x direction is given by,

$$\frac{\partial \tilde{F}_{ijk}\left(x,y,z\right)}{\partial x} = \sum_{i',j',k'=-1}^{+1} -\frac{\pi}{h}\sin\left(\pi\frac{x - x_{i+i'}}{h}\right)\left[1 + \cos\left(\pi\frac{y - y_{j+j'}}{h}\right)\right] \times$$

$$\left[1 + \cos\left(\pi\frac{z - z_{k+k'}}{h}\right)\right] F\left(x_{i+i'}, y_{j+j'}, z_{k+k'}\right)$$

In the HF method, the estimation of a discrete height function, $h\left(\mathbf{x}\right)$, in the neighborhood of the cell of interest allows for the calculation of the normal vector and the curvature of the interface. This method is denoted as HF. The first step is to determine the direction of the interface, because the discrete height function is computed along that direction. At the interface, the maximum variation of F occurs in the normal direction. Therefore, the component of ∇F with the maximum absolute value determines the direction. The second step is to compute the height on each node of the stencil from the values of F in the neighborhood. If $\left|\frac{\partial F}{\partial x_3}\right| > \left|\frac{\partial F}{\partial x_1}\right|$ and $\left|\frac{\partial F}{\partial x_3}\right| > \left|\frac{\partial F}{\partial x_2}\right|$, the local heights are given by the summation of the volume contributions in direction "3". The height function is then computed as,

$$h_{ij} = \sum_{k'=k-3}^{k+3} F_{ij\,k'}\Delta x_3 \tag{5.11}$$

Once the height functions are known at a given surface, the curvature is given by the expression,

$$\kappa_l = \frac{h_{l,11} + h_{l,22} + h_{l,11}h_{l,2}^2 + h_{l,22}h_{l,1}^2 - 2h_{l,12}h_{l,1}h_{l,2}}{\left(1 + h_{l,1}^2 + h_{l,2}^2\right)^{3/2}} \tag{5.12}$$

where $h_{l,i}$, $h_{l,ii}$ are the first and the second derivatives of h_l in the direction "i", and $h_{l,12}$ is the crossed derivative. The first and second derivatives of the height function are estimated using a 3-point second-order finite difference scheme for non-uniform meshes (Ferziger and Peric, 1999). The curvature is computed using a seven-point 3×3 stencil ($7 \times 3 \times 3$), that is, seven cells along the direction with the largest gradient of F, and nine discrete heights to estimate the height function. Once the normal vector at the interface, $\hat{\mathbf{n}}$, is provided, the height function is computed with the stencil that has the closest normal to $\hat{\mathbf{n}}$.

By using other stencils or projections, different types of height functions can be found. Here, only the

traditional HF method provided with additional directions is addressed. On the model denoted as HF-PD, standing for the main planes diagonals, that is, the principal diagonals in the xy, xz and yz planes. Another model, denoted as HF-AD, standing for all diagonals, the HF-PD model is provided with the additional diagonals of each octant in the xyz system. The curvature is computed using a $5 \times 3 \times 3$ stencil along the diagonal directions. The direction of the stencil is determined by a region of influence, depending on the largest gradient of F or after knowing $\hat{\mathbf{n}}$. For instance, if the direction of the gradient is close to any PD direction, then that stencil is activated, and similarly for the AD stencil. An example of the stencils used to compute the n^{th} plane for these techniques is shown in Figure 5.2. The final implementation of the HF-PD model used a cutoff angle of $\alpha = \beta = 63.25°$: xy diagonals satisfy $|n_1| > \cos(\alpha)$, $|n_2| > \cos(\alpha)$, $|n_3| < \cos(\beta)$; xz diagonals satisfy $|n_1| > \cos(\alpha), |n_3| > \cos(\alpha), |n_2| < \cos(\beta)$; and yz diagonals satisfy $|n_2| > \cos(\alpha)$, $|n_3| > \cos(\alpha)$, $|n_1| < \cos(\beta)$. In the case of the HF-AD, the normals are required to satisfy $\cos\alpha < n_i$, where $\alpha = 62°$. The angles were selected based on the inspection of the zones with maximum error, together with reducing the lack of convergence on mesh refinement.

The error in the traditional height function can also be improved by applying a correction at certain angles estimated from the local osculating sphere at the interface (López and Hernández, 2010). This method is also analyzed here and denoted as HF-LH.

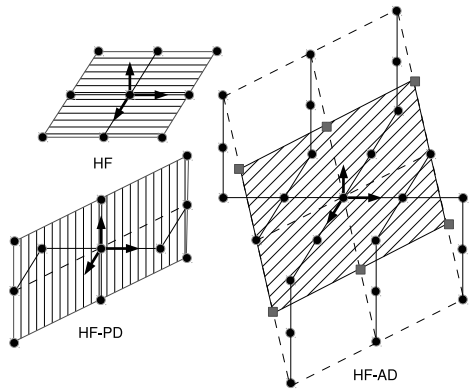

Figure 5.2: Stencils for the referential planes of constant height: HF method with normal $(0, 0, 1)$, HF-PD method with normal $(1, 1, 0)$ and the HF-AD method with normal $(1, 1, 1)$. The volume fraction, F, is located at the p cell ($\bigcirc$). A compact stencil is chosen on a 3×3 layout, given best results when compared to extended versions. The referential plane pointing along the main diagonal (HF-AD) is enclosed by the interpolated values of F ($\square$). Interpolations of F are also considered to produce the middle plane in between referential planes (compact stencil).

The error in the traditional height function can also be improved by applying a correction at certain angles estimated from the local osculating sphere at the interface (López and Hernández, 2010). This method was used for testing purposes and is denoted as HF-LH.

The height function could be obtained from the distance function ϕ_{RDF} under the reconstructed distance

function method (RDF). However, the height function computation based on ϕ is more prone to result in undefined interface heights than when F is used Liovic et al. (2010).

Our latests simulation used another approach, based on the height functions. The normal vector is found after solving a 2D least-squares problem, or plane fit, from the information provided by the height function, $h(\mathbf{x})$, in a 3×3 stencil. The central-difference scheme is used to predict the main direction or as the actual value if the minimization problem is not possible. The equation to be minimized is $E(A, B, C) = \sum_{i=1}^{N} [A\zeta_{1i} + B\zeta_{2i} + h_i + C]^2$, which is related to the difference between the plane position at a given coordinate and the h value. It is implied that $n_1^* = A$, $n_2^* = B$, $n_3^* = 1$, $n_3^*\zeta_3 = h$ and n_3^* points in the direction of the maximum absolute gradient of F. The value of N is increased by one for each case where non-zero and non-full values of h are found. This problem is only solved for $N \geq 3$, out of 9 candidates, from the linear system,

$$\begin{bmatrix} \sum \zeta_1^2 & \sum \zeta_1\zeta_2 & \sum \zeta_1 \\ \sum \zeta_1\zeta_2 & \sum \zeta_2^2 & \sum \zeta_2 \\ \sum \zeta_1 & \sum \zeta_2 & N \end{bmatrix} \begin{bmatrix} A \\ B \\ C \end{bmatrix} = \begin{bmatrix} -\sum \zeta_1 h \\ -\sum \zeta_2 h \\ -\sum h \end{bmatrix} \tag{5.13}$$

After finding A and B, the normal is given by $\hat{\mathbf{n}} = \left(A\hat{\mathbf{i}} + B\hat{\mathbf{j}} - \hat{\mathbf{k}}\right)/\sqrt{A^2 + B^2}$. To compute h, only three layers are considered ($3 \times 3 \times 3$). The cases where a filled or partially filled cell is surrounded by void, or a void is surrounded by full cells, were not given especial treatment. However, this issue should be addressed because the central-difference scheme and the 2D least-squares method will fail in this scenario.

5.2.3 The continuous surface force model

The face-centered CSF model of Francois et al. (2006) showed the capability of reducing spurious currents and estimates the correct pressure jump when the exact curvature is prescribed. Here, the CSF force is staggered on the u, v and w cells and computed as,

$$f_l^{CSF} = \sigma\kappa_l \frac{\partial F}{\partial x_l} \tag{5.14}$$

which can be weighted by the volume fraction (Brackbill et al., 1992; van Sint Annaland et al., 2005) (F-CSF),

$$f_l^{CSF} = 2\sigma\kappa_l \langle F \rangle_l \frac{\partial F}{\partial x_l} \tag{5.15}$$

or by the density (ρ-CSF),

$$f_l^{CSF} = \sigma \kappa_l \frac{\langle \rho \rangle_l}{[\rho]} \frac{\partial F}{\partial x_l} \tag{5.16}$$

where l is the direction (i.e. x, y or z), $\kappa_l = avg\left(k_m, k_{m-1}\right)$, $\frac{\partial F}{\partial x_l} = \frac{F_m - F_{m-1}}{\Delta x}$ on uniform grids and $m = i, j\, or\, k$ in accordance with l. Here, the unweighted formulation of the force is employed and the curvature is computed at a face of a uvw cell, which is the center of a p cell, while the gradient is defined at the center of the uvw cell. For the avg function, better results were observed in the convergence of the pressure with mesh refinement when the projected curvature is computed using the average-maximum (AvM) function, Equation 5.17, instead of using an arithmetic average, suggesting that even more accurate estimations can be used.

$$\kappa_l = \begin{cases} \left(k_m + k_{m-1}\right)/2 & |k_m| > 0, |k_{m-1}| > 0 \\ k_m & k_{m-1} = 0, |k_m| > 0 \\ k_{m-1} & k_m = 0, |k_{m-1}| > 0 \\ 0 & k_m = k_{m-1} = 0 \end{cases} \tag{5.17}$$

5.2.4 DDR and BDR schemes

When the donating region is given by the BDR method, the volumetric flow at a face is $\mathcal{V}_{BDR} = uA\Delta t$, where the "wet area" is computed as shown in Table 5.2 and u is the normal velocity to the face.

Table 5.2: Area of the dispersed fluid at the control surface of a given cell for different the types of planes as determined from the intersection of the plane with the cell boundaries in a transformed (oriented) control volume.

	Type I	Type II	Type III	Type IV	Type V
$\frac{A_E}{\delta x_2 \delta x_3}$	0	$\frac{1}{2}\frac{(d-n_1)^2}{n_2 n_3}$	$\frac{1}{2}\frac{(d-n_1)^2}{n_2 n_3}$	$\frac{1}{2}\frac{(d-n_1)^2}{n_2 n_3}$	$\frac{\left(d-n_1-\frac{1}{2}n_2\right)}{n_3}$
$\frac{A_W}{\delta x_2 \delta x_3}$	$\frac{1}{2}\frac{d^2}{n_2 n_3}$	$\frac{1}{2}\frac{d^2}{n_2 n_3}$	$\frac{\left(d-\frac{1}{2}n_2\right)}{n_3}$	$\frac{\left[d(n_2+n_3)-\frac{1}{2}\left(d^2+n_2^2+n_3^2\right)\right]}{n_2 n_3}$	$\frac{\left(d-\frac{1}{2}n_2\right)}{n_3}$
$\frac{A_N}{\delta x_1 \delta x_3}$	0	0	$\frac{1}{2}\frac{(d-n_2)^2}{n_1 n_3}$	$\frac{1}{2}\frac{(d-n_2)^2}{n_1 n_3}$	$\frac{\left(d-n_2-\frac{1}{2}n_1\right)}{n_3}$
$\frac{A_S}{\delta x_1 \delta x_3}$	$\frac{1}{2}\frac{d^2}{n_1 n_3}$	$\frac{\left(d-\frac{1}{2}n_1\right)}{n_3}$	$\frac{\left(d-\frac{1}{2}n_1\right)}{n_3}$	$\frac{\left[d(n_1+n_3)-\frac{1}{2}\left(d^2+n_1^2+n_3^2\right)\right]}{n_1 n_3}$	$\frac{\left(d-\frac{1}{2}n_1\right)}{n_3}$
$\frac{A_T}{\delta x_1 \delta x_2}$	0	0	0	$\frac{1}{2}\frac{(d-n_3)^2}{n_1 n_2}$	0
$\frac{A_B}{\delta x_1 \delta x_2}$	$\frac{1}{2}\frac{d^2}{n_1 n_2}$	$\frac{\left(d-\frac{1}{2}n_1\right)}{n_2}$	$\frac{\left[d(n_1+n_2)-\frac{1}{2}\left(d^2+n_1^2+n_2^2\right)\right]}{n_1 n_2}$	$\frac{\left[d(n_1+n_2)-\frac{1}{2}\left(d^2+n_1^2+n_2^2\right)\right]}{n_1 n_2}$	1

In the case of the DDR method, the volume of the DR is enforced to match that volume of a basic DR. Once this volume is determined together with the direction of the velocity at the corners of the control surface, the extension of the DR is known and therefore, the 8 vertices of the DR. The planes formed by these points are then intersected with the interfacial plane and the volume that is "below or inside" becomes the volumetric flow at the given area. These volumes or flows are computed analytically in a case-by-case

manner, using the code developed for the BDR method. A few examples are presented in Figure 5.3. The reversed single vortex problem and the deformation field problem were used to find the most common cases.

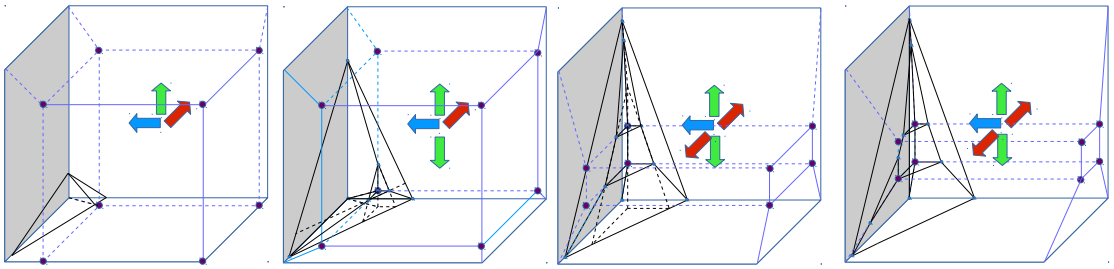

(a) Case 1

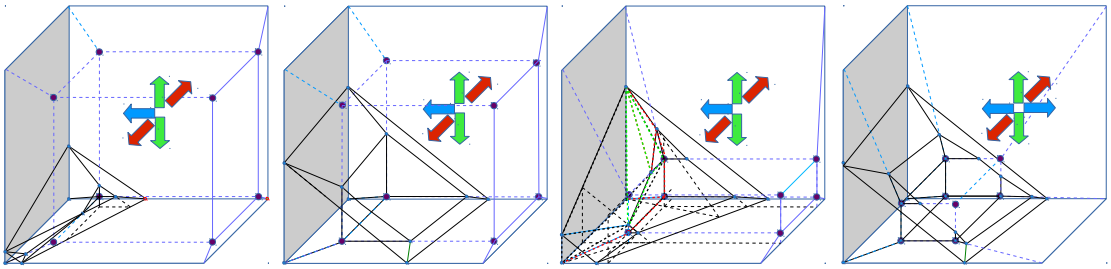

(b) Case 2

Figure 5.3: Example of cases 1-2 in the DDR method

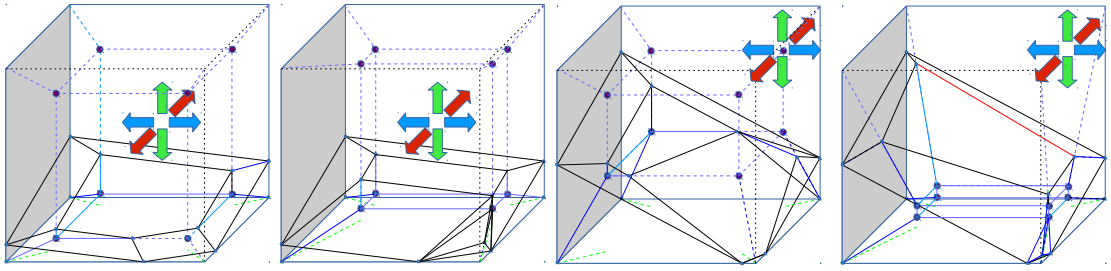

(a) Case 3

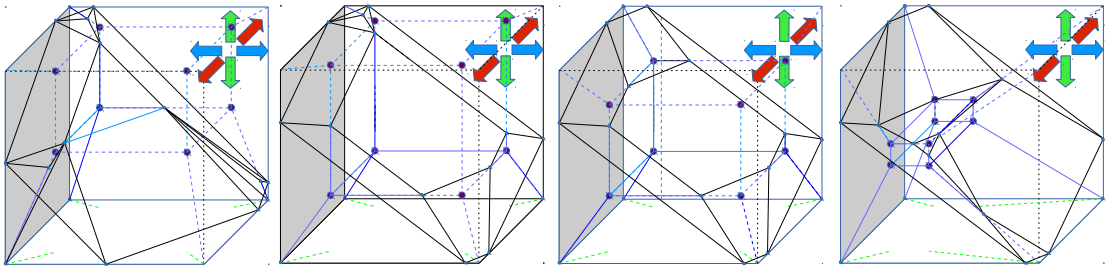

(b) Case 4

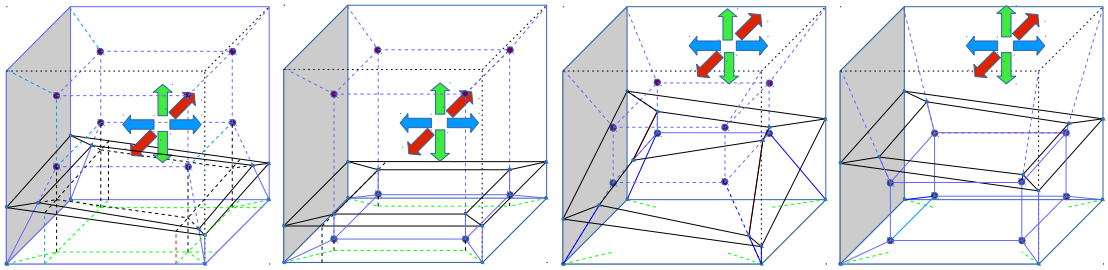

(c) Case 5

Figure 5.4: Example of cases 3-5 in the DDR method

Chapter 6

Numerical Validation

On this section different benchmarks are used to validate our model. The following problems are selected: planar Poiseuille flow, static drop, oscillation of a viscous drop, flow past a cylinder and the settling of a sphere in a channel. Unless otherwise stated, all units are CGS.

6.1 Advection problems

6.1.1 Nonlinear Advection of a Square Wave

This problem is governed by the inviscid Burger's equation (conservative form),

$$\frac{\partial u}{\partial t} + \frac{\partial u^2}{\partial x} = 0$$

The initial condition is given by $u = u_0 \left(\mathcal{H}\left(x + aL\right) - \mathcal{H}\left(x + bL\right)\right)$, where $u_0 = 1$, $L = 1$ is the domain, $\mathcal{H}$ is the step function and $a = 0.4$, $b = 0.6$. The time step is selected based on $\Delta t = CFL\Delta x/u_0$, $CFL = 0.25$ and $N = 101$ mesh points.

The time discretization is summarized in table 6.1, and the fluxes used are summarized in table 6.2, where the functions $UDS\left(x\right)$ and $HR\left(x\right)$ compute the value of x at the face, based on the values of the neighbors, following an upwind difference scheme or a high resolution scheme, respectively. In figure 6.1 it is shown how a Crank-Nicolson scheme and the implicit second order scheme achieve a similar shape for $CFL = 0.25$. The profile deviates for higher CFL number using a DeBlois linearization method with the implicit second order scheme in time, but improves considerably for $CFL = 0.125$.

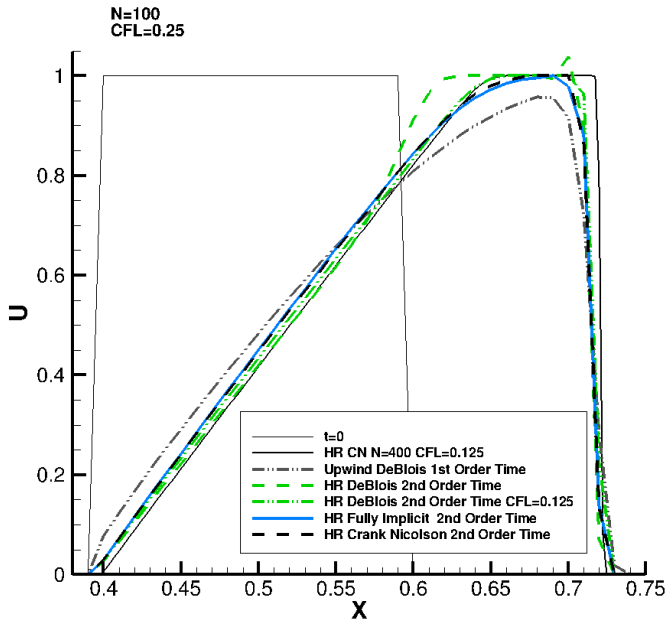

Figure 6.1: Nonlinear advection of a square wave: comparison of different schemes at $t = 50$ ($CFL = 0.25$ and $\Delta t = 0.1225$).

Table 6.1: Time marching schemes

Method	Equation
Explicit Euler	$u_i^{n+1} = u_i^n + \frac{\Delta t}{\Delta x}\left(\mathcal{F}_{i+1/2}\left(u^n\right) - \mathcal{F}_{i-1/2}\left(u^n\right)\right)$
Implicit Euler	$u_i^{n+1} = u_i^n + \frac{\Delta t}{\Delta x}\left(\mathcal{F}_{i+1/2}\left(u^{n+1}\right) - \mathcal{F}_{i-1/2}\left(u^{n+1}\right)\right)$
Implicit 2nd Order	$u_i^{n+1} = \frac{2}{3}\left[2u_i^n - \frac{1}{2}u_i^{n-1} + \frac{\Delta t}{\Delta x}\left(\mathcal{F}_{i+1/2}\left(u^{n+1}\right) - \mathcal{F}_{i-1/2}\left(u^{n+1}\right)\right)\right]$
Crank-Nicolson	$u_i^{n+1} = u_i^n + \frac{\Delta t}{2\Delta x}\left[\mathcal{F}_{i+1/2}\left(u^{n+1}\right) - \mathcal{F}_{i-1/2}\left(u^{n+1}\right) + \mathcal{F}_{i+1/2}\left(u^n\right) - \mathcal{F}_{i-1/2}\left(u^n\right)\right]$

Table 6.2: Momentum flux for different schemes (Conservative form)

Method	Equation
DeBlois	$\mathcal{F}\left(u^m\right) = UDS(u^n u^{n+1})$
HR Fully Implicit	$\mathcal{F}\left(u^m\right) = HR\left(\left(u^{n+1}\right)^2\right)$
HR DeBlois	$\mathcal{F}\left(u^m\right) = HR(u^n u^{n+1})$
HR Crank-Nicolson	$\mathcal{F}\left(u\right) = HR\left(u^2\right)$

6.1.2 The Reversed Single Vortex

The reversed single vortex problem is simulated to estimate the spatial and temporal order of convergence of the PLIC-VOF advection methods. The original problem is extended to 3D by extruding a disk to a length of 0.3, in a cubic domain of size 1. In this manner, planar convergence can be compared directly to other authors by extracting the middle plane information. Additionally, the consistency of the method can be verified by comparing the interface location and convergence rate for different planes. The remaining parameters are similar to (Rider and Kothe, 1998; Harvie and Fletcher, 2000). The planar streamfunction of this flow is given by $\psi = \frac{1}{\pi}\cos\left(\frac{\pi t}{T}\right)\sin^2(\pi x)\sin^2(\pi y)$. The velocity field is given by $u = -\cos\left(\frac{\pi t}{T}\right)\sin^2(\pi x)\sin(2\pi y)$, $v = \cos\left(\frac{\pi t}{T}\right)\sin^2(\pi y)\sin(2\pi x)$ and $w = 0$, for a time reversal at $t = T$, where $T = 2$ and $t \in [0, T]$. The cylinder has radius 0.15 and is located at (0.50, 0.75, 0). The time step is determined from the CFL condition at $t = 0$. The L-1 error is computed from all the N cells that contain an interface on the xy plane ($z = 0$) as $L_1 = \sum_{i=1}^{N} V_i \left|F_{\text{final}} - F_{\text{initial}}\right|_i$.

Table 6.3: Middle-plane-L_1 error for the single vortex problem, $T = 2$, HF-BDR method

Grid	$CFL = 1/4$	$O(\Delta x^n)$	$CFL = 1/10$	$O(\Delta x^n)$	$CFL = 1/40$	$O(\Delta x^n)$
32^3	7.23×10^{-3}	–	3.55×10^{-3}	–	2.97×10^{-3}	–
64^3	3.42×10^{-3}	1.08	1.58×10^{-3}	1.16	7.94×10^{-4}	1.90
96^3	2.26×10^{-3}	1.02	1.04×10^{-3}	1.03	3.77×10^{-4}	1.83
128^3	1.64×10^{-3}	1.12	8.75×10^{-4}	0.60	2.59×10^{-4}	1.31
160^3	1.53×10^{-3}	0.3	5.52×10^{-4}	2.07	1.96×10^{-4}	1.24

The convergence of the L_1 error on mesh refinement using the BDR method shows zero to second order of convergence, depending on the CFL_u number, as shown in Table 6.3. If the CFL_u is small, as it is the case for low Re and low Ca problems, the BDR method is convergent and at least first-order accurate, where the accuracy degrades with mesh refinement. The global error is determined by the reconstruction error and the fluxing error, where the least convergent of the two determines the order of the method. For small CFL_u numbers, the effect of the fluxing is reduced and the error is mainly determined by the reconstruction error, which is shown to be second-order convergent. More benchmark or theoretical analysis would be needed to precise the order of convergence of both, the normal and the fluxing. For large CFL_u, the method fails to convergence on mesh refinement. When the volume of the DR is relatively large, the fluxed volume and the exact fluxed volume differ from each other and local variations of the plane due to rotations and translations are not captured. When $CFL_u > 1$, the cell-cell DR overlaps, setting an maximum upper limit in CFL. In general, the nature of the flow does not normally allow for large time stepping, $CFL_u \sim 1$, therefore, the method can be second-order accurate at best. This is expected because in the limit when $\delta t \to 0$, the fluxing methods become exact and the error incurred comes mostly from the reconstruction error.

A similar statement can be made for the DDR method from the results shown in Table 6.4. For $CFL \leq 1/4$, the method is at least first order. Because the velocity field is known for all times, a direct comparison between the semi-implicit and the explicit approach can be performed. In all the cases, the semi-implicit approach produced better results, which is shown to be first order at least, even at $CFL = 1/2$. For $CFL \leq 80$, both methods are second-order accurate, while for $CFL \leq 40$ the semi-implicit method is second-order accurate. Although the semi-implicit method is better in terms of convergence, the overhead comes from the PLIC method when it is coupled with the remaining governing equations.

Table 6.4: Middle-plane-L_1 error for the single vortex problem, $T = 2$, HF-DDR method

	$CFL = 1/2$				$CFL = 1/4$			
Grid	Explicit		Semi-Implicit		Explicit		Semi-Implicit	
32	8.35×10^{-3}		4.59×10^{-3}		4.92×10^{-3}		3.66×10^{-3}	
64	4.53×10^{-3}	(0.88)	1.84×10^{-3}	(1.39)	2.34×10^{-3}	(1.07)	1.22×10^{-3}	(1.59)
96	3.12×10^{-3}	(0.92)	1.21×10^{-3}	(1.04)	1.52×10^{-3}	(1.06)	7.24×10^{-4}	(1.28)
128	2.27×10^{-3}	(1.11)	8.60×10^{-4}	(1.18)	1.12×10^{-3}	(1.07)	5.29×10^{-4}	(1.09)
	$CFL = 1/10$				$CFL = 1/10$			
Grid	Explicit		Semi-Implicit		MS-Explicit*		MS-Semi-Implicit**	
32	3.35×10^{-3}		3.06×10^{-3}		3.27×10^{-3}		2.96×10^{-3}	
64	1.20×10^{-3}	(1.48)	7.90×10^{-4}	(1.95)	1.13×10^{-3}	(1.53)	7.40×10^{-4}	(2.00)
96	7.15×10^{-4}	(1.28)	4.10×10^{-4}	(1.62)	6.72×10^{-4}	(1.28)	3.64×10^{-4}	(1.75)
128	5.08×10^{-4}	(1.19)	2.70×10^{-4}	(1.45)	4.65×10^{-4}	(1.28)	2.19×10^{-4}	(1.77)
	$CFL = 1/40$				$CFL = 1/80$			
Grid	Explicit		Semi-Implicit		Explicit		Semi-Implicit	
32	2.96×10^{-3}		2.92×10^{-3}		2.94×10^{-3}		2.92×10^{-3}	
64	7.40×10^{-4}	(2.00)	6.53×10^{-4}	(2.16)	6.93×10^{-4}	(2.08)	6.61×10^{-4}	(2.14)
96	3.64×10^{-4}	(1.75)	2.97×10^{-4}	(1.95)	3.12×10^{-4}	(1.97)	2.85×10^{-4}	(2.07)
128	2.19×10^{-4}	(1.77)	1.65×10^{-4}	(2.03)	1.75×10^{-4}	(2.01)	1.55×10^{-4}	(2.13)

Note: The order of convergence is expressed in parenthesis.
* The multi-step explicit method with $N = 4$.
** The multi-step method with a linear interpolation of the velocity (locally explicit).

Additionally, two multi-step approaches were simulated, also shown in Table 6.4, where $N = 4$ sub-steps were considered. For the multi-step explicit case (MSE), the velocity used for the fluxing is $\mathbf{u}^n$, while for the multi-step semi-implicit case (MSSI), the velocity comes from an interpolation between $\mathbf{u}^n$ and $\mathbf{u}^{n+1}$ in such a way that each sub-step is explicit. The sub-steps can also be advanced using a semi-implicit scheme. For $CFL = 1/10$ and the MSE case, the convergence is slightly better than the single-step explicit method at the same CFL, while the MSSI case behaves very similar to the single-step explicit method at $1/4^{th}$ of the original CFL, which is $CFL = 1/40$ in this case. The multi-step semi-implicit approach differs from the equivalent explicit method without sub-steps only in the interpolation procedure of the velocity, which is exact for the explicit method. The important conclusion is that the MSE method is the least computationally expensive MS method and does not show considerable improvements over the explicit method at the same CFL. However, a feature of the MS method is that it reduces undershots and overshots present in the

BDR method, which in turn reduces the amount of redistribution needed. The DDR method does not need mass redistribution because the fluxing is exact up to machine precision error, making a MSE techniques completely unnecessary.

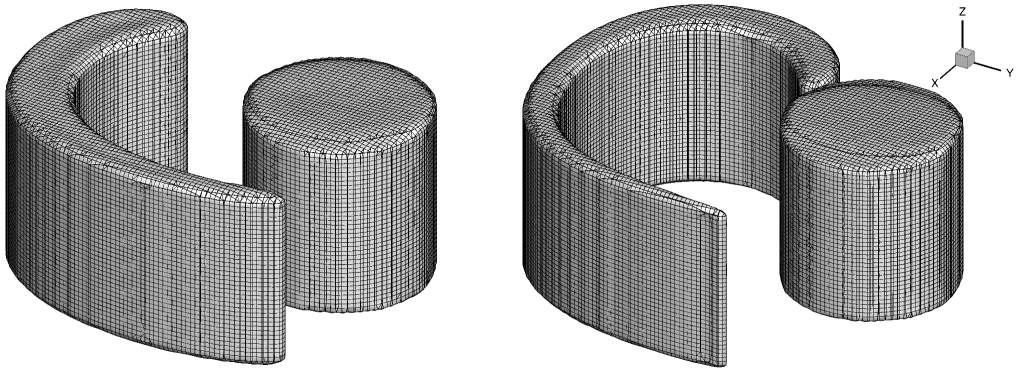

(a) $T = 2$ (b) $T = 3$

Figure 6.2: Iso-surface, $F = 0.5$, of the reversed single vortex problem at $t = \frac{1}{2}T$ and $t = T$. For the DDR-explicit method, mesh 128^3 and $CFL = 1/4$.

The order of convergence observed here with the semi-implicit scheme at $CFL = 0.5$ is similar to convergence of the Rudman vortex of Harvie and Fletcher (2001), reported to be within $1.2 - 1.4$ when using the Youngs method and within $1.2 - 1.7$ when using the Puckett method. Additionally, the initial and final volume inside the domain are the same as expected for the DDR method.

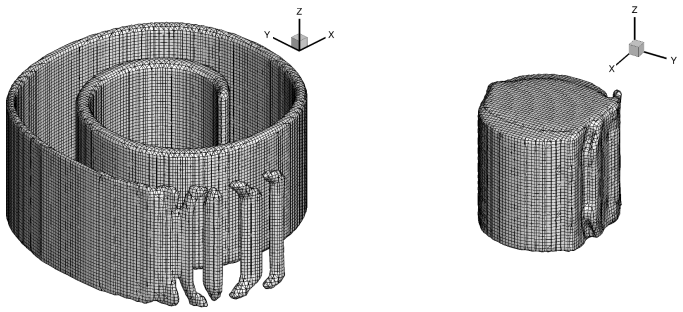

Figure 6.3: The reversed single-vortex problem: Iso-surface $F = 0.5$ at $t = \frac{1}{2}T$ and $t = T$ for the DDR-explicit method, mesh 128^3, $CFL = 1/4$ and $T = 8$.

For larger values of T, the interface must be resolved within one cell due to the formation of thin sheets. For cases where subgrid structures are present, the interface is not well resolved because only one plane is assigned to a topology that requires two or more planes coexisting within the same cell. This leads to a numerical problem that reassembles a surface tension effect because it produces globs, but not related to any force because the velocity field is prescribed. The numerical surface-tension effect is shown in Figure 6.3 for $T = 8$ where only four detached pillars were formed at the trailing edge.

6.1.3 The Deformation Field problem

The three-dimensional deformation field problem, introduced by LeVeque (1996), is used to estimate the order of convergence of the DDR method. This flow was initially employed to complete and debug the DDR code because it manifests more fluxing cases than the single vortex problem. The velocity field is given by,

$$\begin{aligned} u &= 2\sin^2(\pi x)\sin(2\pi y)\sin(2\pi z)\cos\left(\tfrac{\pi t}{T}\right) \\ v &= -\sin(2\pi x)\sin^2(\pi y)\sin(2\pi z)\cos\left(\tfrac{\pi t}{T}\right) \\ w &= -\sin(2\pi x)\sin(2\pi y)\sin^2(\pi z)\cos\left(\tfrac{\pi t}{T}\right) \end{aligned} \tag{6.1}$$

The error is computed as $L^n = \sqrt[n]{\sum_{i=1}^{N}\left[V_i\left(F_{\text{final}} - F_{\text{initial}}\right)_i\right]^n}$, where V is the volume of the cell. The average order convergence of the L^1 error is 1.75, while it is 2.55 for the L^2 error, as shown in Figure 6.4. This convergence is superlinear and better than the planar convergence of the reversed single-vortex problem, which happens to be linear at best. Moreover, the solution improves slightly with mesh resolution. In comparison, the CVTNA-PCFSC-unsplit method of Liovic et al. (2006) showed quadratic convergence, between 2.14 and 2.69, while their Youngs-split method showed superlinear convergence, between $1.68-1.87$, for the range of mesh resolutions used here. The L^1 errors and converge of the Young-split method are similar to the results here observed. In terms of volume conservation, the volume remained constant at all times to a value of 1.413717×10^{-2}. The interface at $t=\frac{1}{2}T$ and $t=T$ is presented in Figure (6.5) for different mesh resolutions.

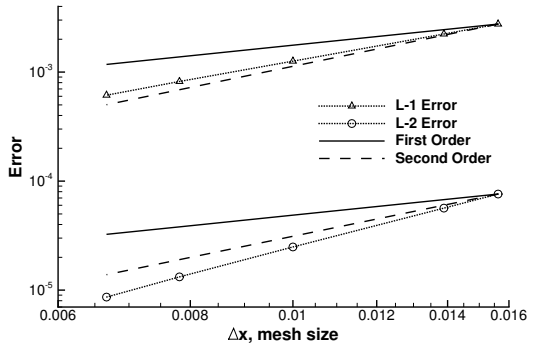

Grid	L^1 Error	$O(\Delta x^n)$	L^2 Error	$O(\Delta x^n)$
32^3	8.21×10^{-3}	–	3.92×10^{-4}	–
64^3	2.76×10^{-3}	1.57	7.61×10^{-5}	2.37
72^3	2.23×10^{-3}	1.79	5.65×10^{-5}	2.52
100^3	1.26×10^{-3}	1.74	2.49×10^{-5}	2.50
128^3	8.19×10^{-4}	1.74	1.32×10^{-5}	2.56
150^3	6.14×10^{-4}	1.82	8.64×10^{-6}	2.69
160^3	5.49×10^{-4}	2.43	7.33×10^{-6}	3.59
150^3*	5.01×10^{-4}	–	7.63×10^{-6}	–

Figure 6.4: Estimation of the error in the three-dimensional deformation field problem, $T=3$, HF-DDR-explicit method, $CFL=0.5$. * $CFL=\frac{1}{8}$.

A direct comparison with the level set (LS) and particle level set (PLS) methods of Enright et al. (2002) at $CFL=1$ is not possible because the Courant number is limited to $CFL\leq0.5$ for the DDR-VOF method (when the velocities at opposite faces in a given cell have different directions, $CFL>0.5$ could produce overlapping donating regions). However, a qualitative comparison ($CFL=0.5$, mesh 100^3) indicates that

the DDR-VOF method produces a slightly larger pattern of numerical surface tension than the PLS method at $t = \frac{1}{2}T$, but it is significantly better than the LS method. The numerical surface tension reduces with mesh refinement, as observed for a 150^3 mesh. The protrusions and indentations observed at $t = T$ where also present and discussed in the coupled VOF-LS method of Ménard et al. (2007) and Chenadec and Pitsch (2013). Their results showed no signs of numerical surface tension at $t = \frac{1}{2}T$ because the former author, using a 150^3 mesh, employed a correction when two interfaces are present in the stencil, while the latter used a 192^3 mesh.

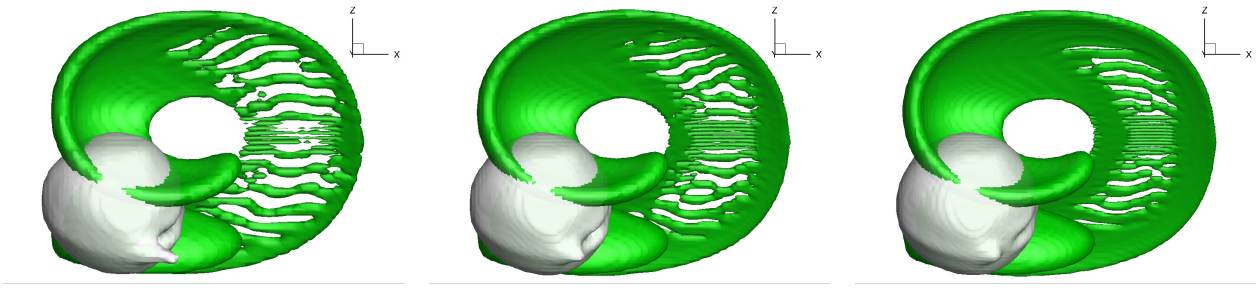

(a) Mesh 100^3 (b) Mesh 128^3 (c) Mesh 150^3

Figure 6.5: The 3D deformation field problem: Iso-surface $F = 0.5$ at $t = \frac{1}{2}T$ (green) and $t = T$ (white), for the HF-DDR-explicit method, $CFL = 0.5$ and $T = 3$.

6.2 Newtonian-Fluid Solver

6.2.1 Starting Flow between Parallel Plates

The classical problem of the starting flow between parallel plates subject to a constant pressure gradient is presented to verify the consistency between the numerical scheme and the governing equations. An implicit second-order scheme in time was employed and the result is shown in Figure 6.6. As it can be observed, the results are in excellent agreement with the analytical solution of the Navier-Stokes equations for a Newtonian fluid, given by (Waters and King, 1969),

$$\frac{u}{u_o}(y_1, t_1) = -4y_1(y_1 - 1) - 32\sum_{n=1}^{\infty} \frac{\sin Ny_1}{N^3} e^{-N^2 t_1}$$

where $y_1 = y/h$, $t_1 = \eta t/\left(\rho h^2\right)$, $u_o = -dp/dx\, h^2/(8\eta)$, $N = (2n-1)\pi$

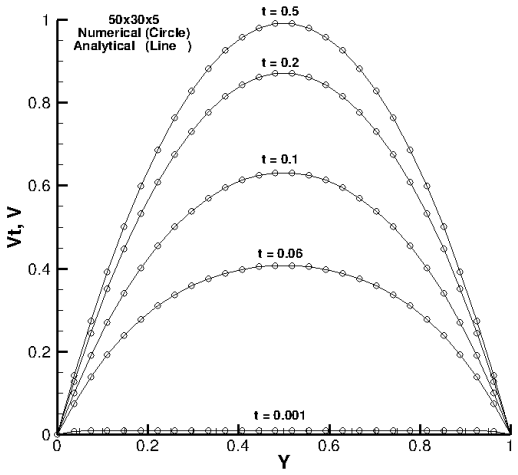

Figure 6.6: Velocity profile for the starting flow between parallel plates for $CFL = 0.25$, time step $\Delta t = 2 \cdot 10^{-4}$, $\Delta x = 3.7 \cdot 10^{-2}$ using a mesh of $50 \times 30 \times 5$ cells.

6.2.2 Lid-driven Cavity Flow

The fluid inside a cavity flows due to viscous stresses created by a lid moving at a velocity U. The domain is a box of size 1. Wall boundary conditions with zero velocity are prescribed on left, right and bottom boundaries, a moving wall at the top boundary and symmetries at the front and back boundaries. In the absence of density variations (no temperature gradients), this flow is characterized by the Reynolds number only, $Re = UH/\nu$. When $Re \gtrsim 100$, the effect of advection is crucial, and low order schemes degrades accuracy considerably. The numerical solution is compared with the results of Ghia et al. (1982) on Fig. 6.7

and Table 6.5. The simulation of a $90 \times 90 \times 5$ variable mesh shows an error as large as 8% when compared with a multigrid method at a higher resolution (129×129).

Table 6.5: Properties of primary and secondary vortices at $Re = 1000$

Vortex	Property	Ghia et al. (1982)	$90 \times 90 \times 5$	Error (%)
Primary	ψ_{min}	-0.117929	-0.1133	3.4
	Location (x,y)	$0.5313, 0.5625$	$0.5324, 0.5677$	0.2,0.9
BL	ψ_{max}	2.31129×10^{-4}	2.500×10^{-4}	7.9
	Location (x,y)	$0.0859, 0.0781$	$0.0820, 0.0769$	4.5,1.5
BR	ψ_{min}	1.75102×10^{-3}	1.701×10^{-3}	2.9
	Location (x,y)	$0.8594, 0.1094$	$0.8661, 0.1121$	0.8,2.5

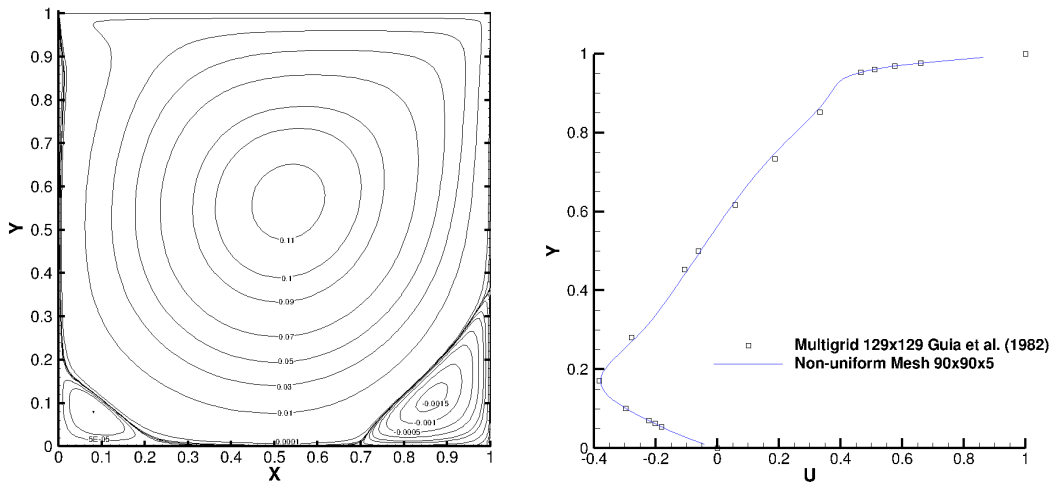

(a) (b)

Figure 6.7: Lid-driven cavity flow at $Re = 1000$, using $CFL = 50$. (a) Streamfunction for a mesh $90 \times 90 \times 5$ (b) Comparison of the velocity u .

6.2.3 Flow after a sudden expansion

The flows after sudden expansions are studied for different geometries and flow conditions to compare the behavior of the recirculation zone against the literature and to perform a mesh sensitivity analysis when the mesh is uniform.

Planar symmetric expansion

The flow in a planar sudden expansion of $1:4$ ratio is simulated to validate the numerical model for conditions where the solution is symmetric. This flow is dependent on the Reynolds number, $Re = \frac{\rho U d}{\mu}$, where U is the upstream average velocity. A recirculation zone is present for low Re and grows in size and strength as Re increases until a condition where the vena contracta is created. The streamfuncion, the velocity profile and the recirculation-zone length are being compared with the results of Wahba (2007) for the cases of $Re = 0$ (Stokes limit approximation) and $Re = 30$. The case of an asymmetric solution was also addressed for an expansion 1:3 and $Re = 80$ by Fearn et al. (1990) and Oliveira (2003) in Newtonian and viscolastic fluids, respectively. The boundary conditions are prescribed as follows: velocity $u = U = 1$ at the inlet, pressure $p = 0$ and normal velocities at the outlet, symmetries in the z direction, and walls ($\mathbf{v} = 0$) for $|y| \geq \frac{1}{2}d$ if $x \leq 0$ and for $|y| \geq \frac{ed}{2}$ if $x > 0$, where e is the expansion ratio. The normalized streamfunction is defined as $\Psi(x, y) = (\psi - \psi_o) / (\bar{u}d)$, where $\bar{u}$ is the averaged upstream velocity. The coordinates are normalized by d and the velocity by U. The domain is limited to a rectangle of size 22×4 and the mesh is uniform.

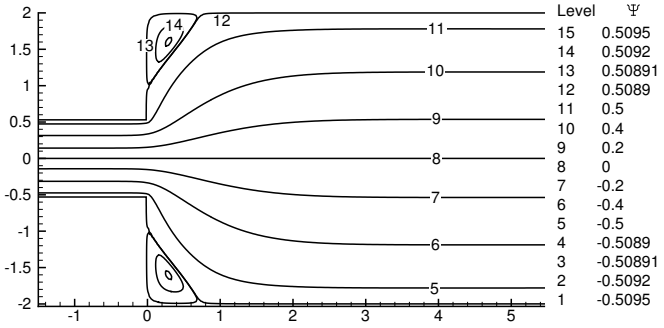

(a) $Re = 0$

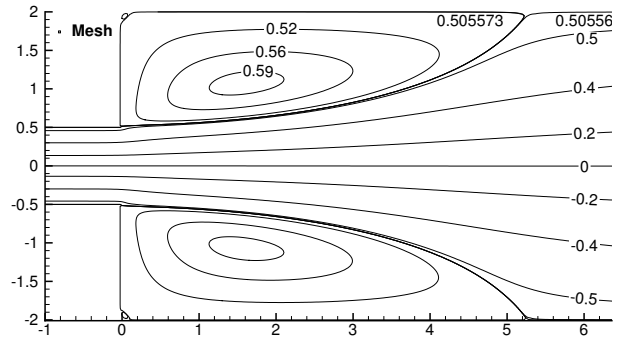

(b) $Re = 30$

Figure 6.8: Streamlines for a planar symmetric sudden expansion of ratio $1:4$ (a) $d/\Delta x = 29.25$ and (b) $d/\Delta x = 40$.

The streamlines of this flow are shown in Figure 6.8 for $Re = 0$ and $Re = 30$. It is noticed a relatively small single recirculation zone for $Re = 0$, while two types are present for $Re = 30$, the large principal vortex and a very small vortex at the corner. It is also observed a very small detachment region at the exit of the expansion for $Re = 30$. The result for $Re = 0$ is in good agreement with the results obtained by Wahba (2007). The case of $Re = 30$ is qualitatively similar to $Re = 40$ and $Re = 60$. The re-attachment length is given by $L_r/d = 0.178Re$ and is valid for $Re > 1$ (Scott et. al, 1986), and it is $L_r = 5.34d$ for $Re = 30$.

A direct comparison of the velocity field at different cross sections is presented in Figure 6.9a for $Re = 30$. The error of the velocity profiles at the center of the channel for different locations using a mesh resolution $d/\Delta x = 9.25$ and in comparison with Wahba (2007) are: $x/d = 2.5$, 0.09%, $x/d = 5.35$, 3.2%, $x/d = 10$, 9%. The profiles are sufficiently accurate for low mesh resolutions in the expansion regions.

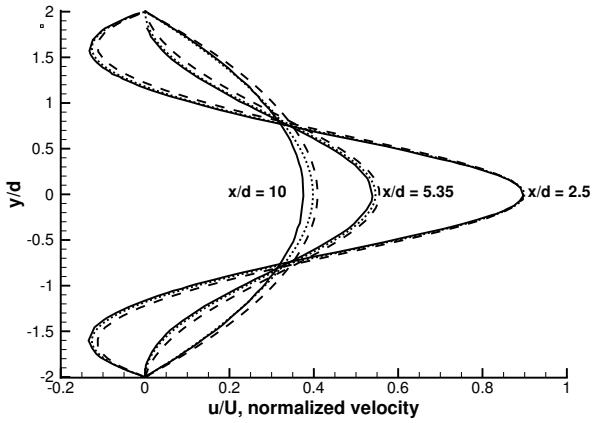

(a)

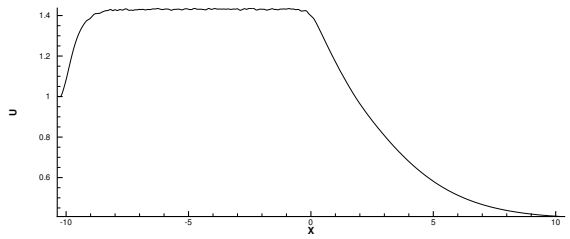

(b)

Figure 6.9: Velocity profile for for the flow in a planar symmetric sudden expansion at $Re = 30$: (a) velocity at different channel locations (b) centerline velocity. Mesh resolutions: $d/\Delta x = 9.25$ ($N_y = 40$) ($- - -$) and 29.25 (120) ($\cdots\cdots$). Reference, Wahba (2007) (——).

The velocity along the center line is presented in Figure 6.9b to show the effect of mesh resolution on the maximum velocity and the development length for $Re = 30$. The flow in the narrow channel becomes developed after $L_d/d = 5.32$. Downstream of the expansion, the velocity profile requires a length of $x_{max}/d \sim$

10 to redevelop. Finally, the size of the recirculation zone is $L_r/d = 5.29$ for a mesh $d/\Delta x = 29.25$ ($N_y = 120$), which is within 0.9% error of the referential value.

Axisimmetric sudden expansion

An axisymmetric sudden expansion flow is simulated in three dimensions for $Re_d = \rho U_{max} d/\mu = 12$, 50.9, and compared with the experimental results of Khodaparast et al. (2014). A piecewise wall boundary condition is impose and its effect on the accuracy of the solution is verified. An uniform mesh with $\Delta x = \Delta y = \Delta z$ is generated inside a parallelepiped domain, and the cylindrical shape is obtained from the wall boundary conditions. The boundary conditions are prescribed as follows: inlet $u = 1$, outlet $p = 0$ with normal velocities, and $\mathbf{v} = \mathbf{0}$ is prescribed at radius $r(x) \geq d/2$ for $x \leq 0$ and $r(x) \geq de/2$ for $x > 0$, where e is the expansion ratio and d is the pipe diameter before the expansion.

The flow is visualized on the xy plane ($z = 0$) using a streamfunction given by $u = \frac{1}{y}\frac{\partial \psi}{\partial y}$, $v = -\frac{1}{y}\frac{\partial \psi}{\partial x}$, which is normalized as $\hat{\psi} = \frac{8}{Ud^2}(\psi - \psi_o)$. The streamlines for an expansion $e = 1.961$, and two flow conditions, $Re = 12$ and $Re = 50.9$, are shown in figure 6.10.

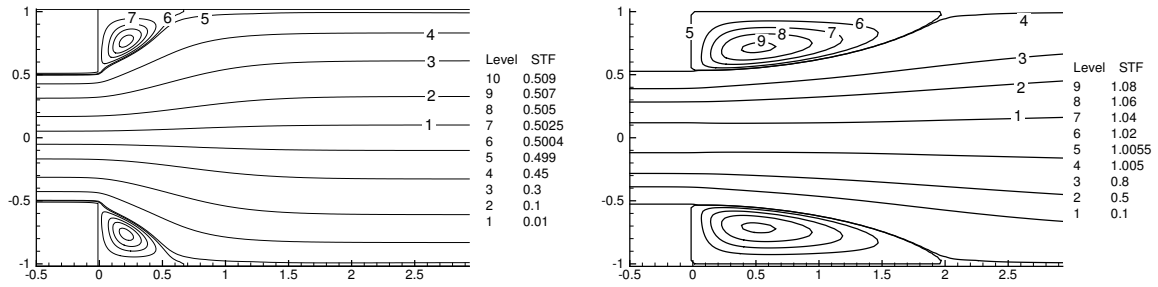

(a) $Re = 12$, Mesh $300 \times 90 \times 90$

(b) $Re = 50.9$, mesh $500 \times 75 \times 75$

Figure 6.10: Streamlines of the flow in axisymmetric sudden expansion for different Re and $e = 1.96$ at steady-state conditions.

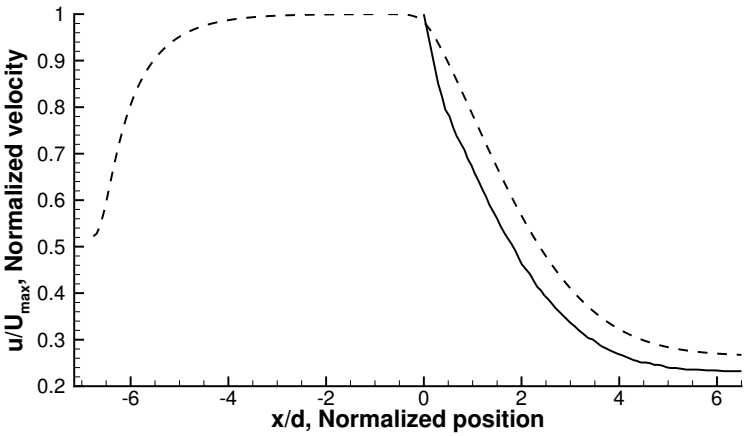

Figure 6.11: Centerline horizontal velocity, u, for $Re = 50.9$

A comparison is made with the experimental figures of Khodaparast et al. (2014) and the results are reported in Table 6.6. Here, the subindex c indicates vortex coordinates, $R_c = r_c/d$ is its radial distance and $L_c = x_c/d$, where $d = D/e = 1.02$. The error of the position is within 10%, considering the complications with reading the vortex location in the original source, this is acceptable.

Table 6.6: Comparison of the vortex geometry.

	Khodaparast et al. (2014)		*Mesh* $N_y = 60, 80$	
Re	12	50.9	12	50.9
L_c	0.211	0.54	0.214	0.48,0.503
R_c	0.706	0.705	0.7653	0.7056, 0.7024
L_r	0.51	1.95	0.548	2.07

As it can be observed, Re has to be below the transitional $Re_t \sim 50$ to reduce the size of the vortex structure. In that sense, the remaining of the study is kept below Re_t.

These results show that a mesh resolution between 60 to 80 radial elements, has a minor effect on the position of the vortex, while the maximum velocity is within 5% from the theoretical value. Considering that the mesh is uniform and Cartesian, and the comparison is held against experimental data, these results are acceptable.

Bilateral Sudden Expansion

A sudden bilateral centered expansion in a channel at subcritical Reynolds number is analyzed in the Results, together with the expansions of drops. From the main streamlines it is possible to observe which geometries

and flow conditions produce large recirculating zones. Avoiding recirculation zones permits larger advective accelerations near the expansion region. Aside from Re_d, this problem also depends on the aspect ratio, defined either as $\alpha = W/d$ or $AR = h/W$, and the expansion ratio $e = H/d$, where W is the channel breadth, H is its height and $h = (H - d)/2$. The recirculation zones are expected for large Re_d and α, and closer to the centerline for large e. For a geometry and flow conditions where a vortex is present, the center of the vortex moves downstream while the jet structure becomes larger by increasing Re.

6.3 Viscoelastic-Fluid Solver

6.3.1 Flow Past a Cylinder

A cylinder is included inside a channel filled with an Oldroyd-B fluid by using a rigidifying force obtained from DLM method. Among different benchmarks for non-Newtonian fluids, the flow past a cylinder offers all-in-one capabilities: the stress tensor can be found in tension, compression and there is an important shear stress; transient solutions are found for high Re or high De; drag coefficient has values sufficiently accepted in Newtonian and viscoelastic fluids; velocity and stress profiles along the center line can be compared near the leading edge and wake for different De or viscoelastic models. The region close to the body is subject to high gradients in velocity and stress, and high resolution is required to capture viscoelastic boundary layers, which increase in size and intensity as De increases. For the problem of the flow past a cylinder, the dimensionless force K and Deborah number De are,

$$K = \frac{D}{\eta_0 U} = \frac{\int \boldsymbol{\sigma}\mathbf{n}\cdot\mathbf{i}\, dS}{\eta_0 U} \qquad De = \frac{\lambda_1 U}{R}$$

The investigation of Oliveira et al. (2000) studied the error in the dimensionless drag coefficient C_D based on diffusion (or K) after using different techniques. They found that C_D has spatial order of convergence of 1, 1.8 and 2 for the streamline upwinding (UDS), and the high-resolution schemes MINMOD and SMART, respectively. When $\Delta r/R = 0.01$ ($N_x = 100$ volumes across the cylinder radius $R = 1$), the corresponding difference in drag coefficient is $\Delta K_{UDS} \approx 10$ or $\Delta K_{SMART} \approx 1$. Since $K \sim 100$, this would predict an error of 10% for UDS and 1% for SMART under an extremely demanding mesh of at least 400 cells perpendicular to the flow direction. Similar errors were obtained performing a simulation with 500 horizontal mesh points, as shown in figure 6.12. Now, considering also the time step required to achieve steady state and the large entry-exit length required at higher De, an error in K of $\sim 10\%$ is justified. This clearly shows that a DLM method is not efficient or accurate because of the size of the first cell in the flow. High resolution methods are required, namely SMART, MINMOD, CUBISTA, etc, combined with an adaptable mesh. For that reason SMART was chosen here.

Many authors, according to Hulsen et al. (2005), conclude that comparing C_d along is not a proof of accuracy, since different viscoelastic models arrive to the same drag coefficient under low De (UCM, Olroyd-B, FENE-P, etc.). Here, without using body fitted meshes it was observed that achieving the right drag force is a challenge. In that sense, the velocity along the centerline and pressure-stress distribution around the immersed body are better suited for comparison between rheological models because each of them predict different velocities on the wake of the particle.

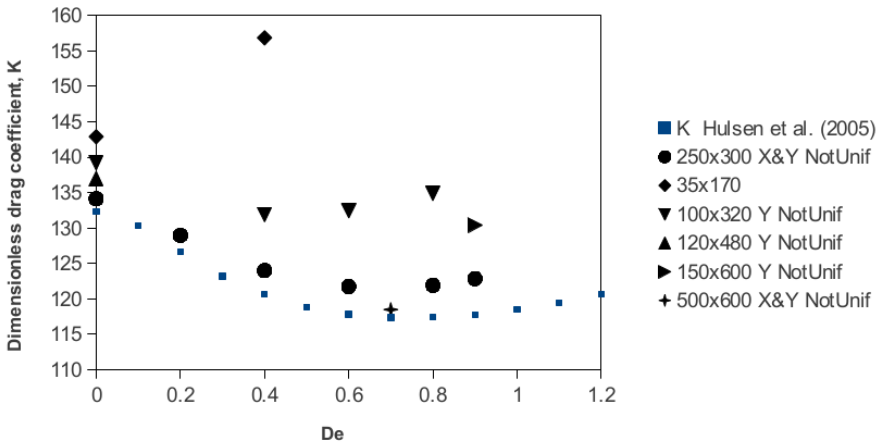

Figure 6.12: Effect of the mesh resolution on the dimensionless drag force as a function of De. Comparison with Hulsen et al. (2005).

In order to test the overall model and its limitations, pressure and stress are computed around the cylinder and the drag coefficient is determined by two methods. For the first method, the total stress is integrated over the surface of the cylinder, from leading to rear stagnation points. Neglecting acceleration terms, drag force on a cylinder inside a vertical channel is given by,

$$D = 2R \int_0^{\pi} \left[(\tau_{xx} - p) \cos\theta + \tau_{xy} \sin\theta \right] \, d\theta$$

For the second method, the force over the cylinder is given by the rigidifying force computed from the DLM method in the vertical direction, where gravity force can be considered (settling of a sphere problem). Since both methods achieve similar results, the reported dimensionless drag force is,

$$K = \frac{F_{DLM\,y} + m_p g}{\eta_o U z}$$

A sensitivity analysis on drag coefficient is shown in figure 6.12, where different mesh sizes and De are selected, based on $\eta_0 = 1$P, a cylinder of radius $R = 0.25$, and a channel width $W = 1$. The error observed is less than 4% for 250 mesh points ($R/\Delta r \backsim 60$), and less than 1% for 500 mesh points (non-uniform mesh). Polymer stresses for $De = 0.8$ are shown in figure 6.13, where the contour lines predict regions in tension ($\tau_{ii} > 0$) and compression ($\tau_{ii} < 0$) in detail. These contours are qualitative similar the results from Oliveira et al. (2000) at $De = 0.9$. Even though the reference uses a different Deborah number, $De = 0.9$, this model still captures the same structures near the front of the cylinder, the wake and at the wall. However, important differences are observed in a detailed plot of the stresses due to a poor resolution near the sphere (not shown).

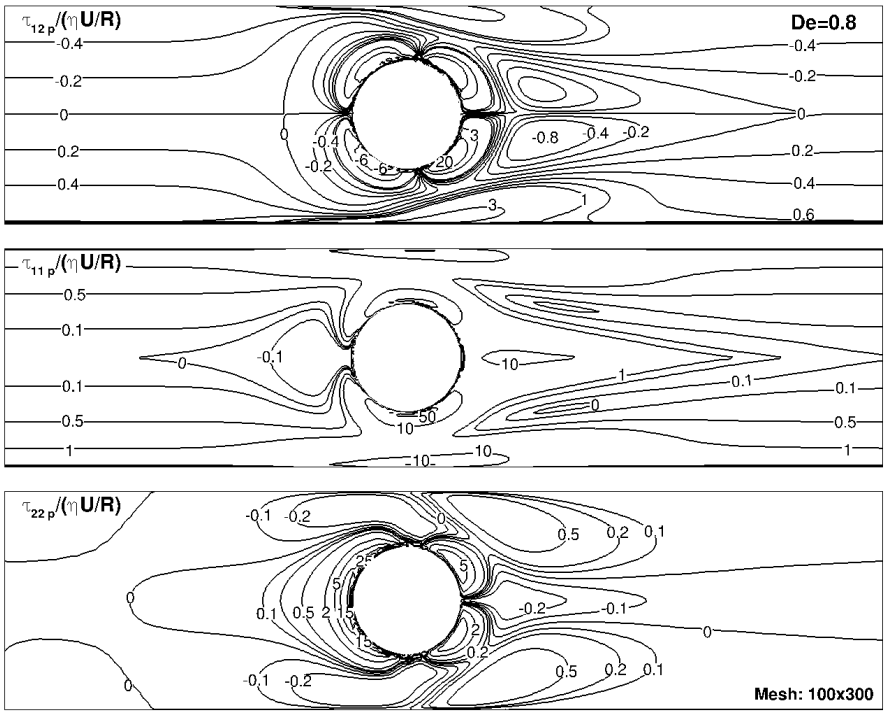

Figure 6.13: Contour plot of normalized variables for the flow past a cylinder: (a) $\frac{\tau_{12}}{\eta U/R}$, $\frac{\tau_{11}}{\eta U/R}$, $\frac{\tau_{22}}{\eta U/R}$ for the current simulation at $De = 0.8$ and 100x300 mesh points.

6.3.2 Settling of a Sphere in a viscoelastic fluid

The motion of a sphere settling inside a square channel filled with an Oldroyd-B fluid is used to validate the temporal scales, hydrodynamic forces and the motion of the particle. A sphere of radius R_s is being released from rest in a tube/channel of radius/width R_c with geometric ratio $\kappa = R_s/R_c$ and moves under the action of gravity. The standard benchmark considers an axisymmetric domain filled with an upper convected Maxwell fluid (UCM) and $Re = 0$, where the drag correction factor (defined below) changes considerable for low De when compared with Oldroyd-B fluid. However, the comparison is made with numerical results that consider solvent viscosity and small Re.

Dimensionless numbers are defined in terms of the terminal velocity of a Newtonian fluid U_s as done by Becker et al. (1994), instead of the actual velocity, in order to predict De and Re.

$$Re = \frac{2R_s\rho_f U_s}{\eta_0} \qquad De = \frac{\lambda_1 U_s}{R_s} \qquad U_s = \frac{(4/3)\,\pi R_s^3\,(\rho_s - \rho_f)\,g}{6\pi\eta_0 R_s K_N}$$

Actual values are computed using the viscoelastic settling velocity U_∞ as,

$$Re_1 = \frac{2R_s\rho_f U_\infty}{\eta_0} \qquad De_1 = \frac{\lambda_1 U_\infty}{R_s}$$

The elasticity number for this case is,

$$E = \frac{\lambda_1 \eta_o}{2a^2 \rho_f}$$

The presence of the walls of the cylinder is taken into account using the wall correction factor K_N stated by Happel and Brenner, provided with the Faxén-Bohlin series, for the Newtonian fluid,

$$K_N = \frac{1}{1 - 2.10444\left(\frac{R_s}{R_c}\right) - 2.08877\left(\frac{R_s}{R_c}\right)^3 - 0.95\left(\frac{R_s}{R_c}\right)^5}$$

For the viscoelastic fluid, the wall correction factor $K\left(De, \kappa\right)$ is computed based on the drag force (Becker et al., 1994)

$$K = \frac{\text{Drag on sphere}}{6\pi\eta_o R U_\infty}$$

where the drag is equal to the addition of the particle weight and the rigidifying force because they are in equilibrium with the hydrodynamical forces in steady-state conditions.

In order to reproduce the results of Becker et al. (1994), it is considered a geometric ratio $\kappa = 0.243$, a sphere of $R_s = 1.27cm$ (different material may change De) and an Oldroyd-B fluid with, $\eta_0 = 137.6$P, $\beta = 0.59$, $\lambda_1 = 0.794$ and its density is estimated to be $\rho_f = 889g/cm^3$. In figure 6.14 it is noted a viscoelastic transient behavior taking place in a timescale $t/\lambda_1 \sim 1$, which is smaller than the viscous timescale for at least one order, where at initial stages the particle increases its velocity over the settling velocity of a Newtonian fluid (overshot) and then decays monotonically to the terminal velocity. Also, the error in velocity is within $\sim 5\%$ for a particle resolution $R_s/\Delta r \sim 10$.

Based on the behavior of the steady state drag coefficient for different aspect ratios, Owens and Phillips (2002) concluded that the capability of a model to fit very well viscometric functions and transient uniaxial extensional properties of a given fluid does not imply accuracy for complex problems like the flow around a sedimenting sphere. That is a serious limitation, added the actual complexity of the models involved and the computational time added.

6.3.3 Settling of a Sphere in a Newtonian fluid

The motion of a sphere settling inside a cylindrical channel filled with a Newtonian fluid is now used to determine the error and convergence of the viscous and rigidifying forces. In this problem, the pipe is generated by imposing a wall boundary condition in a parallelepiped domain of size $L_x \times R_c \times R_c$ for $r \geq R_c$. The other two boundaries are wall (left) and pressure $p = 0$ (right). Gravity is $-980\,\mathrm{cm}/s^2\,\mathbf{i}$. The comparison

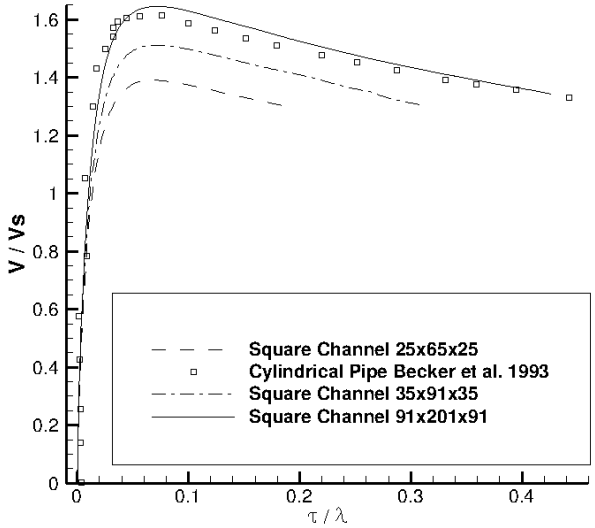

Figure 6.14: Settling velocity as a function of dimensionless time for different mesh size, Delrin sphere $\rho_s = 1.38 g/cm^3$, $Re = 0.011$, $De = 0.406$, $E = 38.1$, $\kappa = 0.243$.

is made at low Re where the dimensionless numbers are the same as in the previous section. For this test, the geometric ratio used is $\kappa = 0.5$, resulting in a drag correction factor of $K_N = 5.9475$ (Boddart and Chroche, 1994).

The parameters used for the simulation are the following: $R_s = 0.05$cm, $\rho_s = 1.05\,\mathrm{g/cm^3}$, $\rho_f = 1\,\mathrm{g/cm^3}$, $\eta = 0.2$P, $\rho_s = 1.05\,\mathrm{g/cm^3}$, $\rho_f = 1\,\mathrm{g/cm^3}$. Under these conditions, the terminal velocity is $U_s = 0.02289\,\mathrm{cm/s}$, producing a Reynolds number $Re = 0.011$. A variable mesh in the x direction was employed, where the meshing near the particle and along its path is uniform. The particle is initially located at $x = 0.025\,\mathrm{cm}$, and the domain size in x is $L_x \sim 1\,\mathrm{cm}$.

The velocity of the particle as a function of time is presented for different mesh resolutions in Figure 6.14 and a comparison is summarized in Table 6.7.

Table 6.7: Velocity of the particle at $t = 0.02$ for different grids

Mesh	$\frac{R_s}{\Delta x}$	Settling Velocity
$100 \times 45 \times 45$	11.25	-0.02077
$80 \times 30 \times 30$	7.5	-0.02077
$55 \times 20 \times 20$	5	-0.01763
Exact, U_s	-	-0.02289

The mesh sensitivity analysis shows that the terminal velocity is within $\sim 9\%$ error for a particle resolution $R_s/\Delta x < 7.5$. This value will be used for further studies. The terminal velocity does not change by refining to $R_s/\Delta x = 11.25$. A coarser mesh of $R_s/\Delta x = 5$ has an error of 15% when compared to the finer mesh,

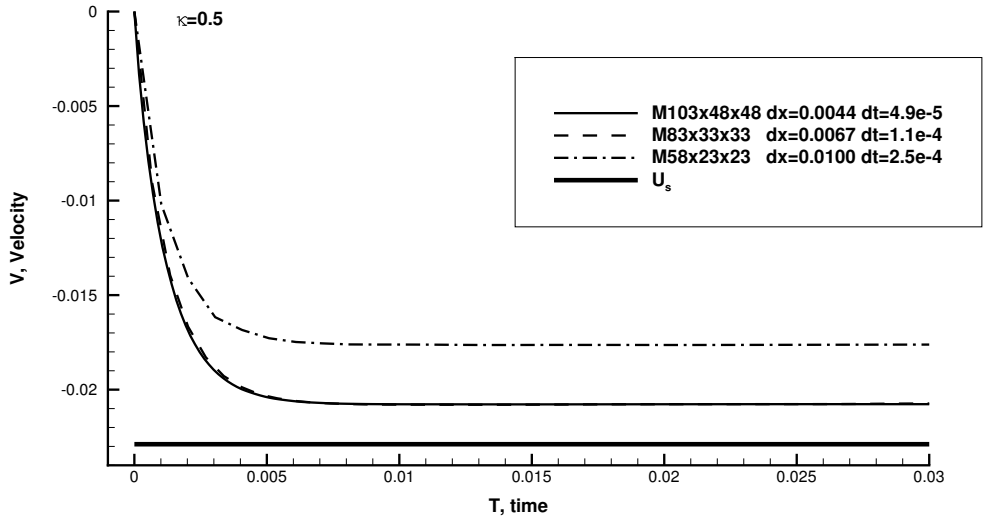

Figure 6.15: Evolution of the velocity for the settling of a rigid particle in a squared channel. For $\rho_s = 1.05\,\mathrm{g}/cm^3$, $Re = 0.011$, $De = 0$ and $\kappa = 0.5$.

which is considerably large.

6.3.4 Collision of particles

The problem of two co-aligned particles moving towards each other is simulated to determine the constants of the collision model and to understand its limitations. In order to isolate relevant forces the linear Euler equation is used with uniform density, that is, gravity, advection and viscous terms are not computed. Only the DEM-based collisional model is employed and any lubrication is due to pressure forces. The particles are accelerated by a piecewise force, $F_x = F_o \mathcal{H}(t_o - t)$ in Ω_p, where $\mathcal{H}$ is the Heaviside step function.

The constant K related to Equation (4.15) is set to 100 and $t_o \approx 0.12$. Even though the model is elastic, the coefficient of restitution deviated from the unity. Increasing the rugosity ϵ improves the elastic behavior, but it increases the minimum distance between the particles, $L_{12} = |\mathbf{x}_2 - \mathbf{x}_1| / (2a)$. This is shown in Figure 6.16, where the coefficient of restitution is $e = 0.70, 0.67, 0.63$ and the minimum distance is $L_{12}/(2a) = 1.15, 1.08, 1.04$, for $\epsilon = 5\Delta x, 4\Delta x, 3\Delta x$. The collision was completely inelastic for $\epsilon \leq \Delta x$. When $L_{12} < 2\Delta x$, a singularity in the pressure field is noticed, and it can be avoided by imposing $\epsilon > 2\Delta x$, depending on the value of K. This behavior limits the applicability of this model if elastic collision are to be reproduced.

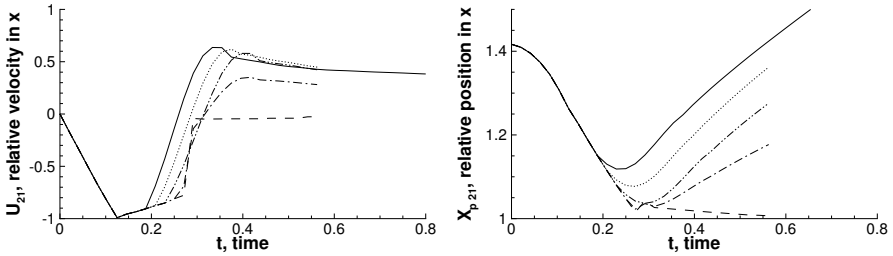

Figure 6.16: Relative motion of two particles in a horizontal collision. For $R_p/\Delta x = 12$ and ϵ: $5\Delta x$ (——), $4\Delta x$ ($\cdots\cdots$), $3\Delta x$ ($- \cdot\cdot -$), $2\Delta x$ ($- \cdot -$) and Δx ($- - -$).

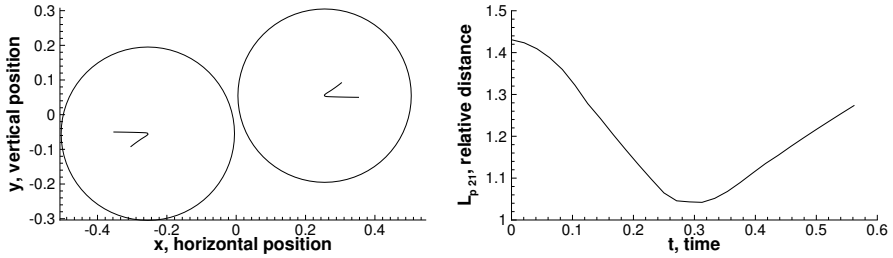

Figure 6.17: Relative motion of two particles in oblique collision. For $R_p/\Delta x = 12$ and $\epsilon = 3\Delta x$.

Now, the initial position in the vertical direction is changed to produce an oblique collision. Similarly as before, the motion is induced by a horizontal force. The results for $\epsilon = 3\Delta x$ are shown in Figure 6.17. The minimum distance is $L_{12} = 1.04$, as in the case with a horizontal collision.

From this study it was found that using the lubrication force is not necessary if $\epsilon > 2\Delta x$ because the

criteria of $2/3\Delta x$ for its activation is never reached. The results show a singular pressure for smaller values of ϵ , i.e. $\epsilon = \Delta x$, and even then, lubrication force does not activate. Only when $\epsilon < \Delta x$ it will activated. Therefore, the two options are $\epsilon = 0$ for fully inelastic collisions, or $\epsilon = 3\Delta x$ for partially elastic collisions. Considering that the coefficient of restitution is highly dependent on ϵ, large errors are expected for a frictional-force model (shearing).

6.4 Problems involving Surface Tension

6.4.1 Static drop problem

In this section, the problem of a static drop in a quiescent fluid is investigated to understand the capabilities or limitations of the CSF method when surface tension is relevant. The objective is to show how different curvature models, transport models and techniques affect the accuracy of the results. It is of interest to determine the convergence rate of the curvature model with mesh refinement, the errors incurred in the calculation of the the pressure jump and the intensity of the spurious currents. The exact pressure jump at the interface is given by the Young-Laplace equation, $\Delta p = \kappa\sigma$, where κ is the curvature and σ is the surface-tension coefficient. The exact curvature for a sphere of radius a is $\kappa = 2/a$. This problem is governed by a modified Reynolds number $Re_{osc} = \sqrt{\rho_d \sigma a}/\eta_d$, where ρ_d and η_d are the drop density and a dynamic viscosity, respectively. This problem is subject to the initial condition $\mathbf{u}(\mathbf{x}, 0) = \mathbf{0}$ and $p(\mathbf{x}, 0) = 0$.

The FCT Algorithm

The following simulations consider a spherical drop of radius $a = 2$ contained in an cube of size $H = 6$ where the fluids have uniform properties: density ratio, $\gamma = \frac{\rho_d}{\rho_m} = 1$, and viscosity ratio, $\lambda = \frac{\eta_d}{\eta_m} = 1$. The first group of simulations focuses on showing the errors in pressure jump and curvature for several schemes. The surface-tension coefficient $\sigma = 73$ and $Re = 340$ are used. The exact curvature and pressure jump are $\kappa = 1$ and $\Delta p = 73$.

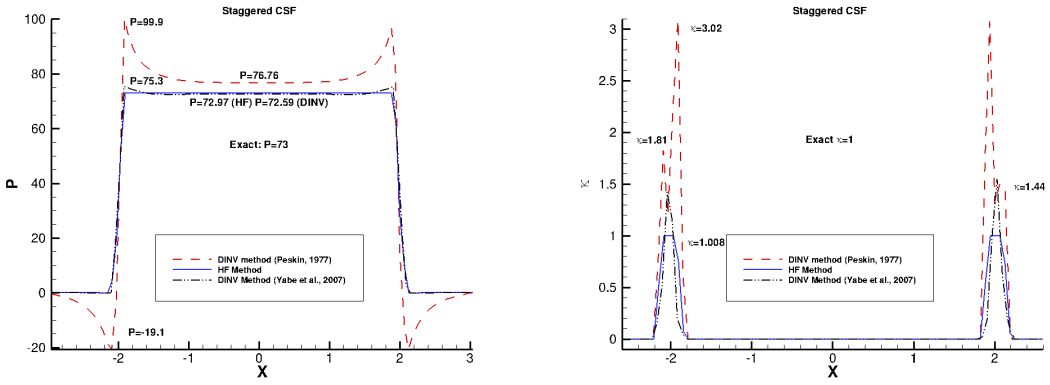

(a) Pressure profile, p

(b) Curvature, κ

Figure 6.18: Comparison of curvature models for the static drop problem. The properties are measured along the x axis at $y = 0$. The curvatures are computed from the divergence of a smoothed interfacial normal vector model (DINV), where the smoothed $\hat{F}$ is computed using the technique of Yabe et al. (2007) or Peskin (1977), and using the height functions formulation (HF). Results shown after one time step $\Delta t = 1.2 \cdot 10^{-3}$ ($CFL = 1$) using a mesh $70 \times 70 \times 70$ or $a/\Delta x = 23$.

The HF method captures the pressure jump Δp distributed along 3 cells and provides an estimation of the curvature with an error $9 \cdot 10^{-3}$, for an interface thickness $\delta/a \sim 0.2$, as shown in figure 6.18. A larger error was observed when the curvature was computed using the interface normal vector (DINV). Despite that the addition of a smoothed color function reduces the error considerably, in comparison to estimating the curvature from a raw color function (not shown), the error is as low as 44% and as large as 300%. Among the two DINV method tested, the approach suggested by Yabe et al. (2007) presents a smaller error in curvature and better pressure jump than the method of Peskin (1977). Considering that only one time step was advanced, these results are independent of the transport model.

The viscous dissipation becomes negligible for $Re_{osc} \gtrsim 100$, which in turn enhances the growth of the spurious currents. For larger values of Re_{osc}, numerical breakdown can happen. That is why knowing the scale of such velocities is important. The scales of the spurious currents in former simulations using the HF-FCT method are now compared and presented in figure 6.19. Two mesh resolutions are used: $a/\Delta x = 16$ and $a/\Delta x = 30$. Mesh refinement shows first-order reduction of the maximum velocity, as expected. A less pronounced reduction is noticed when the time step is reduced. As it can be observed, the interface degrades considerably for the coarser mesh. More detailed studies on the spurious currents are shown next.

We now change the properties across the interface and consider a new test with high density and viscosity ratios for different curvature and force models. Within a given CSF approach, two different models are chosen: a density based and the unweighted staggered (not mollified). Additionally, the term ∇F is computed either from a first-order finite difference (sharp/staggered) or from a second-order finite difference (three point).

The curvature is estimated from the traditional height function computed along a main axis (HF), considering additional directions, that is, on the diagonals of the main planes (diagonals or HF-PD), or the main diagonal of the cell (all diagonals or HF-AD), and from the divergence of the interfacial normal vector. The comparison is held at the same Reynolds number, $Re_{osc} = 340$, but for density ratio $\gamma = \rho_d/\rho_m = 1000$, viscosity ratio $\lambda = \mu_d/\mu_m = 1000$, and a cubed domain of size $H = 5$.

The pressure profiles for different cases are shown in figure 6.20. In this case, the lowest error with respect to the steady state solution is obtained by the DINV-Peskin method. The density-based three-point mollified case showed large interface degradation. One of the effects of using large stencils is that the pressure jump takes more cells. The mollification was incorporated to improve the stability, but the main reason of the increase in the error is the three-point technique. The HF method kept the interface within two cells (sharp), but with higher local curvatures (stairs). It is noticed how the FCT method compresses the transport along main directions, which produces stair-like patterns of the interface. The DINV-Peskin method smoothed the interface, therefore reducing those effects, and the final spherical shape was captured with an acceptable range of curvatures across the interface. This is the reason why it produced better results. Considering that

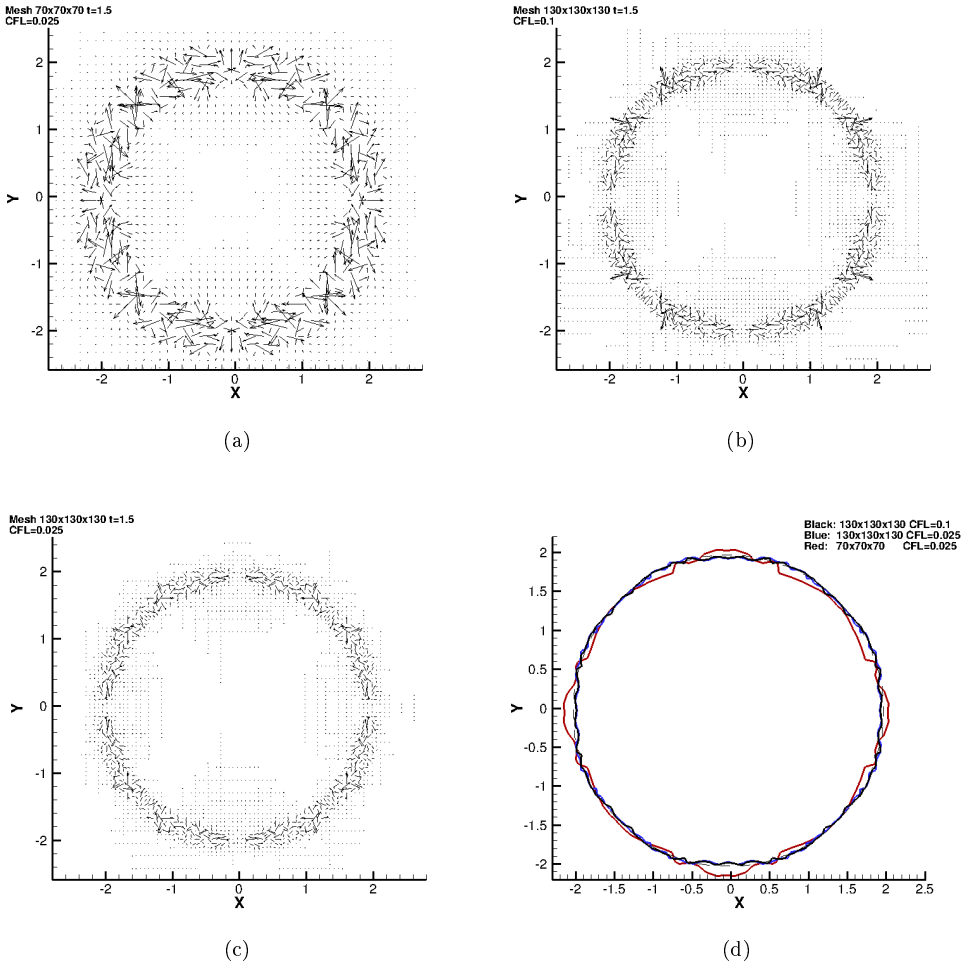

Figure 6.19: Spurious currents at $t = 1.5$ for different mesh resolution and CFL conditions for the HF-FCT method and uniform properties: (a) For $70 \times 70 \times 70$ ($a/\Delta x = 16$) and $CFL = 0.025$, $|u_{max}| = 0.92$ (b) For $130 \times 130 \times 130$ ($a/\Delta x = 30$) and $CFL = 0.1$, $|u_{max}| = 0.53$ (c) For $130 \times 130 \times 130$ ($a/\Delta x = 30$) and $CFL = 0.025$,$|u_{max}| = 0.31$ (d) Contour of the interface for the mentioned cases.

DINV-Yabe performed better than DINV-Peskin in the previous simulations, it is expected that DINV-Yabe together with the staggered force (SF-Y) will offer better stability and accuracy than the other methods when employing the FCT algorithm in high property ratio conditions.

The PLIC Algorithm

The surface-tension force is now computed using the staggered CSF approach, equation (5.14), unless stated otherwise and advanced in time using the FCT and the first PLIC algorithms. The curvature models adopted for the comparison are the kernel based (SF-Y) (Yabe et al., 2007) and the height function family of methods (HF, HF-PD, HF-AD and HF-LH). The simulations are performed in a cubic domain of size $H = 6$, for a drop with radius $a = 2$, $\gamma = 1$ and $\lambda = 1$. The drop is initialized with sub-grid resolution. This problem is

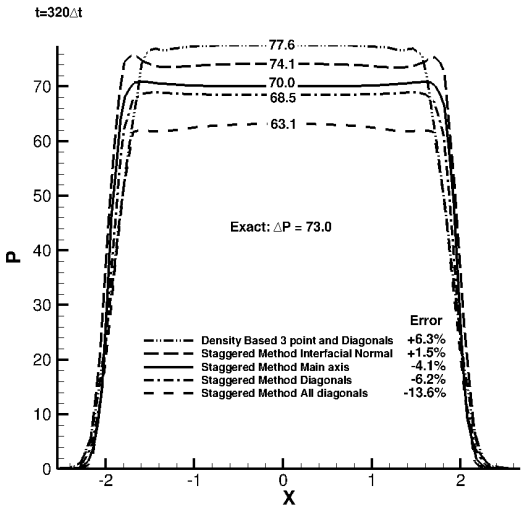

Figure 6.20: Comparison of the pressure profile along x axis ($y = 0$) after $320\Delta t \approx 0.2$, using a mesh $50 \times 50 \times 50$, $a/\Delta x = 20$ and $CFL = 0.5$, within a three point or a sharp (staggered) technique to compute ∇F.

subject to the initial condition $\mathbf{u}(\mathbf{x}, 0) = \mathbf{0}$, $p(\mathbf{x}, 0) = 0$, advanced in time with a time step $\Delta t = 3.4 \cdot 10^{-3}$ ($CFL_\sigma = 0.25$), using a mesh 60^3 and the residual criterion for mass conservation is set to 10^{-8}. The new flow conditions are $Re_{osc} = 200$ and a surface-tension coefficient of $\sigma = 1$ are chosen, which represents a low Ohnesorge number problem, $Oh = \eta / (\rho \sigma R)^{1/2} = 0.005$. The exact curvature and pressure jump are $\kappa = 1$ and $\Delta p = 1$, respectively.

The CSF method is capable of resolving the pressure jump, Δp, across two cells, while the PLIC-VOF method keeps the interface without degradation in time, as show in Figure 6.21. The HF method shows a better pressure jump than the HF-PD and SF-Y models and is capable of keeping the pressure jump accurately after $t = 100\Delta t$. This is expected since the HF method computes the curvature of a sphere with high accuracy.

The curvature profile is presented in Figure 6.22, where a remarkable maximum error of 43% is observed for the SF-Y method. It is noticed how the use of the SF-Y model can affect the solution in multiple directions, while the HF-PD model shows a degradation at angles around 30° and 60°. The height function method can produce inaccurate values of κ if the mesh is too coarse or if κ is relatively large, as when resolving highly curved interfaces, grid-sized structures, or when the interface is not resolved sharply (more than 3 cells) like it happens with diffusive non-compressive schemes. The calculation of the height function along different directions (HF-PD or HF-AD) can provide a solution to the first problem, considering that a maximum error can occur at angles $(2n + 1)\pi/4$ in 2D, but at the expense of a larger error in spherical or simpler shapes, as shown here.

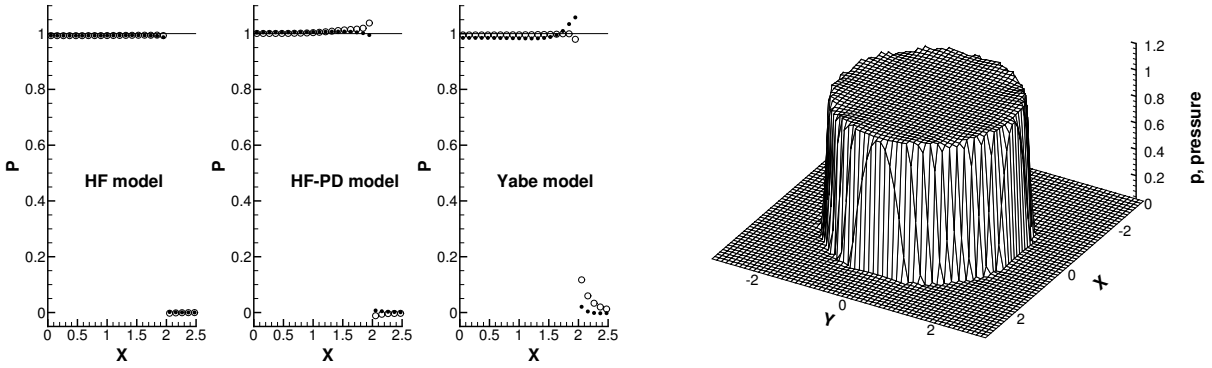

(a) (b)

Figure 6.21: Pressure distribution using the PLIC-VOF method. (a) The curvature is computed along the line $y = 0$, $x > 0$ using the following models: HF (Left), HF-PD (Middle) and SF-Y (Right) at $t = \Delta t$ ($\bullet$), or at $t = 100\Delta t$ ($\bigcirc$), for $CFL_\sigma = 0.25$ ($\Delta t = 3.4 \cdot 10^{-3}$), a mesh 60^3 ($a/\Delta x = 19$) and uniform properties. (b) Representation of HF-PD model on the xy plane.

A summary of the average and maximum error of the curvature ($\langle\kappa\rangle - 1$, $\kappa_{max} - 1$) on the xy plane for several curvature models is presented in Table 6.8. Two mesh resolutions and a smaller time step were considered for this test to determine the raw order of convergence on mesh refinement. The HF-PD, HF-AD and SF-Y did not show convergence on mesh refinement. Those methods had a similar maximum error in curvature. Only the HF and the HF-LH models showed convergence of the curvature on mesh refinement, where better results were obtained with the HF method.

Table 6.8: Error of the curvature κ in the xy plane after one time step $\Delta t = 1 \times 10^{-3}$ for different models. $Re_{osc} = 200$ and uniform properties, $\lambda = \gamma = 1$.

	Mesh 60^3		Mesh 120^3		
Model	$\langle\kappa\rangle - 1$	$\kappa_{max} - 1$	$\langle\kappa\rangle - 1$	$\kappa_{max} - 1$	Order
HF	1.1×10^{-3}	0.003	4.6×10^{-4}	0.015	1.2
HF-PD	1.1×10^{-2}	0.12	6.0×10^{-2}	0.8	<0
HF-AD	5×10^{-2}	0.12	6.0×10^{-2}	0.8	<0
HF-LH	1.1×10^{-3}	0.003	5.1×10^{-4}	0.016	1.07
SF-Y	1.2×10^{-1}	0.43	1.6×10^{-1}	0.7	<0

It is also important to show the effect of the curvature estimations on the calculation of the pressure. The error of the pressure is based on its value at the center of the drop, $P(\mathbf{0}) - 1$. A mesh sensibility analysis was performed using the HF, HF-PD and SF-Y models, and the results are summarized in Table 6.9. These results (and the results up to this point) were obtained without the AvM technique, Equation 5.17. The comparison shows a small order of convergence and even negative in some cases. There is no correlation between the pressure and the curvature when the grid is refined for the HF model, because the curvature has positive order of convergence, while the pressure has negative order of convergence. On the other hand,

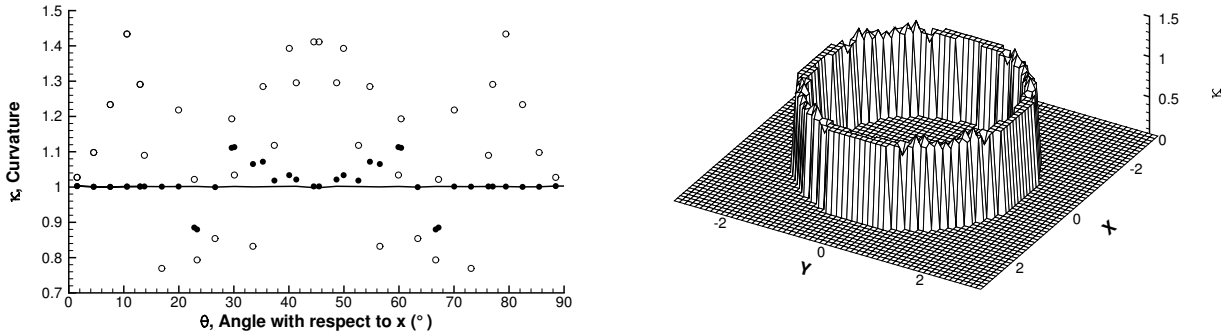

(a) Curvature, κ, along the curve $F = 0.5$ on the xy plane

(b) Curvature, κ, on the xy plane for the HF-PD model

Figure 6.22: Estimation of the curvature for a static drop of radius $a = 2$, using: HF (——), HF-PD (•) and SF-Y (○). Results are shown after one time step, $CFL_\sigma = 0.25$ ($\Delta t = 3.4 \cdot 10^{-3}$), using a mesh 60^3 ($a/\Delta x = 19$).

the HF-PD model manifests positive order of convergence of the pressure on fine grids, but negative order of convergence of the curvature. Aside from the observation that none of the methods has a fixed order of convergence on grid refinement, there is no correlation between the convergences of curvature and pressure. Therefore, the curvature model initially chosen determines the overall error of the pressure distribution, where a bias error could be carried on even with grid refinement. Because the HF-PD model shows the lowest error on fine meshes, it was the preferred model for a while during this work. Also, it presents the lowest error of the pressure in time as it is discussed next.

Table 6.9: Effect of the curvature model on the error in the pressure measured at the origin after one time step of $\Delta t = 1 \times 10^{-3}$. No AvM.

Model	HF		HF-PD		SF-Y	
Grid ($a/\Delta x$)	$P(\mathbf{0}) - 1$	Order	$P(\mathbf{0}) - 1$	Order	$P(\mathbf{0}) - 1$	Order
$15^3(4)$	7.4×10^{-3}	–	4.6×10^{-3}	–	2.8×10^{-2}	–
$30^3(9)$	7.9×10^{-5}	5.6	1.3×10^{-2}	–	1.1×10^{-2}	1.1
$60^3(19)$	7.3×10^{-3}	-6.1	4.4×10^{-3}	0.2	1.5×10^{-2}	-0.4
$120^3(39)$	8.3×10^{-3}	-0.2	3.9×10^{-3}	0.4	1.5×10^{-2}	0.03

Now, several curvature models and the two transport models, the FCT and the first BDR-PLIC method, are studied. The comparison is made after Δt and $100\Delta t$. The pressure at the center of the drop, the maximum velocity and the details of the simulations are presented in Table 6.10. The error in the pressure is less than 0.7% after Δt for the HF and HF-PD methods, which is due to an accurate estimation of the curvature with an average error smaller than 1%. For the SF-Y method, an error of 12% in the average curvature implies an error of 1.5% in the pressure. Even though the HF-AD method shows 5% error in the average curvature, the error in pressure increases to 2.7%, larger than SF-Y. It is also noted how all the values of the pressure improve after $100\Delta t$ for the PLIC method, while they deviate for the FCT method,

particularly in the case of the HF-AD model.

Table 6.10: Pressure at the center of the drop and spurious currents development using different methods. For $Re_{osc} = 200$, $\lambda = \gamma = 1$, $CFL_\sigma = 0.25$ ($\Delta t = 3.4 \times 10^{-3}$), mesh 60^3 and the unweighted CSF model. No AvM.

	FCT				PLIC			
Model	$p_{\Delta t}$	$p_{100\Delta t}$	$\lvert V_{max}\rvert_{\Delta t}$	$\lvert V_{max}\rvert_{100\Delta t}$	$p_{\Delta t}$	$p_{100\Delta t}$	$\lvert V_{max}\rvert_{\Delta t}$	$\lvert V_{max}\rvert_{100\Delta t}$
HF	0.9927	0.9871	2.5×10^{-4}	4.2×10^{-2}	0.9927	0.9927	2.5×10^{-4}	2.1×10^{-2}
HF-PD	1.0044	0.9924	3.2×10^{-3}	8.6×10^{-2}	0.9940	1.0005	3.2×10^{-3}	7.1×10^{-2}
HF-AD	0.9735	0.9480	3.3×10^{-3}	8.6×10^{-2}	0.9735	0.9770	3.3×10^{-3}	7.6×10^{-2}
SF-Y	0.9847	0.9810	3.4×10^{-3}	3.2×10^{-1}	0.9847	0.9953	3.4×10^{-3}	1.9×10^{-1}

The velocity of the parasitic currents is in the order of $0.01\sigma/\eta$ for the parabolic interface reconstruction method (PROST) of Renardy and Renardy (2002). Given the properties of the drop used here, the equivalent value of the spurious currents is $V_{max\,PROST} \sim 1.4$, which is definitely large. As a reference, spurious currents are measured and presented in Table 6.10. The maximum velocities are smaller such estimation, for $t < 100\Delta t$, with values as low as 2×10^{-2}. The method with the lowest value is the standard HF method, followed by the HF-PD, HF-AD and SF-Y. This is expected since the spurious currents are reduced as the curvature becomes exact. Additionally, the PLIC method showed slightly smaller spurious currents than the FCT method. A more detailed study is presented later on for the DDR-PLIC method.

It is of interest to obtain a curvature model that converges with mesh refinement. After analyzing the reasons of a non-converging pressure on mesh refinement, it was found that the technique to average the curvature was having a significant impact on the results. The effect of mollification and the use of the AvM technique, Equation (5.17), is now studied. When the HF-LH model (López and Hernández, 2010) is combined with the F-based CSF force and AvM is used, convergence with mesh refinement is observed. The curvature and pressure are presented in Table 6.11. As it can be observed, the error in the pressure reduces with grid refinement and the convergence is always positive, being considerably more accurate for finer mesh resolutions than the HF model without AvM, shown in Table 6.9. When AvM was deactivated, that is, the curvature is given by the average between neighbors, the HF-LH model showed slightly worst results than the HF model. The curvature accuracy of the HF-LH model is similar to the HF model in the xy plane, but it improves in the other directions (not shown). Finally, the mollification or weighting by volume fraction produced a second-order convergence of the pressure on mesh refinement.

Table 6.11: Error of the curvature κ in the xy plane and pressure at the origin after one time step $\Delta t = 1\times10^{-3}$ for the HF-LH model (López and Hernández, 2010). $Re_{osc} = 200$ and uniform properties, $\lambda = \gamma = 1$.

	Curvature			F-Based		Unweighted		Unweighted No AvM	
Mesh	$\langle\kappa\rangle - 1$	$\kappa_{max} - 1$	Order	$P(\mathbf{0}) - 1$	Order	$P(\mathbf{0}) - 1$	Order	$P(\mathbf{0}) - 1$	Order
30^3	5.1×10^{-3}	5.8×10^{-3}	–	6.0×10^{-3}	–	7.6×10^{-3}	–	1.2×10^{-3}	–
60^3	1.1×10^{-3}	2.8×10^{-3}	2.00	1.1×10^{-3}	2.28	1.4×10^{-3}	2.28	-7.2×10^{-3}	< 0
90^3	5.3×10^{-4}	4.1×10^{-3}	1.80	4.7×10^{-4}	2.01	6.3×10^{-4}	1.85	-8.2×10^{-3}	< 0
120^3	5.1×10^{-4}	1.6×10^{-2}	0.16	2.1×10^{-4}	2.72	3.7×10^{-4}	1.80	-8.4×10^{-3}	< 0

These methods are proven to be accurate on the mesh sizes used ($a/\Delta x > 4$), within 3% error and as accurate as 2×10^{-6}%, which is useful when small particles are not fully resolved, or when there is a spectrum of curvatures.

The BDR and DDR algorithms

In this section, the convergence rate of the curvature model with mesh refinement, the errors incurred in the calculation of the the pressure jump and the intensity of the spurious currents for the BDR and DDR methods are formally sought. Similarly as before, the drop has radius $a = 2$, it is initialized in a quiescent flow, with $\mathbf{u}(\mathbf{x}, 0) = \mathbf{0}$, and $p(\mathbf{x}, 0) = 0$. The initial volume fraction is computed using the "baby-cell" method with a sub-grid resolution of $\Delta l = \Delta x/250$. The domain is a cube of size $H = 6$. The drop-medium density ratio is $\gamma = \rho_d/\rho_m = 10^3$ and viscosity ratio is $\lambda = \eta_d/\eta_m = 10^3$, unless stated otherwise. A Reynolds number $Re_{osc} = 200$, equivalently to a Ohnesorge number of $Oh = \eta_d/\sqrt{\rho_d\sigma a} = 0.005$, and a surface-tension coefficient of $\sigma = 1$ are considered again. The simulations are advanced in time with $CFL_\sigma = 0.25$, using a normalized residual criterion for mass conservation of 10^{-8}. The surface-tension force is computed using the staggered CSF approach, Equation (5.14). The curvature is computed from the directional height functions and the AvM technique is activated.

$$L_n(\boldsymbol{\phi}) = \sqrt[n]{\frac{\sum_{i=1}^{N} |\phi_i - \phi_{\text{exact}}|^n}{N\phi_{\text{exact}}^n}} \tag{6.2}$$

In order to compare the error in curvature and pressure, the L_1 and L_2 relative error norms are computed using Equation 6.2, while L_∞ stands for the maximum error. The curvature is extracted at the interface, $F = 0.5$, meanwhile the pressure is only measured inside the drop, $F = 1$. The error in curvature can also be estimated as $\Delta\kappa \sim \frac{2}{na}$, where $n = a/\Delta x$. Similarly, the L_1 and L_2 normalized norms of the spurious

currents are measured across the interface, $0 < F < 1$, from $L_n(\boldsymbol{\phi}) = \sqrt[n]{\frac{1}{N}\sum_{i=1}^{N}|\phi_i|^n}$, while L_∞ is measured in the whole domain.

The effect of mesh resolution on the curvature after one time step, Δt, is shown in Table 6.12. The convergence of the L_1 norm is superlinear with an overall convergence of order 1.95 (for N between 15 and 140) and a minimum order of convergence of 1.72. These results are expected because a second-order scheme was employed in Equation 5.12. In the case of the L_2 error, the order of convergence varied between first and third order, with an overall order of 1.81, and a minimum of 0.96. Except for the case of $N = 5$, the L_1, L_2 and L_∞ errors were smaller than the estimated error $\Delta\kappa$ (normalized by $\kappa = 1$). The L_∞ error was observed to increase for fine meshes. The HF method is known to increase the error of the curvature when at least one radius of curvature is comparable to the mesh size. These results suggest that a mesh resolution of $a/\Delta x > 3$ is required to be within 10% error. In cases where $r_1 \gg r_2$ (planar cases), the curvature can be approximated as $\kappa = \frac{1}{r_1} + \frac{1}{r_2} \approx \frac{1}{r_2}$, and the error behaves like $\Delta\kappa \approx \frac{\Delta x}{r_2^2}$. Thereby, a slightly coarser mesh can be used.

Table 6.12: Error of the curvature κ at the interface, $F = 0.5$, after one time step, $CFL = 0.25$, for different mesh resolutions. $Re_{osc} = 200$ and $\lambda = \gamma = 10^3$.

Mesh	L_1 Error		L_2 Error		L_∞ Error	
$\frac{a}{\Delta x}$ (N^3)	Error	Order	Error	Order	Error	$\Delta\kappa \sim \frac{2\Delta x}{a^2}$
$1\frac{2}{3}(5^3)$	0.865	–	0.865	–	0.865	0.6
$2\frac{2}{3}(8^3)$	9.5×10^{-2}	4.7	0.127	4.1	0.356	0.375
$5(15^3)$	1.8×10^{-2}	2.7	1.9×10^{-2}	3.0	3.4×10^{-2}	0.2
$10(30^3)$	4.9×10^{-3}	1.83	9.9×10^{-3}	0.96	7.7×10^{-2}	0.1
$20(60^3)$	1.0×10^{-3}	2.27	1.3×10^{-3}	2.96	5.9×10^{-3}	5×10^{-2}
$40(120^3)$	3.1×10^{-4}	1.72	6.1×10^{-4}	1.07	9.3×10^{-3}	2.5×10^{-2}
$46\frac{2}{3}$ (140^3)	2.4×10^{-4}	1.76	4.1×10^{-4}	2.54	1.5×10^{-2}	2.1×10^{-2}

In general, the maximum error in curvature when using the HF method occurs near the main diagonal of the cell ($\hat{\mathbf{i}} + \hat{\mathbf{j}} + \hat{\mathbf{k}}$), as shown in Figure 6.23, where the iso-surface of the interface is presented for a mesh resolution $a/\Delta x = 46.7$. In this case, that maximum error is 2% after Δt and it grows up to 5% after $100\Delta t$. The surrounding error remain within 2%.

One of the benefits of using the HF model is the improvement of the pressure distribution. In the case of a static drop, the pressure distribution inside is uniform. This behavior is recovered numerically, as it is shown for a coarse mesh and after $100\Delta t$ in Figure 6.25. In contrast to the HF-PD model, shown in Figure 6.21, the profile does not present spikes near the interface.

The error in pressure is also presented after one step Δt, Table 6.25, after $100\Delta t$, Table 6.14, and at $t = 1$, Table 6.15. The order of convergence in pressure is more or less similar to the convergence of the curvature, between first and second order. However, for later times, $t = 1$, the order of convergence degrades. This

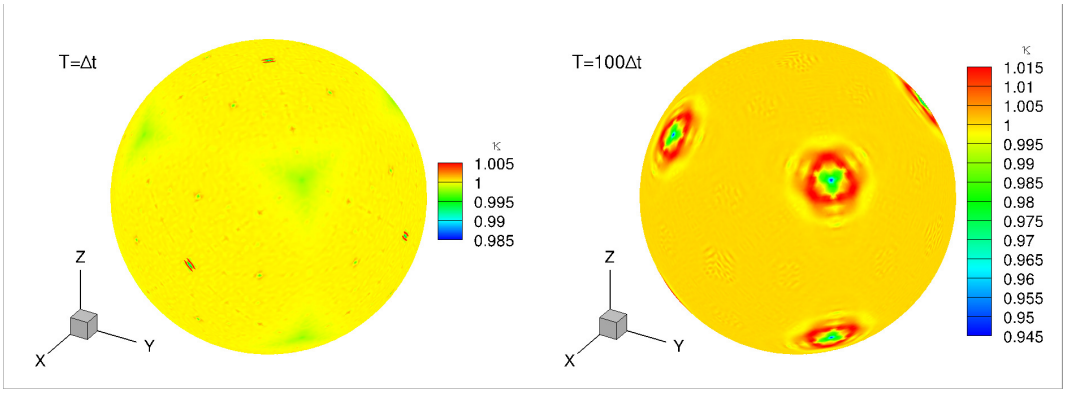

Figure 6.23: Curvature κ on the iso-surface $F = 0.5$ for a drop of radius $a = 2$, using the HF method and $\lambda = \gamma = 10^3$. Results are shown after Δt and $100\Delta t$ ($\Delta t = 6.3 \times 10^{-4}$) for a mesh of 140^3 ($a/\Delta x = 46.7$).

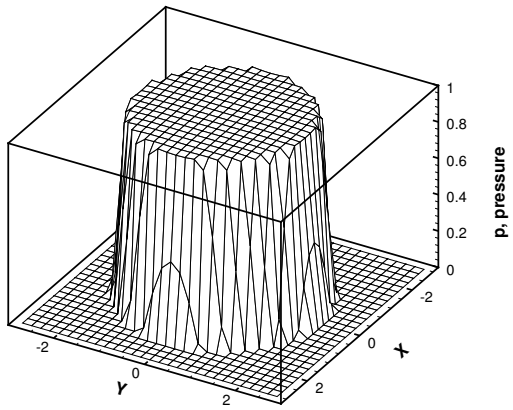

Figure 6.24: Pressure distribution of a drop on the xy plane using the HF and the staggered-unweighted CSF models. Mesh 30^3, $t = 100\Delta t$ and $\lambda = \gamma = 10^3$.

is attributed to the growth in the spurious currents, which bend the interface and produce local changes in curvature.

Table 6.13: Error in pressure at $t = \Delta t$, $CFL = 0.25$.

Mesh ($a/\Delta x$)	L_1 Error	Order	L_2 Error	Order	L_∞ Error
$15^3(5)$	2.1×10^{-2}	–	2.1×10^{-2}	–	1.1×10^{-2}
$30^3(10)$	4.8×10^{-3}	2.13	4.9×10^{-3}	2.12	1.8×10^{-2}
$60^3(20)$	1.6×10^{-3}	1.6	1.8×10^{-3}	1.41	1.6×10^{-2}
$120^3(40)$	4.4×10^{-4}	1.86	5.1×10^{-4}	1.84	4.8×10^{-3}

The velocity of the parasitic currents can be estimated from $\langle V \rangle = C\sigma/\eta$. If the velocity employed is the maximum velocity, then a higher bound of C can be found. For that reason, the L_∞ norm of the velocity is used. In the case of $\gamma = 1$, the spurious current constant is $C \sim 10^{-4}$, and it increases for $\gamma = 10^3$ up to $C \sim 10^{-1}$. As a reference, spurious currents are measured and presented in Table 6.16. The values of C for uniform properties are similar to the reported values using PROST (Renardy and Renardy, 2002).

Table 6.14: Error in pressure at $t = 100\Delta t$, $CFL = 0.25$.

Mesh $(a/\Delta x)$	L_1 Error	Order	L_2 Error	Order	L_∞ Error
$15^3(5)$	3.8×10^{-2}	–	3.8×10^{-2}	–	4.2×10^{-2}
$30^3(10)$	9.8×10^{-3}	1.96	1.0×10^{-2}	1.87	2.8×10^{-2}
$60^3(20)$	2.3×10^{-3}	2.07	2.6×10^{-3}	2.03	7.0×10^{-3}
$120^3(40)$	6.7×10^{-4}	1.79	8.4×10^{-4}	1.61	7.2×10^{-3}

Table 6.15: Error in pressure at $t = 1$, $CFL_\sigma = 0.25$.

Mesh $(a/\Delta x)$	L_1 Error	Order	L_2 Error	Order	L_∞ Error
$15^3(5)$	3.1×10^{-2}	–	3.1×10^{-2}	–	3.7×10^{-2}
$30^3(10)$	8.5×10^{-3}	1.87	9.1×10^{-3}	1.79	2.2×10^{-2}
$60^3(20)$	3.0×10^{-3}	1.52	4.0×10^{-3}	1.18	3.9×10^{-2}

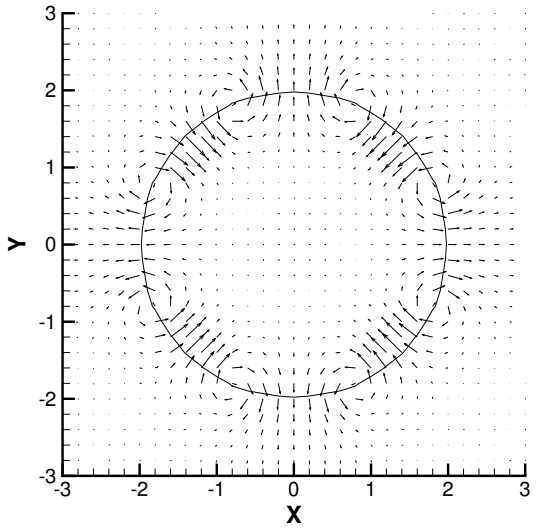

Figure 6.25: Spurious currents on the xy plane using the HF, PLIC, DDR and the staggered-unweighted CSF models. Mesh 30^3, $t = 1$ and $\lambda = \gamma = 1$. The velocity field is scaled $75 : 1$.

Table 6.16: Spurious currents at $t = 1$, for $Re_{osc} = 200$, $CFL_\sigma = 0.25$.

	$\gamma = \lambda = 1$				$\gamma = \lambda = 10^3$			
Mesh	L_1 norm	L_2 norm	L_∞ norm	$\frac{L^\infty \mu}{\sigma}$	L_1 norm	L_2 norm	L_∞ norm	$\frac{L^\infty \mu}{\sigma}$
30^3	8.6×10^{-3}	1.3×10^{-2}	5.7×10^{-2}	4.1×10^{-4}	1.2×10^{-1}	5.2×10^{-1}	6.4	4.5×10^{-2}
60^3	1.9×10^{-3}	3.7×10^{-3}	5.0×10^{-2}	3.5×10^{-4}	3.2×10^{-2}	1.0×10^{-1}	5.6	4.0×10^{-2}
120^3	8.3×10^{-4}	1.6×10^{-3}	4.3×10^{-2}	3.0×10^{-4}	3.5×10^{-1}	1.2	39.2	0.28

6.4.2 Oscillation of a liquid drop

The numerical method is further studied for the motion of an initially deformed drop in a quiescent flow. This problem allows for a full validation of the numerical method because it combines high drop deformation with relatively large Re and variations in viscosity and density. This flow is governed by $Re_{osc} = \sqrt{\rho_d \sigma a}/\eta_d$, where a is the radius of equilibrium. The parameters used for the comparisons are the first period of the oscillation, τ_1, and the dorp aspect ratio A/B, where A and B are the horizontal and vertical lengths, respectively. The domain is limited by a cube of side 2. All the boundaries are prescribed with pressure $p = 0$ and normal velocities, while the initial condition is $\mathbf{u} = \mathbf{0}$, $p = 0$. Following the work of Basaran (1992), the initial deformation of the drop is given by a departure of the n^{th} spherical harmonic,

$$r(\theta) = \gamma_n^{1/3} a \left[1 + f_n P_n(\cos\theta)\right] \qquad 0 \leqslant \theta \leqslant \pi,\ n > 1 \tag{6.3}$$

where r is the radius from the origin in spherical polar coordinates, the angle θ is measured with respect to the horizontal axis, f_n is the amplitude of the initial deformation, γ_n is a normalization factor that ensures constant volume for different initial deformations and P_n is the n^{th} Legendre's polynomial. For $n = 2$, the normalization is $\gamma_2 = \frac{35}{35+21f_2^2+2f_2^3}$ for the prolate deformation, while $\gamma_2 = \frac{280}{280+420f+378f_2^2+103f_2^3}$ for the oblate deformation.

The FCT Algorithm and the Oblate Drop

In this part we study the deformation of drops using the FCT algorithm for the case of the oblate shape deforming at $Re_{osc} = 40$. For a negligible matrix fluid dependence, high viscosity and density ratios are used: $\lambda = \frac{\eta_d}{\eta_m} = 1000$, $\gamma = \frac{\rho_d}{\rho_m} = 1000$. The simulations are based on $\rho_d = 1$, $\sigma = 1$, $a = 1$ and $\eta_d = 0.025$. For $Re_{osc} = 40$, the constants for the Rayleigh-Lamb model are $b = 0.125$ and $\omega = 2\sqrt{2}$, which relates to a complex frequency of $\beta_n = 0.125 \pm i\,2.8312$.

The motion of the interface is shown in Figure 6.26, where a sharp interface is obtained. The aspect ratio for the oblate case using two curvature models is shown in Figure 6.27, where the results of Basaran (1992) using the BIM method are also included as a reference (prolate case). It can be observed how the oblate case is in better agreement with the Rayleigh-Lamb solution than the prolate case. The comparison with the theoretical model shows an average difference of 7% and a maximum of 19%. When the curvature is computed from Height functions (HF), severe degradation of the interface was obtained (not shown), confirming that the FCT model works better with a convolution/smoothening method than with the HF method.

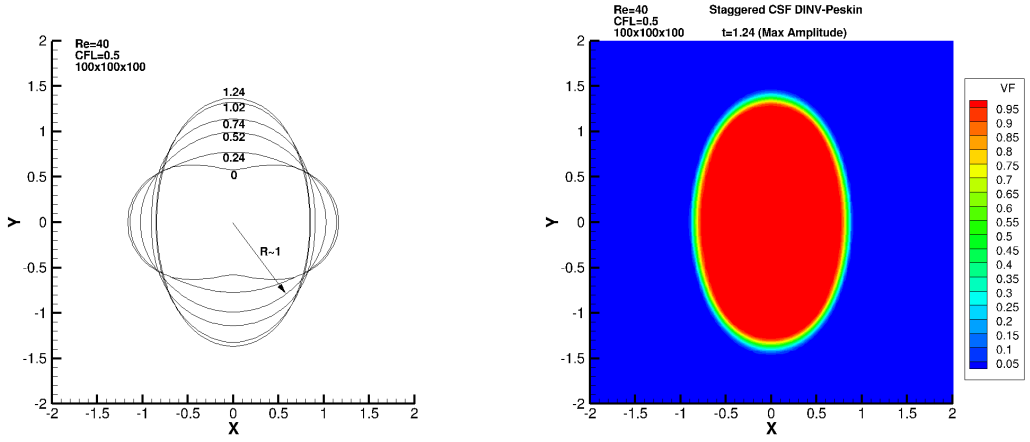

(a) Interface motion

(b) Contour of the volume fraction at the maximum amplitude of the first cycle

Figure 6.26: Interface of the oscillating viscous drop problem at $Re = 40$, $\gamma = \lambda = 1000$, and $CFL = 0.5$. The curvature is computed from the divergence of the interface normal vector (DINV).

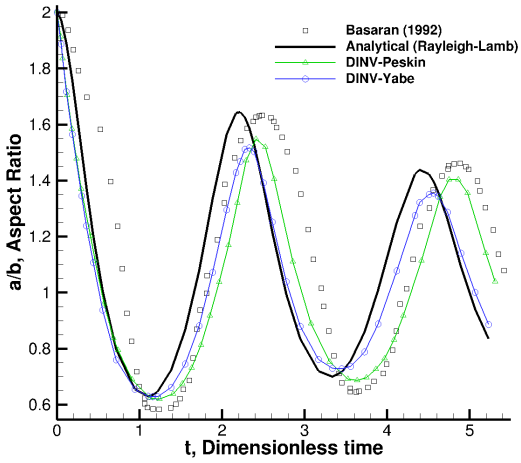

Figure 6.27: Aspect ratio a/b of a viscous drop initialized from a departure of the 2^{nd} spherical harmonic (oblate case) at $Re = 40$ and $\gamma = \lambda = 1000$ using two smoothening functions. The curvature is computed from the divergence of the interfacial normal vector (DINV) using the Peskin and Yabe approach. References are Basaran (1992) (prolate case) and the theoretical Rayleigh-Lamb model.

The Former PLIC Algorithm and the Prolate Drop

The next step in improving accuracy is by means of PLIC and the HF method. Now, the comparison is made for a drop initialized with the prolate shape (departure of the 2^{nd} spherical harmonic) with an equivalent radius $a = 1$ for $Re_{osc} = 10$, $Re_{osc} = 40$ and $Re_{osc} = 100$. The CFL number is kept small to reduce time-step dependency. The interface is transported using the FCT-VOF and PLIC-VOF algorithms. The

surface-tension force is calculated using the mollified ρ-CSF model together with the HF, HF-PD, HF-AD and HF-LH curvature models. The normal vector is computed from a combination of the central difference and the HF method.

The shape of the drop during the first half period is shown in Figure 6.28, where it can be noticed similar amplitudes and timescales for different Re. Several more simulations are summarized in Table 6.17. The aspect ratio is also studied in time and is presented in Figures 6.29-6.31.

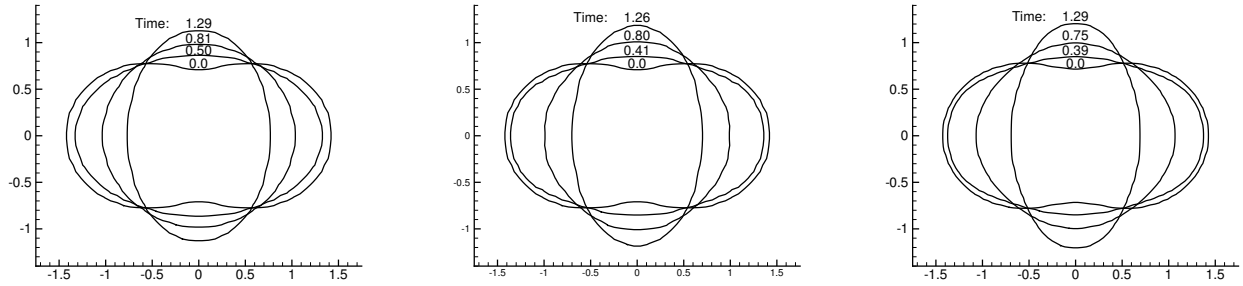

(a) $Re = 10$ (b) $Re = 40$ (c) $Re = 100$

Figure 6.28: Shape of a drop ($F = 0.5$) released from a departure of the 2^{nd} spherical harmonic (deformation $f_2 = 0.5$) on the xy plane. (a-b) Using the FCT method, the HF-AD curvature model and a relatively coarse mesh (60^3). (c) Using PLIC and HF-LH (90^3).

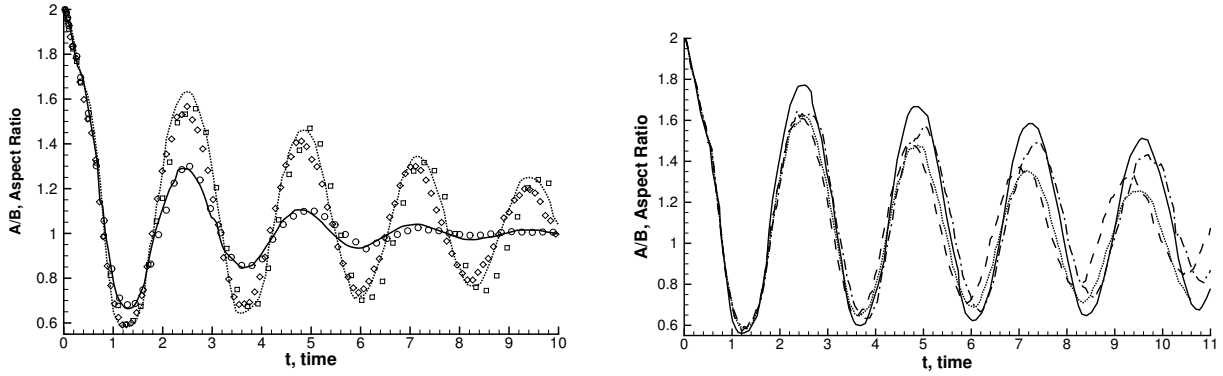

(a) $Re = 10$ (◯) and $Re = 40$ (□,◇) (b) $Re = 100$

Figure 6.29: Evolution of the aspect ratio A/B for a drop released from a departure of the 2^{nd} spherical harmonic (deformation $f_2 = 0.5$), using the FCT-VOF method and for large drop-medium property ratio ($\lambda = \gamma = 10^3$). The simulations are performed on a relatively coarse mesh (60^3) at $CFL_\sigma = 0.125$. (a) The HF-AD curvature model is presented for $Re = 10$ (◯) and $Re = 40$ (□), while the HF-PD for $Re = 40$ (◇). (b) For $Re = 100$ using the models: HF ($\cdots\cdots$), HF-PD ($- - -$), HF-AD ($- \cdot -$). The reference is Basaran (1992) at $Re = 10$ (——), $Re = 40$ ($\cdots\cdots$) and $Re = 100$ (——).

The FCT algorithm is employed for $Re = 10$ and $Re = 40$, where the error in the aspect ratio at the first period, $[A/B]_1$, on a mesh 60^3, is smaller than 4% in amplitude and 5% in phase when compared with the

Table 6.17: Sensitivity analysis on mesh refinement of the aspect ratio, A/B, at the first period, τ_1, for a deformation $f_2 = 0.5$.

FCT algorithm, $\lambda = \gamma = 10^3$, $CFL_\sigma = 0.125$						PLIC algorithm, $\lambda = \gamma = 10^2$, $Re = 100$, $\Delta t = 2.5 \times 10^{-4}$				
Re	Mesh	$\frac{a}{\Delta x}$	τ_1 ($\mathcal{E}$)	$\left(\frac{A}{B}\right)_1 \mathcal{E}$ (%)	Order	Mesh	$\frac{a}{\Delta x}$	τ_1 $\mathcal{E}$(%)	$\left(\frac{A}{B}\right)_1 \mathcal{E}$(%)	Order
	HF-AD					HF-PD				
	30^3	6.75	2.52 (2)	1.34 (24)	–	30^3	6.75	2.65 (2)	1.66 (6)	–
	60^3	14.25	2.53 (2)	1.62 (8.1)	1.46	60^3	14.25	2.50 (1)	1.755 (0.4)	3.6
100	120^3	29.25	2.71(9)	1.82 (3.3)	1.25	90^3	21.75	2.40 (3)	1.800 (2)	<0
	HF-PD					HF-LH*				
	30^3	6.75	2.50 (1)	1.64 (6.9)	–	40^3	9.25	2.52 (2)	1.729 (2)	
	60^3	14.25	2.47 (1)	1.61 (8.6)	<0	60^3	14.25	2.47, (1)	1.753 (0.5)	–
	90^3	21.75	2.41 (3)	1.65 (6.3)	0.72	90^3	21.75	2.46 (1)	1.753 (0.5)	~0
	120^3	29.25	2.38 (4)	1.68 (4.9)	1.05	120^{3**}	29.25	2.50 (1)	1.748 (0.8)	<0
	Ref.		2.4800	1.7622		HF-AD				
	HF-PD					60^3	14.25	2.47 (1)	1.776 (0.8)	–
	60^3	14.25	2.493 (1)	1.567 (3.9)		90^3	21.75	2.46 (1)	1.773 (0.6)	0.58
40	HF-AD					Ref.		2.4800	1.7622	
	60^3	14.25	2.638 (6)	1.558 (4.4)						
	Ref.		~ 2.48	~ 1.63						
	HF-AD									
	30^3	6.75	2.49 (2)	1.312 (1.6)	–					
10	60^3	14.25	2.537 (4)	1.299 (0.6)	1.3					
	Ref.		2.4436	1.2909						

* F-CSF force model

** $\Delta t = 1.5 \times 10^{-4}$

Error is provided in parenthesis (%).

Reference is Basaran (1992).

boundary integral method of Basaran (1992). For $Re = 40$, the evolution of the aspect ratio obtained with the HF-PD method was slightly more accurate in space and time than HF-AD, as presented in Table 6.17 and Figure 6.29a. However, for $Re = 100$ the HF-AD method performed better than HF and HF-PD in time and space, as shown in Figure 6.29b. The problem is more challenging for $Re = 100$, since more mesh points are required ($> 90^3$) to be within 5% error. In the case of a mesh 120^3 and the HF-AD model, the error is less than 3.3% in amplitude, but a shift of 9% in phase is observed due to a subharmonic. These results at high density ratios show how a mesh resolution of $a/\Delta x \sim 15$ is sufficient to resolve major deformations when Re is small, but at moderate Re, more resolution is required. The principal source of error is the curvature model because relevant differences in the aspect ratio are observed for different models.

For the case of the PLIC-VOF method at $Re = 100$, a considerably smaller time steps are required to ensure stability when the density ratio is high, so it was lowered to $\lambda = \gamma = 10^2$. By comparing the aspect ratio for different methods, shown in Figure 6.30a using a mesh 60^3 and for the first period in Table 6.17, the curvature models are ordered in terms of accuracy as: HF-PD, HF-LH and HF-AD. If now the fourth period is considered, the HF-AD performs slightly better than HF-PD and HF-LH. For larger mesh resolutions, HF-LH performs better because this method converges with grid refinement. The SF-Y model was also

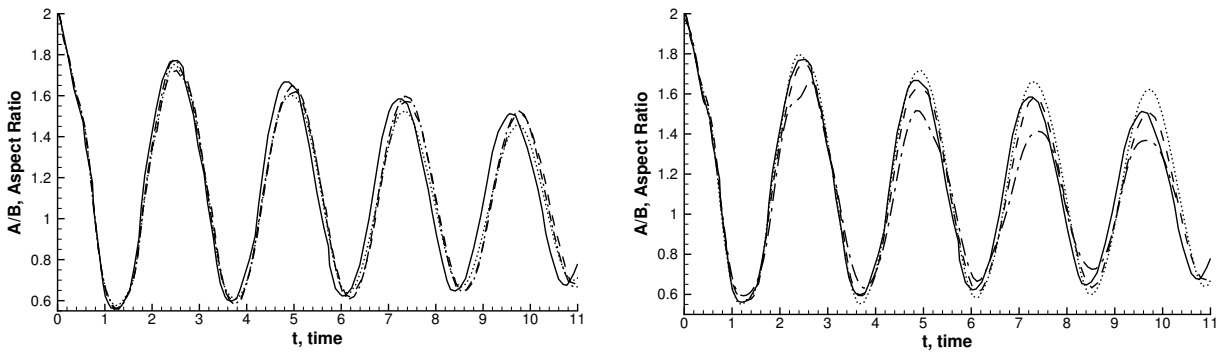

(a) (b)

Figure 6.30: Evolution of the aspect ratio A/B when a drop is released from a departure of the 2^{nd} spherical harmonic, $f_2 = 0.5$, using the PLIC-VOF method at $Re = 100$, for a low drop-medium property ratio ($\lambda = \gamma = 10^2$). (a) Curvature model comparison for a mesh 60^3 and $\Delta t = 2.5 \times 10^{-4}$: HF-AD ($- \cdot -$), HF-PD ($- - -$) and HF-LH ($\cdots\cdots$). (b) Sensitivity to mesh resolution using the HF-PD model: mesh 30^3 ($- \cdot -$), 60^3 ($- - -$) and 90^3 ($\cdots\cdots$). The reference is Basaran (1992) (——).

tested, but the interface degradation was severe and the results were discarded. A mesh sensitivity using the HF-PD model is shown in Figure 6.30b, where it can be observed how the oscillations amplify with grid refinement more than expected. Even though these results are within 6% of error, convergence with grid refinement is possible when the F-CSF force and the HF-LH model are used, as shown in Figure 6.31.

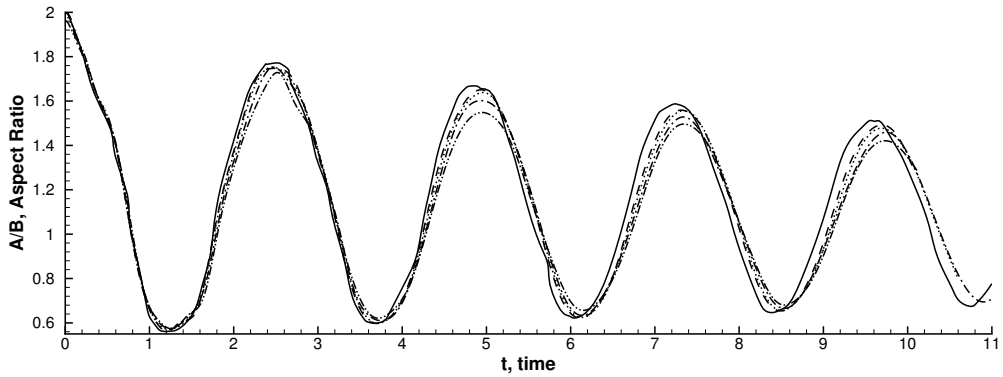

Figure 6.31: Sensitivity to mesh resolution of the aspect ratio A/B when a drop is released from a departure of the 2^{nd} spherical harmonic, $f_2 = 0.5$, using the PLIC-VOF method, F-CSF force and the HF-LH curvature model at $Re = 100$, $\lambda = \gamma = 10^2$. For mesh 40^3 and $\Delta t = 2.5 \times 10^{-4}$ ($- \cdot \cdot -$), 60^3 and $\Delta t = 2.5 \times 10^{-4}$ ($- \cdot -$), 90^3 and $\Delta t = 2.5 \times 10^{-4}$ ($\cdots\cdots$), 120^3 and $\Delta t = 1.5 \times 10^{-4}$ ($- - -$). The reference is Basaran (1992) (——).

The DDR-PLIC Algorithm

The interface is now transported using the BDR-PLIC and DDR-PLIC methods and the curvature used is HF model provided by normals computed with the HF method as well. The surface-tension forces are

calculated using the unweighted CSF model. In difference to the previous subsections, the average viscosity is computed with the harmonic-mean function.

The shape of the drop is very similar to the previous results, however, the change of the interface during the first half period is shown in Figure 6.32.

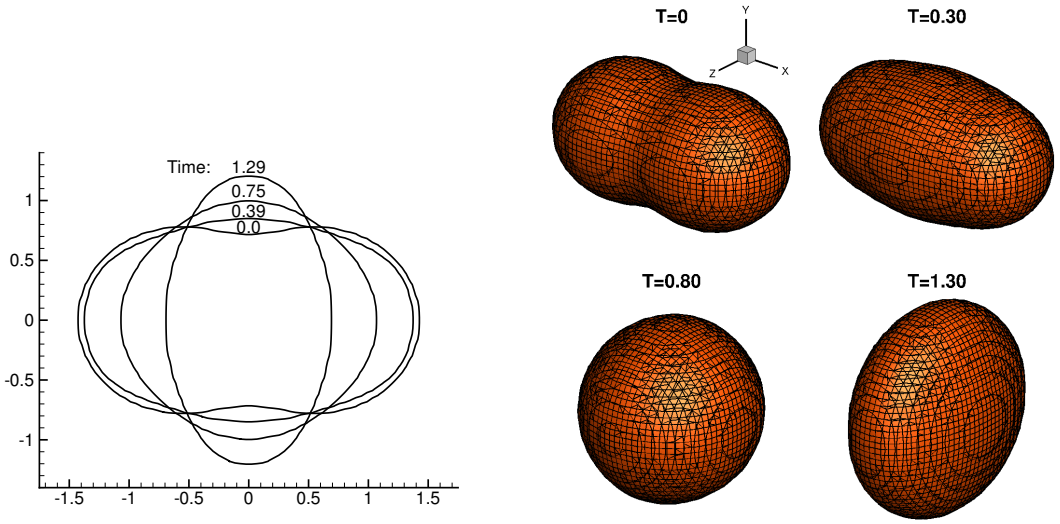

(a) Contours for $F = 0.5$ on the xy plane

(b) Iso-surface for $F = 0.5$

Figure 6.32: Motion of a drop released from a departure of the 2^{nd} spherical harmonic (deformation $f_2 = 0.5$), using the DDR-PLIC method with the HF curvature model, $\lambda = \gamma = 100$, mesh 60^3 and $\Delta t = 2.5 \times 10^{-4}$.

Table 6.18: Sensitivity analysis on mesh refinement of the aspect ratio, A/B, at the first period, τ_1, for a deformation $f_2 = 0.5$ using PLIC. Flow conditions at $Re = 100$, $\lambda = \gamma = 100$. The normalized error is presented in parenthesis.

		DDR Algorithm			BDR Algorithm		
Δx	Δt	τ_1	$\left(\frac{A}{B}\right)_1$	Order $(\Delta x)^n$	τ_1	$\left(\frac{A}{B}\right)_1$	Order $(\Delta x)^n$
$2a/15$	2.5×10^{-4}	2.488	1.6251 (7.7×10^{-2})	–	2.489	1.6238(7.9×10^{-2})	–
$a/15$	1.0×10^{-4}	2.40	1.6808 (4.6×10^{-2})	0.752	2.40	1.6802(4.7×10^{-2})	0.755
$a/30$	1.0×10^{-4}	2.45	1.7151(2.7×10^{-2})	0.790	2.46	1.7147(2.7×10^{-2})	0.787
Ref. (Basaran, 1992)		2.48	1.7622				

A comparison between the BDR and DDR methods is shown in in Table 6.18 and Figure 6.33. The difference between the methods is negligible, which means that the drop aspect ratio is not sensitive to the fluxing algorithm. Considering that the order of convergence between the BDR and DDR methods is slightly different and the results are very similar, it can be concluded that the main source of error for this type of problem is not due to the fluxing algorithm of F itself, but due to the forces. The aspect ratio is observed to converge on mesh refinement with an order of $\sim 0.75 - 0.79$. The surface-tension force depends on curvature and the gradient of the volume fraction. In the case of curvature, the local error reduces superlinearly with

mesh refinement (static drop problem), but such error may contribute to increase the accumulated error. Advection and viscous forces may also contribute to the error, leading to a final sublinear convergence of the drop aspect ratio.

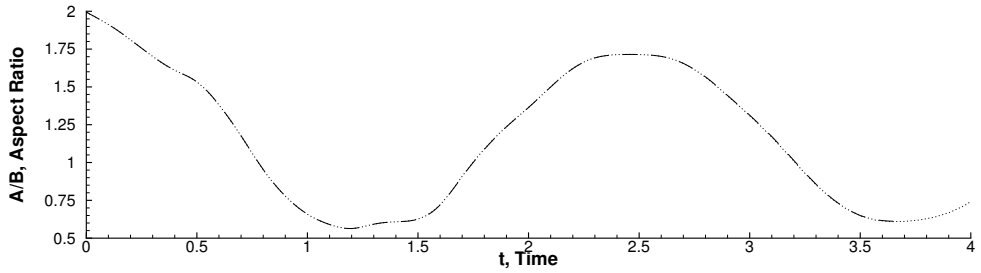

Figure 6.33: Comparison of the aspect ratio A/B for a drop released from a departure of the 2^{nd} spherical harmonic (deformation $f_2 = 0.5$) between the BDR $(- - -)$ and the DDR $(\cdots\cdots)$ methods at $Re = 100$. For $\lambda = \gamma = 10^2$, mesh 120^3 ($\Delta x = a/30$) and $\Delta t = 10^{-4}$.

The aspect ratio is also presented in Figure 6.34 for $Re = 10$ and $Re = 100$. For $Re = 10$, the phase and the aspect ratio $[A/B]_1$ are in excellent agreement with the results of Basaran (1992), where only 60^3 internal cells are required to obtain such accuracy. This not only shows that our method is consistent, but shows how the curvature model is also accurate for non-spherical shapes. As Re is increased, more cells are needed to be within a given error. For $Re = 100$, the equivalent spherical drop must be resolved with $\Delta x \leq a/15$ to be within 5% error. The convergence on mesh refinement for $Re = 100$ is shown in Figure 6.34b. Because the error increases with Re, it is then expected that advection forces are responsible for the error contribution.

It is also of interest to show how the kinetic energy evolves in time. It is computed in the whole domain as $KE(t) = \sum_i \frac{1}{2} \left(\rho(t) \|\mathbf{u}(t)\|^2 \Delta \mathcal{V} \right)_i$ and presented in Figure 6.35. The maximum kinetic energy decreases due to viscous dissipation as expected, but not as periodically or with the decay observed in cases of small deformations or when the drop is initially spheroidal.

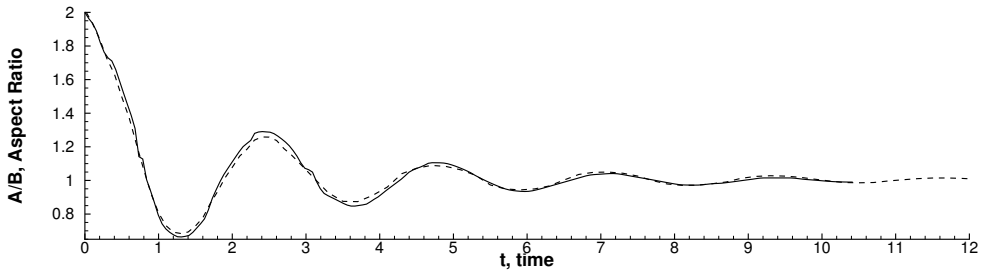

(a) $Re = 10$

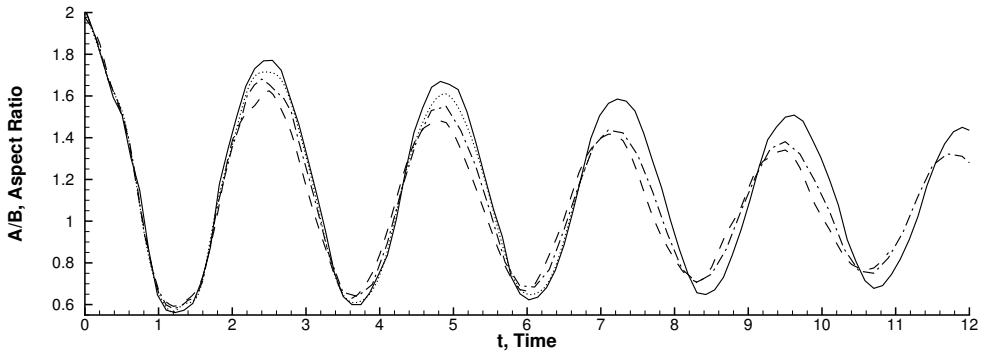

(b) $Re = 100$

Figure 6.34: Evolution of the aspect ratio A/B for a drop released from a departure of the 2^{nd} spherical harmonic (deformation $f_2 = 0.5$), using the PLIC-VOF-DDR method and the HF curvature model. (a) For $\lambda = \gamma = 10^3$ and $Re = 10$: mesh 60^3 ($\Delta x = a/15$) and $\Delta t = 10^{-4}$ ($- - -$). (b) For $\lambda = \gamma = 10^2$ and $Re = 100$: mesh 30^3 ($\Delta x = 2a/15$) and $\Delta t = 2.5 \times 10^{-4}$ ($- - -$), 60^3 ($\Delta x = a/15$) and $\Delta t = 10^{-4}$ ($- \cdot -$), 120^3 ($\Delta x = a/30$) and $\Delta t = 10^{-4}$ ($\cdots\cdots$). The reference is Basaran (1992) at $Re = 10$ and $Re = 100$ (——).

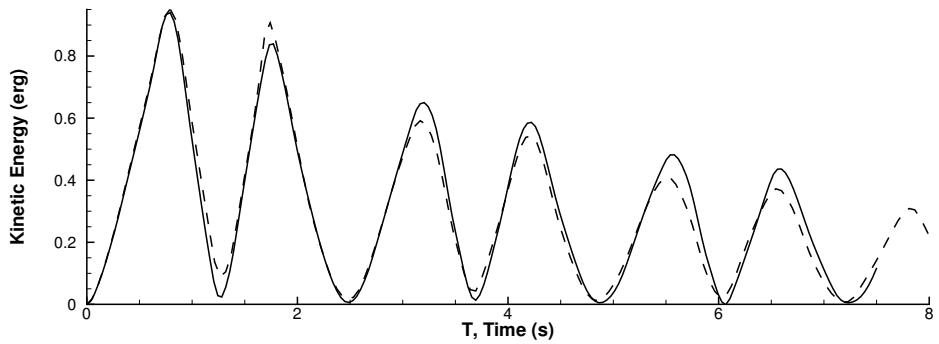

Figure 6.35: Evolution of the kinetic energy for the problem of a drop released from a departure of the 2^{nd} spherical harmonic, $f_2 = 0.5$ at $Re = 100$. For $\lambda = \gamma = 10^2$, mesh 60^3 and $\Delta t = 2.5 \times 10^{-4}$ ($- - -$), 120^3 and $\Delta t = 1.5 \times 10^{-4}$ (——).

This benchmark is widely used in the community for small deformations, but not so much for non-spheroidal shapes, large deformations f_2 and $Re \gtrsim 100$. As Re, density and viscosity ratio increase, the

problem becomes more challenging, making it useful for testing overall accuracy of methods as it was shown here.

6.4.3 Drop Deformation in a Simple Shear Flow

An initially-spherical drop of radius a subject to a simple shear flow adopts a spheroidal shape as it deforms. The drop is located between two plates moving at a shear rate $\dot{\gamma}$ and separated by a distance d. The respective dimensionless separation or clearance ratio is $\beta = d/(2a)$. For $\beta \gtrsim 4$, the deformation is slightly dependent on d (Li et al., 2000). This problem is governed by the external Reynolds number, $Re = \rho_m \dot{\gamma} a^2/\eta_m$, capillary number, $Ca = \eta_m \dot{\gamma} a/\sigma$, the viscosity ratio, $\lambda = \eta_d/\eta_m$, and the density ratio, $\gamma = \rho_d/\rho_m$. The referential time and velocity are $t_{ref} = \dot{\gamma}^{-1}$ and $u_{ref} = \dot{\gamma} a$.

The topology of the drop becomes steady when the surface-tension force is relatively important, or unsteady otherwise, conducing to breakup and daughter drops. Common parameters to characterize the deformation are the Taylor deformation, D, given by $D = (l-b)/(l+b)$, where l and b are the half-length and half-breadth of the drop, respectively, and the orientation angle, θ, which is the angle between the drop semi-major axis and the horizontal.

The advection terms of the momentum equation are not computed because the Stokes flow limit is enforced ($Re = 0$). Uniform properties between the drop and the medium are considered, $\lambda = \gamma = 1$. The initial conditions are $\mathbf{u}(\mathbf{x}, 0) = \mathbf{0}$ and $p(\mathbf{x}, 0) = 0$, while the boundary conditions are prescribed as follows: pressure $p = 0$ at the inlet/exit regions in the x direction, no-slip conditions at the walls in y direction and symmetries in z direction.

The FCT Algorithm

The results of drop deformation and angle of orientation are now shown using the FCT algorithm. Changes in the drop contour in time are shown in Figure 6.36, while the steady-state conditions are presented in Table 6.19 and Figure 6.37. If the capillary number is below the critical value, $Ca < 0.41$, then drop breakup is avoided. Since the time step is limited by viscous forces, the semi-implicit scheme is stable for large CFL. Here, $CFL > 1$ is employed. Several values of Ca were simulated, for subcritical and supercritical conditions.

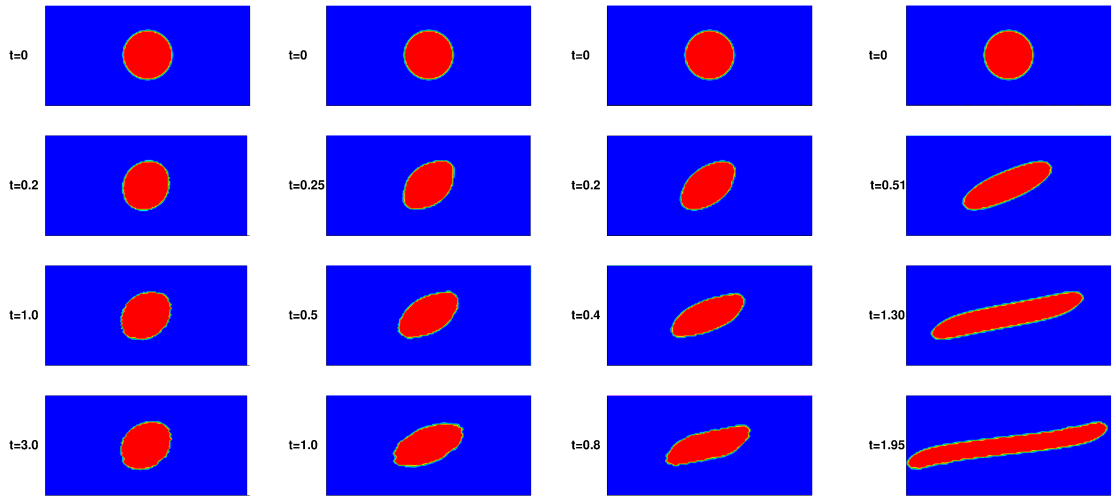

(a) $Ca = 0.1$ (b) $Ca = 0.3$ (c) $Ca = 0.42$ (d) $Ca = 0.5$

Figure 6.36: Cross-section view of the deformation of a viscous drop in simple shear flow, for equal densities, $\lambda = 1$ and Stokes flow, using an uniform mesh $120 \times 60 \times 60$, $CFL = 1$, $a/\Delta r = 14$, the staggered surface-tension model provided with $\kappa = -\nabla \cdot \hat{\mathbf{n}}$.

Table 6.19: Parameters of the simulation (Stokes flow* $Re = 0$), $\lambda = 1$

η	ρ	$\dot{\gamma}$	σ	a	Re*	Ca	$a/\Delta r$	D_{Num}	D_{Theo}	$45° - \theta$	$45° - \theta_{theo}$
1	1	1	2.5	0.25	0.0625	0.1	14	0.119	0.123	6.9	6.27
3	1	3	7.5	0.125	0.015625	0.15	7	0.172	0.180	10.4	9.4
3	1	3	7.5	0.25	0.0625	0.3	14	0.360	0.229	19.7	18.8
4.2	1	4.2	10.5	0.25	0.0625	0.42	14	0.508	(0.32)	32.9	26.3
5	1	5	12.5	0.25	0.0625	0.5	14	-	-	-	-

This problem was addressed with several advection schemes in the FCT algorithm, until acceptable results were achieved. Initially, a high-resolution scheme applied to the transport of F was too diffusive and the interface was blurred out, as shown in Figure 6.38. The next type of scheme that can be used is a downwind scheme. Among limiting-like schemes, the FCT algorithm is the only method capable of getting accurate results, but it is prone to creating stairs on inclined interfaces and detachment. For instance, large values of Ca show a severe degradation of the interface.

In the next section, the PLIC algorithm is employed and several problems associated with the FCT algorithm are solved, however, at the expense of creating voids and wisps (first PLIC implementation).

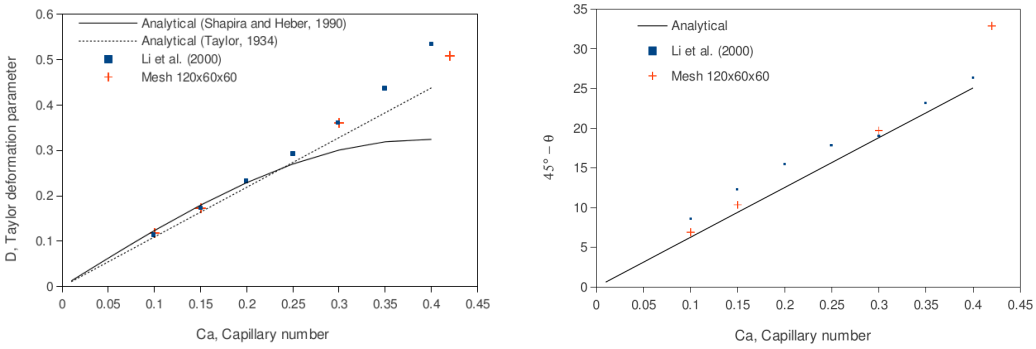

(a) (b)

Figure 6.37: Deformation of a viscous spherical drop in simple shear flow. Comparison for equal densities, $\lambda = 1$ and Stokes flow, using an uniform mesh 120x60x60, $CFL = 1$, $a/\Delta r = 7 - 14$. The CSF model is the staggered surface-tension model with $\kappa = -\nabla \cdot \hat{\mathbf{n}}$. (a) Taylor deformation parameter D as a function of Ca under steady-state conditions (b) Drop orientation angle θ.

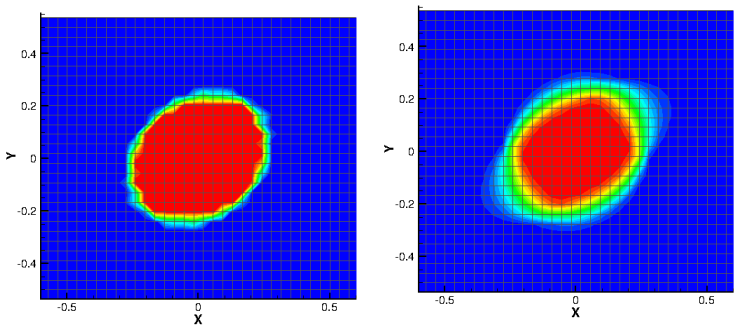

(a) (b)

Figure 6.38: Cross-section view of the deformation of a viscous drop in simple shear flow, for equal densities, $\lambda = 1$, $Ca = 0.1$ and Stokes flow, using an uniform mesh 60x30x30, $CFL = 1$, $a/\Delta r = 7 - 14$, the staggered surface-tension model provided with $\kappa = -\nabla \cdot \hat{\mathbf{n}}$ and $t = 0.91$. (a) For FCT-VOF and second-order backwards (b) For VOF and Second Order backwards

Former PLIC algorithm

The same problem is now analyzed using our first PLIC algorithm, which is similar to the BDR method. The following results were obtained using the HF-PD curvature model. Using the oscillating viscous-drop problem as a reference for $Re < 100$, accuracy is within 5% error when the drop resolution is $a/\Delta x \gtrsim 15 - 20$.

The parameters for this simulations are the following: radius $a = 0.25$, shear rate $\dot{\gamma} = 1$, plates separation $d = 2$, clearance ratio $\beta = d/(2a) = 4$, external Reynolds number $Re^* = \rho_m \dot{\gamma} a^2/\eta_m = 0.0625$, uniform properties across the interface $\lambda = \gamma = 1$, rectangular parallelepiped domain of size $3 \times 2 \times 1$ and the time step is limited to $\Delta t \leq 0.001$.

The steady-state shape for different capillary numbers is presented in Figure 6.39a. The transient solu-

Table 6.20: Steady-state Taylor deformation parameter, D, and angle of orientation, θ, for an initially spherical drop of radius $a = 0.25$, subject to a simple shear flow in a domain $3\times2\times1$ and a mesh $180\times120\times60$. Stokes flow ($Re = 0$) with uniform properties.

	PLIC-VOF				Phenomenological model (Minale, 2008)	
Ca	L/a	B/a	D	$45° - \theta$	D	$45° - \theta$
0.1	1.122	0.897	0.1166	8.8	0.109	6.27
0.15	1.202	0.846	0.1736	11	0.164	9.40
0.20	1.293	0.809	0.2348	15	0.219	12.5
0.25	1.417	0.764	0.2991	17	0.273	15.7
0.30	1.545	0.722	0.3631	21	0.328	18.8
0.35	1.703	0.671	0.4348	24	0.383	21.9
0.4	2.116	0.621	0.5461	29	-	-

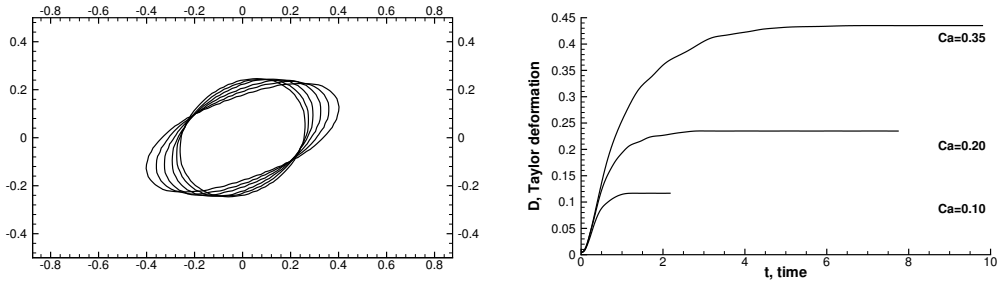

(a) Steady-state shape contours

(b) Evolution of the Taylor deformation

Figure 6.39: Deformation of a viscous drop subject to a simple shear flow under the Stokes flow assumption ($Re = 0$) in a domain of size $3 \times 2 \times 1$, using an uniform mesh $180 \times 120 \times 60$ ($a/\Delta x = 14.625$, $\Delta x \sim 1/60$), $\Delta t \leq 0.001$, the HF-PD model and uniform properties ($\lambda = \gamma = 1$). (a) Each contour correspond to a different capillary, $Ca = \begin{pmatrix} 0.1 & 0.15 & 0.2 & 0.25 & 0.3 & 0.35 \end{pmatrix}$, where $Ca = 0.35$ has the largest deformation.

tions were considered for a different capillary numbers. The time scale of the deformation changes with the capillary number as it is shown in Figure 6.39b. For large Ca, the effect of the surface-tension force becomes weak and larger physical times are required to achieve steady-state conditions, demanding a stable method. In this sense, PLIC represents an improvement over the FCT algorithm.

The half-length, L, and the half-breadth, B, are extracted from each contour, and the Taylor deformation parameter is computed, while the angle of orientation is obtained from the direction of the semi-major axis. These results are summarized in Table 6.20 and Figure 6.40. As it can be observed, these results are in excellent agreement with the solutions of Li et al. (2000) (PROST), where simulations using similar mesh resolution and domain size were performed. The analytical results of Taylor (1934), Barthès-Biesel and Acrivos (1973), and the phenomenological model of Minale (2008) are presented to show the deviation of the numerical solution as Ca increases.

Now, a mesh sensitivity analysis is performed at $Ca = 0.35$ using the half-length distance as parameter. The following steady-state values are obtained: for $\Delta x \sim 1/60$ the deformation is $L/a = 1.702$, while for

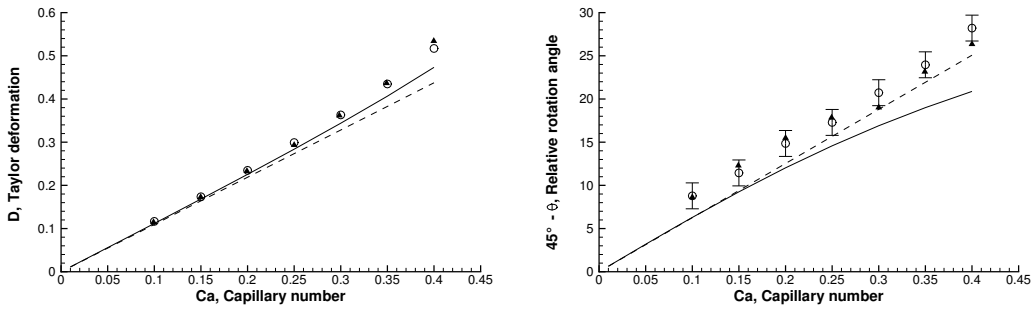

(a) Taylor deformation, D (b) Angle of orientation, θ

Figure 6.40: Comparison of the steady-state condition of a sheared viscous drop for different capillary numbers. Simulations using the PLIC method (◯), the Stokes flow approximation, uniform properties ($\lambda = \gamma = 1$), mesh $180 \times 120 \times 60$ ($a/\Delta x = 14.625$), and $\Delta t < 0.001$. Prediction from the phenomenological model Minale (2008) (——). Analytical solutions are from (a) Taylor (1934) and (b) Barthès-Biesel and Acrivos (1973) (– – –). The numerical solutions are from PROST (Li et al., 2000) (▲).

$\Delta x \sim 1/90$, $L/a = 1.715$. The transient solutions are shown in Figure 6.41, achieving excellent agreement with the results using PROST (Renardy and Renardy, 2002) and the boundary integral method of Cristini et al. (2001). The major difference between profiles is attributed to the initial condition because the velocity is initialized in their case, while here an initially quiescent flow is considered. A remarkable improvement in accuracy is obtained from using the HF-PD over the HF curvature model. Later on it was found that such improvement are related to an increased in curvature in the HF-PD model.

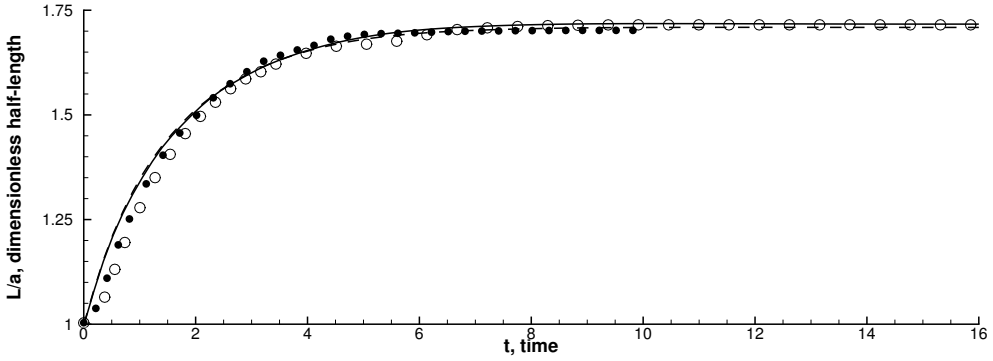

Figure 6.41: Evolution of the half-length, L/a, of a viscous drop subject to a simple shear flow, for uniform properties ($\lambda = \gamma = 1$), Stokes flow approximation, and the curvature model HF-PD. For a mesh $180 \times 120 \times 60$ ($\Delta x \sim 1/60$), $\Delta t = 1.25 \times 10^{-4}$ (•) and $270 \times 180 \times 90$ ($\Delta x \sim 1/90$), $\Delta t = 7.5 \times 10^{-5}$ (◯). The references are PROST ($\Delta x = 1/128$) (– – –) and BIM (——) (Renardy and Renardy, 2002; Cristini et al., 2001).

Renardy and Renardy (2002) used PLIC and PROST in their simulations and observed that the CSF model (PLIC) produces a lack of accuracy. However, a half-length of $L/a = 1.715$ was obtained here with a CSF-PLIC method, which presents a smaller error than the best effort ($\Delta x = 1/128$, $\Delta t = 5 \times 10^{-4}$) using

PROST, $L/a = 1.709$. The referential value is $L/a = 0.717$ in the work of Cristini et al. (2001). This shows the relevance of using a "sharp" CSF force model together with an accurate curvature model (HF-PD).

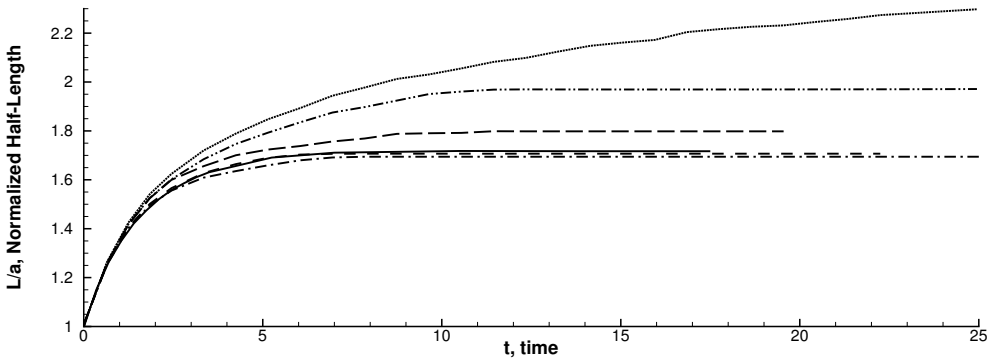

Figure 6.42: Sensitivity of the evolution of the half-length, L/a, to the curvature model and type of CSF model. Properties are uniform ($\lambda = \gamma = 1$), Stokes flow approximation is considered and $\Delta t = 1 \times 10^{-3}$. For a mesh $240 \times 160 \times 80$ ($\Delta x \sim 1/80$) HF-PD ($- \; - \; -$), and $180 \times 120 \times 60$ ($\Delta x \sim 1/60$) HF-AD ($- \; \cdot \; -$), HF-PD with F-CSF (— —), HF-LF with CSF ($- \; \cdot \; \cdot - $) and HF-LH with F-CSF ($\cdots\cdots$). The references is BIM (——) (Cristini et al., 2001).

Considering the excellent results produced by the combination HF-LH and F-CSF for the problem of the initially-deformed drop, its performance is analyzed for shearing flows and compared with the other methods. This time, the initial condition of the velocity field is $u(y, 0) = \dot{\gamma} y$, as done by the references. Now, the result of the half-length matches the solution using BIM (Cristini et al., 2001) at the initial stages of the drop deformation for all methods. However, the half-length at steady-state conditions varies depending on the method employed. These results are summarized in Figure 6.42 and Table 6.21. When the HF-PD and HF-AD models are combined with the unweighted CSF force, the steady-state values are in excellent agreement with the reference, where differences of 0.6% and 1.3% are observed, respectively. When the HF-LH model is combined with the weighted CSF, the error increases monotonically without achieving steady-state conditions. In order to determine whether the cause is the F-CSF force or the curvature model, the model HF-PD is combined with the F-CSF force, producing a relatively small deviation of 4.7%. When the HF-LH model is combined with the unweighted CSF force, a significant difference of 15% is observed. Even though weighting the CSF model introduces error, the use of the HF-LH model causes the largest impact, producing unacceptable results when both models are combined. Because of this departure from the steady-state solution, the HF-LH model was not employed in our studies, and the weighted-CSF model was avoided.

Table 6.21: Comparison of the drop half-length for various curvature and surface-tension force models at $Ca = 0.35$ and $t = 15$ against the BIM solution (Cristini et al., 2001) ($L/a = 1.717$).

Staggered-CSF			Staggered-F-CSF		
Model (Δx)	Half-length (L/a)	Difference (%	Model (Δx)	Half-length (L/a)	Difference (%
HF-PD (1/80)	1.707	0.6	HF-PD (1/60)	1.798	4.7
HF-PD (1/60)	1.692	1.5	HF-LH (1/60)	2.161	26
HF-AD (1/60)	1.694	1.3			
HF-LH (1/60)	1.970	15			

In shearing flows, the PLIC method remains stable whereas the FCT method degrades promptly. Since long-term simulations are required when Ca is large, the PLIC method is preferred.

DDR-PLIC algorithm

Similarly as before, the sphere has radius $a = 0.25$ and subject to a shear rate $\dot{\gamma} = 1$ for the same clearance ratio $\beta = d/(2a) = 4$. The porpoise of this section is to show that the deviation of the deformation observed by other authors is due to the size of the domain. The selected domains are of sizes $3 \times 2 \times 1$ and $3 \times 2 \times 2$, equivalent to $12a \times 8a \times 4a$ and $12a \times 8a \times 8a$, respectively. It will be shown that the results are sufficiently accurate for the second domain, confirming that only the symmetric boundary conditions in z, or the periodic condition for other authors, are affecting the values of the half-length, discarding the fluxing methods, mesh resolutions and curvature models as the possible reasons of the deviation. Renardy et al. (2002) performed a sensitivity analysis of the domain size, mesh resolution and time step on L/a, showing that for $L_x = L_y = L_z = 12a$, $\Delta x = 3a/32$ and $\Delta t = 10^{-4}$ an error of 2.5% is achieved. Here, an error of 0.6% is achieved for the second domain, but as large as 6% with the first domain.

For the following results, the HF curvature model, the PLIC method and both fluxing strategies are employed. Accuracy is within 6% error for a drop resolution of $a/\Delta x \gtrsim 15$, as expected from the results of the oscillating viscous-drop problem. The time step is limited to $\Delta t \leq 5 \times 10^{-4}$, for a typical $CFL_u < 0.01$ which is low enough to assume superlinear convergence on mesh refinement of the fluxing algorithms. Moreover, the HF curvature model is selected in order to keep convergence on mesh refinement. Therefore, the error due to interface advection is minimized.

The transient shape of a drop at capillary number $Ca = 0.35$ and its deformation are presented in Figure 6.43. The steady-state Taylor deformation, normalized half-length and orientation angle are $D = 0.435$, $L/a = 1.728$ and $\theta = 24.6°$, respectively, for a domain of size $3 \times 2 \times 2$, mesh resolution $a/\Delta x = 15$ or $\Delta x = 1/60$ and $\Delta t = 5 \times 10^{-4}$. This result is within 0.6% of error with respect to the solution of Cristini

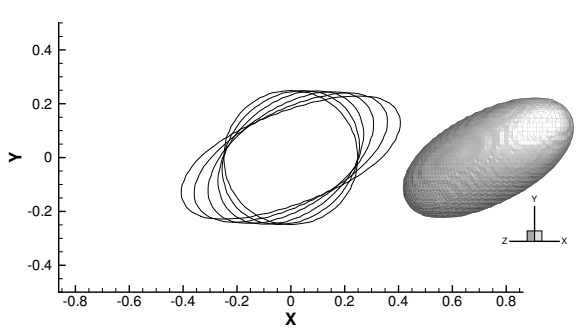

(a) Close-up of the $F = 0.5$ contours

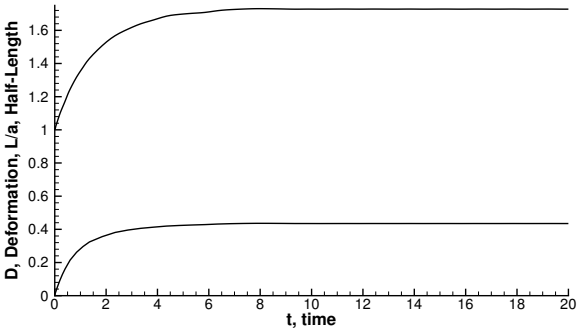

(b) Evolution of the Taylor deformation and Half -Length

Figure 6.43: Deformation of a viscous drop subject to a simple shear flow under the Stokes flow assumption ($Re = 0$) at $Ca = 0.35$ in a domain of size $3 \times 2 \times 2$, using an uniform mesh $180 \times 120 \times 120$ ($a/\Delta x = 15$, $\Delta x = 1/60$), $\Delta t = 5 \times 10^{-4}$, the HF model and uniform properties ($\lambda = \gamma = 1$). (a) Each contour corresponds to a different time, $t = (0,\ 0.2,\ 0.5,\ 1.1,\ 2.35,\ 20)$.

et al. (2001) using the boundary integral method.

A mesh sensitivity analysis is performed at $Ca = 0.35$ for a domain of size $3 \times 2 \times 1$ to show the dependence of the drop half-length on L_z, which is $L_z/a = 4$ for this case. The steady-state results are presented in Table 6.22, while the transient results in Figure 6.44. As it can be observed, L/a diverges from the reference value Cristini et al. (2001), 1.717, as the mesh resolution and time step are refined. The results are also independent of the VOF fluxing strategy, namely BDR or DDR, as expected. Because of the Stokes flow assumption, the steady-state values of L/a will not depend on Re^*. Only when domain size in the z direction is increased from $4a$ to $8a$, the error reduces from $\sim 5\%$ to 0.6%. Therefore, accurate values can only be obtained if the domain is sufficiently large. To the present, it was not clear if PLIC methods were capable of obtaining accurate solutions in this problem. Now, it is shown to be possible, but more accuracy would be directly related to the curvature model, the mesh resolution and the size of the domain in all directions.

Table 6.22: Comparison of the drop half-length for various curvature and surface-tension force models at $Ca = 0.35$ and $t = 15$ against the BIM solution.

BDR			DDR		
Mesh ($a/\Delta x$)	Half-length (L/a)	Difference (%)	Mesh ($a/\Delta x$)	Half-length (L/a)	Difference (%)
$180 \times 120 \times 60(15)$	1.798	4.7	$180 \times 120 \times 60(15)$	1.794	4.5
$240 \times 160 \times 80(20)$	1.809	5.4	$180 \times 120 \times 120(15)$	1.728	0.64
$300 \times 200 \times 100(25)$	1.826	6.4	Cristini et al. (2001)	1.717	–

It is also possible to compare against the results of Renardy et al. (2002). When they used a domain of $12a \times 12a \times 12a$, $\Delta x = 3a/32$ and $Re^* = 0.03125$, the drop half-length was $L/a = 1.76$, which represents a

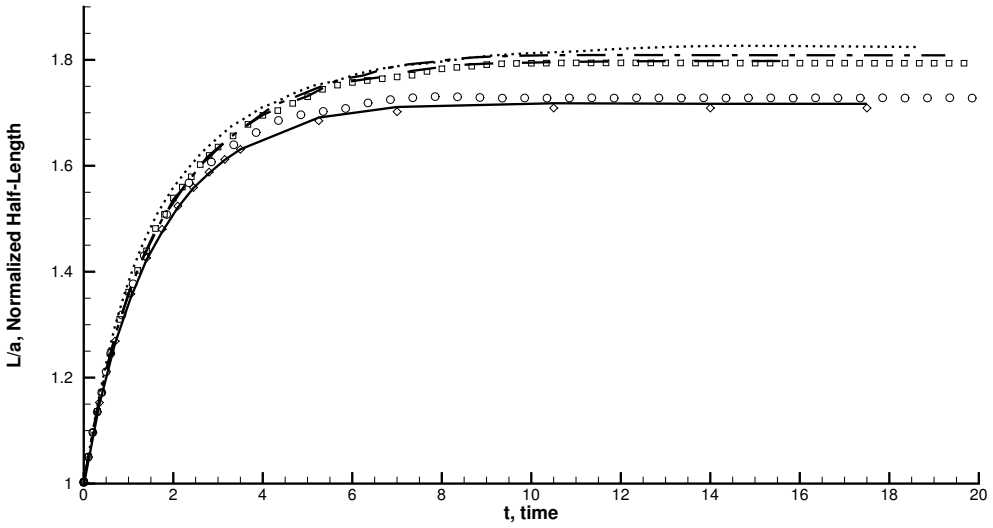

Figure 6.44: Effect of the mesh refinement and domain size on the evolution of the half-length, L/a, of a viscous drop subject to a simple shear flow under uniform properties ($\lambda = \gamma = 1$) and Stokes flow approximation. Using BDR: mesh $180 \times 120 \times 60$ ($\Delta x = 1/60$, $a/\Delta x = 15$) and $\Delta t = 5 \times 10^{-4}$ ($- - -$), $240 \times 160 \times 80$ ($\Delta x \sim 1/80$, $a/\Delta x = 19.6$) and $\Delta t = 5 \times 10^{-4}$ ($- \cdot -$), $300 \times 200 \times 100$ ($\Delta x = 1/100$, $a/\Delta x = 25$) and $\Delta t = 1 \times 10^{-4}$ ($\cdots\cdots$). Using DDR: mesh $180 \times 120 \times 60$ ($12a \times 8a \times 4a$) and $\Delta t = 5 \times 10^{-4}$ ($\square$), $180 \times 120 \times 120$ ($12a \times 8a \times 8a$) and $\Delta t = 5 \times 10^{-4}$ ($\bigcirc$). The references are PROST ($\Delta x = 1/128$) ($\diamond$) and BIM (——) (Renardy and Renardy, 2002; Cristini et al., 2001).

difference of 2.5. This difference only goes below 4.8% when they use the domain of size $12a$ and could have been lower for smaller Δx. Nevertheless, mesh resolution is very limiting factor. For instance, the simulations using $a/\Delta x = 25$ require about 6 million uniformly spaced cells. Such simulation requires several weeks to months to complete.

These results indicate that PLIC-VOF is fully capable of obtaining accurate solutions in this type of problems when the curvature, the fluxing and the reconstruction are convergent on mesh refinement, together with the proper domain size and resolution. Previously, other methods were required to obtain accurate solutions, like PROST or BIM. Here, a mesh resolution of $a/\Delta x = 15$ and $L_z = 8a$ was sufficient to be within 0.6% error. This parameters let us understand the error incurred in future simulations.

These results are obtained at $Ca = 0.35$ where a steady-state conditions can be achieved. For $Ca > 0.42$, the drop stretches considerably and breakup is expected, as it is discussed next.

6.4.4 Breakup of a Drop in a Simple Shear Flow

It is known that a droplet subject to a simple shear flow at low Reynolds (i.e. $Re = 0.0625$) breaks up at $Ca_c \approx 0.43$ for a clearance ratio $\beta = 4$. The case now studied is $Ca = 0.44$, which allows for a comparison with the VOF method of Renardy and Renardy (2002) (PROST) and the boundary integral method (BIM) of Cristini et al. (2001). In this section, the predicting capabilities of the PLIC algorithm are tested for the deformation and breakup of drops. The external Reynolds is the same as in the previous problem and the Stokes flow limit is also enforced. The parameter for the comparison is the drop half-length, L, because it is a direct indicative of accuracy and the time for breakup.

Weak wall effect: Former PLIC algorithm

In this section, the results from using PLIC and the HF-PD curvature model are analyzed. The domain selected for this test is a parallelepiped of size $3 \times 2 \times 1$. The interface contours of a drop breaking up is shown in Figure 6.45. As it can be observed, the deformation of the drop is large enough to produce breakup and three daughter drops of ellipsoidal shape. Lobes are produced as the drop stretches. Then, whole-drop recirculation diminishes as the neck forms and contracts. When lobe recirculation starts, a filament is produced and remains stable until the final rupture.

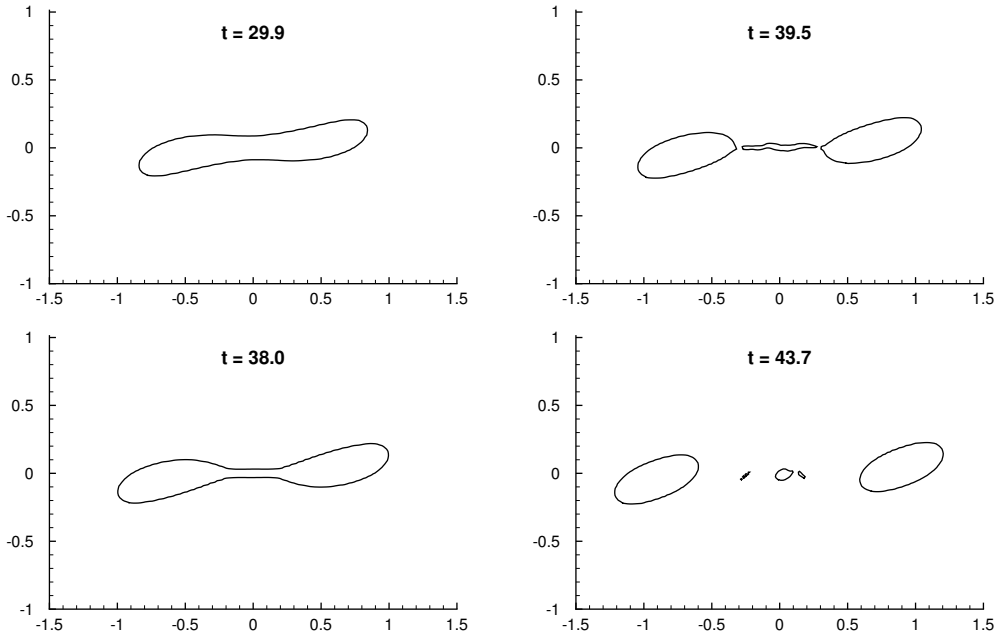

Figure 6.45: Breakup of a viscous drop in a simple shear flow. For uniform properties, $\lambda = \gamma = 1$, $Re^* = 0.0625$, $Ca = 0.44$, $\Delta t = 1.25 \times 10^{-4}$, mesh $180 \times 120 \times 60$ ($a/\Delta x = 14.6$).

The results for a mesh $180 \times 120 \times 60$ ($\Delta x \sim 1/60$) presented drop breakup at $t_{0.5} = 38.9$ for a half-length

of $L/a = 4.14$. The filament is completely detached from the daughter drop when $t_{0.001} = 39.8$, where the subindex indicate the contour-level criterion. For a coarser mesh, $160 \times 80 \times 40$ ($\Delta x \sim 1/40$), breakup occurs at $t_{0.5} = 41.0$ and $t_{0.001} = 44.0$. The references reported breakup at $t_c = 47.8$ (PROST) and $t_c = 49$ (BIM), where the half-length is $L/a = 5.39$ for the latter. This discrepancy is attributed to the lack of mesh resolution at the filament region (around one cell), leading to a high error in curvature and fluxes, which in turn induced an earlier breakup. Also, the HF-PD model is expected to increase the curvature, therefore larger forces and early ruptures.

The evolution of the half-length of the drop is compared against the finest mesh resolution ($\Delta x = 1/160$) of (Renardy and Renardy, 2002) (PROST), as shown in Figure 6.46. It is worth noting that the method here presented is capable of achieving a correct drop deformation, which is given by the solution using BIM Cristini et al. (2001). The difference of L with respect to BIM is within 2% up to time $t = 39$.

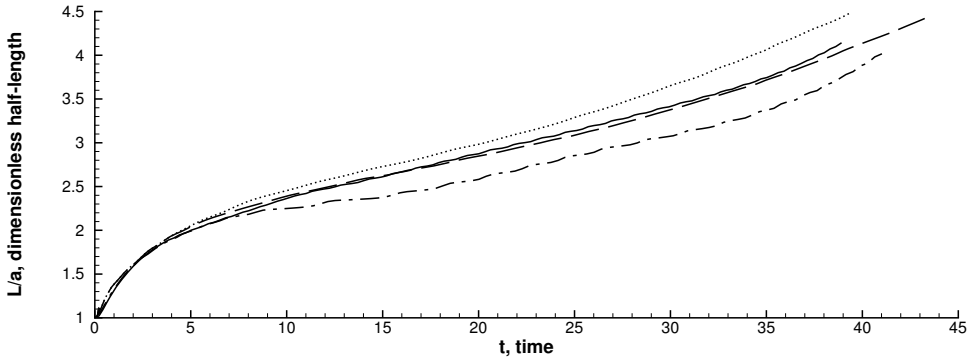

Figure 6.46: Evolution of the half-length of a viscous drop in a simple shear flow. Uniform properties ($\lambda = \gamma = 1$), $Re^* = 0.0625$, $\Delta t = 1.25 \times 10^{-4}$. The HF-PD and PLIC methods used for $Ca = 0.44$, mesh $180 \times 120 \times 60$ ($a/\Delta x = 14.6$) (——) and $160 \times 80 \times 40$ ($a/\Delta x = 9.6$) ($- \cdot -$). The references are PROST ($\Delta x = 1/160$) ($\cdots\cdots$) and BIM ($- - -$) (Renardy and Renardy, 2002; Cristini et al., 2001).

One of the capabilities of the VOF method is to conserve mass, feature that is required in long-term simulations. The volume of the drop measured at time $t = 0$ is $V_0 = 6.544992 \times 10^{-2}$, while at $t \sim 39$ is $V_0 = 6.544840 \times 10^{-2}$, which represents a normalized difference of 2×10^{-5}. This was achieved with a normalized residual of the pressure-correction equation of 10^{-3}, the former PLIC method, which is similar to the BDR scheme, and without any redistribution algorithm which enforces mass conservation.

Weak wall effect: DDR-PLIC algorithm

Now, the same problem is repeated, but using the most recent DDR-PLIC algorithm. It is important to mention that results as accurate as before were not possible and the effect of the mesh size was investigated. Even though the method is superior to the previous PLIC method, the curvature model used is the HF

model. The reason behind the selection of this model is that it converges with mesh refinement, unlike the HF-PD, and the viscous stress field is more smooth. In order to investigate the convergence of the method, two parallelepiped domains of sizes $3 \times 2 \times 1$ and $3 \times 2 \times 2$ are considered. The deformation of the interface for $Ca = 0.44$ is shown in Figures 6.47 and 6.48, while the drop half-length is presented in Figure 6.49.

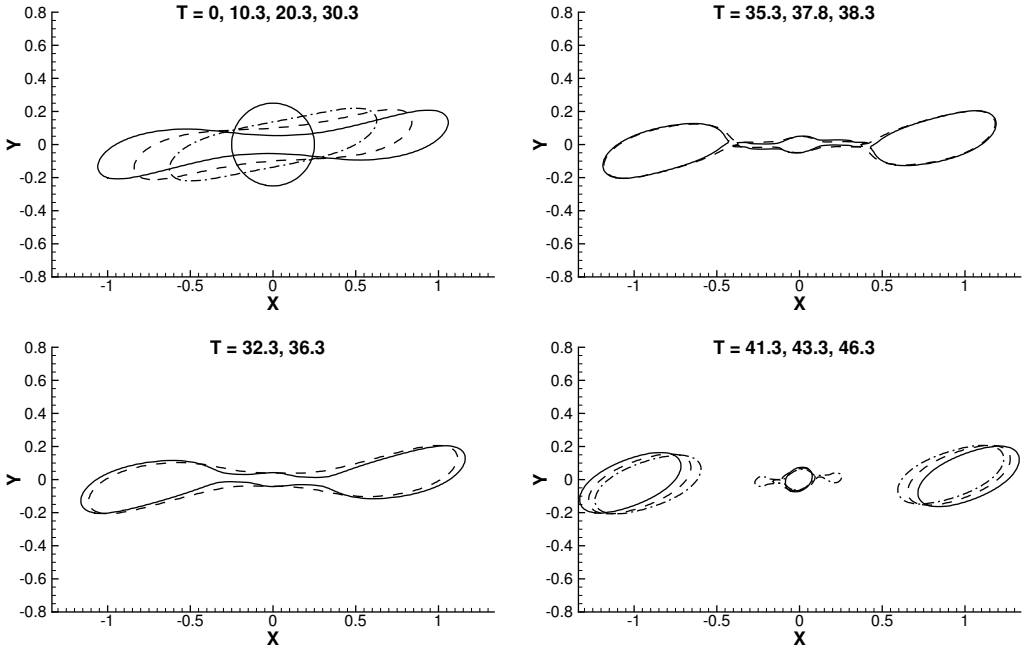

Figure 6.47: Breakup of a viscous drop in a simple shear flow. For uniform properties, $\lambda = \gamma = 1$, $Re^* = 0.0625$, $Ca = 0.44$, $\Delta t = 5 \times 10^{-4}$, mesh $270 \times 180 \times 90$ ($a/\Delta x = 22.5$).

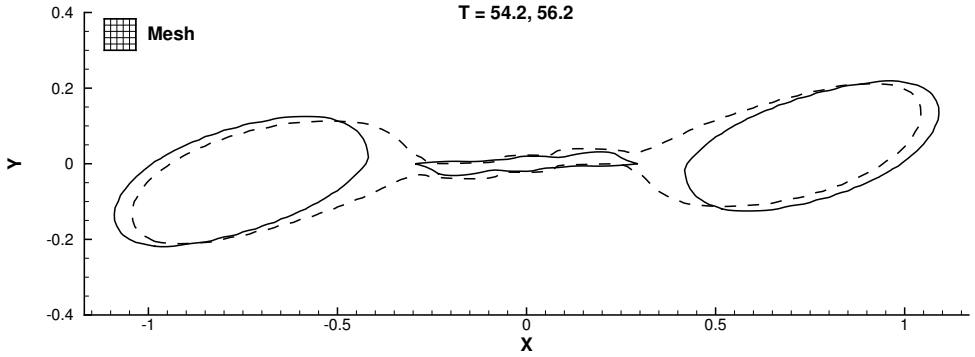

Figure 6.48: Breakup of a viscous drop in a simple shear flow. For uniform properties, $\lambda = \gamma = 1$, $Re^* = 0.0625$, $Ca = 0.44$, $\Delta t = 5 \times 10^{-4}$, mesh $180 \times 120 \times 120$ ($a/\Delta x = 15$).

Using the mesh $270 \times 180 \times 90$ ($\Delta x = 1/90$ or $a/\Delta x = 22.5$), the drop breaks up with half-length $L/a = 4.77$ at $t = 38$, which represents an error of 12% in L/a and 22% in time. For a coarser mesh, $180 \times 120 \times 60$ ($\Delta x = 1/60$), breakup occurs with half-length $L/a = 4.66$ at $t = 41$, equivalent to 14% error

in L/a and 16% in time. This indicates that mesh refinement increase the deformation, but breaks up the drop sonner, as expected. The references reported breakup at $t = 47.8$ (PROST, $\Delta x = 1/160$) and $t_c = 49$ (BIM), where the half-length is $L/a = 5.39$ for the latter. These results are obtained with the smaller domain in z.

When a larger domain in z is employed, mesh $180 \times 120 \times 120$, the drop breaks up at $t = 55$ for a half-length $L/a = 4.28$, representing a 12% difference in time and 20% in space. Analyzing how accurate this method was for previous problems, it is then expected that these discrepancies are due to the boundary conditions and mesh refinement. Numerical errors in the filament region are prone to occur because the one-cell resolution problem and the fact that the error in curvature is large for an interface not resolved within 3 cells.

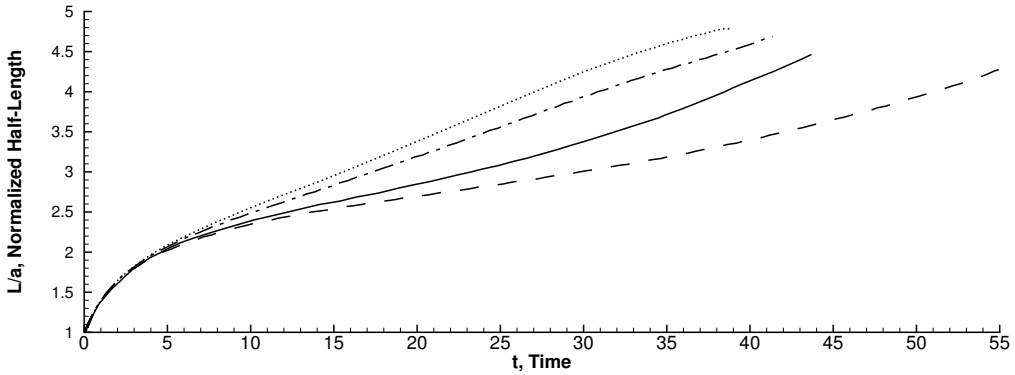

Figure 6.49: Effect of the mesh size and resolution on the evolution of the half-length of a viscous drop in a simple shear flow at $Ca = 0.44$ under uniform properties ($\lambda = \gamma = 1$) and $Re^* = 0.0625$. Using the HF-DDR method for $\Delta t = 5 \times 10^{-4}$ and meshes $177 \times 117 \times 57$ ($a/\Delta x = 14.6$) ($- \cdot -$), $180 \times 120 \times 120$ ($a/\Delta x = 15$) ($- - -$), $270 \times 180 \times 90$ ($a/\Delta x = 22.5$) ($\cdots\cdots$). The reference is BIM (——) (Renardy and Renardy, 2002; Cristini et al., 2001).

Considering that mesh refinement increases the deformation, it is expected that finer meshes in a wider domain would produce more accurate solutions. Producing solutions at the required mesh resolution $\Delta x \lesssim 1/160$ and time step is quite limiting.

In terms of mass conservation, the volume of the drop measured within time $t = 0 - 30$ remained as $V = 6.54498 \times 10^{-2}$ for $a/\Delta x = 22.5$.

Despite our best efforts to show accurate solutions of this problem, the important conclusion is that the method is capable of predicting drop breakup, but with limited accuracy.

6.4.5 Drop Deformation in a Straight Capillary Tube

The problem of a spherical viscous drop located in capillary tube with a started pressure-driven Stokes flow is analyzed for different capillary number and mesh resolutions. The objective is to compare the shape of the drop obtained using PLIC-VOF with the boundary integral method (BIM) of Tsai and Miksis (1994). This comparison is held at $Re = 0$ for a blockage ratio $\beta = a/R = 0.9$, and a range of $Ca = \mu U/\sigma$ from 0.05 to 1.0, where U is the upstream average velocity. The domain in consideration is a parallelepiped of size $16.7 \times 2 \times 2$, where a pipe is generated by prescribing wall boundary conditions as required. The drop is initially located at $x_o = -6a$, position where the flow is already fully developed since $L_d/d > 0.62$ for $Re = 0$. A sensitivity analysis to the mesh resolution is performed based on the velocity and geometrical parameters of the drop, as shown in Fig 6.50. The aspect ratio is defined as L/B, where L is the maximum horizontal length of the drop and B is the maximum vertical breadth. Drops with re-entering cavities are characterized by the the the tip-to-end length at $y = 0$, A.

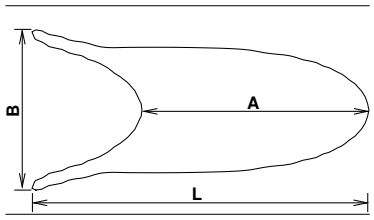

Figure 6.50: Geometrical properties of a deformed drop in a capillary tube. The shape is given for $Ca = 1.0$ at $t = 2$ and a mesh resolution $d/\Delta x = 30$.

Table 6.23: Centerline and maximum tip-to-end length of the drop for different mesh resolutions at $Ca = 1$. Error shown in parenthesis (%).

		time					
$\frac{d}{\Delta x}$	Δt	2		4		6	
		A	L	A	L	A	L
30 ($Re = 0.1$, MS $N = 5$)	1×10^{-4}	2.33 (2.1)	3.44 (1.1)	–	–	–	–
60 ($Re = 1$, RK $N = 4$)	5×10^{-4}	2.06 (11)	3.45 (0.9)	0.91 (35)	3.77 (4.6)	0.41 (28)	3.65 (5.2)
60 ($Re = 0.1$, MS $N = 10$)	2.5×10^{-4}	2.398 (0.8)	3.392(2.5)	1.292 (7.7)	3.769 (4.6)	0.474(17)	3.608(6.3)
Tsai and Miksis (1994)	–	2.38	3.48	1.40	3.95	0.57	3.85

The evolution of the shape of the drop for $Ca = 1$ is presented in Fig 6.51, where a re-entering cavity is observed as in the simulations of Tsai and Miksis (1994). It was noticed that a good parameter for comparison

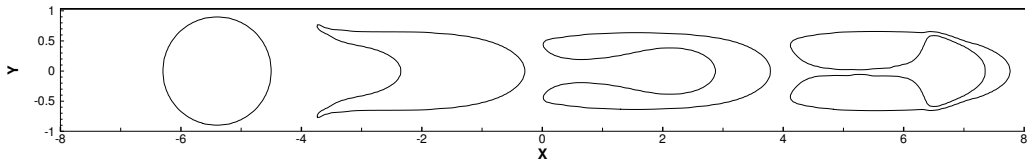

(a) $Re = 1$, $\Delta t = 5 \times 10^{-4}$

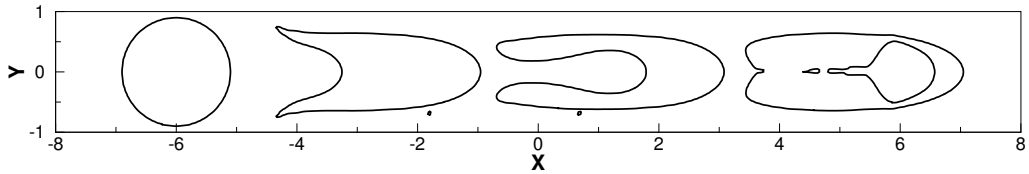

(b) $Re = 0.1$, $\Delta t = 2.5 \times 10^{-4}$

Figure 6.51: Evolution of an initially spherical drop of radius $a = 0.9$ in a capillary tube of radius $R = 1$ for $\lambda = 0.1$ and $Ca = 1.0$ at $t = 0$, 2, 4, 6. Mesh resolution $d/\Delta x = 60$. Advection terms are not computed.

is the tip-to-end length A. As it can be observed from Table 6.23, the error incurred in the shape is large. Several simulations were performed to find the reasons of the discrepancy. This problem motivated the study of multistep, Runge-Kutta and DDR-PLIC methods in VOF. The multistep method with $N = 5$, 10 was employed with the former PLIC algorithm to minimize the errors in time and due to fluxing of the volume fraction. The HF-PD curvature model is also employed in order to improve the curvature for coarse meshes. It was found as the main reason for the discrepancy the effect of the local acceleration term in the momentum equation. This error let us understand the difference between having $Re \sim 0$ and using the Stokes approximation with finite values of Re. This study showed that the error incurred for $Ca = 1$ is as large as 17% for a mesh resolution $d/\Delta x = 60$ and $Re = 0.1$. The main contribution to this error is the high curvature at the rear side of the drop, that is, at the tips of the re-entrant cavity. A case like this one may take benefit of multigrid solutions.

Table 6.24: Aspect ratio, A/B, of the drop for different mesh resolutions and Capillary numbers

$\frac{d}{\Delta x} \setminus Ca$	0.05	0.2	0.5
30 ($Re^* = 1$)	1.113 (1.1)	–	–
57 ($Re^* = 1$)	–	1.465 (11)	2.044 (9)
60 ($Re = 0.1$)	1.102 (2.1)	1.590(3.6)	2.139 (4.8)
Tsai and Miksis (1994)	1.126	1.650	2.246

The drop contours at lower capillary numbers are presented in Figure 6.52. The aspect ratio is compared in Table 6.24. The cases with mesh resolution $d/\Delta x = 57$, $Re^* = 1$ (advection is not computed), the former

PLIC and the HF curvature model showed a maximum difference of 11% for $Ca = 0.2$. For $d/\Delta x = 60$, DDR-PLIC-HF and $Re = 0.1$ (advection is now considered), the maximum difference reduces to 4.8% for $Ca = 0.5$. The solution for highly spherical drops is accurate as expected, meanwhile the error for higher Ca decreases with a lower Re. This benchmark shows that drops with resolutions of $a/\Delta x \sim 27$ produce results that are sufficiently accurate. Lowering Re may improve the results further.

By using multisteps methods, an important reduction in wisps and improved interfaces are observed, meanwhile using DDR-PLIC eliminates those problems. Results of the latter where more accurate because a lower Re is employed. This concludes the validation of the VOF-DDR-PLIC method.

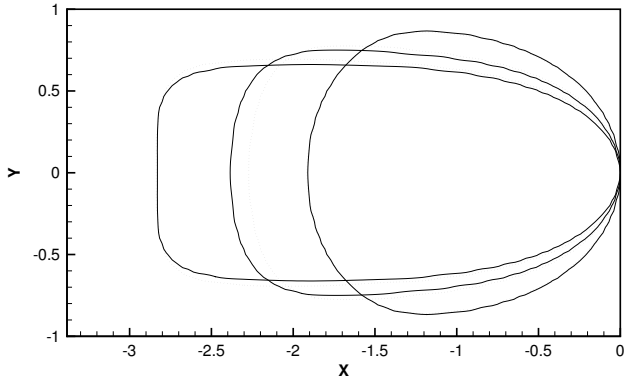

Figure 6.52: Steady-state deformation of an initially spherical drop of radius $a = 0.9$, $\lambda = 0.1$. For $Ca = 0.05, 0.2, 0.5$, using the former BDR ($Re^* = 1$) ($\cdots\cdots$) and DDR ($Re = 0.1$) (——). Deformation increases with Ca.

6.5 Elastic-Solid Solver

6.5.1 Beam in a cantilever

Consider a horizontal built-in beam of length L, squared cross section A and moment of inertia I, subject to a punctual vertical force P at the extreme pointing downwards. The steady-state solution of this problem using the elastic curve theory gives, $y = -Px^2\,(3L - x)\,/\,(6EI)$, where $A = bh$ and $I = bh^3/12$. Here, a numerical model is employed based on linear elasticity with added diffusion (to achieve steady-state), a non-uniform grid and provided with the following properties: $\rho = 1$, $E = 2000$, $\nu = 0$, $L = 0.5$, $h = 0.1$, $b = 1$. Equivalence to the elastic curve is obtained using a "thin" mesh, as shown in figure 6.53.

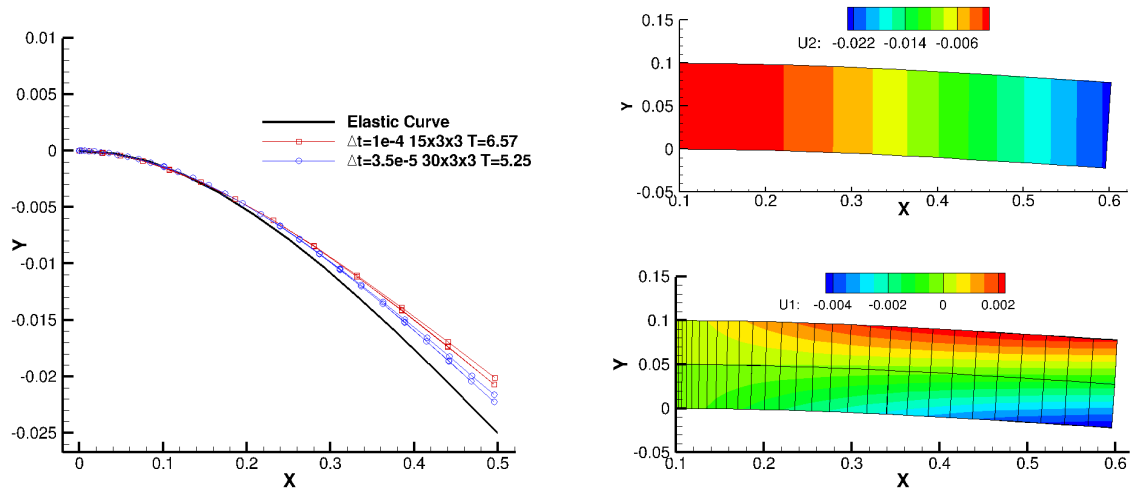

(a) (b)

Figure 6.53: Displacement of a beam in a cantilever after the application of a punctual force at the extreme: (a) Effect of mesh refinement (b) Contour of U_1 and U_2.

6.5.2 Effect of simple shear on an elastic cylindrical shell

On the previous section, a simple shear is applied on a drop and the respective Taylor deformation parameter was obtained. A similar problem was performed by Ramanujan and Pozrikidis (1998) on a spherical shell (following the strain energy function of Skalak et al. (1973), which allows for shear deformation but resists local and global dilatation) using a boundary element method in axisymmetric coordinates. Here, a fully 3D finite volume method is considered, following an elastic model for the stress tensor. To stabilize the solution and achieve steady state, a volumetric force is added as, $\mathbf{F}_d = C\tilde{\mathbf{v}}\Delta\mathcal{V}$, where C is a damping constant and $\mathcal{V}$ is the volume of the cell.

An external shear flow is applied and a zero-way coupling is considered: a constant shear stress acting on

the external faces. The 2-way coupling required more numerical research in order to get relatively accurate solutions. The stress applied to the external face of the membrane is given by $\tau_{xy} = \eta_m \dot{\gamma}$, where $u = \dot{\gamma} y$ and $v = 0$. It is assumed no flow inside the shell or low viscosity, therefore, the shear stress is only imposed on the external faces. For this problem, the capillary number is replaced by the dimensionless shear rate as,

$$G = \eta_m \dot{\gamma} R / E_s$$

where η_m is the viscosity of the matrix fluid, R is the particle radius and E_s is the surface elastic modulus, Eh, being h is the thickness of the membrane. The results are shown in figure 6.54, where a similar trend is found between the simulated cylindrical shell and thin capsule of the reference using G. The angle with the horizontal remains at 45° for large G in this simulation, while it is observed to reduce in the literature. The shell bends inwards while the capsule bends outwards.

Despite that a cylindrical shell with zero-way coupling and a capsule with full coupling are two different problems, the solutions showed similarities in deformation. Because of the equivalence between G and Ca, it may be possible to find a relationship between the behavior of a drop and a biological cell. In a dynamical sense, elasticity may produce oscillations, while viscoelasticity may produce dampening, as it will be shown next.

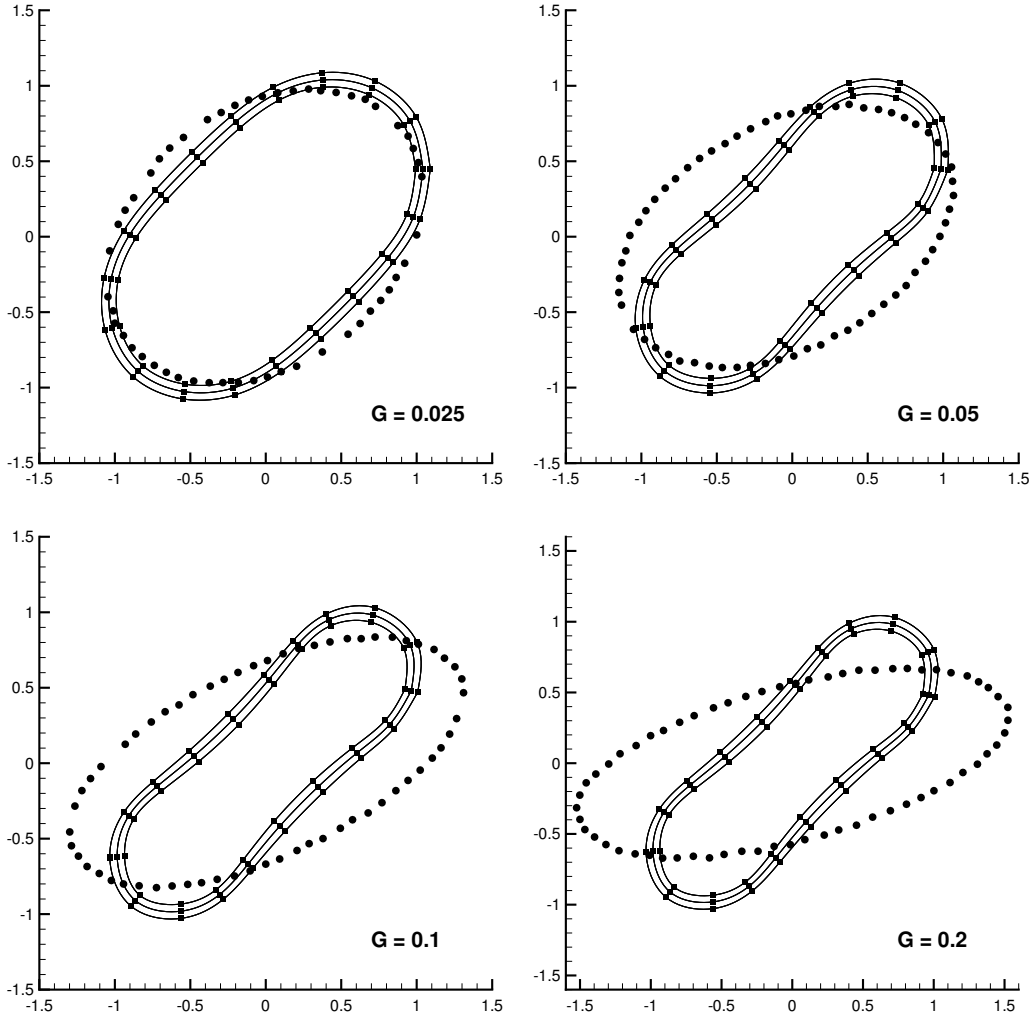

Figure 6.54: Deformation of an elastic body for several dimensionless shear rate, G. Results for the deformation of a cylinder after the application of a constant stress, $\boldsymbol{\tau}_{12}$, on the external side ($-\blacksquare-$). Comparison with the deformation of a thin capsule subject to a simple shear flow and $\lambda = 1$ ($\bullet$), from Ramanujan and Pozrikidis (1998).

6.5.3 Effect of simple shear on an elastic sphere

Results using the experimental code with 2-way coupling are now presented, basically to show the qualitative oscillatory behavior of the problem. For simplicity, a sphere is now compared with a drop. The pressure and shear stress contours, together with the solid surface, the streamlines and the maximum deformation of the solid are presented in Figure 6.55.

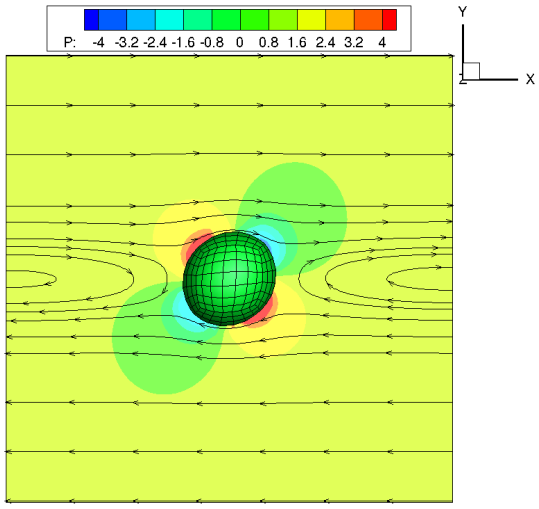

(a) Pressure contour, $G = 0.35$

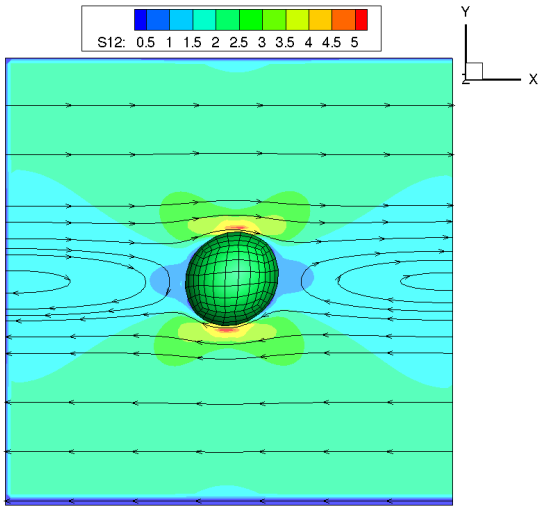

(b) Shear stress contour, $G = 0.35$

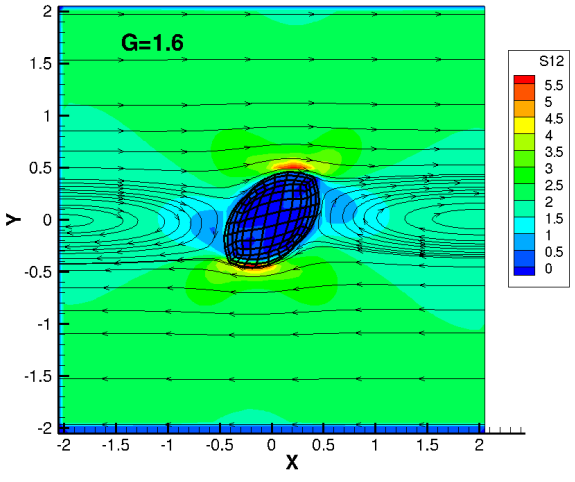

(c) Shear stress contour, $G = 1.6$

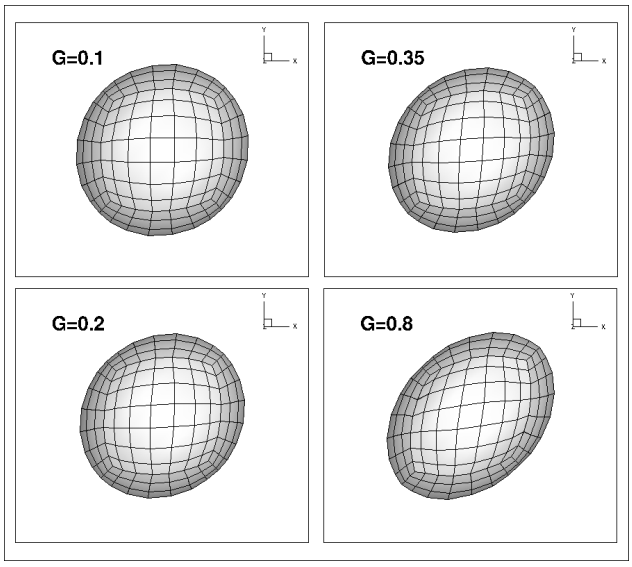

(d) Maximum deformation

Figure 6.55: Stresses and deformation for a solid sphere in a simple shear flow

By comparing several results using the drop deformation and the solid sphere, the fluid to solid relation for similar deformation is $G \sim 7Ca$. These results are presented in Figure 6.56. The elastic solid shows fully

oscillatory behavior, while the simple-viscoelastic solid shows dampening. This is not the case for drops at relatively low Ca where the Taylor deformation is monotonic.

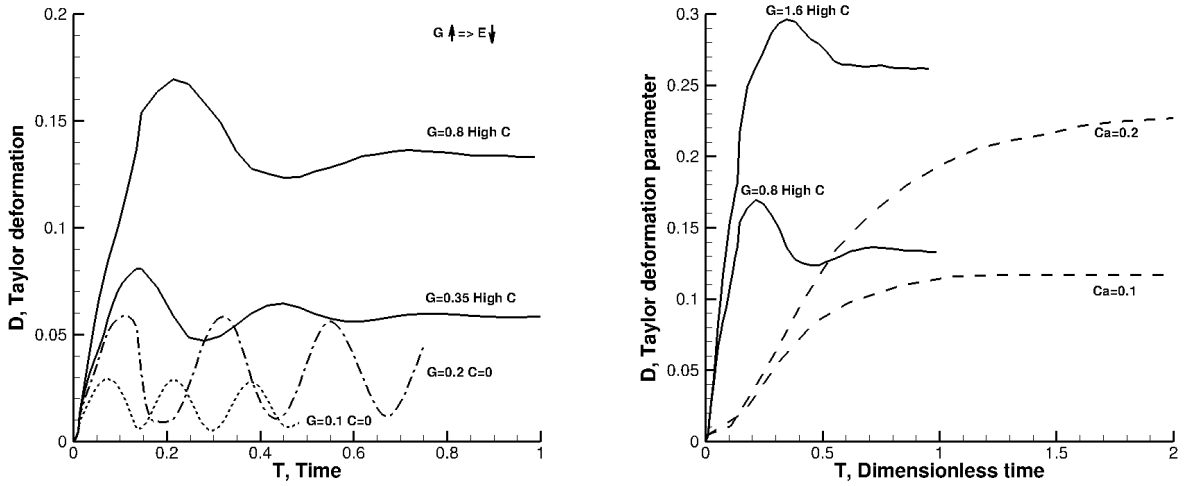

(a) Taylor deformation of the solid

(b) Comparison between the solid and the drop

Figure 6.56: Taylor deformation of a solid sphere in a simple shear flow.

This brief study allow us to understand the main difference between drops and rubber-like solids which is the oscillatory behavior. If such effect is not considered, one can still find similarities between drops and membraned-like objects.

The code for the solid presented unstable behavior when the object had rotated considerably. Also, there are several publications of the behavior of membranes for elastic and viscoelastic solids. A cell membrane is better represented by a thin membrane because of its thickness, so thick-membrane analysis does not apply to that problem. For these reasons, this investigation was not pursued further.

6.6 Conclusions

Different problems were used to validate the forces and submodels required to simulate the particle-drop interaction. The temporal and viscous forces were verified with a Poiseuille flow, while the accuracy of advection forces was analyzed with the cavity flow problem, showing convergence to the exact solution for the former and convergence to solutions in the literature for the later. The problem of a static drop was included to verify of the importance of the spurious currents, accuracy of the pressure jump and curvature, and degree of mass conservation. The motion of the interface and its reconstruction was addressed with the single vortex problem and the deformation field, showing not only excellent volume conservation, but superlinear order of convergence with grid refinement. The problem of an initially deformed drop allowed for

a final verification under a non-linear problem were all the models are relevant. The long-term capabilities of the method and effect of the boundary conditions were addressed in the problem of a drop subject to a simple shear flow.

Chapter 7

Results

7.1 Wall Effect on the Breakup of Drops in Simple Shear Flows

When the confinement is greater than $a/d = 0.15$, the walls affect the drop shape and its critical capillary number, Ca_c, as shown in the phenomenological model of Minale (2008). In this study, a drop is sheared under high confinement geometry for various Ca and the critical conditions for breakup are estimated. The sensibility of the drop deformation and critical conditions to the size of the domain is also analyzed. The symmetry in z direction is brought closer to the drop to increase the drop stability and reduce the mesh points. For moving plates separated by a distance d, the limiting geometry has a clearance ratio of $\beta = d/(2a) = 1$, unless the drop is initially deformed or injected.

Similarly as before, drop radius is $a = 0.25$ and properties are uniform, $\lambda = \gamma = 1$. The clearance ratio is fixed to $\beta = 1.1$, while Ca is varied until breakup is found. The external Reynolds number is $Re^* = 0.0625$ and Stokes flow approximation is used again. Four types of meshes are used: uniform spacing ($M1$), variable spacing throughout the domain ($M2$), variable spacing only away from the drop in the x direction ($M3$), and variable spacing in the x and z directions ($M4$).

The simulations show steady-state drop deformations for $Ca \lesssim 0.48$, where the drop stretches, recoils and then stretches again without breakup. The drop half-length evolves as a mass-spring damped oscillator until steady-state conditions are achieved, as shown in Figure 7.1. Steady-state conditions are achieved after $t \sim 200$ with half-lengths of $L/a = 4.259$, 4.460, 4.664, for $Ca = 0.45$, 46, 47, respectively. The deformation increases as Ca is increased, until drop recovery is no longer possible and breakup occurs. For $Ca = 0.49$ the drop breaks up in a domain with $L_x = 20a$ and $L_z = 5a$, but it is stable in a domain with $L_x = 16a$. The drop breaks up at $Ca = 0.48$ when $L_z = 12a$.

The Taylor deformation, D, shown in Figure 7.2, is very similar between different cases for $t < 30$. The

maximum elongation of the drop is $t \sim 30$. Past this time, D deviates depending on whether the drop manifests breakup or not. The cases with a larger domain in the z direction have smaller values of D. It is noted how the Taylor deformation increases for supercritical cases ($Ca \geq 0.50$) after $t \sim 30$, while it decreases for near critical conditions ($Ca = 0.49$). This behavior could be used to determine the type of breakup because it is different between critical and slightly supercritical conditions. The Taylor deformation parameter is also expected to increase for larger supercritical conditions because the drop breaks up without recoiling. The cross section (xy plane, $z = 0$) of the interface for these cases are presented in Figures 7.3-7.7 for more details.

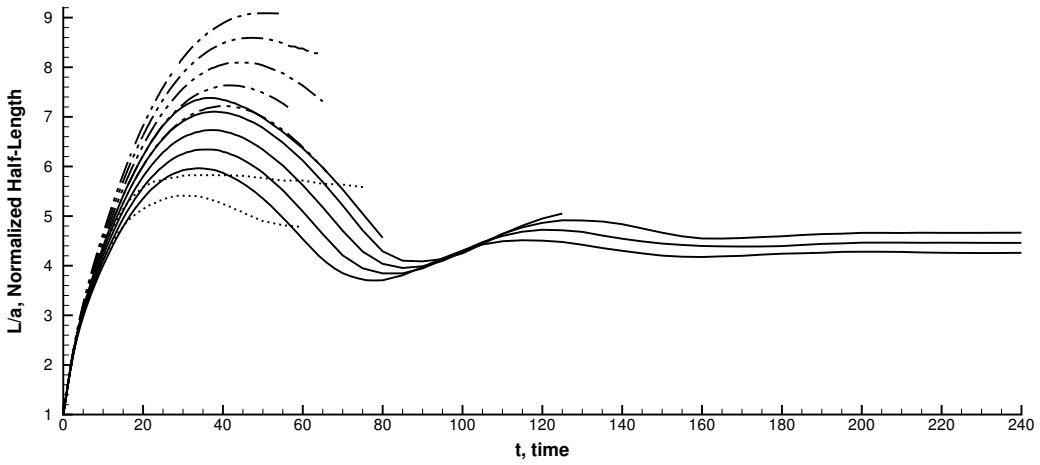

Figure 7.1: Half-length, L/a, of a viscous drop under high confinement geometry, low Re, uniform properties, $\Delta t = 5{\times}10^{-4}$ and domain size $L_x{\times}2.2a{\times}L_z$. For mesh $M1{-}320{\times}44{\times}100$ ($a/\Delta x = 20$), $L_x = 16a$ and $L_z = 5a$: $Ca = [0.45\ 0.46\ 0.47\ 0.48\ 0.49]$ (——). For single/multi-meshes: $Ca = 0.48$ ($M3 - [320,\ 400] \times 44 \times 100$, $L_x = [16a,\ 24.5a]$), $Ca = 0.49$ ($M1 - [320,\ 400] \times 44 \times 100$, $L_x = [16a,\ 20a]$), $Ca = 0.50$ ($M3 - 460 \times 44 \times 100$, $L_x = 28.2a$), $Ca = 0.51$ ($M3 - [340,\ 460] \times 44 \times 100$, $L_x = [21.4a,\ 28.2a]$) and $Ca = 0.52$ ($M3 - [340,\ 400,\ 500] \times 44 \times 100$, $L_x = [21.4a,\ 28.2a,\ 30.6a]$) ($- \cdot\cdot -$). For mesh $M2 - 240 \times 40 \times 85$ ($a/\Delta y > 11$, $16a \times 2.2a \times 12a$), $Ca = [0.46\ 0.48]$ ($\cdots\cdots$). Some simulations were restarted in larger domains in x direction as indicated in brackets.

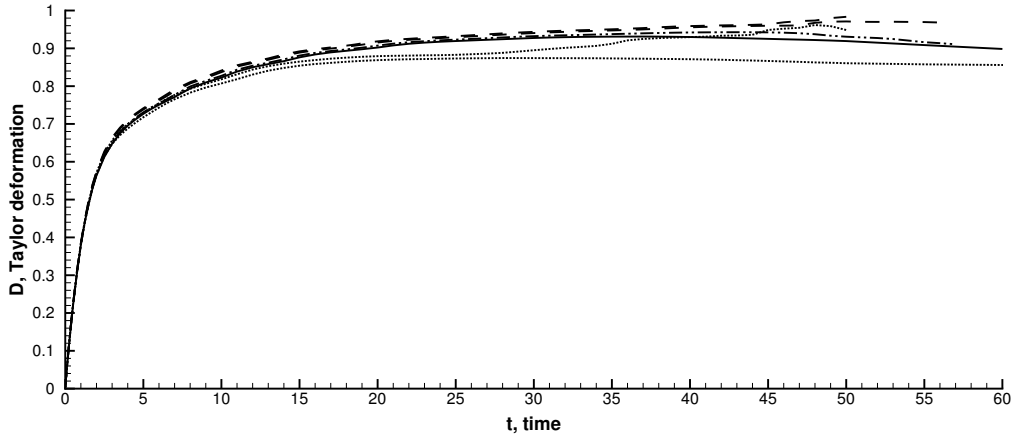

Figure 7.2: Effect of the capillary number on the Taylor deformation, D, of a viscous drop under high confinement geometry, $\beta = 1.1$, low Re, uniform properties and $\Delta t = 5 \times 10^{-4}$. For mesh resolution $a/\Delta x = 20$ and $L_z = 5a$: $Ca = 0.48$ $(M1 - 320 \times 44 \times 100)$ (——), $Ca = 0.49$ $(M3 - [320, 400] \times 44 \times 100)$ $(- \cdot -)$, $Ca = 0.51$ $(M3 - [340, 460] \times 44 \times 100)$ and $Ca = 0.52$ $(M3 - [340, 400, 500] \times 44 \times 100)$ $(- \; - \; -)$. For variable mesh resolution $a/\Delta y > 11$: $Ca = [0.46, 0.48]$ $(M2 - 240 \times 40 \times 85)$ $(\cdots\cdots)$. D increases with Ca.

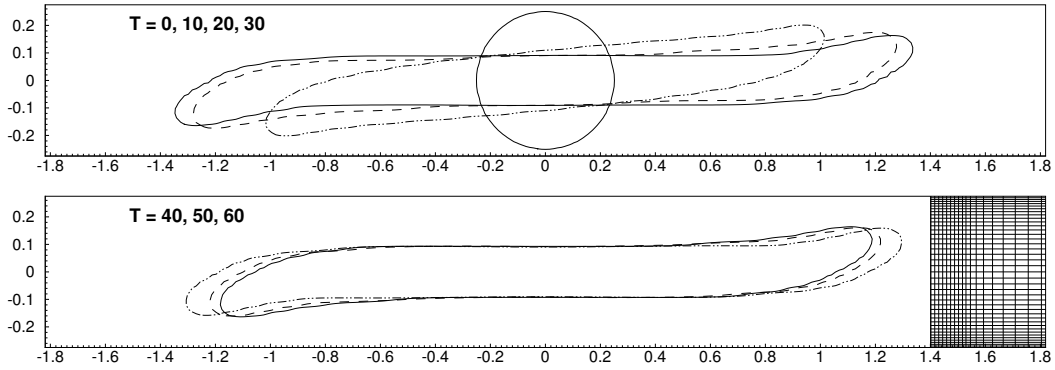

(a) $Ca = 0.46$

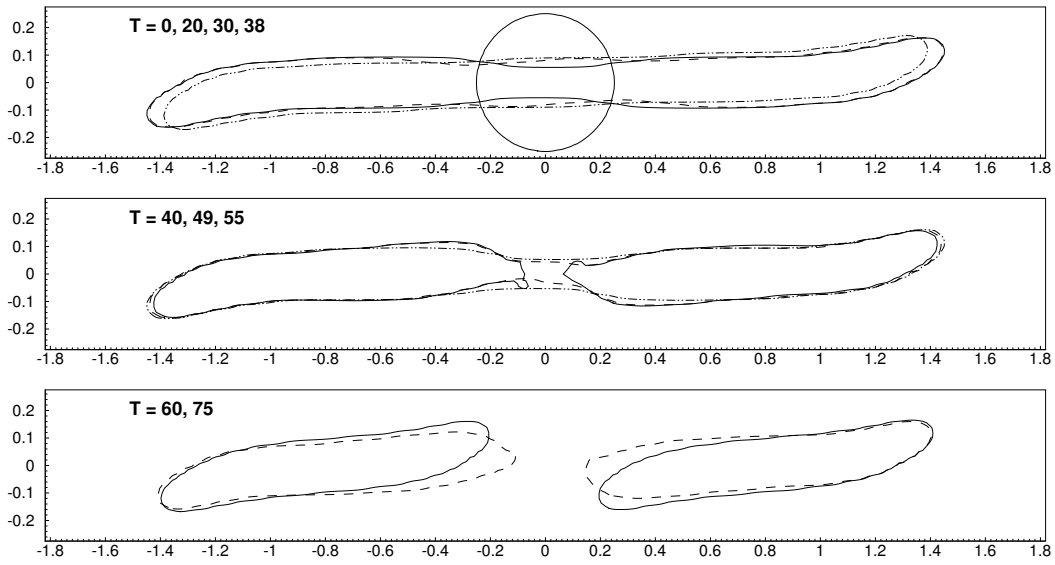

(b) $Ca = 0.48$

Figure 7.3: Breakup of a drop in low Re flows for an extended domain in z, $L_z = 12a$, uniform properties, $\lambda = \gamma = 1$, variable mesh $M2 - 240 \times 40 \times 85$ ($a/\Delta y_{neck} \sim 11$), domain size $16a \times 2.2a \times 12a$, MSE scheme ($N = 10$) and $\Delta t = 5 \times 10^{-4}$. For t_1 ($- \cdot \cdot -$) , t_2 ($- \; - \; -$), t_3 (——).

Using a variable mesh, a large domain in z direction, $L_z = 12a$, and the multistep-explicit method, the simulations at $Ca = 0.46$ and $Ca = 0.48$ show a transition from subcritical to supercritical conditions, as observed in Figure 7.3. For a slightly supercritical Ca, the drop stretching is faster than the inner recoiling process, giving origin to a neck between the main lobes. These lobes do not retract as fast as in subcritical cases with large Ca, leading to an unstable neck that breaks up. This occurs at $t = 50 - 55$ for $L/a \sim 5.74$. In comparison, the BIM solution of Janssen and Anderson (2007) presented a critical capillary number of $Ca = 0.465$ for $\beta = 1.11$.

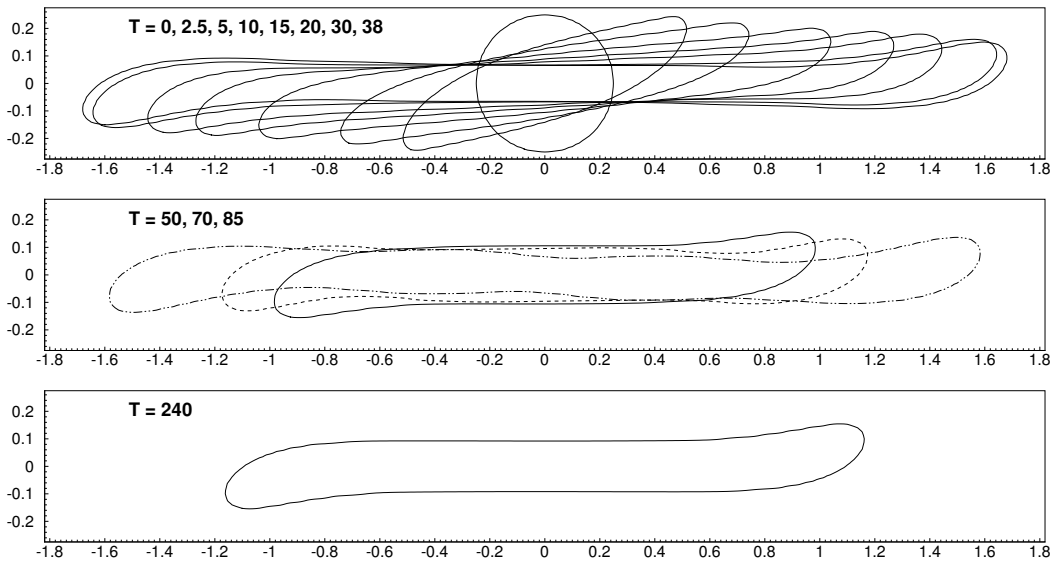

Figure 7.4: Effect of confinement and domain size on the drop interface at subcritical conditions. For $Ca = 0.47$, low Re, uniform properties, $\lambda = \gamma = 1$, mesh $M1 - 320 \times 44 \times 100$ ($a/\Delta x = 20$), $\Delta t = 5 \times 10^{-4}$ and domain $16a \times 2.2a \times 5a$.

When symmetric boundary conditions are brought closer to the drop, the lobes are smaller, the neck is more stable and breakup is delayed until $Ca \gtrsim 0.49$. In the case of $Ca = 0.47$, a neck started to form in the middle, as shown in Figure 7.4 for $t = 50$, but this drop is stable and a steady-state condition is achieved after $t > 200$.

In the case of $Ca = 0.48$, Figure 7.5, four neck-like structures were formed, as shown for $t \sim 50$. These structures are stable for $L_x = 16a$ and $L_x = 24.5a$, even though the latter shows larger deformation. In this sense, there is an effect of the boundary in x direction on the deformation, but it does not induce breakup.

When the domain is reduced in the x direction, the mixed inlet/outlet boundary condition is brought closer to the drop, which makes the flow more stable. This flow can be made physically possible by inserting a rack of fins aligned horizontally and located close to the point of the maximum drop deformation. This effect is more evident for $Ca = 0.49$ because it produces stable or unstable drops. These results are presented in Figures 7.6a, 7.6b and 7.1, the latter in terms of the drop half-length.

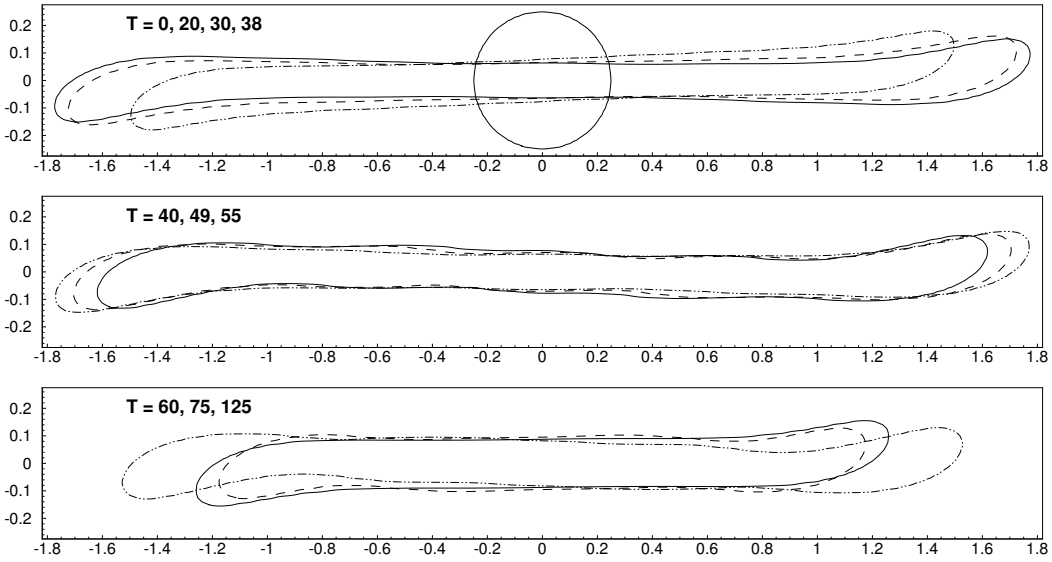

(a) Mesh $M1 - 320 \times 44 \times 100$, domain $16a \times 2.2a \times 5a$

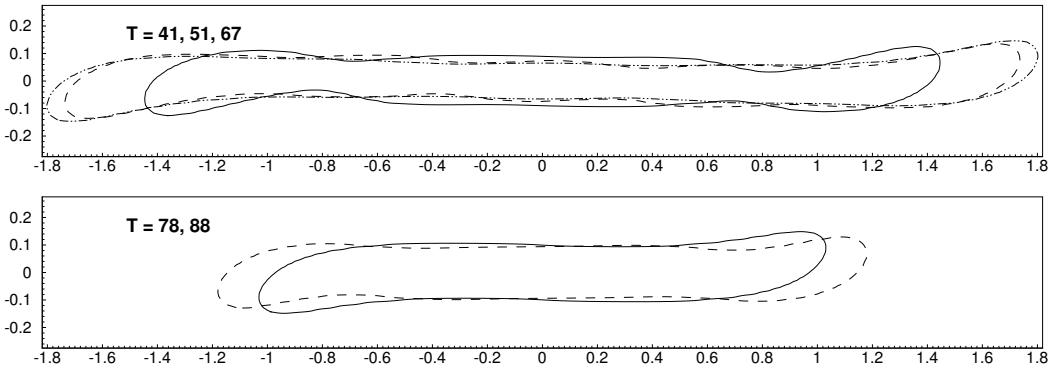

(b) Mesh $M3 - [320, 400] \times 44 \times 100$, domain $[16a, 24.5a] \times 2.2a \times 5a$

Figure 7.5: Continuation of Figure 7.4, for $Ca = 0.48$.

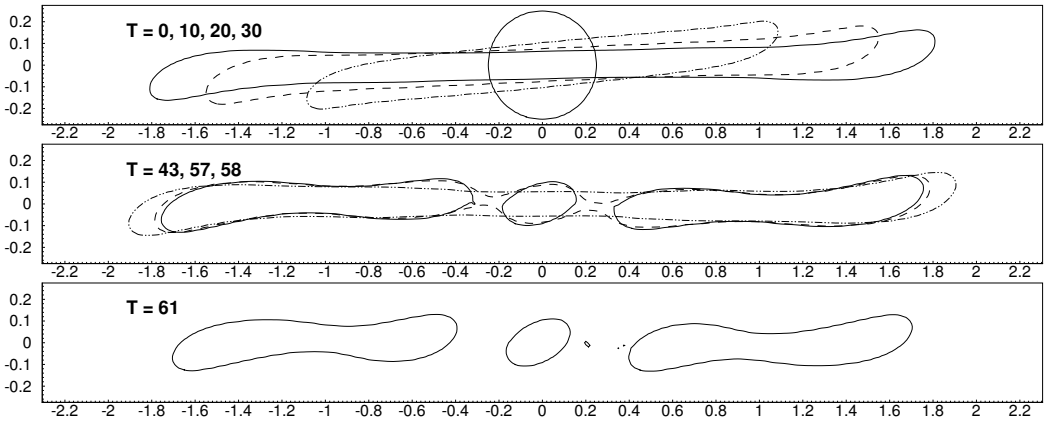

(a) $Ca = 0.49$, meshes $M1 - [320,\ 400] \times 44 \times 100$, domains $[16a,\ 20a] \times 2.2a \times 5a$

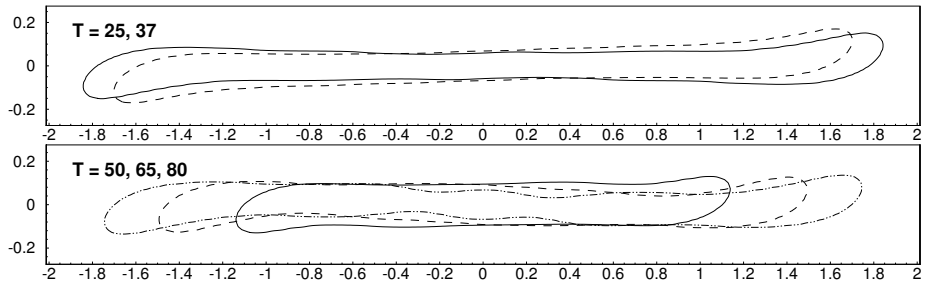

(b) $Ca = 0.49$, mesh $M1 - 320 \times 44 \times 100$, domain $16a \times 2.2a \times 5a$

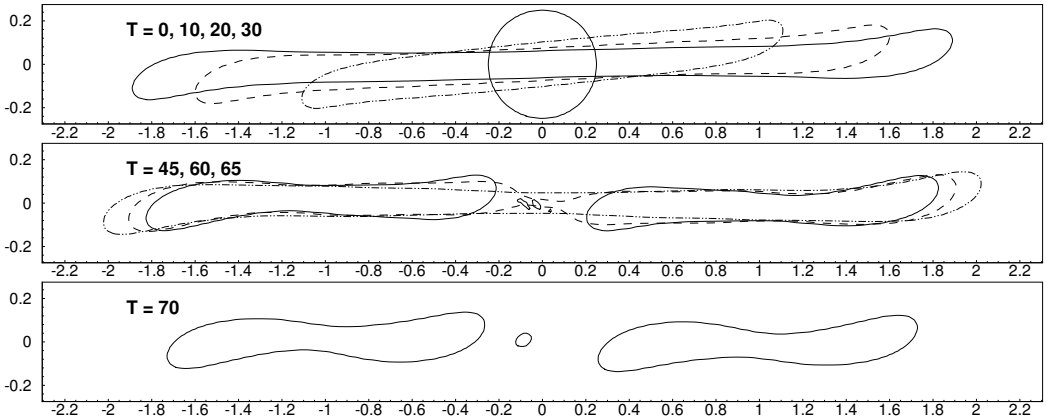

(c) $Ca = 0.50$, mesh $M3 - 460 \times 44 \times 100$, domain $28.2a \times 2.2a \times 5a$

Figure 7.6: Drop interface near critical conditions. Similar parameters of Figure 7.4.

The type of breakup is similar between $Ca = 0.49$ and $Ca = 0.50$ in the sense that two dumbbell-shaped and one spheroidal daughter drops are created after the formation of four constrictions. However, the central drop is smaller for $Ca = 0.5$. The critical deformation are $L/a = 7.15$ at $t = 57$ and $L/a \sim 7.5$ at $t \sim 60$, respectively.

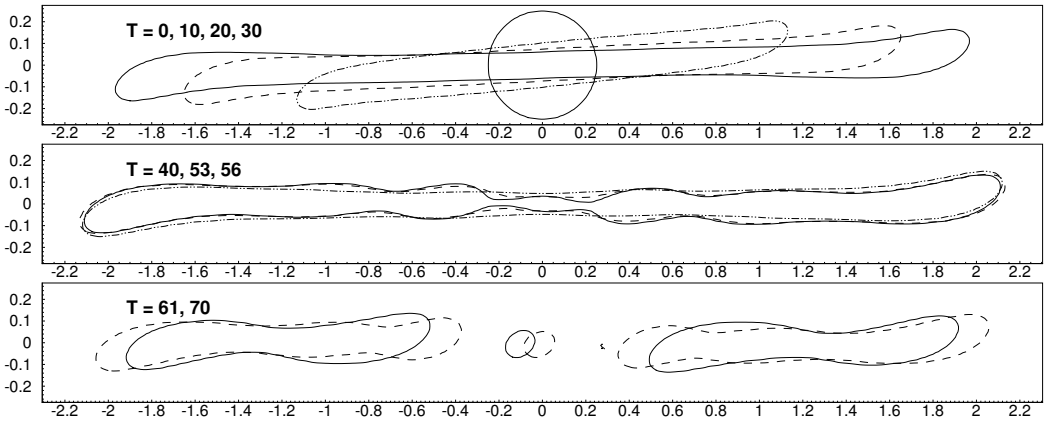

(a) $Ca = 0.51$, meshes $M3 - [340,\ 460] \times 44 \times 100$, domains $[21.4a,\ 28.1a] \times 2.2a \times 5a$.

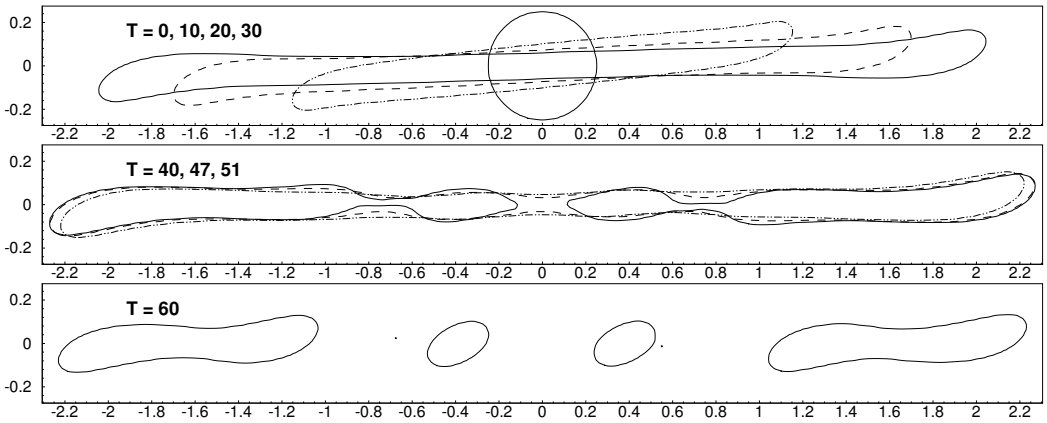

(b) $Ca = 0.52$, meshes $M3 - [340,\ 400,\ 500] \times 44 \times 100$, domains $[21.4a,\ 24.5a,\ 30.6a] \times 2.2a \times 5a$.

Figure 7.7: Drop interface for supercritical conditions. Similar parameters of Figure 7.4.

For $Ca = 0.51$, six constrictions are formed, but only two off-center constrictions are unstable, as shown in Figure 7.7. Breakup is observed at $t = 57$ for $L/a = 8.4$. Two main daughter drops are created and they adopt a stable dumbbell shape. A smaller daughter drop is created in the middle from the neck. For $Ca = 0.52$, three necks gave origin to four daughters: two dumbbell-shaped and two spheroids. The central neck breaks up at $t = 51$ while off-center necks break up at $t = 52$, for $L/a = 9.09$. Considerably more mesh resolution would be needed to capture and track the small fragments, if any. For larger values of Ca, more fragments are expected.

7.1.1 Effect of Viscosity Ratio

The effect of non-uniform viscosity across the interface on the critical conditions is now analyzed. The degree of confinement in y direction and density ratio are the same as in the previous section, $\beta = 1.1$ and $\gamma = 1$, but the viscosity ratio is changed to $\lambda = 0.3$ and $\lambda = 1.9$. A full domain in z is considered because it is the

least critical case and a variable mesh is used in all directions ($M2$), as shown in Figure 7.8a.

For $\lambda = 0.3$, the drop stabilizes considerably. There is no evidence of necking at $Ca = 0.6$, meanwhile a central neck is observed at $Ca = 0.7$ which breaks up at $t = 53.5$ with a drop half-length $L/a = 7.59$. This rupture originates two daughter drops. When compared with $\lambda = 1$, less deformation is observed for a given Ca. Additionally, the case $Ca = 0.7$ and $\lambda = 0.3$ is very similar to the case $Ca = 0.5$ and $\lambda = 1$ in critical half-length and type of breakup. The critical condition for $\lambda = 0.3$ is in the range of $Ca_c = 0.6 - 0.7$, representing $\sim 30\%$ increase from $\lambda = 1$. These results are shown in Figure 7.8.

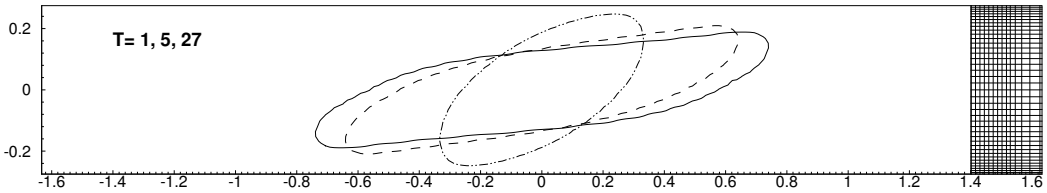

(a) $Ca = 0.5$, mesh $M2 - 240 \times 40 \times 85$, domain $16a \times 2.2a \times 12a$

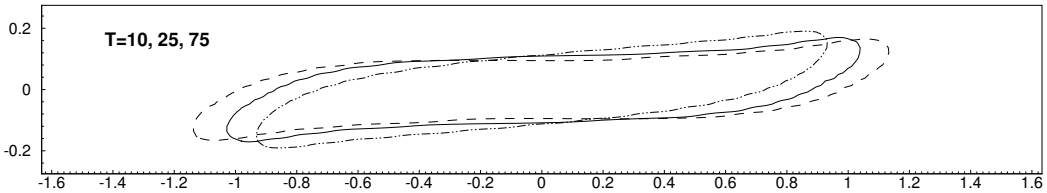

(b) $Ca = 0.6$, mesh $M2 - 240 \times 40 \times 85$, domain $16a \times 2.2a \times 12a$

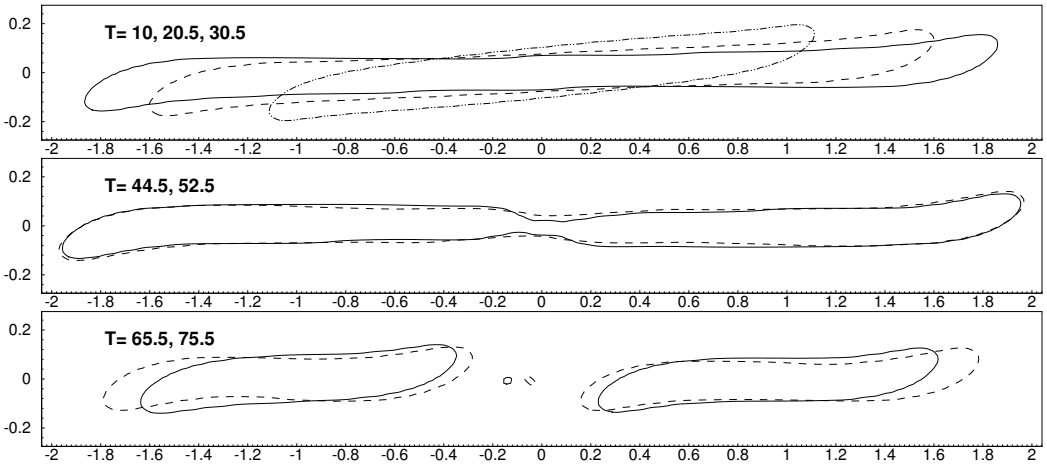

(c) $Ca = 0.7$, mesh $M2 - 380 \times 50 \times 90$, domain $28a \times 2.2a \times 12a$

Figure 7.8: Deformation of a drop of radius $a = 0.25$ in a flow with a more viscous medium, $\lambda = 0.3$, at low Re and $\beta = 1.1$.

For $\lambda = 1.9$, the drop breaks up for $Ca = 0.47$ after the formation of six constrictions and it is stable for $Ca = 0.40$, as shown in Figures 7.9a and 7.9b. The central neck then disrupts and creates a small daughter

drop, while the remaining of the mother drop produces two dumbbell shaped drops. This resembles the case of $\lambda = 1$ and $Ca = 0.49$. Rupture happens at $t \sim 60$ for $L/a = 8.14$. In the case of $Ca = 0.5$, only three constrictions are formed, as shown in Figure 7.9c. In contrast to $\lambda = 1$, the drop pinched at the most external necks. Rupture is observed for $L/a \sim 7.3$ at $t \sim 50$. For $Ca = 0.6$, the drop stretches considerably more and several constrictions appear, as shown in Figure 7.9d. Therefore, several daughter drops are expected. The critical condition is within $Ca_c = 0.4 - 0.5$.

For a more viscous drop, $\lambda = 1.9$, the drop deformation, the critical Ca and the critical time remained similar to the case with $\lambda = 1$, while the type of breakup can be due to central-pinching or end-pinching, depending on Ca. For a less viscous drop, $\lambda = 0.3$, the deformation is reduced considerably, requiring smaller values of the surface-tension coefficient to induce breakup.

Based on these results, an estimation of the critical point is plotted against viscosity ratio λ in Figure 7.10. The fitting shown by Grace (1982) (weak wall effect and low Re) is expressed in terms of the reduced shear E, but here are transformed to Ca. The regions for stable and unstable drop show a different tendency for $\lambda > 1$. It is then expected that a wall increases the range of λ for which drop rupture can happen, which is about 4 for unconfined flows.

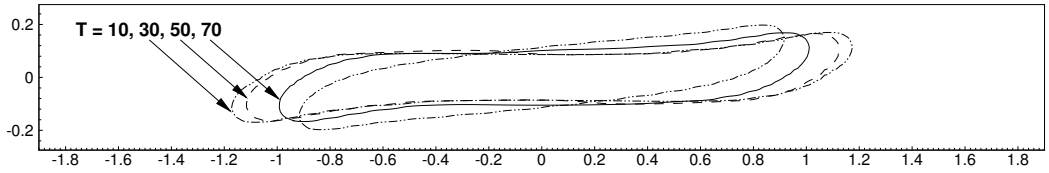

(a) $Ca = 0.4$, mesh $M2 - 240 \times 40 \times 85$, domain $16a \times 2.2a \times 12a$, $\Delta t = 5 \times 10^{-4}$

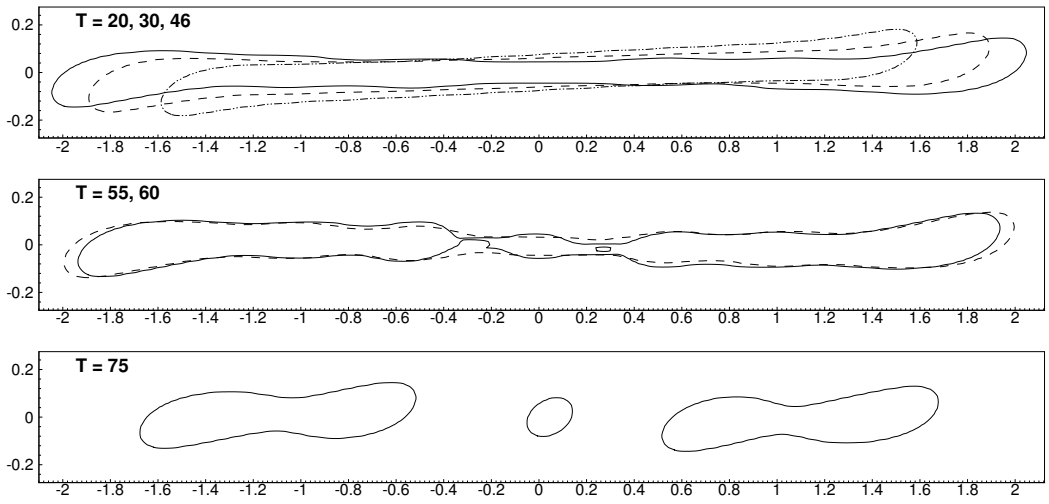

(b) $Ca = 0.47$, mesh $M4 - 385 \times 44 \times 100$, domain $24a \times 2.2a \times 12a$, $\Delta t = 5 \times 10^{-4}$

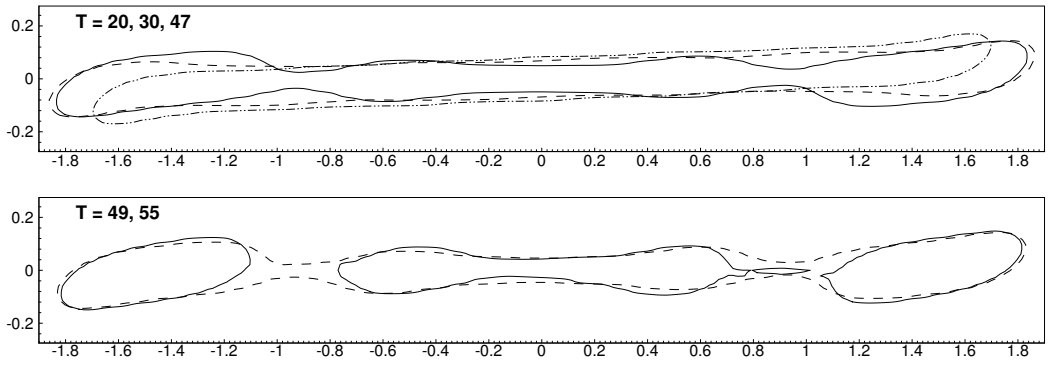

(c) $Ca = 0.5$, mesh $M2 - 240 \times 40 \times 85$, domain $20a \times 2.2a \times 12a$, $\Delta t = 1 \times 10^{-3}$

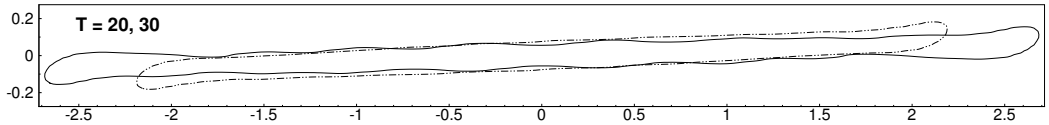

(d) $Ca = 0.6$, mesh $M2 - 340 \times 40 \times 85$, domain $28a \times 2.2a \times 12a$, $\Delta t = 1 \times 10^{-3}$

Figure 7.9: Deformation of a drop in a less viscous medium, $\lambda = 1.9$, at low Re and $\beta = 1.1$.

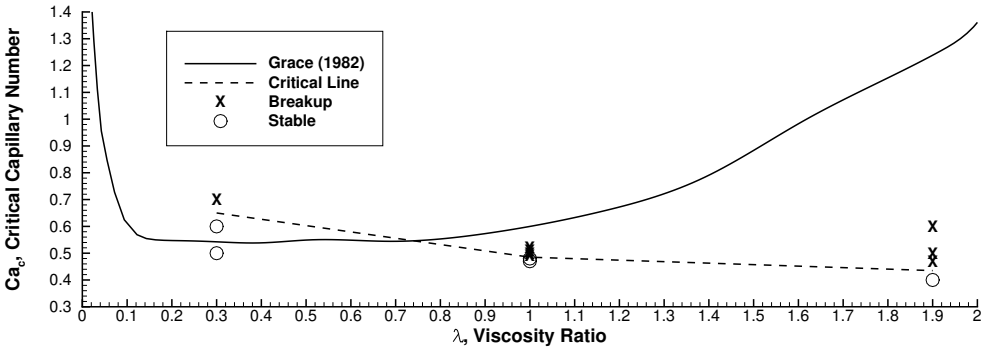

Figure 7.10: Effect of the viscosity ratio on the critical conditions.

The drop deformation is also analyzed and presented in Figure 7.11. The cases with stable and unstable drops show a similar behavior in L/a and D for different values of λ, where the main difference lies in the shift of Ca, as it can be observed. Because cases with breakup have an increasing Taylor deformation in time, it is expected that the critical capillary is smaller than the values reported.

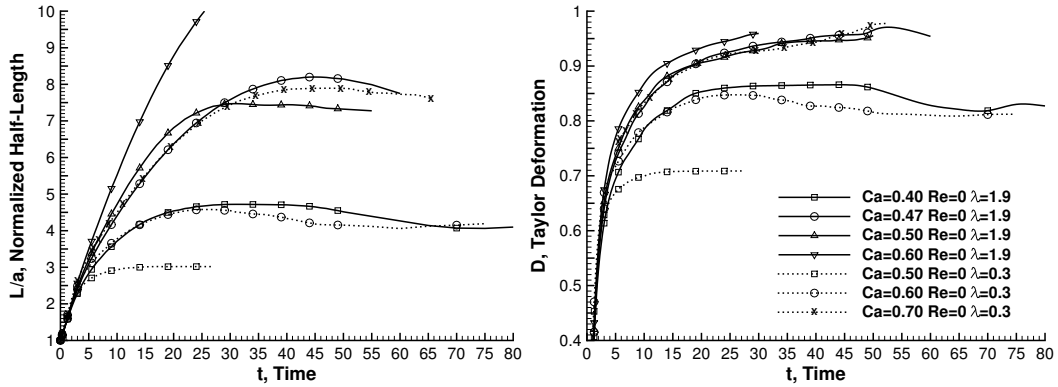

Figure 7.11: Half-length, L/a, and Taylor deformation, D, of a viscous drop under high confinement geometry, and non-uniform properties for $\lambda = 0.3$ ($\cdots\cdots$) and $\lambda = 1.9$ (——). Details of the simulations are presented in Figures 7.8 and 7.9.

7.1.2 Effect of Reynolds Number

The effect of inertia is now analyzed for Reynolds numbers, $Re = \rho_m \dot{\gamma} a^2/\eta_m$, 10 and 40. Strong-wall effect is considered for uniform properties, $\lambda = \gamma = 1$, clearance ratio $\beta = 1.1$, $L_z = 5a$ and $a = 0.25$. When inertia is present, the drop is expected to break at lower Ca. If the clearance ratio is reduced, then the walls stabilize the drop, allowing it to achieve higher values of Ca without breaking. The contours of the interface are presented in Figures 7.12-7.15 and 7.18, while the deformation is summarized in 7.16.

In the case of weak-wall effects and $Re = 10$, the drop breaks for $Ca \gtrsim 0.15$ (Li et al., 2000; Renardy et al., 2002). Breakup is now observed between $Ca_c = 0.35 - 0.40$ when the boundaries are brought closer to

the drop, as shown in Figures 7.12d and 7.13. This represents a $233 - 266\%$ increase in the critical capillary number. The effect of L_z is also verified at $Ca = 0.3$, as shown in Figures 7.12b and 7.12c. The maximum half-lengths are $L/a = 3.94$ for $L_z = 5a$ and $L/a = 3.71$ for $L_z = 12a$, representing a 6% difference. Recoiling end-pinching is observed for $Ca = 0.40$, where breakup occurs at $t = 79$ for a drop half-length $L/a = 7.88$.

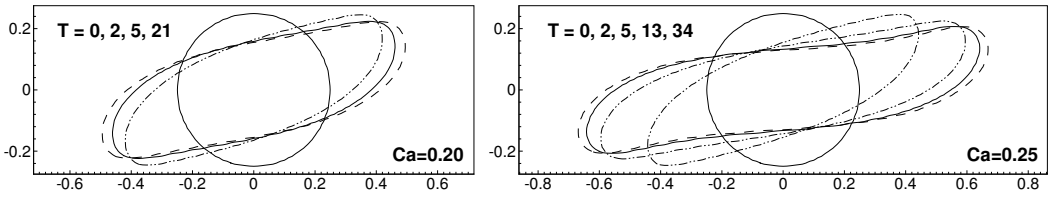

(a) $Ca = 0.20$ mesh $M3 - 300 \times 44 \times 100$, domain $18.4a \times 2.2a \times 5a$ and $Ca = 0.25$, mesh $M3 - 340 \times 44 \times 100$, domain $20a \times 2.2a \times 5a$

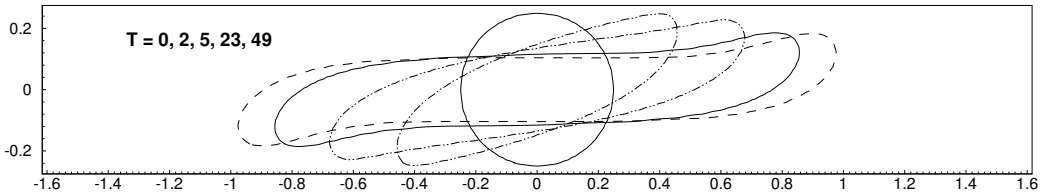

(b) $Ca = 0.30$, mesh $M3 - 340 \times 44 \times 100$, domain $20.8a \times 2.2a \times 5a$

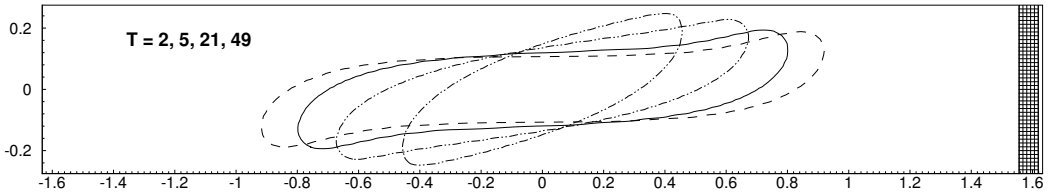

(c) $Ca = 0.30$, mesh $M4 - 325 \times 44 \times 100$, domain $20a \times 2.2a \times 12a$

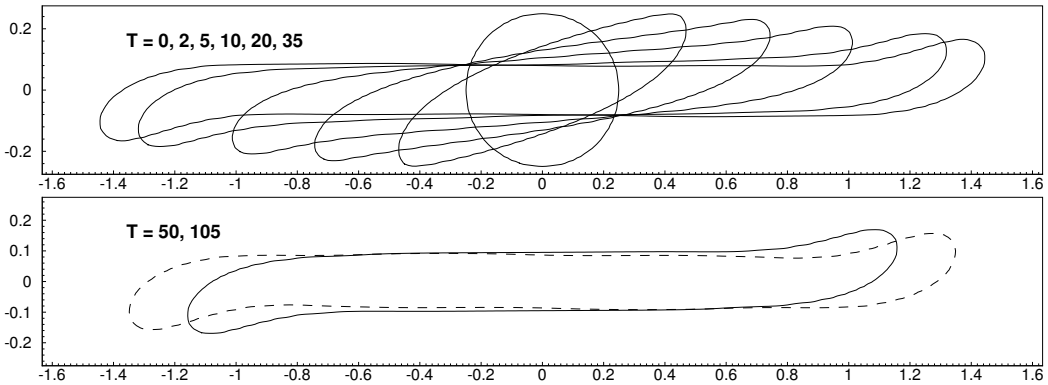

(d) $Ca = 0.35$, mesh $M3 - 340 \times 44 \times 100$, domain $20.8a \times 2.2a \times 5a$

Figure 7.12: Subcritical drop deformation with inertia. For $Re = 10$, $\lambda = 1$, $\beta = 1.1$, mesh resolution on the drop of $a/\Delta x = 20$ and $\Delta t = 10^{-3}$.

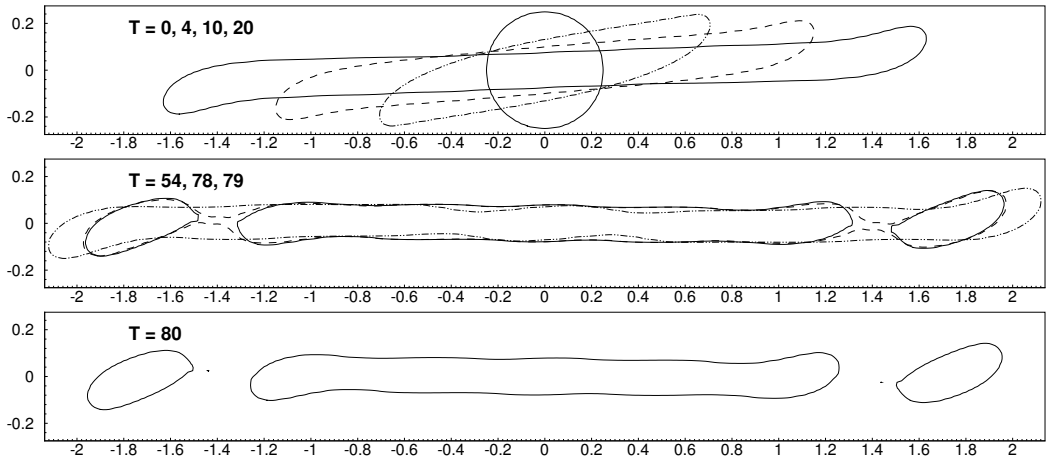

Figure 7.13: Supercritical drop deformation at $Re = 10$ and $Ca = 0.40$. For mesh $M3 - 400 \times 44 \times 100$ and domain $20a \times 2.2a \times 5a$. Continuation of Figure 7.12.

In the case of $Re = 40$, the drop breaks up at lower capillary numbers than $Re = 10$, as expected. Extensional end-pinching occurs at $Ca = 0.25$, for a drop half-length $L/a = 9.27$ and $t = 40$. Extensional end-pinching is also observed at $Ca = 0.20$, for $L/a = 6.54$ and $t = 63$. The critical condition lies in the range $Ca_c = 0.17 - 0.20$. In comparison to $Re = 0$ and $Re = 10$, the drop deformation is larger for any given value of Ca.

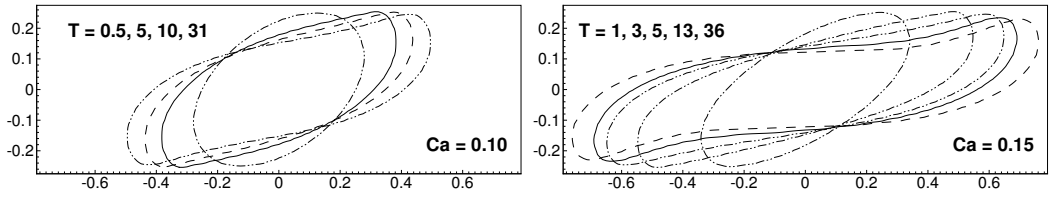

(a) $Ca = 0.10$ and $Ca = 0.15$, mesh $M3 - 300 \times 44 \times 100$, domain $18.4a \times 2.2a \times 5a$

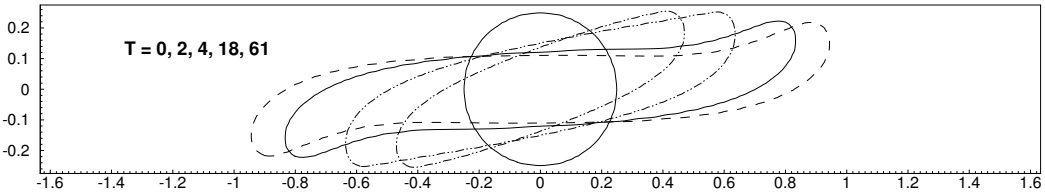

(b) $Ca = 0.17$, mesh $M3 - 400 \times 44 \times 100$, domain $24.5a \times 2.2a \times 5a$

Figure 7.14: Subcritical drop deformation with inertia. For $Re = 40$, $\lambda = 1$, $\beta = 1.1$, mesh resolution on the drop of $a/\Delta x = 20$ and $\Delta t = 10^{-3}$.

For $Re = 10$, the drop retracts after achieving its maximum deformation and then shows end-pinching without any considerable central constriction. Similarly as it is observed for $Re = 0$, near critical conditions showed decreasing L/a and D in time during breakup. In contrast, the cases simulated for $Re = 40$ only

show extensional end-pinching. This is better understood in terms of the drop half-length, as presented in Figure 7.16a, where L/a is shown to decrease for $Re = 10$ and to increase for $Re = 40$ in supercritical conditions. Similar solutions of L/a are observed for different Re in subcritical conditions, mainly shifted by Ca. An equivalent statement can be made for the Taylor deformation, but only with respect to the tendency because the initial behavior is different, as shown in Figure 7.16b.

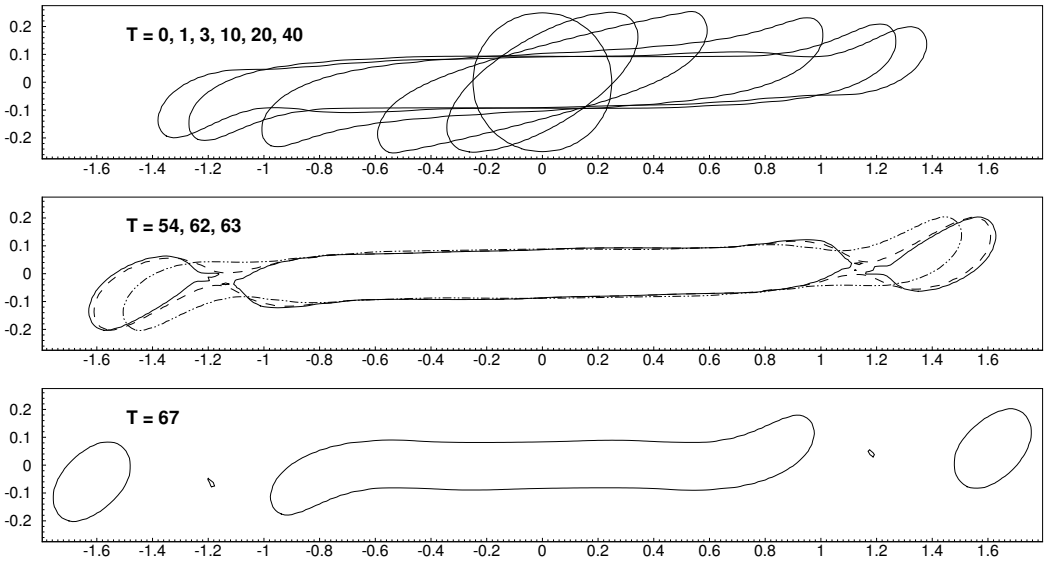

(a) $Ca = 0.20$, meshes $[340, 400] \times 44 \times 100$, domains $[20.8a, 24.5a] \times 2.2a \times 5a$

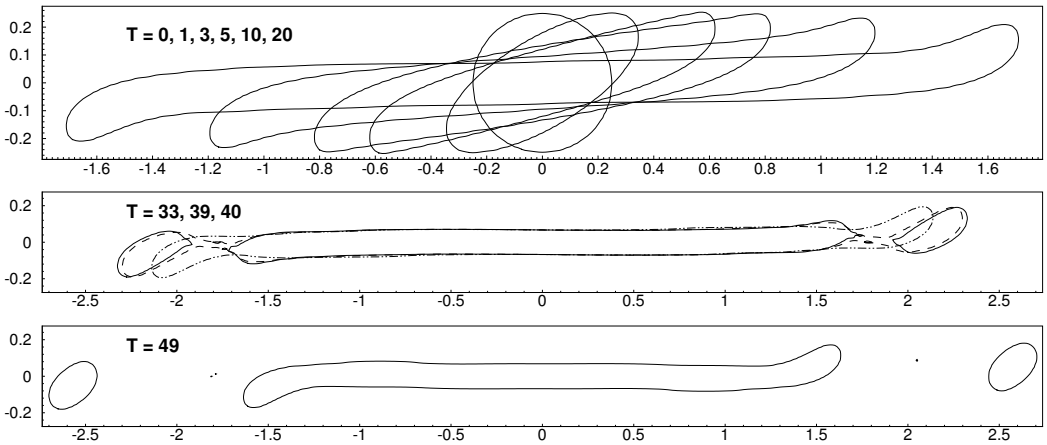

(b) $Ca = 0.25$, meshes $M3 - [300, 400, 500] \times 44 \times 100$, domains $[18.4a, 24.5a, 30.5a] \times 2.2a \times 5a$

Figure 7.15: Supercritical drop deformation at $Re = 40$. Continuation of Figure 7.14

In the case of $Re \gtrsim 40$, the drop manifests a second mode of oscillations in the transversal cross section. This behavior is well captured by the Taylor deformation, D, which is not monotonic during the drop-stretching phase, as show in Figure 7.16b. Because the drop half-length does not show oscillations, then

only the drop half-breadth varies. In this sense, the Taylor deformation can be defined in terms on the half-breadth in y or z. Instead, changes in the cross-sectional aspect ratio are analyzed in terms of the drop radius at $x = 0$ in the y and z directions, R_z/R_y. The interface contours in the transversal cross section and R_z/R_y against time are presented in Figure 7.17. As it can be observed, amplitude and phase increase with Ca. The first maximum amplitude is $(R_z/R_y)_1 = [1.47, 1.58, 1.66]$ and occurs at $t_1 = [1.61, 1.97, 2.02]$ for $Ca = [0.15, 0.20, 0.25]$, respectively. The second maximum amplitude, $(R_z/R_y)_2 = 1.08$, is similar for different values of Ca.

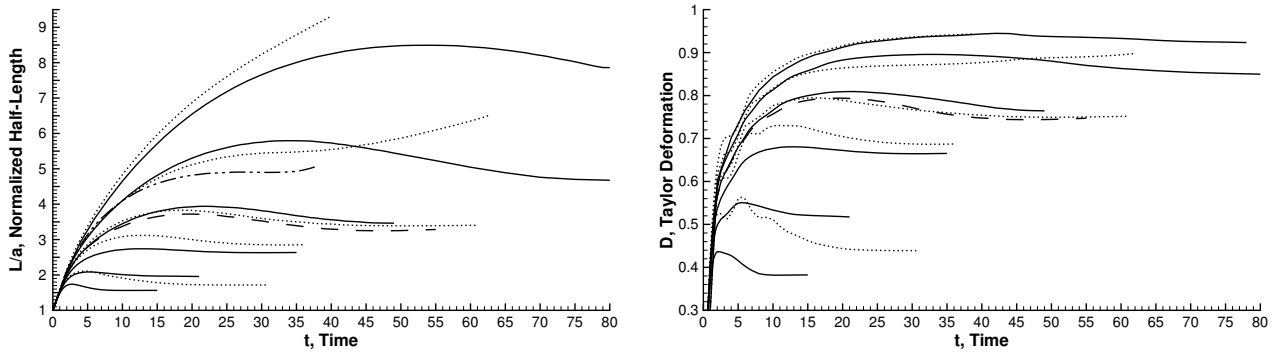

(a) Half-Length (b) Taylor Deformation

Figure 7.16: Half-length, L/a, and Taylor deformation, D, of a viscous drop under high confinement geometry, uniform properties, $\Delta t = 1 \times 10^{-3}$ and mesh resolution on the drop of $a/\Delta x = 20$. For $Re = 10$ and $L_z = 5a$: Ca =0.15, 0.20, 0.25, 0.30, 0.35, 0.40 (——). For $L_z = 12a$: $Ca = 0.30$ ($-\ -\ -$). For $Re = 40$ and $L_z = 5a$: $Ca = 0.10$, $Ca = 0.15$, $Ca = 0.17$, 0.20, 0.25($\cdots\cdots$). For $Re = 110$, $Ca = 0.1$ and $L_z = 5a$ ($-\ \cdot\ \cdot -$). Deformation increases with Ca.

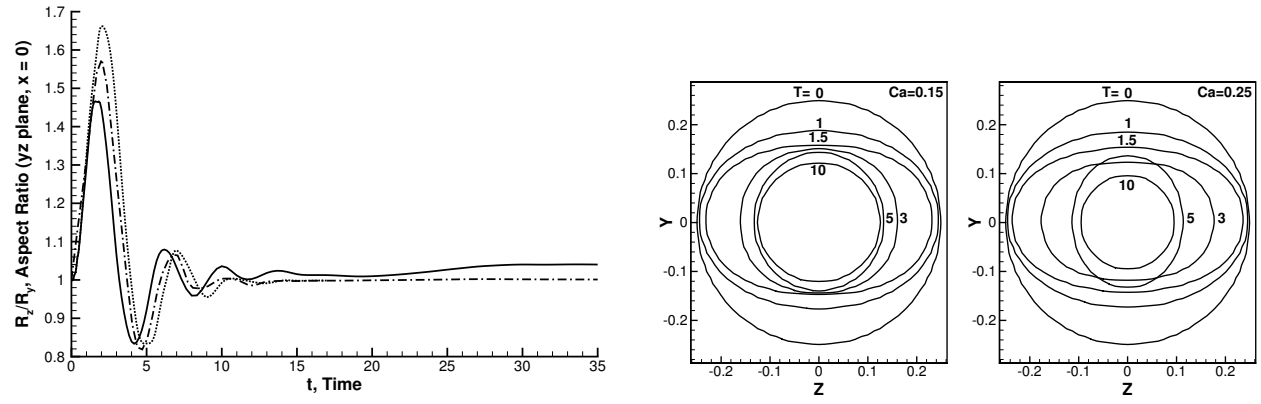

(a) Aspect ratio (b) Interface contours

Figure 7.17: Cross-sectional aspect ratio, R_z/R_y, at $x = 0$ (yz plane) and interface of a drop deforming in a confined simple shear flow at $Re = 40$, $\beta = 1.1$. For $Ca = 0.15$ (——), 0.20 ($-\ \cdot\ \cdot -$), 0.25 ($\cdots\cdots$).

Now, cases with $Re = 110$ are simulated. The first observation is that mesh resolutions like the ones used

for $Re = 40$ produce fictitious wall adhesion. The dynamics for this and larger Re is different because the interface migrates towards the wall, mostly due to the low pressures in the gap between the interface and the wall. Wall adhesion may be possible for wetting surfaces because of the proximity of the wall to the drop. However, a moving contact surface and the respective dynamic contact angle imposes further challenges that are not studied. This issue is partially solved by increasing the mesh resolution near the walls. In this manner, drops with relatively small Ca show recoiling instead of numerical tip-streaming. The type of mesh considered have uniform spacing near the drop in x, bilinear spacing in y and uniform spacing in z ($M5$). Cases with $Ca \leq 0.075$ are stable, while $Ca = 0.1$ shows extensional end-pinching breakup, as presented in Figure 7.18.

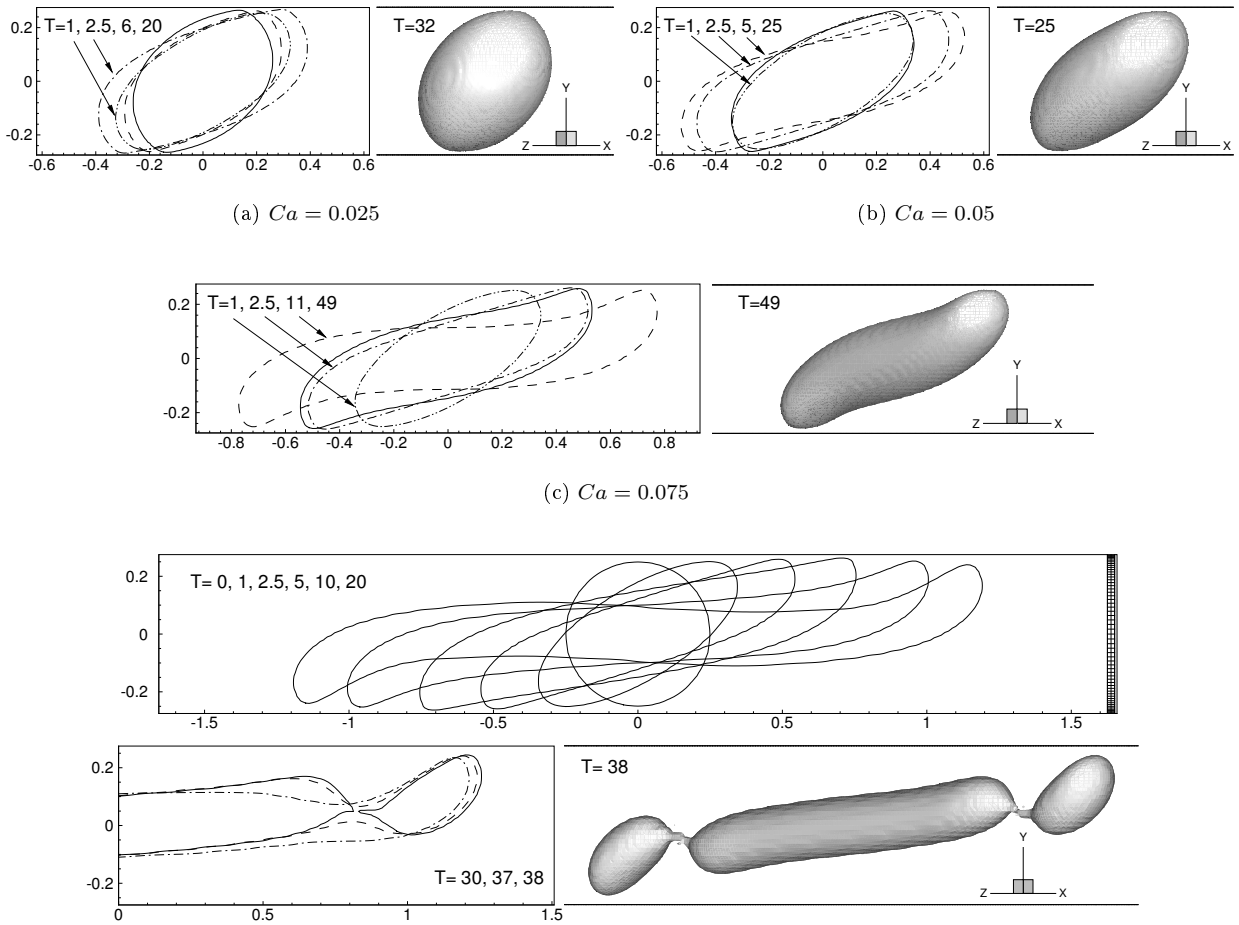

(a) $Ca = 0.025$

(b) $Ca = 0.05$

(c) $Ca = 0.075$

(d) $Ca = 0.1$

Figure 7.18: Drop deformation at $Re = 110$ and $\beta = 1.1$. a) Mesh $M5{-}240{\times}56{\times}100$, domain $11.5a{\times}2.2a{\times}5a$ $\left(\frac{a}{\Delta y}\right) = [15.8,\ 62]$, $\left(\frac{a}{\Delta x}\right) = 25$ b) mesh $M5 - 280 \times 56 \times 100$, domain $17.1a \times 2.2a \times 5a$ $\left(\frac{a}{\Delta y}\right) = [14.9,\ 86.9]$ $\left(\frac{a}{\Delta x}\right) = 20$ c) and d) mesh $M5 - 300 \times 56 \times 100$, domain $18.4a \times 2.2a \times 5a\left(\frac{a}{\Delta y}\right) = [14.6,\ 87.3]$ $\left(\frac{a}{\Delta x}\right) = 20$.

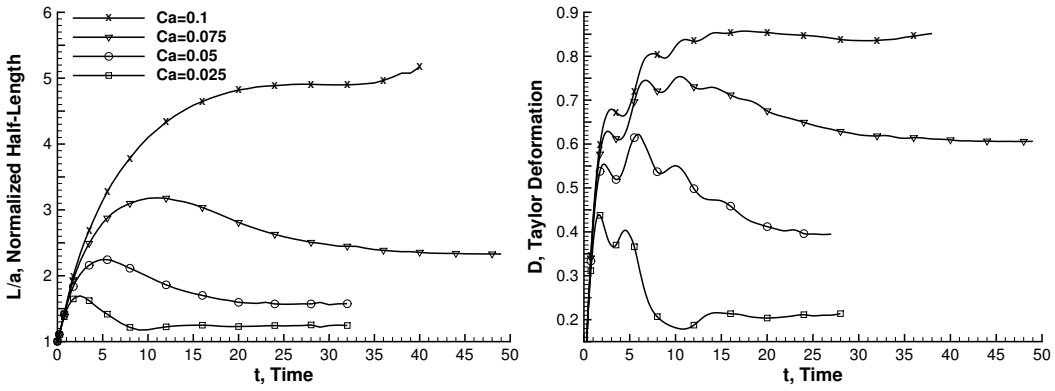

Figure 7.19: Half-length, L/a, and Taylor deformation, D, of a viscous drop under high confinement geometry, uniform properties, for $Re = 110$. Deformation increases with Ca. Details of the simulations are presented in Figure 7.18.

For $Re = 110$, the half-length is similar to the previous cases, but the Taylor deformation shows more oscillation than the $Re = 40$ case, as observed from Figure 7.19. For $Ca = 0.25$, D shows two maximums, while four maximums are noticeable for the remaining cases. Despite the oscillations, D increases in time for the case that breaks up, $Ca = 0.1$, which is characteristic of extensional end-pinching. The oscillations are expected in these cases because the modified or oscillatory Reynolds is considerably larger than 1, $Re_{\text{osc}} = \sqrt{\rho_d \sigma a}/\eta_d = 33 - 66$.

In the case of transversal oscillations at $Re = 110$, the amplitude of R_z/R_y and the time required to reach the first maximum increases with Ca. The first maximum aspect ratio is $(R_z/R_y)_1 = [1.24, 1.41, 1.63]$ at $t_1 = [1.16, 1.57, 1.85]$ for $Ca = [0.025, 0.05, 0.1]$, respectively. The second maximum is also similar in amplitude, ~ 1.26, but with a larger offset in time. The behavior of the aspect ratio at large times results in $R_z/R_y > 1$ for supercritical cases, while $R_z/R_y \lesssim 1$ for subcritical cases. These results are shown in Figure 7.20.

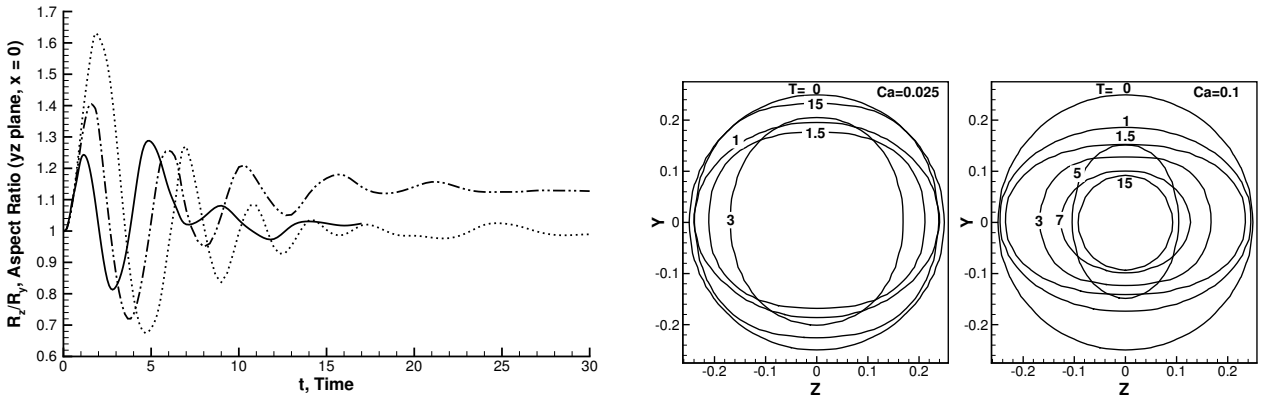

(a) Aspect ratio

(b) Interface contours

Figure 7.20: Cross-sectional aspect ratio, R_z/R_y, at $x = 0$ (yz plane) and interface of a drop deforming in a confined simple shear flow at $Re = 110$, $\beta = 1.1$. For $Ca = 0.025$ (——), 0.05 ($- \cdot - \cdot -$) and 0.1 ($\cdots\cdots$).

A final analysis is performed to determine the correlations between the maximum stable drop half-length, the flow parameters and the critical conditions. These results are summarized in Table 7.1 for power and exponential fittings, where the latter showed better agreement with the data. Because these relations are found for conditions near the critical point, the error increases for a given Re as $Ca \to 0$ and for supercritical conditions where the behavior is different. This information is also presented in Figure 7.21, where the critical line is included.

Table 7.1: Fitting of maximum drop half-length

Re	L_{max}/a (Power)	R^2	Error (%)	L_{max}/a (Exponential)	R^2	Error (%)	Ca
0	$1 + 79.0\,Ca^{3.47}$	0.9986	0.5	$1 + 0.173\,e^{7.46\,Ca}$	0.9991	0.3	0.45-0.48
10	$1 + 42.7\,Ca^{2.21}$	0.970	10	$1 + 0.169\,e^{9.49\,Ca}$	0.9972	1.9	0.15-0.35
40	$1 + 58.4\,Ca^{1.73}$	0.9938	2.9	$1 + 0.291\,e^{13.3\,Ca}$	0.9994	0.8	0.1-0.17
110	$1 + 29.2\,Ca^{1.02}$	0.982	5	$1 + 0.393\,e^{22.9\,Ca}$	0.9998	0.6	0.025-0.075

The maximum critical half-length grows linearly with respect to Ca_c for small Re, while it tends to asymptote as Re increases,

$$L_{max}/a \approx \begin{cases} 10.93\,Ca_c + 1.97 & \text{for } Re \leq 40 \\ 5.94\,Ca_c^2 + 6.86\,Ca_c + 2.59 & \text{for } Re \leq 110 \end{cases} \tag{7.1}$$

while it decreases with Re_c as,

$$L_{max}/a \approx 7.31 e^{-\frac{1.085\, Re_c}{Re_c + 30.96}} \tag{7.2}$$

with an error $< 3.5\%$ with respect to the data and within $2 - 20\%$ due to the grid resolution and range of Ca employed. The half-length shows an asymptotic behavior for large Re, meanwhile Ca_c decreases with Re, as presented in Figure 7.22. The relation between Re_c and Ca_c can be obtained by solving Equations (7.1) and (7.2). Larger Re are required to determine the trend of Ca_c with certainty.

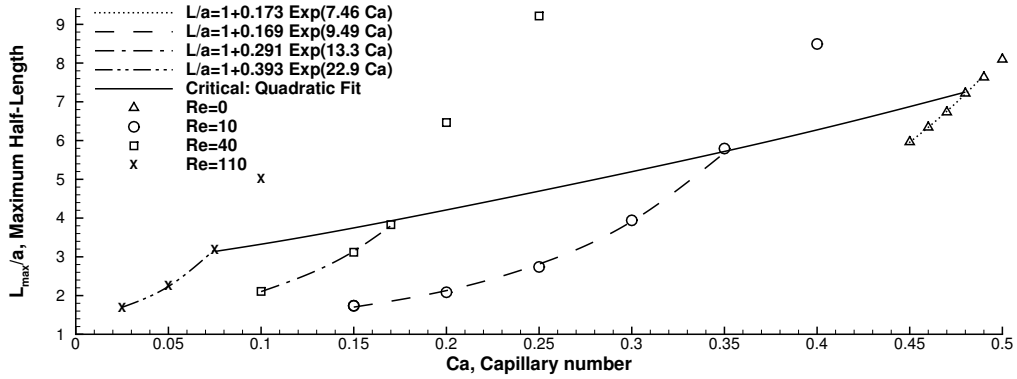

Figure 7.21: Maximum drop half-length as a function of Ca for different Re. The fitting is based on subcritical data. For supercritical cases, the maximum half-length before rupture is presented. The critical line connects the cases with the highest subcritical Ca simulated.

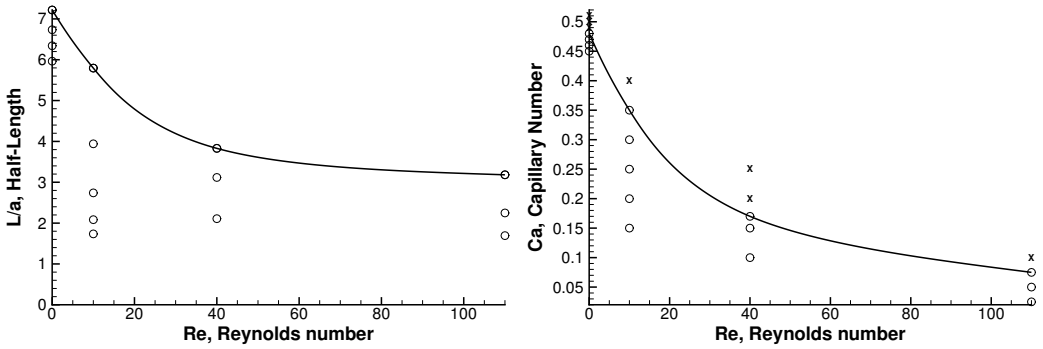

Figure 7.22: Critical conditions in terms of drop half-length, Re and Ca separating stable drops ($\circ$) from unstable drops ($\times$).

7.1.3 Viscoelasticity

The effect of viscoelasticity on the drop is to reduce the deformation for $De \lesssim 1$, and to increase it for $De \sim 3$, when $Ca = 0.3$ Mukherjee and Sarkar (2009). It is observed that viscoelasticity induce complex flow and overshoots with oscillatory behavior. Furthermore, the second normal stress N_2 was predicted to be an stabilizing agent against droplet breakup, since highly stable strings resembling a dumbbell can be

formed (Guido, 2011). Considering the limitation in mesh resolution required to simulate viscoelastic flows and the amount of publications in this field, this problem was not addressed.

7.1.4 Conclusions

For uniform properties, the critical capillary increases from the unconfined case, and it increases even more if the symmetric boundary conditions or the mixed inlet/outlet boundaries are brought closer to the drop. This allows for a drop to be fully stable at capillary numbers as high as 0.49. When the drop is more viscous than the medium, the critical capillary number remains similar to the uniform case. However, different types of daughter drops are observed. When the medium is more viscous, the drop is considerably stable and requires large capillary numbers to induce breakup.

Increasing inertia also increases the deformation for a given capillary number, but the drop is more stable than the unconfined cases because the critical capillary number is now larger. Inertia also produces traversal oscillations. The maximum drop half-length increases exponentially in terms of Ca near critical conditions for a constant Re, while it may asymptote for large Re. In the case of Ca_c, it decreases monotonically with increasing Re.

7.2 Drop-rigid-particle Interaction in Simple Shear Flows

The previous results leads to the observation that drops subject to simple shear flows under low Re and Ca do not break up, and the addition of closer walls increase the stability. In order to bring in another disruptive element, rigid particles are included into the domain.

Two rigid spheres and an initially spherical drop are simulated under different flow and geometric conditions to analyze different flow phenomena. In the absence of particles, certain conditions of several parameters (Re, Ca, G, λ, κ) are needed to produce drop breakup. Now, two rigid particles are included to understand their effect on the drop and find critical conditions where the drop is being punctured. The study focuses on Stokes flow, $Re \ll 1$, to moderate Re, and low Ca flow, also called weak flow limit, $Ca \ll 1$. For a constant Ca, increasing Re enhances the deformation and produces drop breakup, but for low Ca, the drop is stable. Therefore, to produce a disruption on a stable drop, external forces are necessary. To enforce the hypothesis that breakup is possible at low Ca, the case of a single drop in confinement has shown to decrease critical capillary number, Ca_{crit}, as the obstruction increase when the drop is more viscous than the medium, $\lambda > 1$Minale (2008), shown in figure 2.1-b, and shown in the previous section for $\lambda = 1.9$ where $0.4 < Ca_{crti} < 0.5$.

A dimensional analysis of this problem reduces to a correlation of the following properties:

$$Breakup = f(x_p,\, y_p,\, R_p,\, R_d,\, \rho_p,\, \rho_m,\, \rho_d,\, \eta_m,\, \eta_d,\, \sigma,\, \dot{\gamma},\, H)$$

where ρ_p, x_p, y_p, R_p are the particle density, coordinates and radius; R_d, ρ_d, η_d are the drop density, viscosity and radius; ρ_m, η_m are the medium density and viscosity; $\dot{\gamma}$ is the shear strain-rate; and H is the separation of the plates. In order to compare with previous results, this problem is studied in terms of the flow parameters: $Re = \frac{\rho_m \dot{\gamma} R_d^2}{\eta_m}$, capillary number $Ca = \frac{We}{Re} = \frac{\eta_m \dot{\gamma} a}{\sigma}$.

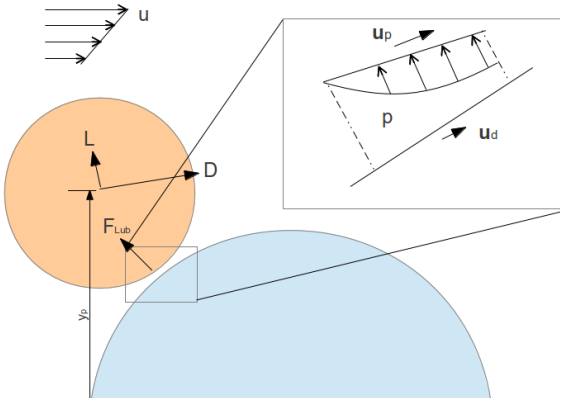

Figure 7.23: Schematic of the problem.

The problem is depicted in figure 7.23 where the relevant forces acting on the sphere are shown. The flow will induce drag, lift and torque on the particles, but as the gap between the particle and the drop reduces, a lubrication force will also be present. As the particles approach each other, the pressure in the gap increases due to lubrication effects. While the drop deforms and adopts the final shape, which might be quasi-spherical for low Ca, the vertical force exerted on the rigid particles is responsible for their deviation and distancing from each other. The location of the particles has an important role because when the vertical distance is large enough, the shearing effect on the drop is minimized, but higher velocities and gradients could be present, and when the vertical distance is small, the particles go in collisional trajectory and could puncture the drop. For the former case, breakup could happen due to enhanced shearing stresses, normally for moderate Re, while for the later, the drop is disrupted and punctured. For this reason, the objective is to minimize the vertical acceleration of the rigid particles and enforce a horizontal path, in order to reproduce the later case, which is one way of producing breakup at low Ca and low Re without using self-propelled particles.

A particle could be capable of distorting the shape of the drop if the pressure in the gap increases to the order of $\sim \kappa\sigma$. At later stages in the deformation process, the drop adopts a concave shape with negative curvature that produces minimal lubrication force, and another region with highly positive curvature that produce a restoring force. Therefore, the critical condition is at the beginning of the motion when the curvature is positive everywhere. In that sense, disruption could be induced if the vertical deviation of the particles is minimized at the initial stages. A simplified balance of forces on the particle gives the following,

$$m_p \mathbf{a} = \mathbf{D}_{no-drop} + \mathbf{L}_{no-drop} + \mathbf{F}_{lub}$$

The time scale is selected as $t_s = (R_d + R_p)/U$, that is, the approximate time required by a particle to reach the center of the drop. The vertical acceleration is considered to be proportional to the horizontal, $a_y \propto U/t_s$. The maximum lubrication pressure over the sphere should be larger than the capillary force responsible of keeping the shape of the drop, $F_{y\,lub} \propto R_p^2 \kappa\sigma$ and $\kappa \sim \frac{2}{R_d}$. Considering that external viscous effects are favorable, this problem can be analyzed using the particle Weber number,

$$We_p = \frac{\rho_p R_P R_d \left(\dot{\gamma} y_o\right)^2}{\sigma \left(R_d + R_p\right)} \tag{7.3}$$

where y_o is the initial vertical distance of the particle as seen from the drop. For very large values of We_p one can expect breakup or disruption.

Another parameter that was found to correlate better with the deformation is the Laplace number,

$$La = \frac{Re}{Ca} = \frac{\frac{\rho_p(\dot{\gamma} y_o) R_P}{\eta}}{\frac{\eta(\dot{\gamma} R_d)}{\sigma}} = \frac{\rho_p \sigma R_p y_o}{\eta^2 R_d} \tag{7.4}$$

It is also of practical to use the Stokes number, defined here as,

$$Stk = \frac{m_p U}{3\pi d_p R_p \eta} = \frac{1}{18} \frac{\rho_p \dot{\gamma} R_p^2}{\eta} \tag{7.5}$$

Depending on the trajectory of the particles and the deformation of the drop, the phenomena can be classified as follows:

- Small drop deformation (negligible effect of the particles).
- Large drop deformation.
  - Drop disruption during the extensional phase (no collision).
- Critical drop deformation (puncturing)
  - Drop disruption during the extensional phase (particle-particle touching).
- Supercritical drop deformation (particle-particle collision)
  - Drop disruption after particle-particle bouncing.

Considering the large amount of simulations required to study all the cases, this research focuses on finding those flow conditions and quantities that enhance large deformations and possible puncturing, with emphasis in low Ca regimes. Determining the mechanisms of the phenomena are also of interest because they allow for a better understanding and classification of the problem. The principal parameter for this study is the dimensionless particle-particle distance, defined as,

$$L_{12} = \|\mathbf{X}_2 - \mathbf{X}_1\| / (2R_p) \tag{7.6}$$

The deformation of the drop can also be quantified in terms of the aspect ratio, the Taylor deformation, the half-length, or half-breadth. However, the particle-particle distance L_{12} is used because it allows for an easy way to determine the critical point, which is when there is collision. Another parameter of relevance is the time to achieve the minimum particle-particle distance, denoted by $t*$. Time is normalized by $t*$ instead of the capillary time for convenience with $L_{12,\min}$.

7.2.1 Uniform properties

In this section, the effects of varying Re and Ca are analyzed under uniform conditions: unity viscosity and density ratios, $\gamma_d = \gamma_p = \lambda = 1$, and unity radius ratio, $R_p/R_d = 1$, where the subindexes d and p stand for drop or rigid particle properties, respectively. The domain is a parallelepiped of size $(10 \times 8 \times 2.5)R_d$. The initial conditions are set to zero velocity and zero pressure. The left and right boundaries (mixed inlet/outlet regions) are prescribed with zero pressure and normal velocities, the top and bottom walls are prescribed with speed U and symmetry is applied at the front and back boundaries. The collision and lubrication models are employed with $\epsilon = 0$ and $\epsilon_l = 2/3\Delta x$. The location of the rigid particles has an important effect on the deformation of the drop. For instance, as the particles get closer to the centerline, their relative velocity reduces, but the projected region for collision increases. In the limit, no shearing due to the particles takes place because they only rotate. However, particles that are closer to the centerline can also return before passing by. For each combination of Ca and Re, there is an optimal location for maximum drop deformation. In this section, the location of the particles is fixed to $|X\,(t=0)| = R_d + R_p$, $|Y\,(t=0)| = 0.8R_d$. Considering the large amount of parameters, this section focuses on the overall effect of the fluid properties on the drop deformation when the plates are suddenly started.

Table 7.2: Particle-particle minimum properties and parameters in uniform conditions

Case	$\frac{R_d}{\Delta x}$	η	ρ_d	ρ_p	$\dot{\gamma}$	σ	$R_d(R_p)$	Re	Ca	$\frac{(x_o,y_o)}{R_d}$	We_p	La	Stk	$L_{12,\min}$	$t*$
I-1	15.6	1	1	1	1	10	1	1	0.1	$(2, 0.8)$	0.1	10	0.06	1.543	4.04
I-2	15.6	1	1	1	1	4	1	1	0.25	$(2, 0.8)$	0.25	4	0.06	1.342	4.27
I-3	15.6	1	1	1	1	2	1	1	0.5	$(2, 0.8)$	0.5	2	0.06	1.204	4.43
I-4	15.6	1	1	1	1	1	1	1	1	$(2, 0.8)$	1	1	0.06	1.110	4.57
I-5	15.6	1	1	1	1	0.5	1	1	2	$(2, 0.8)$	2	0.5	0.06	1.064	4.69
II-1	11.6	0.1	1	1	100	10	0.1	10	0.1	$(2, 0.8)$	1	100	0.56	1.615	0.146
II-2	11.6	0.1	1	1	100	4	0.1	10	0.25	$(2, 0.8)$	2.5	40	0.56	1.417	0.152
II-3	11.6	0.1	1	1	100	2	0.1	10	0.5	$(2, 0.8)$	5	20	0.56	1.269	0.156
II-4	11.6	0.1	1	1	100	1	0.1	10	1	$(2, 0.8)$	10	10	0.56	1.147	0.159
II-5	11.6	0.1	1	1	100	0.5	0.1	10	2	$(2, 0.8)$	20	5	0.56	1.062	0.166
III-1	15.6	0.02	1	1	100	2	0.1	50	0.1	$(2, 0.8)$	5	500	2.8	1.673	0.452
III-2	15.6	0.02	1	1	100	0.8	0.1	50	0.25	$(2, 0.8)$	25	200	2.8	1.484	0.461
III-3	15.6	0.02	1	1	100	0.4	0.1	50	0.5	$(2, 0.8)$	25	100	2.8	1.344	0.468
III-4	11.6	0.02	1	1	100	0.2	0.1	50	1	$(2, 0.8)$	50	50	2.8	1.219	0.476
III-4	11.6	0.02	1	1	100	0.1	0.1	50	2	$(2, 0.8)$	100	25	2.8	1.116	0.484

From previous results, it is expected that a domain of size $L_z > 8a$ has a minimal effect on the results. By lowering L_z to $4a$, the drop deformation may increase due to the presence of closer boundaries, but it may also speed up the dynamics. These effects may seem to affect the solution, but this domain is chosen because it reduces the computational cost. Additionally, because finite Re are considered, symmetries are avoided to allow for unsymmetrical solutions if it is the case.

A relevant parameter to measure the deformation of the drop is the particle-particle distance. Values closer to the rugosity threshold, ϵ, imply strong effects of lubrication forces and large deformations, meanwhile relatively large values are indicative of minimal to no effect on the drop. Collision takes places when the particle-particle distance is smaller than ϵ.

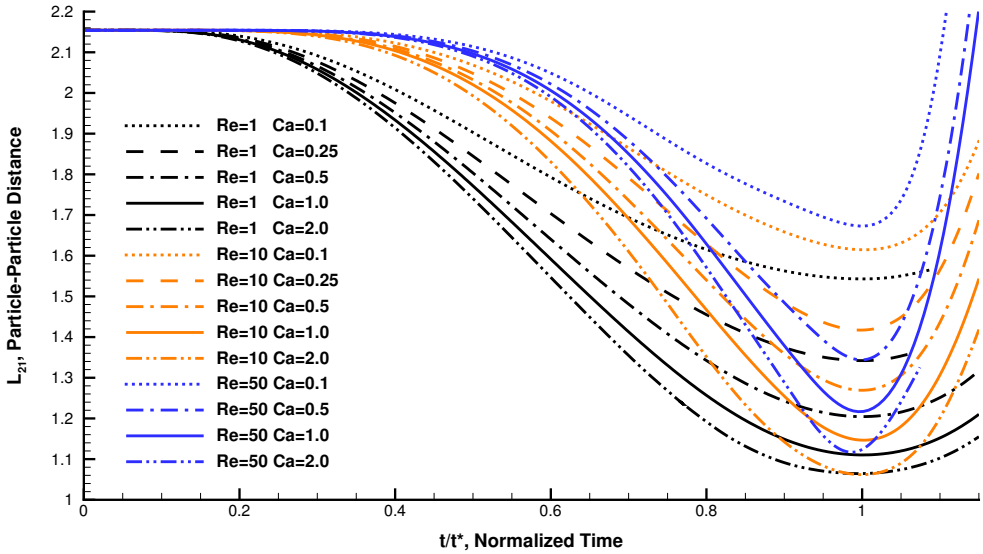

Figure 7.24: Particle-particle distance L_{12}: Effect of Re and Ca.

The degree of resolution of $L_{12,\,\mathrm{min}}$ depends on the mesh refinement in the sense that a coarse meshes produce larger $L_{12,\mathrm{min}}$ than a finer meshes when $L_{12} \sim 1$. For the typical mesh resolutions $R_d/\Delta x =$ (6.66, 8, 11.6, 15.6), the lowest L_{12} that can be resolved are $L_{12,\mathrm{R}} = \frac{2R_p+2\sqrt{2}\Delta x}{2R_p} =$ (1.21, 1.18, 1.12, 1.09), respectively. The $2\sqrt{2}$ factor comes from the fact that the error of the lubrication force is large when the interfaces between two particles are within two cells of distance, one cell per particle, while the $\sqrt{2}$ comes from the typical diagonal approach. In this way, $L_{12,\mathrm{R}}$ is a conservative estimation of the error incurred for a given mesh resolution. Any case with $L_{12,\mathrm{min}}$ below these thresholds implies a large deformation of the drop and possibly puncturing. The finest mesh would be preferred, but the computational times are in the order of several weeks to months, which sets an upper barrier in the waiting times. Another parameter that can be of relevance is the minimum distance where collision or lubrication models are activated, but because $\epsilon = 0$, only the latter is defined: $L_{12,\mathrm{L}} = \frac{2R_p+2/3\Delta x}{2R_p} =$ (1.05, 1.04, 1.03, 1.02).

A summary of the properties and cases is presented in Table 7.2. The effects of three Reynolds numbers, 1, 10 and 50, and several capillary numbers are explored, and conclusions are derived from the comparison of $L_{12,\mathrm{min}}$ among different cases. As it can be observed, the most important effect on the drop deformation is due to variations in Ca. For small Ca, drop deformation is small and $L_{12,\mathrm{min}}$ tends to be large, which implies that the effect of the rigid particles is minimal. Drop deformation also decreases slightly by increasing

Re. If Ca is now increased, the deformation increases considerable until the point that the drop behaves like the surrounding fluid ($Ca \gtrsim 1$). Relevance is given to estimating the critical capillary Ca_{Cr} for a given Re where the drop punctures. The critical conditions are determined from $L_{12,\mathrm{R}}$ and the correlation between $L_{12,\min}$ and Ca. This is presented at the end of this section. The rest of this section is dedicated to analyze the results. It is also important to note that $L_{12,\min}$ does not correlate well with We_p, La or Stk numbers. For that reason, the analysis based on Re and Ca of previous sections will be repeated. Nevertheless, flows with low values of La and Stk numbers produce larger drop deformations.

The results presented do not show particle-particle elastic collisions, which are given by $L_{12,\min} \leq 1+\frac{\epsilon}{2R_p}$, mostly because $\epsilon = 0$ and $L_{12,\min} > 1$ for the cases simulated. The evolution of L_{12} is presented in Figure 7.24, from which $L_{12,\min}$ is extracted. Also, constant $L_{12,\min}$ lines are shown in a plot of Re vs Ca in Figure 7.25, from which it is evident that large Ca are required to produce drop puncturing and particle collisions, while cases with low Ca exhibit large particle-particle distances. This impose an important limitation on drop disruption for cases where Ca is even smaller than 0.1 because external forces may be required.

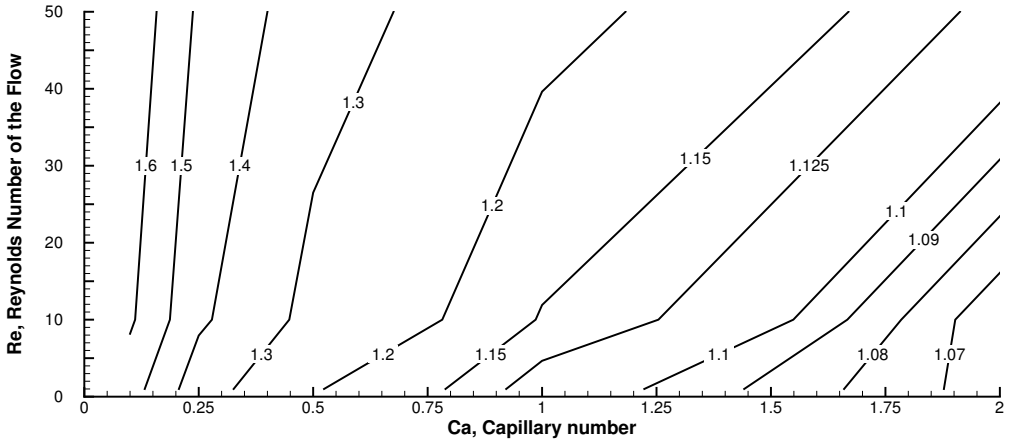

Figure 7.25: Effect of Re and Ca on the minimum normalized particle-particle distance, $L_{12,\min}$.

The cases with $Re = 1$ showed the lowest values of the particle-particle distance. For $Ca = 0.1$, the drop recovers from shearing and particulate effects, achieving $L_{12,\min} = 1.54$ at $t = 4.04$, which is about 5% and 8% lower than the value at $Re = 10$ and $Re = 50$, respectively. That difference decreases for larger values of Ca. At $Ca = 2$, $Re = 1$ shows a slightly lower value of $L_{12,\min}$ than $Re = 10$, which can be attributed to the difference in mesh resolution. This suggests that finer mesh resolutions increase the values of L_{12} due to a larger lubrication force. Several mechanism are observed during the deformation and are discussed for $Re = 10$ given the similarities with $Re = 1$.

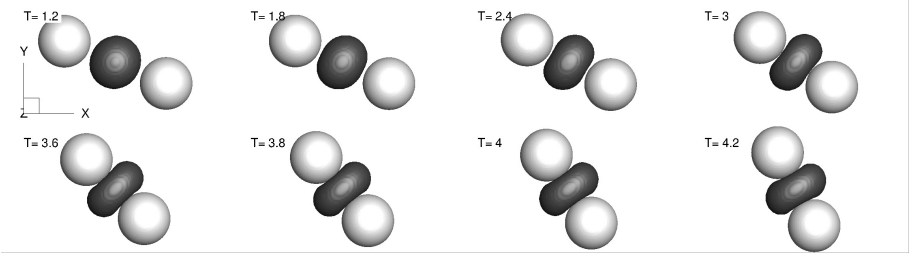

(a) $Ca = 0.1$

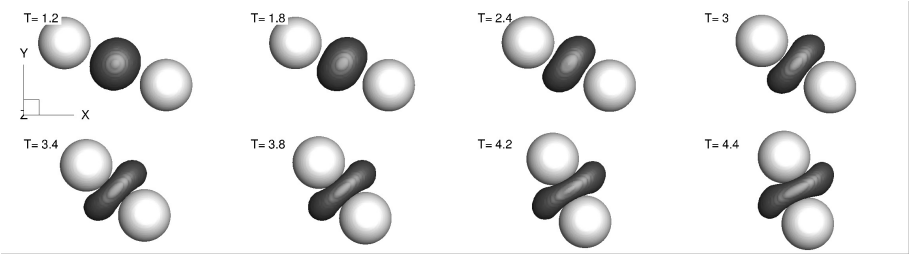

(b) $Ca = 0.25$

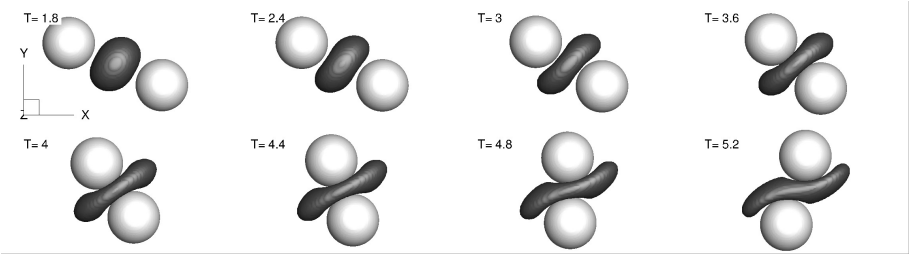

(c) $Ca = 0.5$

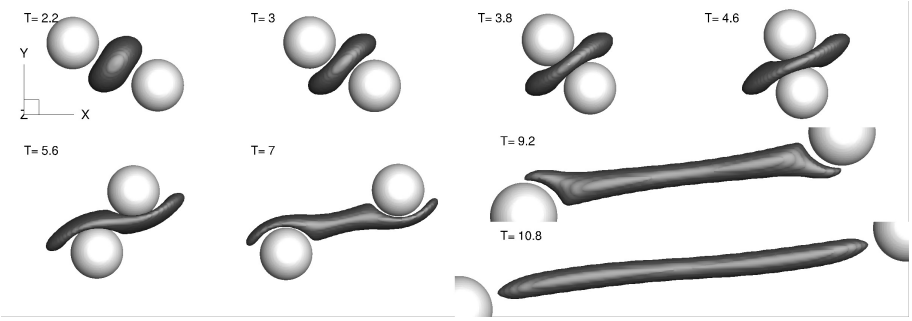

(d) $Ca = 1$

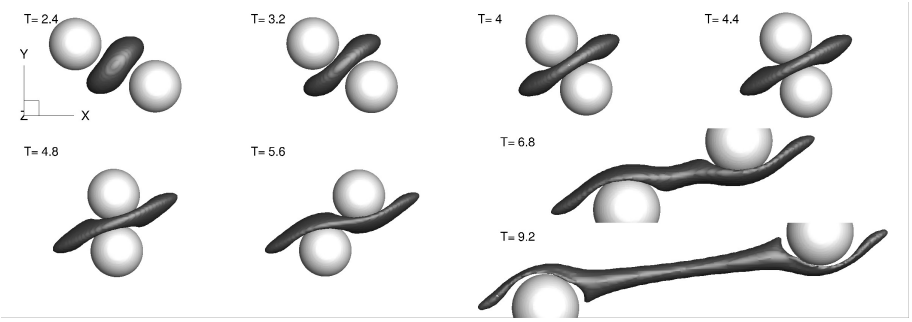

(e) $Ca = 2$

Figure 7.26: Particulate shearing of a drop, $Re = 1$.

The results for $Re = 10$ show less deformation than the equivalent cases at $Re = 1$ after comparing the values of $L_{12\,\mathrm{min}}$ in Table 7.2, or from the 3D representation presented in Figures 7.26 and 7.27. Similarly as the case of $Re = 1$, drop deformation increases with Ca. An analysis for $Re = 10$ is the following:

- For $Ca = 0.1$, the particles produce a biconcave shape on the drop, but such deformation is minimal as noted that the particle-particle distance is large enough, $L_{12\,\mathrm{min}} = 1.6$. After the passing of the particles, the drop recoils to the spheroidal stable shape. The mechanisms observed are as follows: (I) particle approaching, (II) drop-hollowing, (III) tumbling, (IV) drop stretching (V) drop recoiling.

- The deformation is slightly larger for $Ca = 0.25$, since $L_{12\,\mathrm{min}} = 1.4$, but another mechanism is observed: drop spooning and saddling-up. In the former mechanism, the stretching of the drop produce a spoon-shaped region, which is barely noted in this case. For the latter mechanism, the particles are separating from each other while the drop adopts a saddle shape, as observed at $t = 0.18$. In this case the mechanism are then: (I) particle approaching (II) drop-hollowing (III) slight-spooning (IV) saddling-up (V) stretching (VI) recoiling.

- For $Ca = 0.5$, the deformation during the particle-attraction phase is more pronounced, as noted by a reduction in the particle distance to $L_{12\,\mathrm{min}} = 1.27$ at $t = 0.15$. The particle separation phase shows important deformation as well: (III) spooning, $t = 0.17$, (IV) saddling-up, $t = 0.19$ and (V) relevant stretching, $t > 0.21$. The saddle shape is formed due to the rotation of the particles.

- The deformation is even more relevant for $Ca = 1$, as observed from $L_{12\,\mathrm{min}} = 1.15$ at $t = 0.16$ (close to puncturing). This case presents the same mechanisms of $Ca = 0.5$, but the spooning phase is more evident, $t = 0.18 - 0.2$, while the saddling-up phase is accompanied by filamentation, $t = 0.22$. Then, the tip of the drop recovers from the saddle shape while it keeps stretching. The drop is expected to break up for this case, but the simulation was stopped before. Then, a final mechanism should be present: (VI) breakup.

- For $Ca = 2$, the particles produce a hollow in the deformed drop at $t = 0.18$ given that $L_{12\,\mathrm{min}} = 1.06$. For later times, a large filament is formed due to the persistent spooning phase. Because surface-tension forces are considerably less important, the spoon-shaped region remains in time long enough for the production of a large filament. This filament then shows necking at the end of the filament and numerical surface tension in the spoon-shaped region. The mechanism of the deformation are as follows: (I) particle approaching, (II) drop hollowing, (III) drop puncturing, (IV) drop spooning, (V) spooning with filamentation and (VI) drop fragmentation.

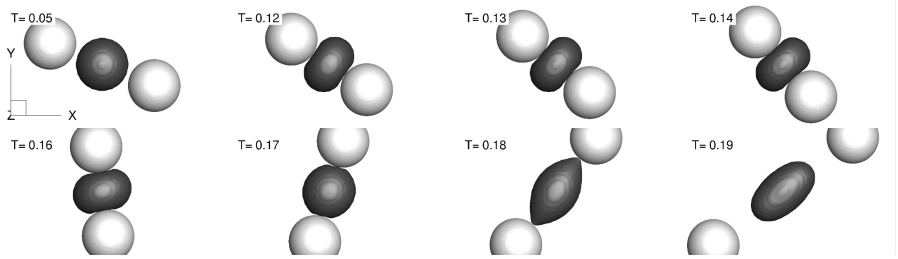

(a) $Ca = 0.1$

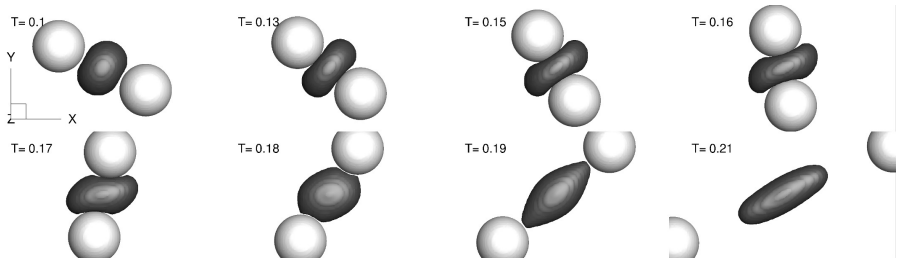

(b) $Ca = 0.25$

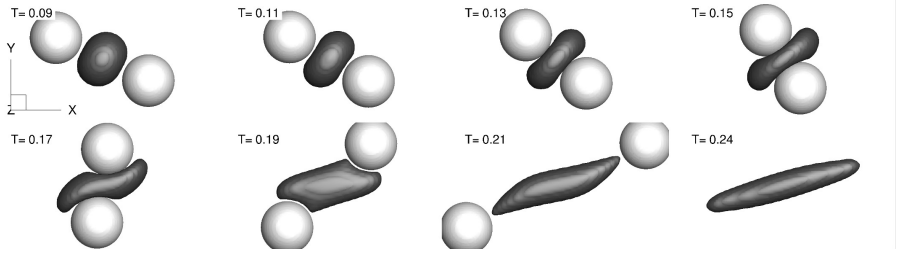

(c) $Ca = 0.5$

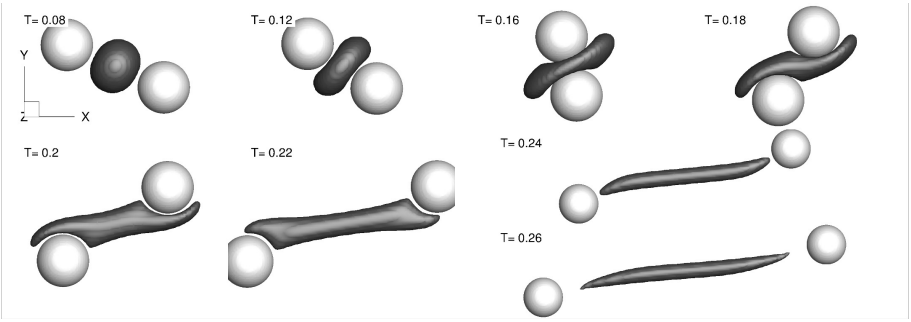

(d) $Ca = 1.0$

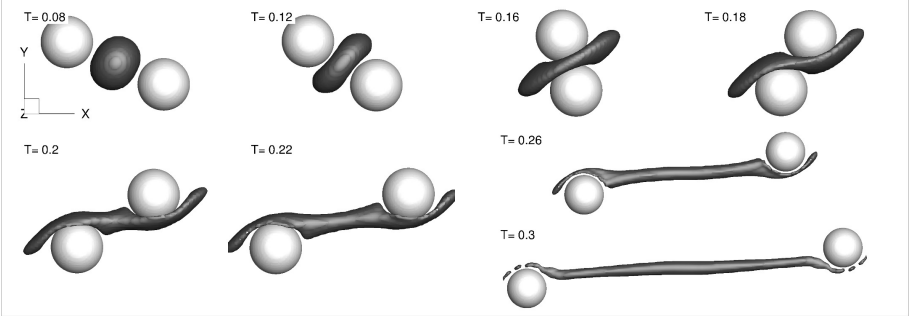

(e) $Ca = 2.0$

Figure 7.27: $Re = 10$

The cases with $Re = 50$ are presented in Figure 7.28 and Table 7.2. This case is similar to $Re = 10$, but because Re is larger, the deformation enhances near the tip of the drop. An analysis for $Re = 50$ is the following:

- For $Ca = 0.1$, the drop deformation is small, as noted by a minimum particle-particle distance of $L_{12\,\mathrm{min}} = 1.67$. The mechanism seems to be dominated by tumbling, but it can still be categorized as (I) approaching, (II) tumbling with hollowing and stretching and (III) recoiling.

- For $Ca = 0.25$, the minimum particle-particle distance is $L_{12\,\mathrm{min}} = 1.48$. The drop deformation is different because the tips of the drop are sharper than what it is observed with lower values of Re. The mechanisms are similar to $Ca = 0.1$.

- For $Ca = 0.5$, the minimum particle-particle distance is $L_{12\,\mathrm{min}} = 1.34$, considerably larger than the cases with lower Re. The mechanisms observed are (I) particle-particle approaching, (II) drop hollowing, (III) drop hollowing with tumbling (IV) saddling, (V) tip-sharpening and (VI) recoiling.

- For $Ca = 1$, the indentation due to the particles is less pronounced than cases with lower Re. For instance, the minimum distance is $L_{12,\mathrm{min}} = 1.22$, which is larger than in previous cases, $6 - 9\%$. The drop also show transversal oscillations that change its shape considerably as it can be observed in the yz planes. Similarly as the cases with strong-wall effect, the maximum half-length of the drop is smaller than cases with lower Re.

- For $Ca = 2$, the results show no sign of puncturing ($L_{12,\mathrm{min}} = 1.12$) as for lower Re. The interface is also different because the drop flattens up and does not produce filaments as before. The saddling-up phase is also more pronounced than before, up to the point that the spooning phase is shortened and not observable at later times. The particles finally detach, leaving the considerably less stretched than for $Re = 10$.

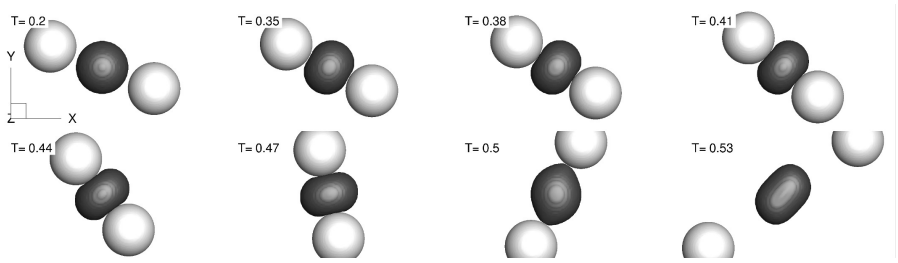

(a) $Ca = 0.1$

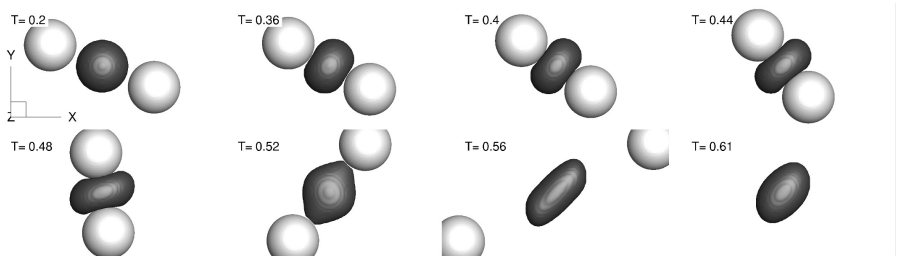

(b) $Ca = 0.25$

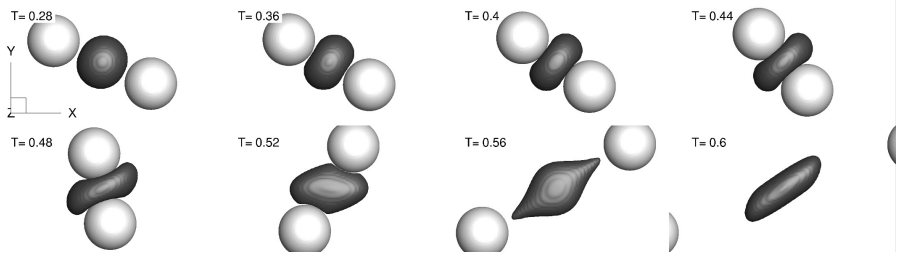

(c) $Ca = 0.5$

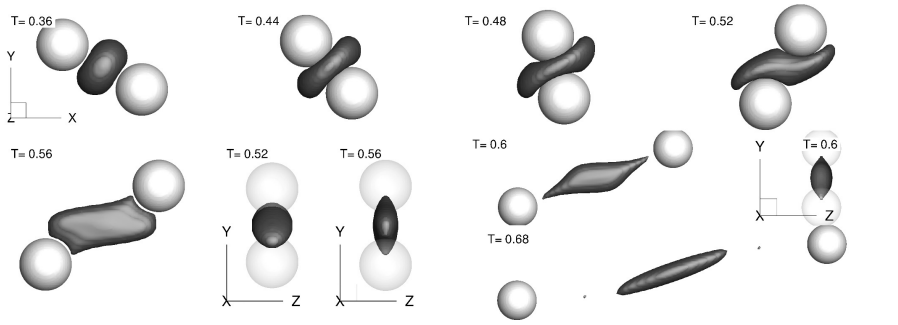

(d) $Ca = 1.0$

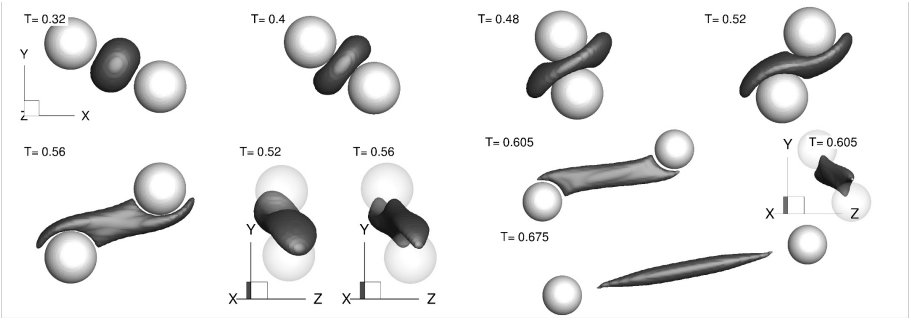

(e) $Ca = 2.0$

Figure 7.28: $Re = 50$

The relevance of viscous and pressure forces is shown in terms of the stress in Figure 7.29. A pressure field increasing towards the drop confirms that such effect is due to lubrication and that pressure is about one order of magnitude larger than viscous forces. The stress σ_{xx}, denoted as S11, shows a combination of tension and compression that requires further analysis to conclude on its effect, but there is an important region away from the center in compression and a relevant region in tension closer to the center, implying that the net horizontal force due to σ_{xx} may be towards the drop. The stress σ_{yy}, denoted as S22, shows tension near the centerline and compression away from the center, which indicates that σ_{yy} produces a net vertical force towards the center. This confirms that viscous forces increase the drop deformation, as observed from the behavior of L_{12} when Reynolds varies.

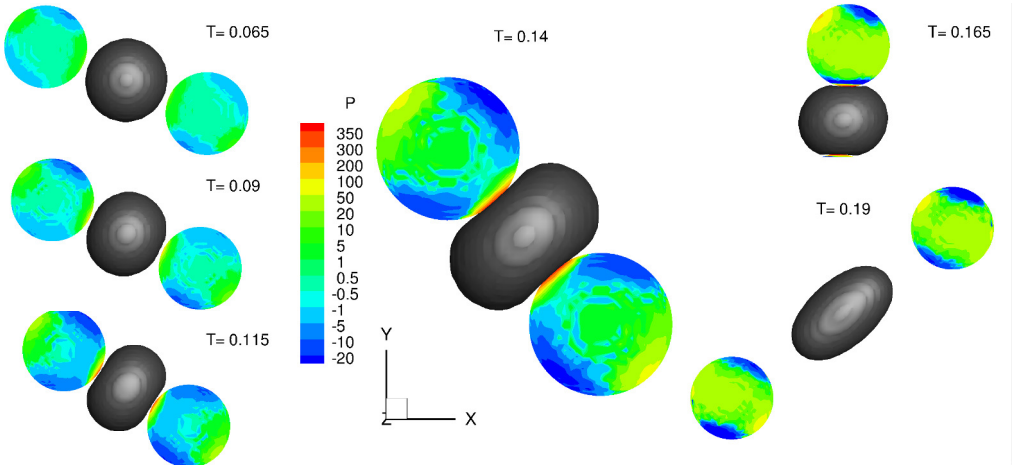

(a) Pressure contours on the particles

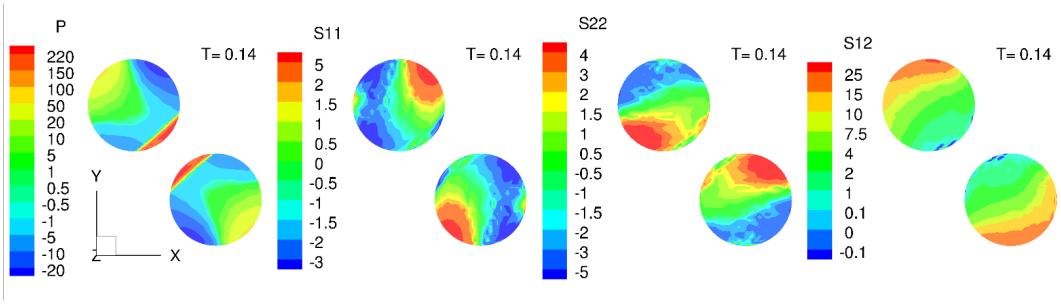

(b) Stress and pressure contours on the particles

Figure 7.29: Stresses acting on the particles for $Re = 10$ and $Ca = 0.1$. The iso-surface is plotted at a) R_p and b) $1.2R_p$

The particle path is now analyzed and presented in Figure 7.30. The pathline of the left particle for a given condition shows that it deviates vertically up (away from the drop) and that the distance from the center increases with Re, which is in agreement with the previous results of the particle-particle distance L_{12}. Cases with larger Re show the following behavior: the horizontal position of the particle is smaller when $t \lesssim t*$ (with the exception of $Ca = 0.1$) and it is larger for $t > t*$, as observed from Figure 7.30b, while

the vertical position is always larger for $t \sim t*$. This behavior confirms that large Reynolds values tend to enforce particle-particle separation. Another interesting behavior happens for $Re = 10$ and $Ca = 2$, where close-to-collision conditions are observed. In this case, the maximum vertical position occurs at $t = t*$ and then, the particle move towards the centerline. Because the two particles are close to each other during this time, lubrication forces are expected to be responsible of such drafting.

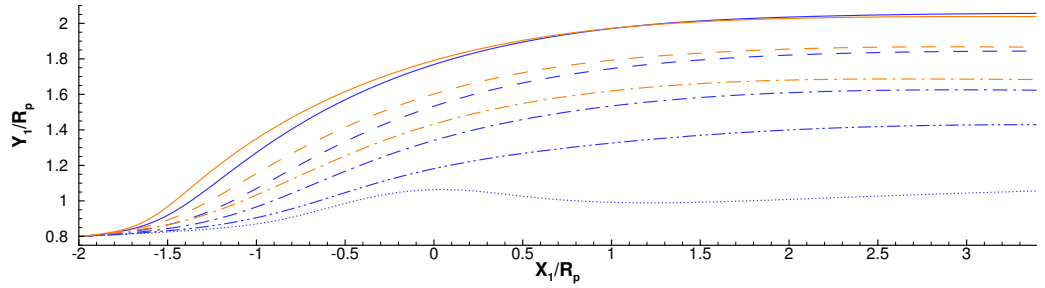

(a) Pathline

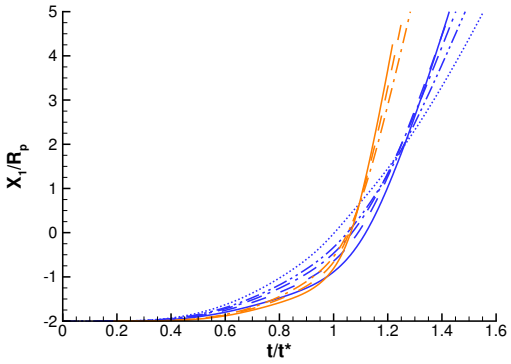

(b) Horizontal position

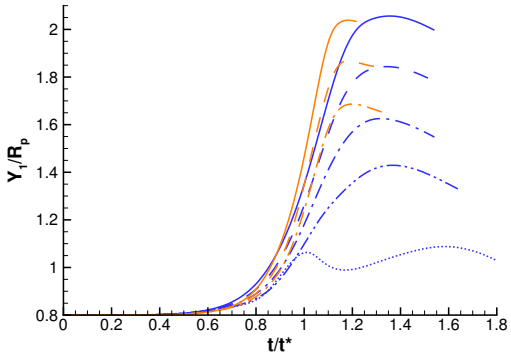

(c) Vertical position

Figure 7.30: Effect of the Reynolds and capillary numbers on the normalized particle path and position (left particle) for $Re = 10$ (blue), $Re = 50$ (orange), $Ca = 0.1$ (——) , $Ca = 0.25$ ($-\ -\ -$), $Ca = 0.5$ ($-\ \cdot\ -$), $Ca = 1$ ($-\ \cdot\ \cdot -$) and $Ca = 2$ ($\cdot\ \cdot\ \cdot$).

It is of interest to find a relationship between the minimum particle-particle distance and the flow parameters. When $L_{12,\,\mathrm{min}}$ is plotted against Ca, a relationship of the form $L_{12,\,\mathrm{min}} \approx (f\,(Ca) + 1) + 1$ agrees well with the data. An additional point is added, knowing that for $Ca = 0$, $L_{12,\,\mathrm{min}} = 2$. To simplify the choice of $f\,(Ca)$, a power fit is used. This type of correlation seems to be very accurate for low Re, but is limited by the error of the data. The correlations obtained are presented in Table 7.3 for each Re and from which an overall regression in Re is obtained. The comparison between the data and the correlations is presented in Figure 7.31. If any of the correlations is now extrapolated to $L_{12,\,\mathrm{min}} < 1.02$, the minimum resolvable value with the most refined mesh, it is observed that $Ca > 6.7$. Therefore, it is expected that for particle-particle collision, large values of Ca are needed as predicted by these correlations. The conclusion

is that collisions are not possible at low Ca for uniform properties.

Table 7.3: Correlations for the particle-particle minimum distance

Case	Correlation	R^2	Max Error
I	$L_{12,\min} = \frac{1}{7.67Ca^{0.968}+1} + 1$	0.99978	0.7%
II	$L_{12,\min} = \frac{1}{6.32Ca^{1.052}+1} + 1$	0.9975	1.7%
III	$L_{12,\min} = \frac{1}{3.78Ca^{0.908}+1} + 1$	0.9659	0.9%
Overall	$L_{12,\min} = \frac{1}{Ca(2.73\times10^{-3}Re+0.129)^{-1}+1} + 1$	0.9891	3.2%

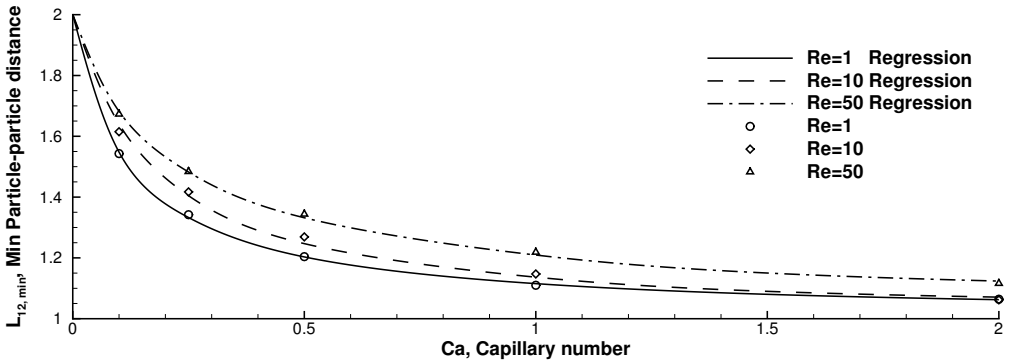

Figure 7.31: Minimum particle-particle distance: Data and non-linear regression model

This section was limited to the analysis of the effect of Re and Ca for uniform conditions. The effect of particle size, density, drop viscosity and initial position of the particles is discussed next.

7.2.2 Effect of particle size and density ratio

When the mass of the particles is increased, it is expected that the drop will require larger recovering forces to resist the deformation. The mass can be increased by either increasing ρ_p or R_p. In situations where the particle size is a factor, the density can be increased up to factors as large as $\times 20$. If gravity is a negative factor, then larger neutrally buoyant particles can be used. Similarly, if only the choice of the material is a factor, then the particle size can be increased for a given density ratio. In general, it is better if both parameters are increased. Considering that our limitation is the amount of cells that can be tackled, the scaling is limited to $3:1$ with uniform meshes, and to $4:1$ with a variable mesh. The initial position is again given by $|X\,(t=0)| = R_d + R_p$, $|Y\,(t=0)| = 0.8R_d$. Therefore, the blockage ratio due to the particles, defined as $B = \frac{y_2 - y_1}{2R_p}$, is kept constant. The separation of the plates is $H = 4\,(R_d + R_p)$.

In this section, We_p is increased further without changing Re. In that way, the ratio of inertial to surface-tension forces is increased while the ratio of inertial to viscous forces is kept constant. As it will be observed, drop puncturing can be achieved with smaller values of Ca as it was originally intended. Lowering

Table 7.4: Effect of the particle size and density on the minimum separation distance, L_{12}

Case	$\frac{R_d}{\Delta x}$	η	ρ_d	ρ_p	$\dot{\gamma}$	σ	$R_d(R_p)$	Re	Ca	$\frac{(x_o,y_o)}{R_d}$	We_p	La	Stk	$L_{12,\min}$	$t*$
II-1	11.6	0.1	1	**1**	100	10	0.1	10	0.1	$(2, 0.8)$	1	100	0.56	1.615	0.146
IV-1	15.6	0.1	1	**10**	100	10	0.1	10	0.1	$(2, 0.8)$	10	100	5.6	1.530	0.181
IV-2	12.5	0.1	1	**20**	100	10	0.1	10	0.1	$(2, 0.8)$	20	100	11	1.488	0.209
V-1	8	0.1	1	1	100	10	0.1(**0.2**)	10	0.1	$(3, 1.6)$	2	100	2.2	1.198	0.193
V-2	8	0.1	1	1	100	10	0.1(**0.3**)	10	0.1	$(4, 2.4)$	3	100	5	1.083	0.244
V-3**	8	0.1	1	1	100	10	0.1(**0.4**)	10	0.1	$(5, 3.2)$	4	100	8.8	$<$1.047	$>$0.27
VI-1	6.67	0.1	1	**10**	100	10	0.1(0.2)	10	0.1	$(3, 1.6)$	20	100	22	1.155	0.271
VI-2	6.67	0.1	1	**20**	100	10	0.1(0.2)	10	0.1	$(3, 1.6)$	40	100	44	1.136	0.321
VI-3	8	0.1	1	**20**	100	10	0.1(**0.3**)	10	0.1	$(4, 2.4)$	60	100	100	1.056	0.425

**Case with variable mesh. The spacing is uniform near the drop to the resolution reported.

B should also effectively increase the deformation, but such case is analyzed later on. The conditions of the simulations are summarized in Table 7.4. Expecting larger deformations for $Re < 10$, such cases were not simulated.

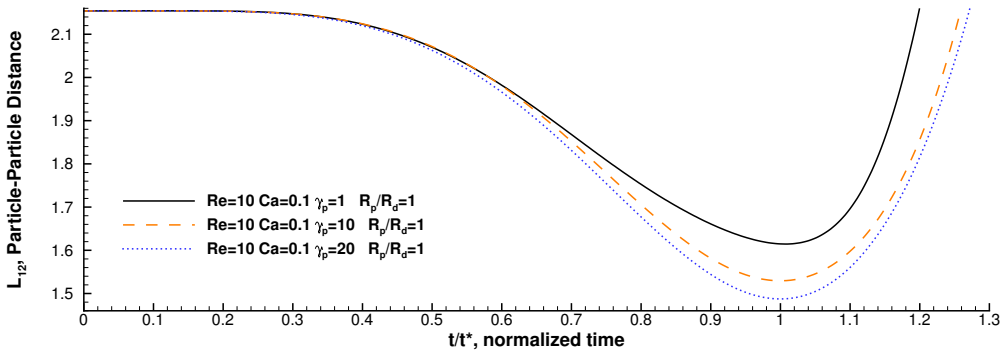

Figure 7.32: Effect of particle density on the normalized particle-particle distance, L_{12}.

The effect of density ratio, case IV, is shown in Figures 7.32 and 7.33. As it can be observed, increasing the density up to twenty times has a minimal impact on the drop disruption, but it does increase the deformation because L_{12} reduces from 1.615 to 1.487. In a sense, such increase in density is close to the physical maximum that it can be achieved with typical super-heavy solids if the medium is like water. The main effect lies in the timescale, where denser particles take longer to achieve the maximum deformation. Even though the mesh resolution varies between different cases, the conclusion is still the same.

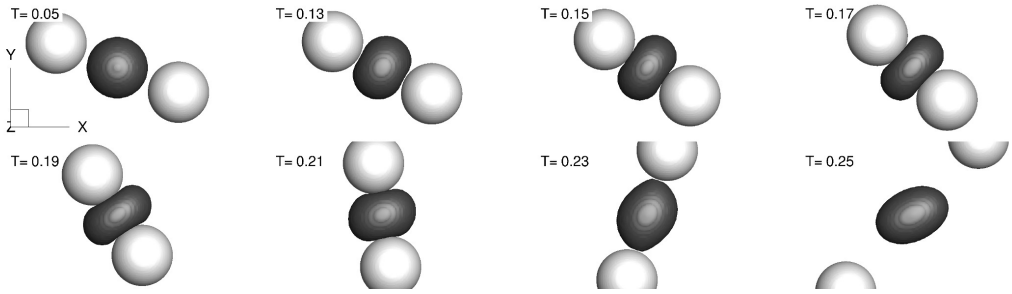

(a) $\rho_p/\rho_d = 10$

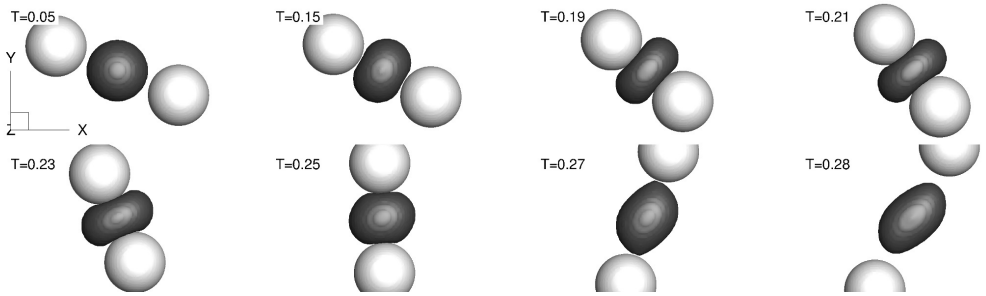

(b) $\rho_p/\rho_d = 20$

Figure 7.33: Effect of density ratio at $Re = 10$ and $Ca = 0.1$ for uniform particle-drop radius and viscosity.

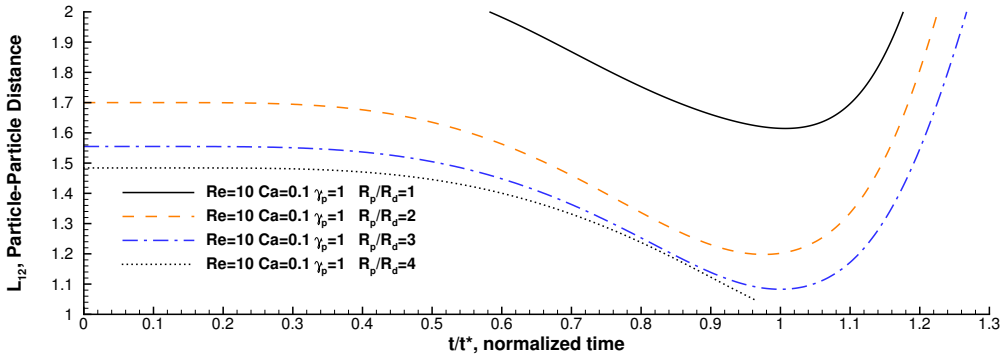

Figure 7.34: Effect of particle size on the normalized particle-particle distance, L_{12}.

The effect of particle radius is now analyzed without increasing the density and the results are presented in Figures 7.34 and 7.35. Particles as large as two times the size of the drop are incapable of producing drop puncturing, $L_{12,\,\mathrm{min}} = 1.2$, but particles three times in size is the lowest needed to produce significant hollowing, $L_{12} = 1.08$. Particles four times larger presents $L_{12,\,\mathrm{min}} < 1.04$.

Now, the density and particle size are increased and the results are presented in Figures 7.36 and 7.37. Cases VI-1 and VI-2 compared to case V-1 show a slight decreased in $L_{12,\,\mathrm{min}}$, from 1.2 to 1.16 and 1.14, respectively.

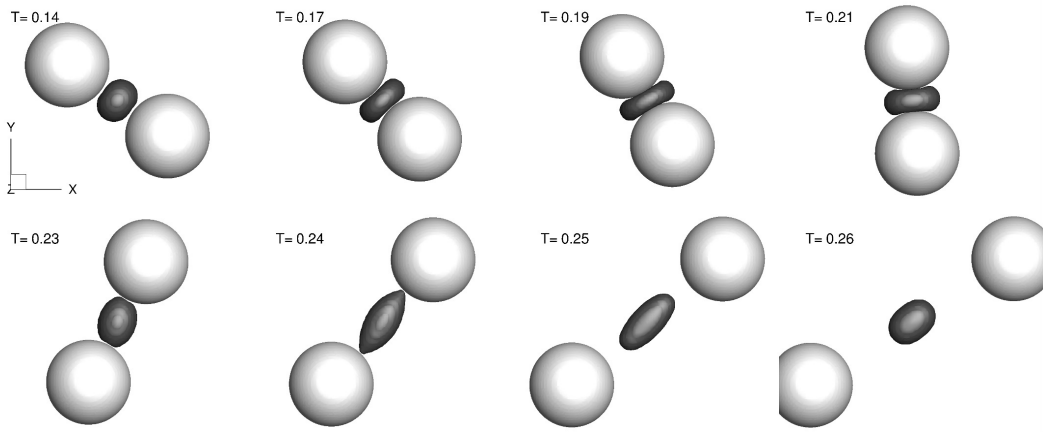

(a) $R_p/R_d = 2$

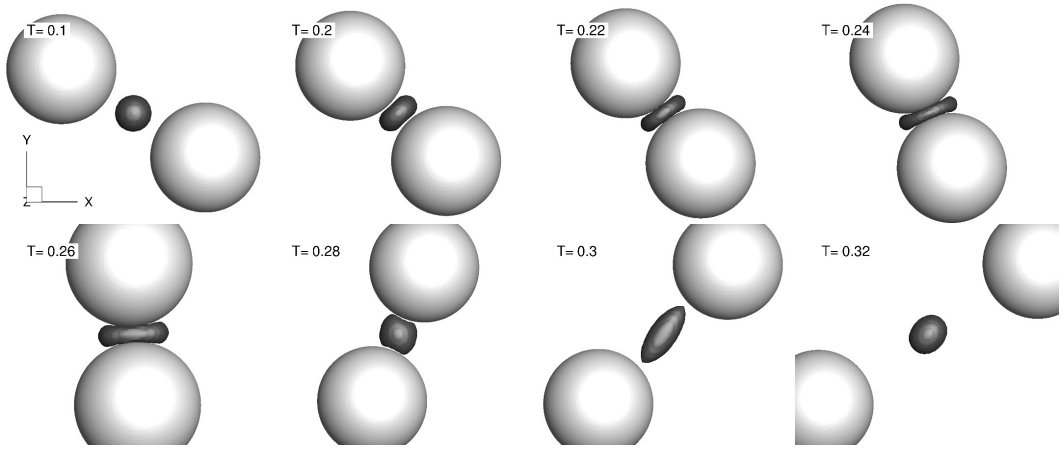

(b) $R_p/R_d = 3$

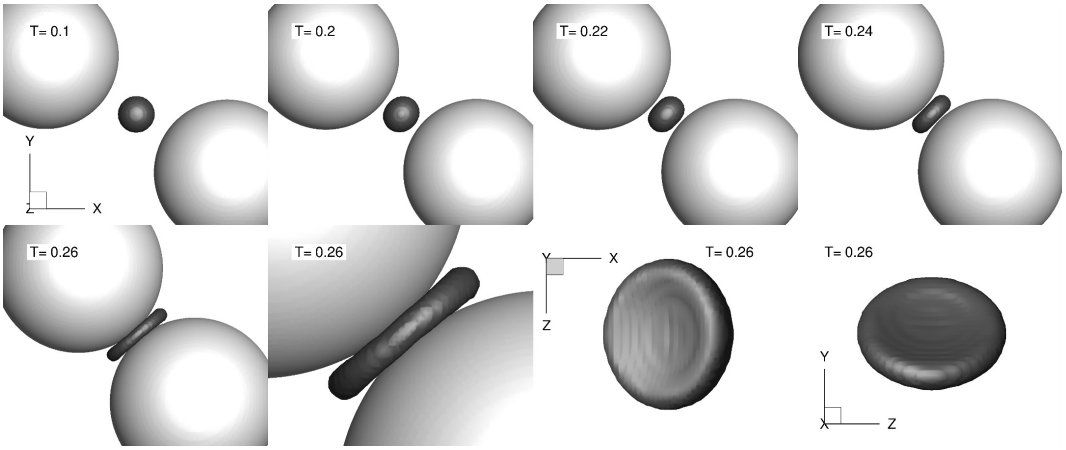

(c) $R_p/R_d = 4$

Figure 7.35: Effect of particle radius at $Re = 10$ and $Ca = 0.1$ with uniform density and viscosity.

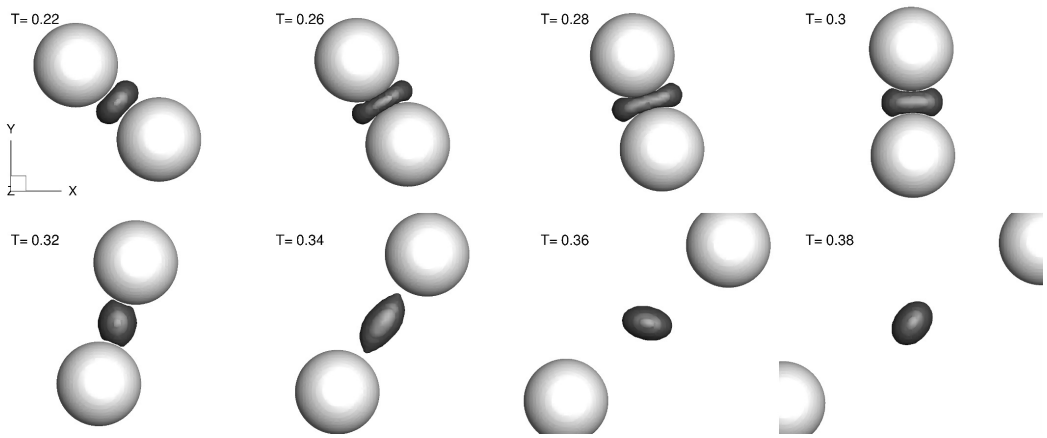

(a) $\gamma_p = 10$

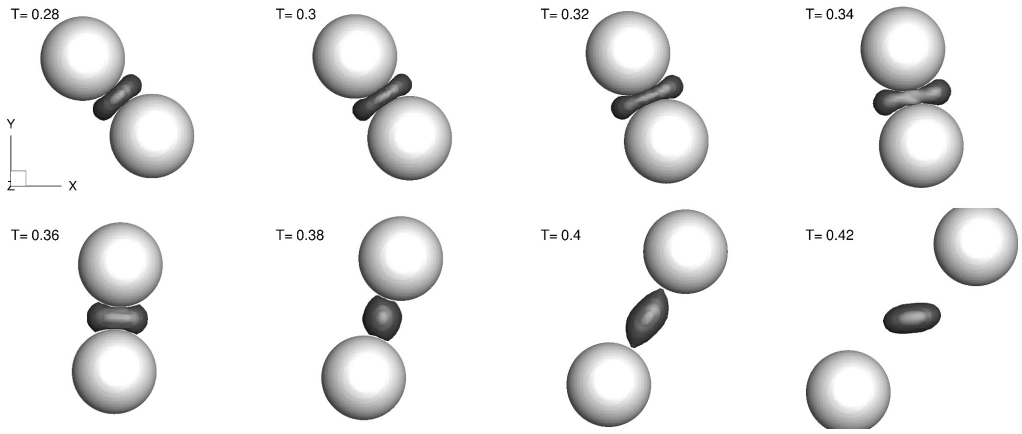

(b) $\gamma_p = 20$

Figure 7.36: Effect of density ratio at $Re = 10$, $Ca = 0.1$ and $R_p/R_d = 2$ (coarse mesh) with uniform viscosity.

Finally, these cases are used to estimate the behavior with respect to density and particle size. The data is fitted using power laws and the results are summarized in Table 7.5. As it can be observed, the exponent due to the size is larger than the exponent due to the density. It is important to mention that these simulations may be within or around 10% error, therefore, these correlations are expected to be around or within the same error.

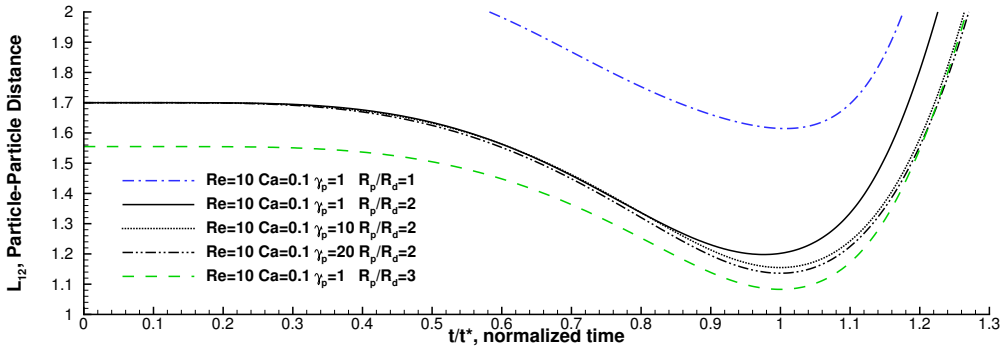

Figure 7.37: Effect of the particle radius and density on the normalized particle-particle distance, L_{12}.

Table 7.5: Correlations for the particle-particle minimum distance

Case	Correlation	R^2	Max Error
IV	$L_{12,\,\min} = 1.684 - 0.0695\left(\frac{\rho_p}{\rho_d}\right)^{0.347}$	1	$5 \times 10^{-5}\%$
V	$L_{12,\,\min} = 0.92 + 0.694\left(\frac{R_d}{R_p}\right)^{1.32}$	1	$6 \times 10^{-3}\%$
Overall	$L_{12,\,\min} = 1 + 0.651\left[\left(\frac{R_d}{R_p}\right)^{1.24} - 0.0905\left(\frac{\rho_p}{\rho_d}\right)^{0.290}\right]$	0.991	2.9%

7.2.3 Effect of viscosity ratio

Literature indicates that lower critical capillary numbers tend to occur for $\lambda \approx 1$ and values of λ away from ~ 1 are stabilizing. Our results with the high-constriction geometry in a simple shear flow show a slight reduction of Ca_c for $\lambda > 1$. In order to determine if a similar effect happens when including particles, cases with the following conditions are considered: $Re = 10$, $Ca = 0.1$, $R_p/R_d = 2$, $\lambda = [0.1,\, 1.9]$, $\frac{R_d}{\Delta x} = 8$ and $\Delta t = 2.5 \times 10^{-5}$.

- For $\lambda = 1.9$, the minimum distance is $L_{12\,\min} = 1.202$ and happens at $t = 0.194$. In comparison, the case with $\lambda = 1$ has a minimum distance $L_{12\,\min} = 1.198$. This represents a difference as small as $+0.3\%$. This difference is not related to mesh resolution or timestep as both are kept constant between cases. It is then expected that larger values of λ may only decrease the deformation. The mechanisms observed are the following (I) hollowing (II) tumbling (III) stretching (IV) recoiling.

- For $\lambda = 0.1$, the minimum distance is $L_{12\,\min} = 1.186$ and occurs at a similar time as before, $t = 0.194$. This represents a -1% difference with respect to $\lambda = 1$. This allows to determine that the minimum deformation does not occur at $\lambda \sim 1$ as expected, but for $\lambda < 1$. Therefore, a medium that is more viscous than the drop is preferred. This result was not expected because drops tend to deform more for $\lambda \sim 1$, nevertheless the change is small.

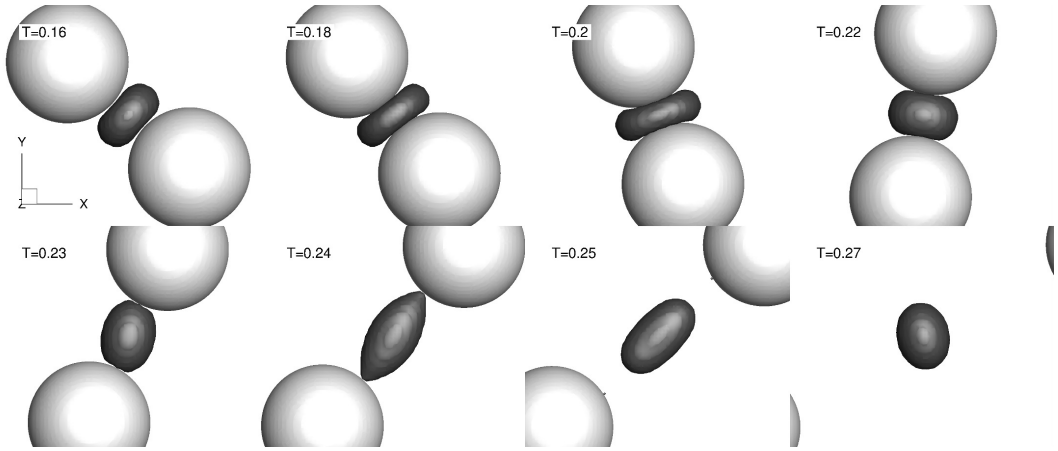

(a) $\lambda = 0.1$

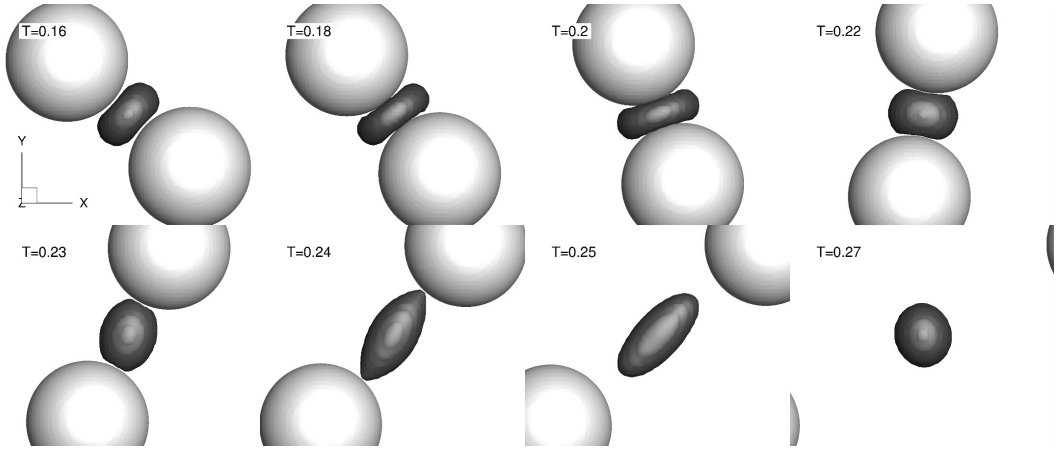

(b) $\lambda = 1.9$

Figure 7.38: Effect of viscosity ratio at $Re = 10$, $Ca = 0.1$ and $R_p/R_d = 2$

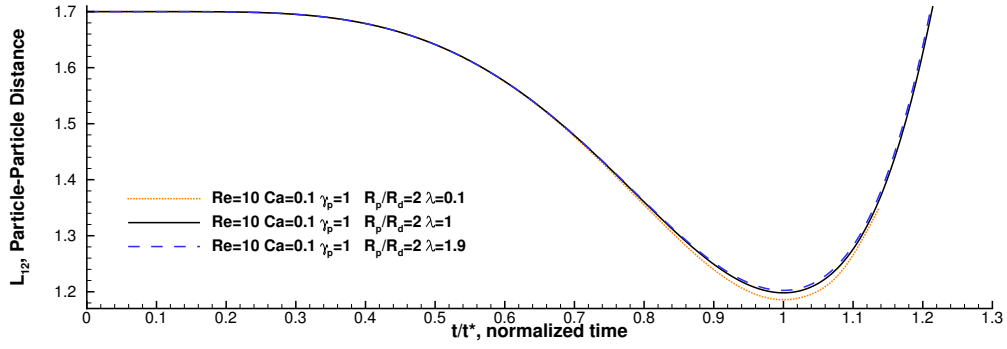

Figure 7.39: Effect of the viscosity ratio on the normalized particle-particle distance, L_{12}, at $Re = 10$ and $Ca = 0.1$.

7.2.4 Effect of Initial Position

The location of the rigid particles play an important role in the deformation of the drop. The first effect is due to the blockage ratio, $B = \frac{y_2 - y_1}{2R_p}$. When $B \to 0$, the particles are aligned with the drop and only wall migration can make them move during the starting phase. As B is increased, the particles separate from each other vertically and the relative velocity increases. The limit for particle-particle collision is when $B = 1$, unless there is drafting, while the limit for significant drop deformation is when $B = 1 + \frac{R_d}{R_p}$, considering that the particles are moving horizontally.

Table 7.6: Effect of the initial position of the particles on the minimum particle-particle distance.

Case	$\frac{R_d}{\Delta x}$	η	ρ_d	ρ_p	$\dot{\gamma}$	σ	$R_d(R_p)$	Re	Ca	$(x_o, y_o)/R_d$	We_p	$L_{12,\min}$	$t*$
II-1	11.6	0.1	1	1	100	10	0.1	10	0.1	$(2, 0.8)$	1	1.615	0.146
II-2	11.6	0.1	1	1	100	4	0.1	10	0.25	$(2, 0.8)$	2.5	1.417	0.152
II-3	11.6	0.1	1	1	100	2	0.1	10	0.5	$(2, 0.8)$	5	1.2691	0.156
VII-1	11.6	0.1	1	1	100	10	0.1	10	0.1	$(\mathbf{5}, 0.8)$	1	1.476	0.233
VII-2	11.6	0.1	1	1	100	4	0.1	10	0.25	$(\mathbf{5}, 0.8)$	2.5	1.237	0.242
VII-3	11.6	0.1	1	1	100	2	0.1	10	0.5	$(\mathbf{5}, 0.8)$	5	1.053	~0.25
VIII-1	12	0.1	1	1	100	10	0.1	10	0.1	$(2, \mathbf{0.6})$	1	1.584	0.168
VIII-2	12	0.1	1	1	100	10	0.1	10	0.1	$(2, \mathbf{0.4})$	1	1.542	0.197
VIII-3	12	0.1	1	1	100	10	0.1	10	0.1	$(2, \mathbf{0.2})$	1	1.493	0.243
IX-1	11.6	0.0125	1	1	100	1.25	0.1	**80**	0.1	$(\mathbf{5}, 0.8)$	8	1.492	0.865
X-1	12	0.1	1	1	100	10	0.1	10	0.1	$(\mathbf{5}, \mathbf{0.2})$	1	3.09	0.331

The objective is to clarify if particles released far away (more inertia) can produce larger deformations on the drop than particles that are closer. First, the effect of the horizontal position is studied. This type of simulations are more challenging due to the increased temporal timescales and only few simulations are performed. Second, the effect of the vertical position is studied. In this way, it can be determined if there is a way to optimize the puncturing due to the initial location and if so, quantify such improvement.

The results summarized in Table 7.6 show how particles released far away in the horizontal direction and closer to the drop in the vertical direction tend to reduce $L_{12,\min}$. The baseline case is II-1, where the minimum distance is 1.615. The case VII-1 (far-away particles in x) presents a minimum distance of 1.476, which is a 9% reduction. This reduction is more relevant when the capillary number is increased. For $Ca = 0.25$, cases II-2 and VII-2, the minimum distance changes from 1.417 to 1.237, which is a 13% reduction. For $Ca = 0.5$, cases II-3 and VII-3, the reduction is larger than 15%, as only a partial solution leading to

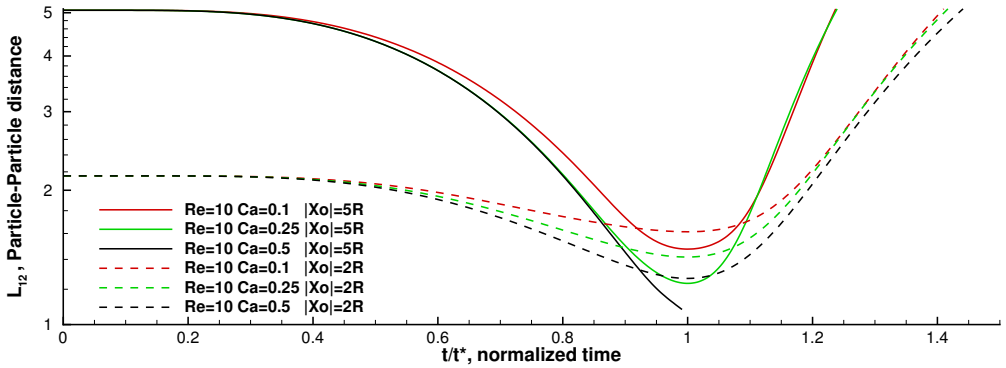

Figure 7.40: Effect of initial horizontal position of the particles on the normalized particle-particle distance, L_{12}.

collision was achieved. These results are also compared in Figure 7.40. This confirms that reductions in the minimum particle-particle distance of up to 15% are possible by changing the horizontal position when $Ca < 0.5$.

The 3D representation of the simulations with different initial position in x is presented in Figure 7.41. As it can be observed, the deformation for $Ca = 0.25$ and $Ca = 0.5$ is considerably larger, where the later case showed puncturing.

The pathline of the particles is presented in Figure 7.42. Particles released closer to the drop tend to do the initial vertical migration away from the drop and they keep separating from vertically until they are finally drafted (positive x). When the particles are released away from each other, they attempt to do a return upon approaching, as observed from the reduction in vertical position around $t/t^* \sim 0.9$, but the drop recoiling push them away for low Ca. For $Ca = 0.5$, surface-tension forces are not sufficiently strong and the particles produce a hole on the drop.

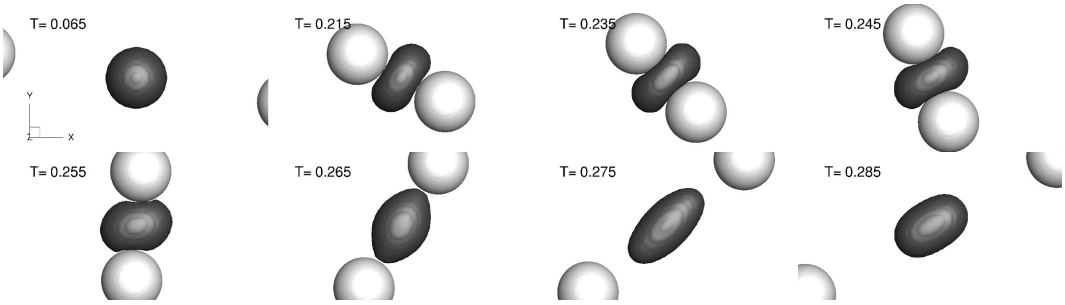

(a) $Ca = 0.1$

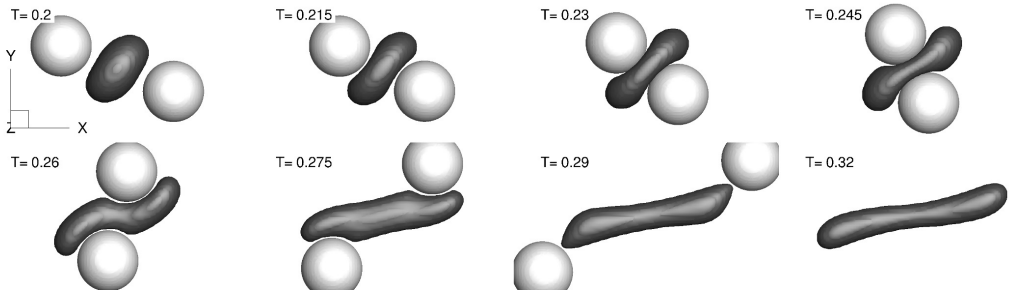

(b) $Ca = 0.25$

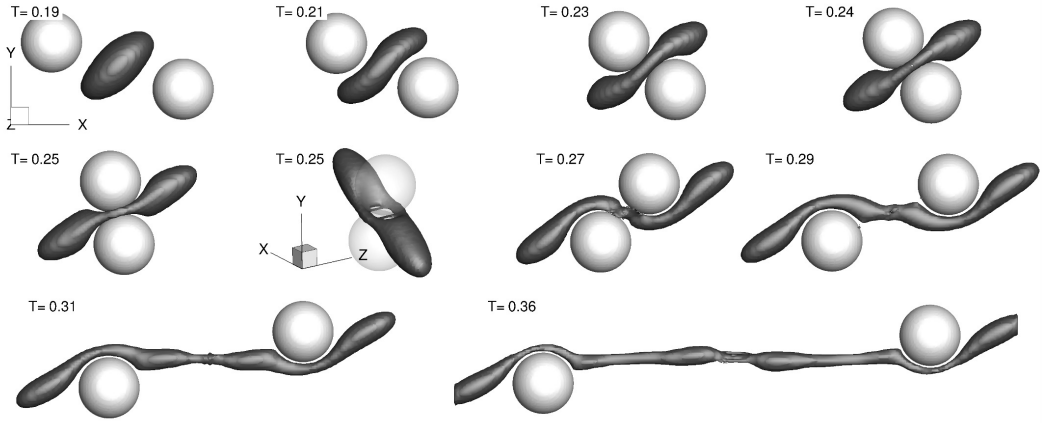

(c) $Ca = 0.5$

Figure 7.41: Solution for various Ca when the particles are released far away in the x direction (case VII).

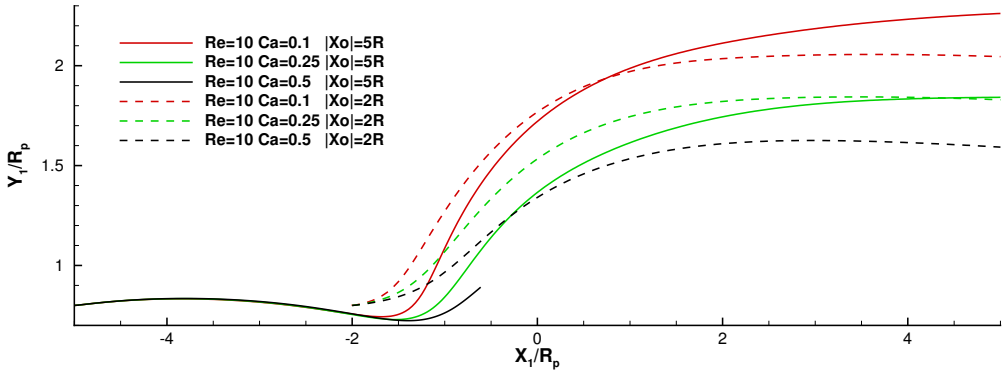

(a) Pathline

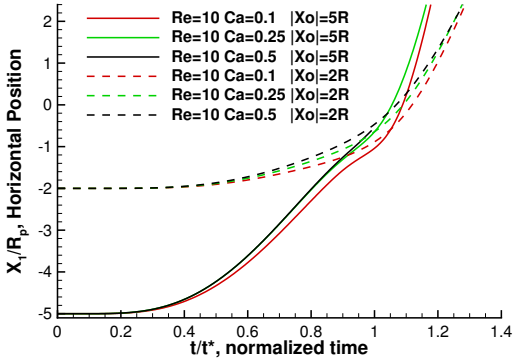

(b) Horizontal position of the particle

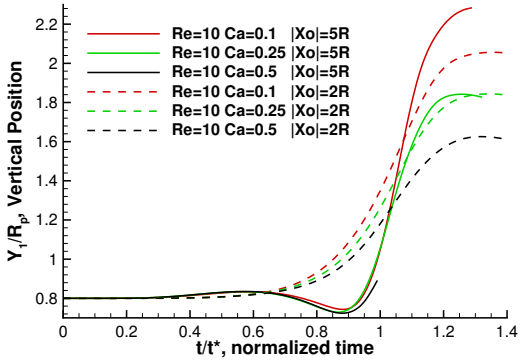

(c) Vertical position of the particle

Figure 7.42: Effect of the initial horizontal position on the normalized particle path and position (left particle) for $Re = 10$.

Changes in the vertical position when the particles are close to each other in the horizontal direction show variations of the minimum particle-particle distance of up to 8%. The comparison among different cases is shown in Figure 7.43.

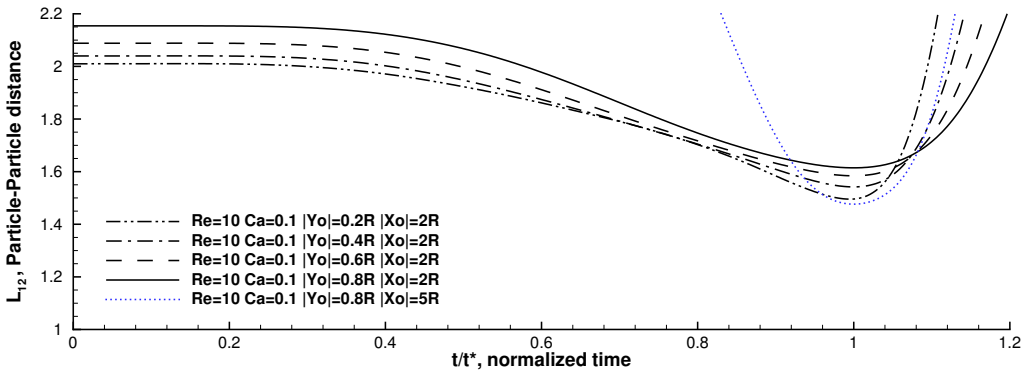

Figure 7.43: Effect of initial vertical position of the particles on the normalized particle-particle distance, L_{12}.

The 3D representation of the effect of changes in the initial vertical position is presented in Figure 7.44. The differences may only be evident at $t = 0.25$, $t = 0.2$ and $t = 0.17$ for $y_o = 0.2R_p$, $y_o = 0.4R_p$ and $y_o = 0.6R_p$, respectively, where the minimum particle-particle distance occurs and the particles are closer. It is also noted that for $t = 0.28$, $t = 0.23$, $t = 0.2$ of the same initial positions mentioned before, the case with lower y_o shows drop tipping. Therefore, more deformation during the approaching phase lead to more deformation in the separating phase.

The vertical position modified the particle-particle distance as $L_{12,\min} = 1 + 0.633\left(\frac{y_o}{R_d}\right)^{0.159}$, with an error of 0.37% and $R^2 = 0.994$. This is obtained at constant x_o, for particles that are close to the drop when the flow starts and for $Ca = 0.1$. The effect of the vertical position presented a smaller exponent than the correlations based on the effects of density and particle size, but it is still comparable and relevant.

Because it is now known that the deformation depends on x_o and y_o, it would be expected that a particle far away in x and closer to the centerline would produce the maximum deformation. However, particles can return for certain flow conditions. Considering the time required to move the particles when the horizontal initialization is large only the case of a particle released far away and closer to the centerline was performed (case X-1). That case showed that particles return for $x_o/R_d = 5$ and $y_o/R_d = 0.8$. This opens up a new study that can be derived, finding the conditions in Re, Ca, λ and γ and $\mathbf{x}_o$ where the particles can return and the optimal position based on critical return-to-pas.s conditions. A case (X-1) with returning particles is shown in Figure 7.45.

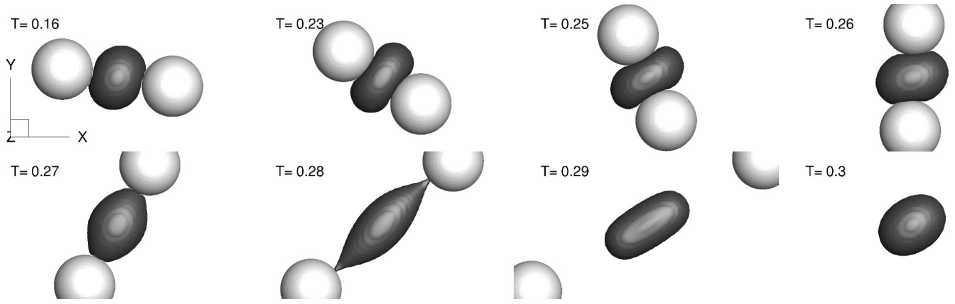

(a) $y_o = 0.2R_p$

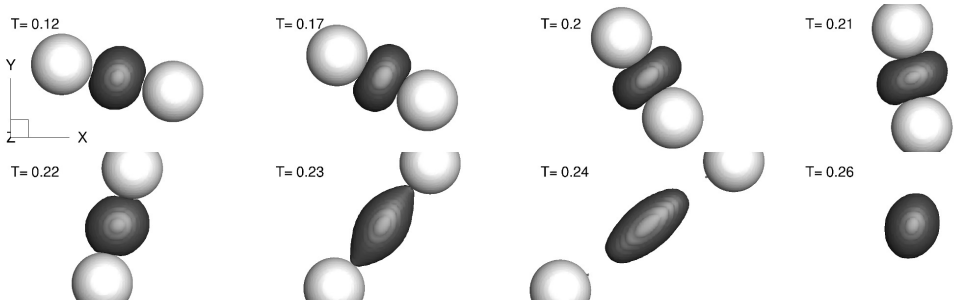

(b) $y_o = 0.4R_p$

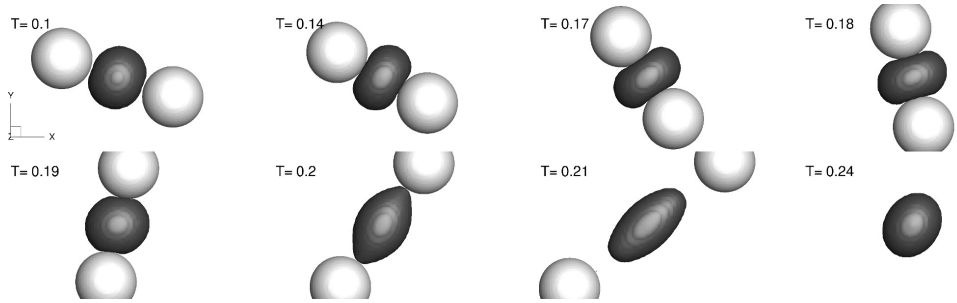

(c) $y_o = 0.6R_p$

Figure 7.44: Effect of the initial position in the y direction (case VIII).

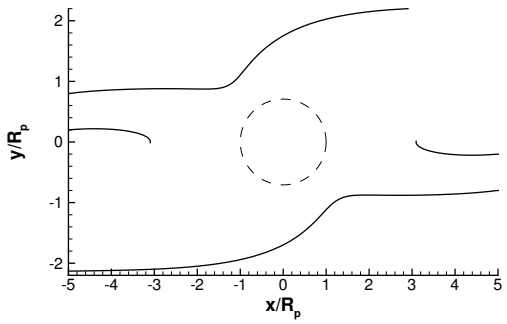

Figure 7.45: Pathline of returning and non-returning particles: $Re = 10$, $Ca = 0.1$, $\mathbf{x}_o/R_p = (5, 0.8, 0)$ (case VII-1) and $\mathbf{x}_o/R_p = (5, 0.2, 0)$ (case X-1).

Another effect that needed to be addressed is whether a particle released far away will produce more deformation on the drop at larger Re. Similarly as previous cases, the deformation decreased with Re. The case IX-1 showed a minimum distance of 1.492, which is 1% larger than case VII-1. In this comparison, only Re is changed from $Re = 10$ to $Re = 80$. At $Re = 80$, an asymmetric solution is observed. This case was enforced with a convergence criteria of the linear momentum equation of 2×10^{-7} and mass conservation of 10^{-3}, which is believed to be sufficiently small to obtain iteration independent solutions for lower Re. It is also possible that a smaller criteria could enforce a symmetric solution. This case also confirms that increasing Re also increases the minimum particle-particle distance. Therefore, low Re conditions are still preferred.

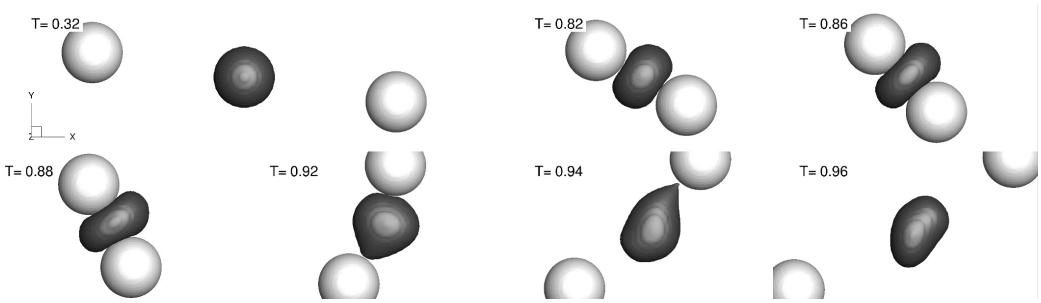

Figure 7.46: Effect of the initial location at $Re = 80$ and $Ca = 0.1$ (case IX).

7.2.5 Effect of particle shape

One way that can be used to lower $L_{12,\,\mathrm{min}}$ is by using cylinders instead of spheres, which can be made long enough that the presence of the drop would only affect its vertical displacement minimally. If a collision takes place, then the drop may be sliced in half instead of punctured.

7.2.6 Discussion on drop puncturing and implications

For the porpoise of breaking a biological cell in shear flows, the results of drop deformation in a starting shear flow can be summarized as follows:

- Increasing Re tends to produce end-pinching, with or without particles. Low Re is better for central-drop disruption.
- The minimum particle-particle distance increases with Re.
- Low constriction geometry β increases the stability of the drop, therefore, large values of β are better.
- Drop disruption is not observed at $Ca = 0.1$ under uniform conditions. Surface-tension forces tend to stabilize the drop after puncturing, or after a large deformation.

- Increasing the density of the particles has only a minimal positive effect on the drop deformation.
- Increasing the radius of the particles has a large impact on the drop deformation. Larger and denser particles are preferred.
- Particles at least three times the radius of the drop are required at capillary as low as 0.1 to produce puncturing. It is expected that considerably larger particles are needed for even smaller capillary numbers.
- Locating the particles far away tends to increase the drop deformation. This may depend on the returning-particle effect.
- Locating the particles closer to the horizontal centerline increases the drop deformation. However, if they are sufficiently far in the horizontal direction, they may return.

7.3 Drop Deformation due to Gravity-driven Particles

Consider the case of two rigid particles with different densities, but equally increased and decreased around the medium density, and a neutrally buoyant drop where the heavy particle is on top and the light particle below. This type of configuration is expected to be metastable, where the particles approach each other and then tumble. The degree of deformation in relationship with the density ratio is sought, but particularly, the conditions that produce puncturing.

A dimensionless analysis of the problem shows that it is governed by $Re_{osc} = \sqrt{\rho_d \sigma R_d}/\eta_d$, viscosity ratio λ, density ratio γ and Bond number, defined as,

$$Bo = \frac{\text{relative weight of the particle}}{\text{surface-tension force}} = \frac{|\rho_p - \rho_d| \, g R_p^3}{\sigma R_d}$$

If the transient effects are taken into consideration, another Re and Ca can be defined. Due to the complexity of this flow with several parameters, uniform properties between the drop and the medium are considered, $\gamma_d = \lambda = 1$, equivalent radius $R_d = R_p$, the density of the particle is given by $\gamma_p = \frac{\max(\rho_{p_i})}{\rho_m}$, while the properties of the drop are $R_d = 0.1\,\text{cm}$, $\rho_d = 1\,\text{g/cm}^3$, $\eta = 0.01$ P and $\sigma = 1\,\text{dyne/cm}$. This flow is then represented by $Re_{osc} = 31.6$ and $Bo = 9.8\,|\rho_p - \rho_d|$ cm^3/g. Gravity is acting in the $-y$ direction. The simulations are performed in a parallelepiped domain of size $6R_d \times 9R_d \times 6R_d$. The initial position of the particles is $y_o = 2.5R_p$. A mesh of $40 \times 60 \times 40$ and $CFL = 0.2$ ($\Delta t = 4.5 \times 10^{-5} - 3.7 \times 10^{-4}$) were employed. The results of this flow are presented in Figures 7.47 and 7.48.

Among many aspects that can be analyzed, it is particularly important that a critical value for drop hollowing Bo between 11.76 and 13.72 is found. For the smallest Bo, gravitational forces are not sufficiently large to produce a hole, but they are sufficiently large to produce large deformations on the drop. Moreover, the drop and the particles exhibit a decaying oscillatory motion until the numerical imbalances produce unstable conditions and the drop is pushed away. It is expected then that any flow below the critical Bo is metastable. For the larger Bo, drop holing takes place, the particles motion is monotonic and the drop shows local oscillations, adopting a final ring shape. In this case, the solution is stable, where collisional forces compensate for the buoyancy force acting on both particles. It is also worth mentioning that because the lower particle has lower density and the upper particle has higher density than the medium, the position, velocity and acceleration are different between them, therefore, the solution is not symmetric in the y direction.

The aspect ratio of the drop and the particle-particle distance are computed and presented in Figure 7.49. The dynamics of the case with larger density difference is faster and overdamped, while the case with the smaller density difference is damped-oscillatory. The maximum aspect ratio of the latter is 16.3 and it is achieved at $t = 0.12$.

Simulations with a smaller particle radius, $R_p \sim 0.01\,\mathrm{cm}$ are more interesting because the solutions can be applied in biological studies. Unfortunately, those cases require considerable more computational time because Re_p is lower.

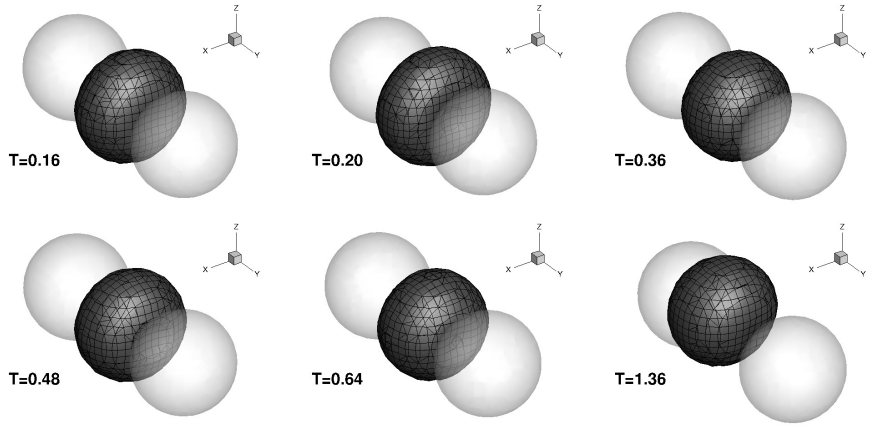

(a) $|\rho_p - \rho_d| = 1.05,\ Bo = 10.29$

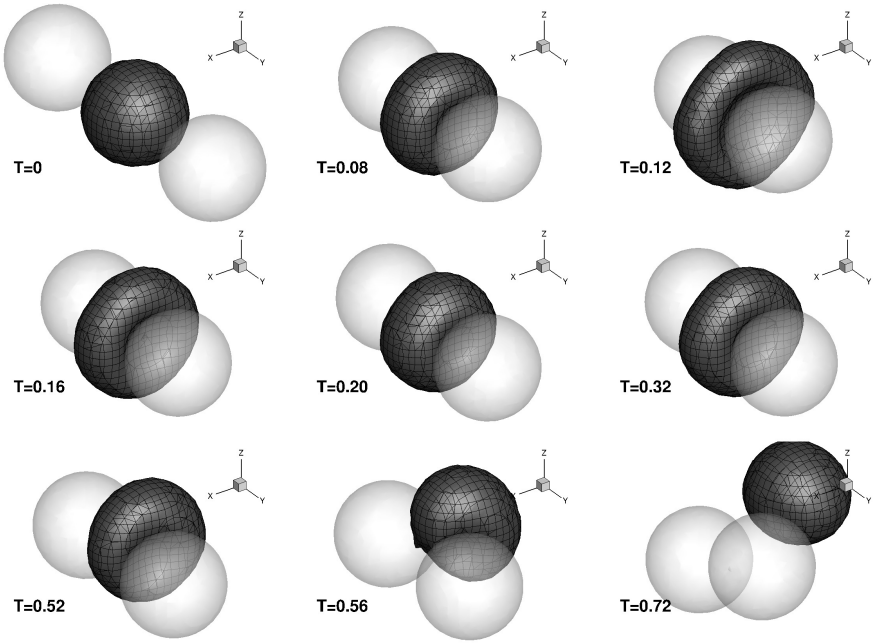

(b) $|\rho_p - \rho_d| = 1.2,\ Bo = 11.76$

Figure 7.47: Effect of particle density on the deformation of a drop at $Re = 31.6$

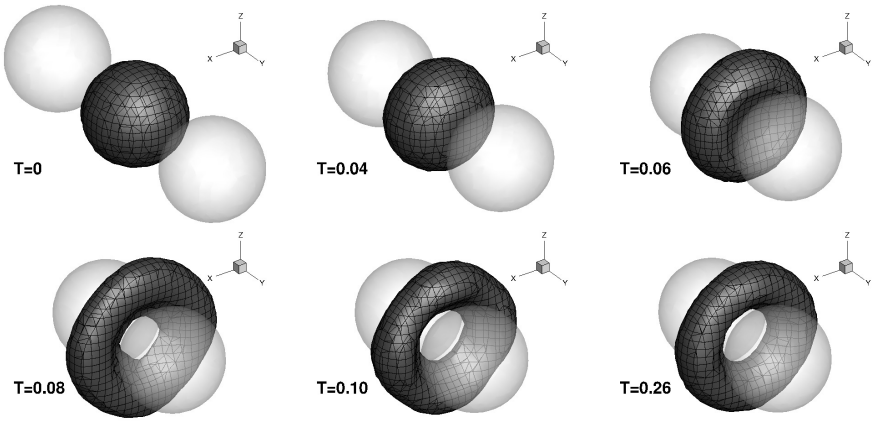

(a) $|\rho_p - \rho_d| = 1.4$, $Bo = 13.72$

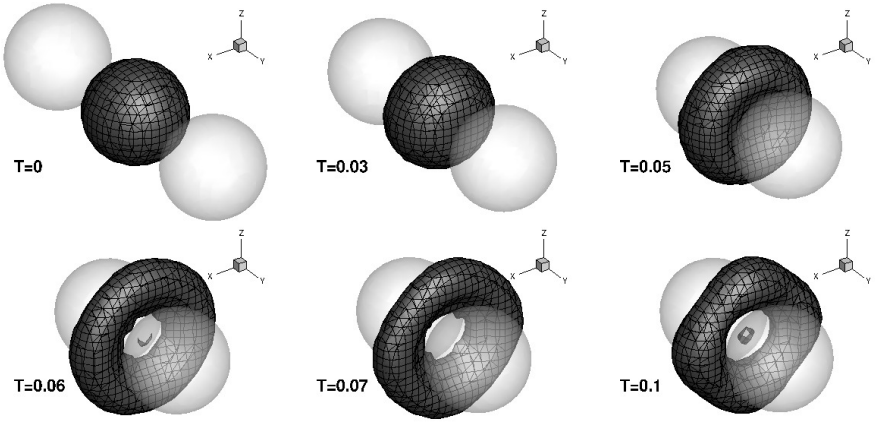

(b) $|\rho_p - \rho_d| = 1.6$, $Bo = 15.68$

Figure 7.48: Continuation of Figure 7.47.

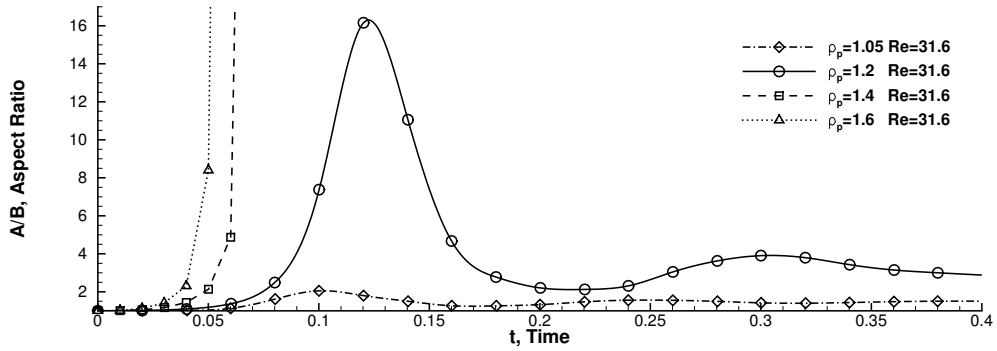

(a) Aspect ratio of the drop

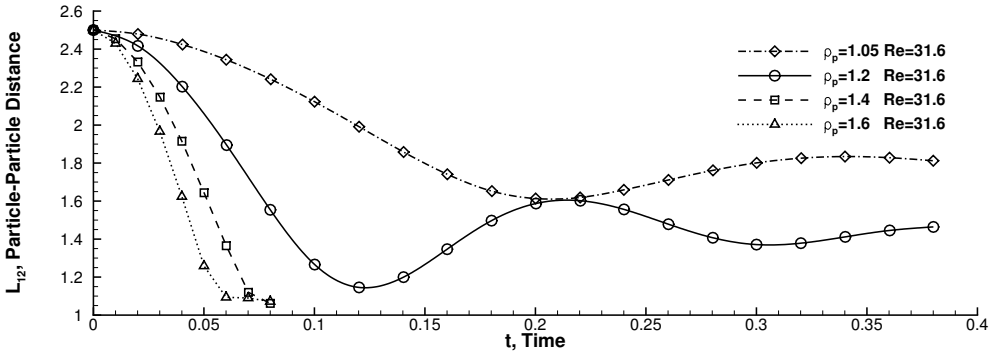

(b) Particle-Particle L_{12} distance

Figure 7.49: Effect of density on the deformation of a drop at $Re = 31.6$

7.4 Breakup of a Drop after a Sudden Expansion

From previous results, it is expected that larger Re will lower the critical Ca and the degree of drop deformation required for breakup. In a sudden expansion, there is a critical Reynolds of the main flow that produces regions of recirculation. Once these regions are produced, the actual change in area of the flow minimizes as a drop moves downstream. Drops may break up if the acceleration in the expansion region is maximized. For that reason, recirculation zones must be avoided. These regions can be reduced if the drop is started in an initially quiescent flow and the drop reaches the expansion before fully developed conditions. Finding mechanisms to break up one drop will allow for the disruption of a stream of drops, but the flow must be pulsating in order to produce expansions without recirculating zones. The domain size, expansion ratio and boundary conditions are studied.

7.4.1 Drop in a Bilateral Sudden Expansion

The problem of a bilateral expansion is studied to analyze the range of conditions where a single drop splits into daughter drops. For a given expansion geometry, Re and Ca are varied until critical conditions are found. These numbers are defined in terms of the narrow channel, $Re = \frac{\rho U d}{\eta}$ and $Ca = \eta U/\sigma$, where U is the upstream average velocity and d is the narrow channel vertical height. If the expansion ratio is relatively small, break up could only be observed in the smaller channel after increasing Ca due to the rear-side re-entering flow. The expansion ratios and flow conditions for which a drop stretches and splits is sought. However, the flow conditions should be such that the drop can achieve steady-state conditions in the narrow channel without fragmenting or breaking up, which is typically the case for low Ca. Again, the interest lies in determining if expansion geometries can induce breakup in otherwise stable conditions. The geometry studied here is limited to expansion ratios $e = H/d = 4 - 8$, aspect ratios of the cross section $\alpha = W/d = 1 - 2.4$ and blockage ratios $\beta = 2a/d = 0.833 - 0.909$. The drop is initially located at $x_o/a \leq -10$. The main flow is either created by a constant pressure difference between the inlet and the outlet, or prescribed by a velocity at the inlet and a pressure at the outlet. For the final study, the pressure difference is kept constant and based on the approximate steady-state conditions for a given Re.

For the cases with no breakup, the effect of the channel is studied in terms of the minimum aspect ratio of the drop A/B, which is used to estimate the critical conditions for breakup. This parameter compares the half-length to the half-breadth, meaning that small values of A/B are indicative of a thinner drop, while a zero value represents central disruption. Two Reynolds numbers are considered, 10 and 50, together with several capillary numbers and expansion ratios. These results are summarized in Table 7.7 for a flow started from fully developed conditions and velocity prescribed at the inlet.

Table 7.7: Minimum aspect ratio after the expansion, $(A/B)_{\min}$ for blockage ratio $\beta = 2a/d = 0.833$. The initial conditions are the fully developed conditions, or suddenly started flow (**), both with velocity prescribed at the inlet. (*) Experiences narrow-channel breakup.

$Re_d = 10$					
	$e = 4$			$e = 6$	$e = 6.66$
Ca	$\alpha = 1$	$\alpha = 2.4$	Ca	$\alpha = 1$	$\alpha = 2.22$**
0.5	0.523	0.565	0.4	0.4061	0.533
0.8	0.447		0.5	0.3829	
1.0*	0.439		0.8	0.3097	
1.2*	0.283				
$Re_d = 50$					
	$e = 4$	$e = 6$		$e = 6.66$	
Ca	$\alpha = 1$	$\alpha = 1$	Ca	$\alpha = 2.22$**	
0.5	0.646	0.618	0.4	0.368	

In the case of $Re = 10$, the flow does not present circulation zones. Despite this condition, a geometry with $e = 4$ and $\alpha = 1$ does not show drop breakup for capillary numbers as large as $Ca = 0.8$, as shown in Figure 7.50b. Because the acceleration at the expansion region is not enough to stretch the drop in the y direction, the deformation is not significant to induce necking, the precursor of breakup. In the case of $Ca = 1$, shown in Figure 7.50c, the drop shows fragmentation. However, this value of Ca is larger than Ca_{cr} of the narrow channel, making the expansion irrelevant for the purpose of producing daughter drops under low Ca. Nevertheless, flows with $Ca > Ca_c$ could be used to produce multiple structures, therefore maximizing the amount of fragments. The initial position of the drop could also be subject of optimization. The small particles appearing in the figures are due to numerical surface tension (lack of mesh resolution near the end tips of the drop) and wisp generation (the old BDR scheme was used in these simulations). Some of these results are also presented in 3D in Figure 7.51.

When α is increased from 1 to 2.4, $(A/B)_{\min}$ also increases, which means that the drop is more stable. Because of that, smaller values of α are preferred to increase the drop deformation.

The circulation zone is present for $Re = 50$, $e = 4$ and $\alpha = 1$. In this flow, the case of $Ca = 0.5$ is also stable, as presented in Figure 7.52. Because of the apparition of the vena contracta, a drop is expected to be stable for $Ca < C_c$. Also, $(A/B)_{\min}$ for $Re = 50$ is 0.646, which is 23% larger than the value at $Re = 10$. A similar reasoning may apply for larger values of Ca. This confirms that steady-state initial conditions diminishes the drop deformation for moderate Re.

Increasing α will also generate circulation zones at lower Re. Increasing Re will increase the size of the circulation zone, which in turn reduces the actual expansion. This implies that splitting is not possible for the geometry and flow conditions studied, that is, $e = 4$ and $Re \lesssim 50$.

When the expansion ratio is increased to $e = 6$, a drop achieving steady-state conditions before the expansion manifest larger deformations, but is still not sufficient to produce drop splitting.

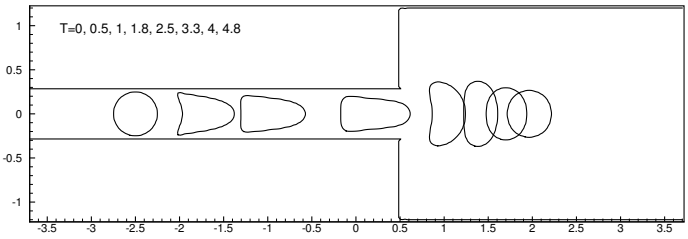

(a) $Ca = 0.5$

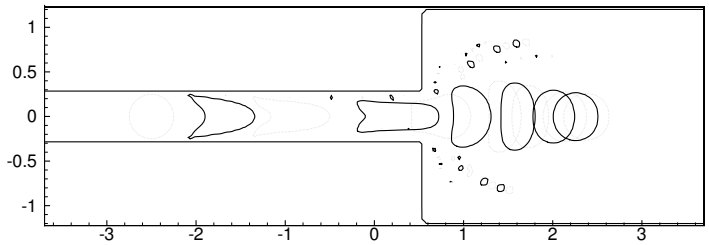

(b) $Ca = 0.8$

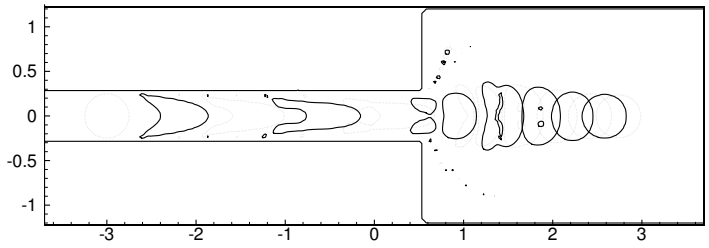

(c) $Ca = 1$

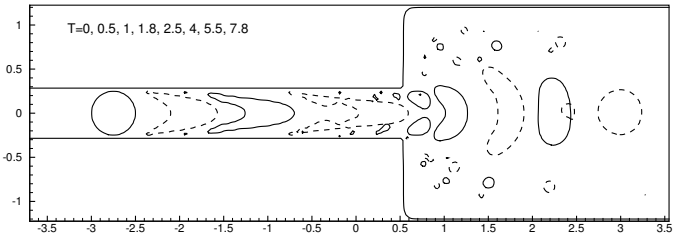

(d) $Ca = 1.2$

Figure 7.50: Evolution of a drop in a bilateral sudden expansion for $e = 4$, $\alpha = 1$ and $Re = 10$. Shown for $t = 0, 1, 2, \ldots$ ($\cdots$) and $t = 0.5, 1.5, 2.5, \ldots$ (—) in a) and b). Time is given for c).

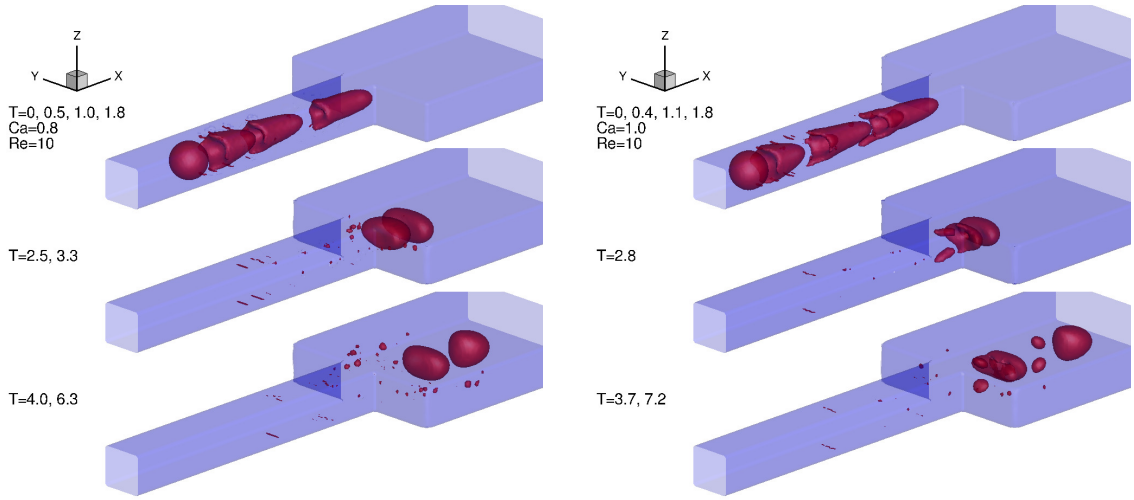

(a) $Ca = 0.8$ (Stable)

(b) $Ca = 1.0$ (Detachments)

Figure 7.51: Deformation of a drop in a bilateral sudden expansion for $Re = 10$, $e = 4$ and $\alpha = 1$, initialized with fully developed conditions. Small fragments are floatsams that appeared in the first BDR code.

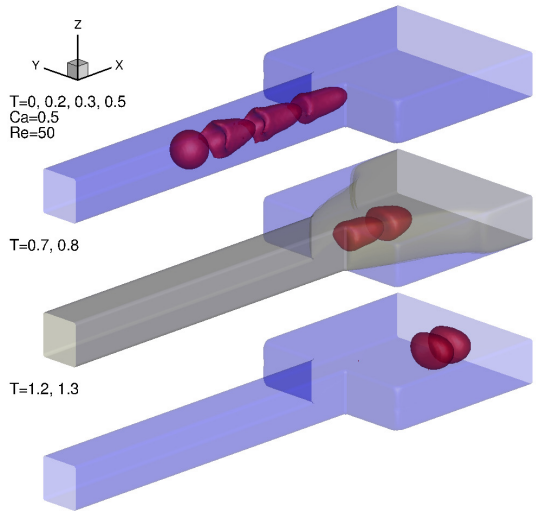

Figure 7.52: Similar as Figure 7.51, $Re = 50$ and $Ca = 0.5$. $U = 0$ is shown in yellow.

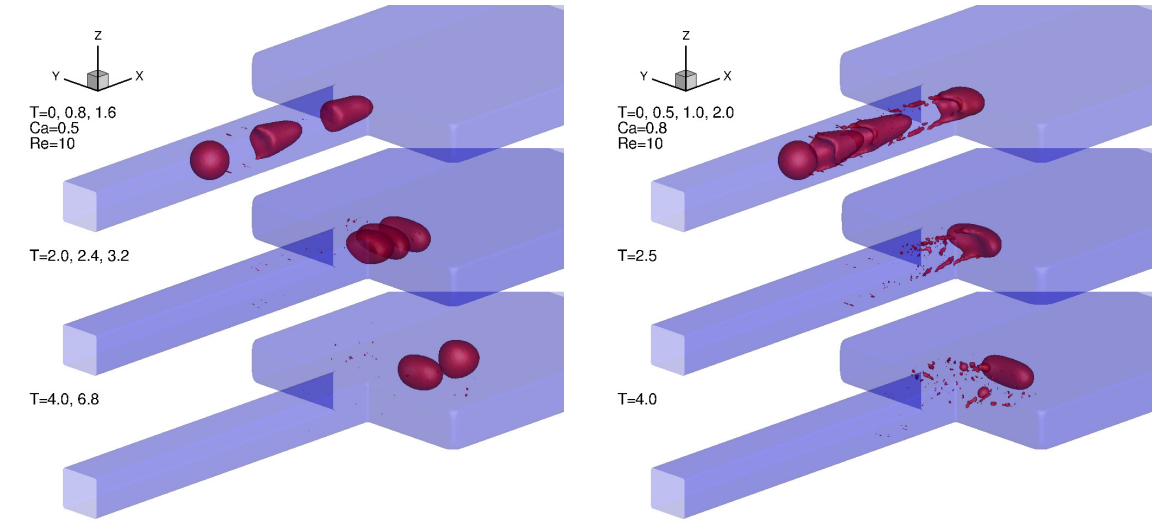

(a) $Ca = 0.5$ (Stable) (b) $Ca = 0.8$ (Detachments)

Figure 7.53: Deformation of a drop in a bilateral sudden expansion for $Re = 10$, $e = 6$ and $\alpha = 1$, initialized with fully developed conditions.

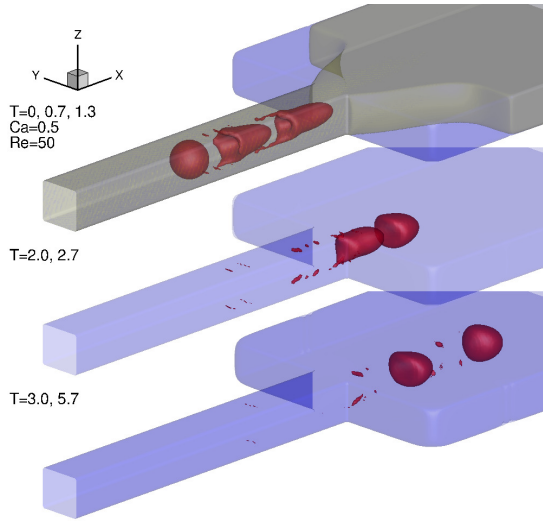

Figure 7.54: Similar as Figure 7.53, $Re = 50$ and $Ca = 0.5$. $U = 0$ is shown in yellow.

For the cases shown before, the drop-splitting was not possible. Now, the initial conditions are changed to explore if the developing circulations affect the the drop expansion further. Two cases are briefly considered. The flow is now initially quiescent and the inlet is prescribed with uniform velocity $u = U$ and a constant pressure at the exit. The geometric parameters are $e = 6.\widehat{6}$ and $\alpha = 2.\widehat{2}$, while the flow conditions are $Re = 10$ and $Re = 50$, for $Ca = 0.4$. The minimum aspect ratio is also presented in Table7.7, while the interface is shown in Figures 7.55-7.58.

These cases also presented circulations. Even thought the drop crosses the expansion after the complete development of the main vortex, both are more or less transported downstream simultaneously.

The main problem encountered in this flow is that the actual expansion of the fluid particles changes due to the apparition of flow recirculation. When a drop is released in a fully developed flow, the recirculation zones are already present if Re is sufficiently large or if α is large enough for a given Re. The objective now is to determine if the drop can expand before the formation of the circulation zones using a defined pressure at the inlet and the outlet. The average velocity U is computed from the latest timestep in order to report Re and Ca.

Table 7.8: Minimum aspect ratio after the expansion, $(A/B)_{\min}$ for blockage ratio $\beta = 2a/d = 0.90\widehat{9}$, $\alpha = 1$, quiescent initial conditions and prescribed pressure at the boundaries.

	$e = 8.04\widehat{5}$							
Case	η	σ	U	$u_{\max}$	Re	Ca	$(A/B)_{\min}$	t^*
DP1	$0.018\widehat{3}$	$0.0152\widehat{7}$	0.596	1.30	17.9	0.716	0.182	7.0
DP2	$0.018\widehat{3}$	0.013095	0.597	1.30	17.9	0.832	0.120	9.0
DP3	$0.018\widehat{3}$	0.010185	0.596	1.30	17.9	1.073	0	

	$e = 6.\widehat{6}$								
Case	η	σ	α	U	$u_{\max}$	Re	Ca	$(A/B)_{\min}$	t^*
	$0.018\widehat{3}$	0.02619	$1.\widehat{1}$	0.376	0.715	11.3	0.263	0.478	5.5
	$0.018\widehat{3}$	$0.0152\widehat{7}$	$1.\widehat{1}$	0.578	1.097	17.3	0.693	0.304	5.7
	$0.018\widehat{3}$	0.011458	$1.\widehat{1}$	0.578	1.097	17.3	0.924	0.239	6.7
	0.01	0.022	$1.\widehat{1}$	0.765	1.45+	38.2	0.382	0.428	5.7
	$0.018\widehat{3}$	$0.011458\widehat{3}$	$1.\widehat{1}$	0.490	1.01	14.7	0.784	0.170	9.8
	$0.018\widehat{3}$	$0.010\widehat{185}$	$1.\widehat{1}$	0.490	1.01	14.7	0.882	–	
	$0.018\widehat{3}$	$0.0091\widehat{6}$	$1.\widehat{1}$	0.490	1.01	14.7	0.980	–	

Considering that it is not possible to break up the drop at low Ca, the cases with $Ca \sim 1$ are explored. Between Figures 7.56 and 7.57 it can be observed there is a critical Re for the apparition of splitting. For $Re = 17.3$, the drop is stable at large Ca, while it shows end-tip splitting for $Re = 14.7$. This is in relationship with the fact that the drop deforms more at lower Re before reaching the expansion. Splitting was observed for a capillary number as low as $Ca = 0.88$.

As it can be observed, for $Re = 38.2$, Figure 7.58, the formation of the circulation zones is immediate and

in phase with the drop moving through the expansion region. At $Ca \sim 0.4$, the deformation of the drop is 0.43, which is similar to the case of $Re = 50$ (sudden startup conditions and $\alpha = 2.2$) where the deformation is 0.37.

Cases with large expansion ratios are shown in Figure 7.59, $e \approx 8$. The deformation shows a central constriction that leads to necking. This neck breaks up at $Ca = 1.07$ and $Re = 17.9$. Considering that lowering Re is favorable, breakup may be possible at lower Ca if Re is reduced.

As it can be observed, the range of conditions for which the drop splits is very narrow. Large values of Ca produce breakup in the narrow channel, while low Ca produce drop recoiling. Also, increasing Re also increase the critical capillary number. This phenomenon is highly dependent on the formation of a reentrant cavity and its shape, which in turn depends on the initial location of the drop and the flow conditions.

The purpose of studying this problem is to determine the conditions that produce drop splitting after a sudden expansion for low Ca. The results indicate that splitting may not not possible for $Ca < Ca_{cr}$ as it was originally sought. Instead, values of $Ca \sim 1$ are required to produce breakup. It is also not possible for large enough values of Re because of the apparition of the vena contracta. Drop splitting is possible for $e = 8$, but the initial location of the drop may be relevant (closer to the expansion than for $e = 4$). Drop detachment for $e = 4$ may have reduced the possible expansion of the drop, but splitting is not possible. Another mechanism was observed for $e = 6.\widehat{6}$ and $Ca \sim 0.9$: end-tip splitting. These results may suggest that it could be possible to produce splitting at lower Ca, but larger expansion ratios are required, and therefore more mesh points. Such cases were not simulated.

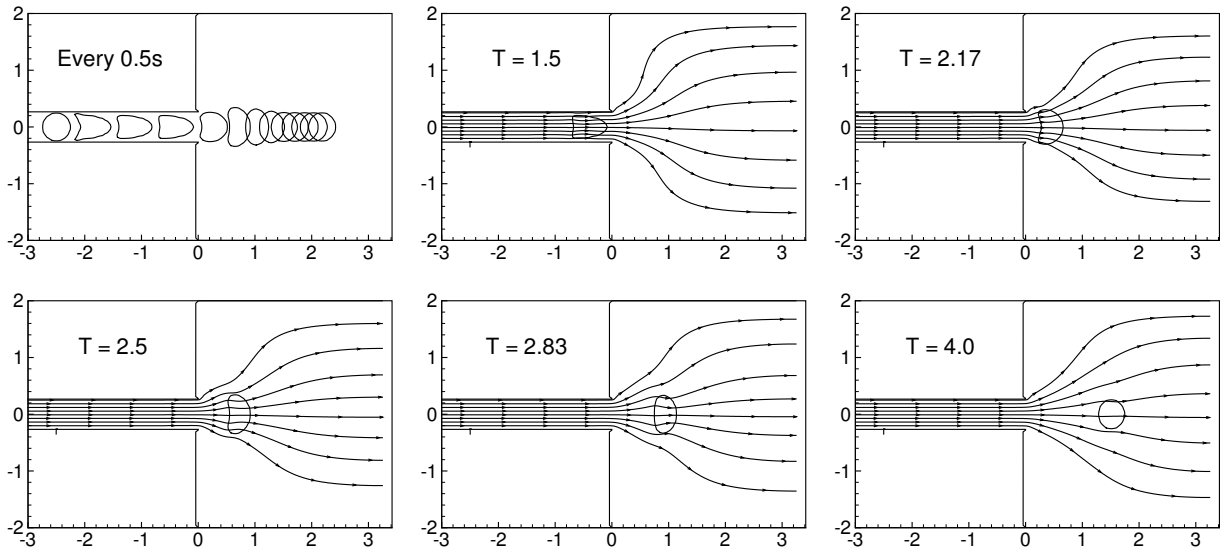

(a) $Re = 10$

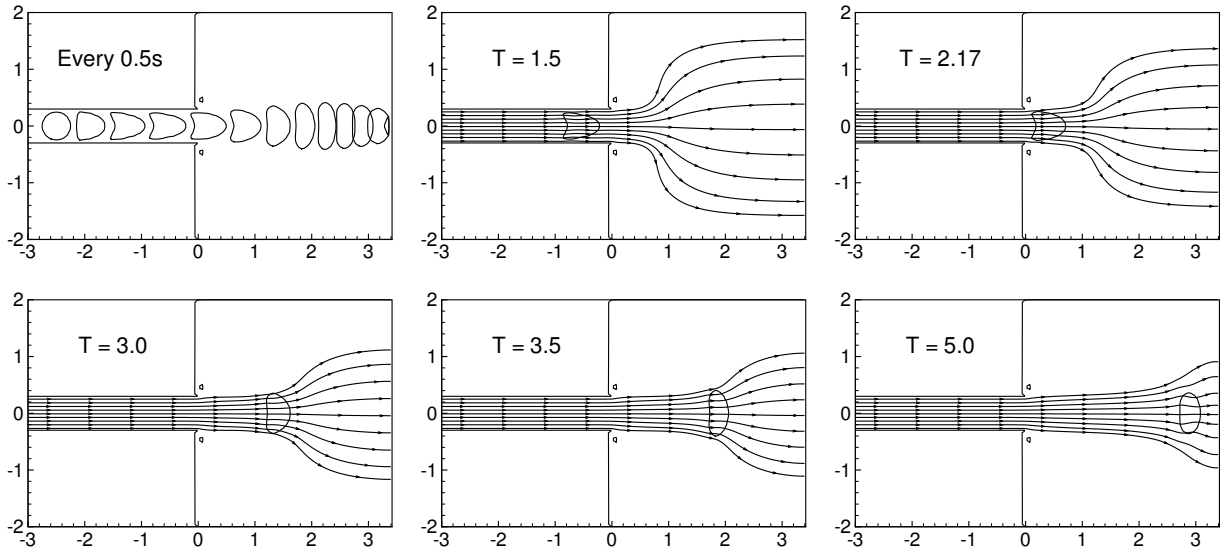

(b) $Re = 50$

Figure 7.55: Effect of Reynolds number on the deformation of a drop in a bilateral sudden expansion for $e = 6.\widehat{6}$, $\alpha = 2.\widehat{2}$, and $Ca = 0.4$.

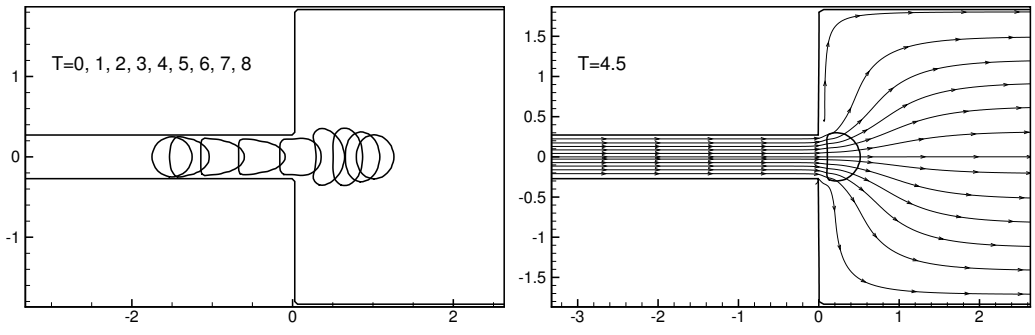

(a) $Re = 11.3$, $Ca = 0.263$

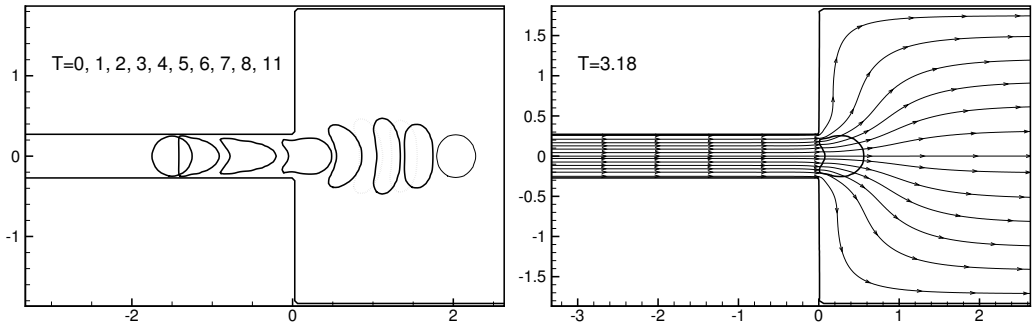

(b) $Re = 17.3$, $Ca = 0.693$

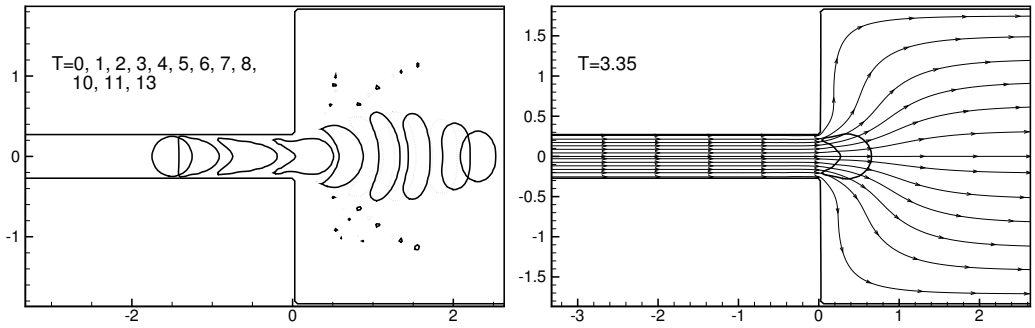

(c) $Re = 17.3$, $Ca = 0.924$

Figure 7.56: Evolution of a splitting drop in a bilateral sudden expansion for $e = 6.\widehat{6}$, $\alpha = 1.\widehat{1}$, $x_o = 6a$ and prescribed pressures.

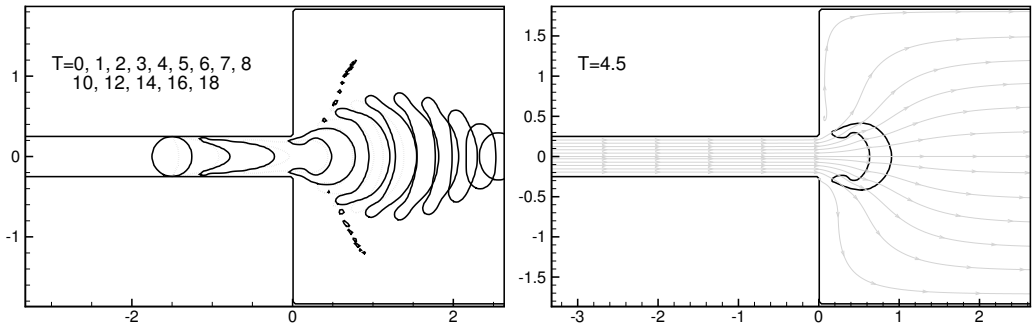

(a) $Ca = 0.784$

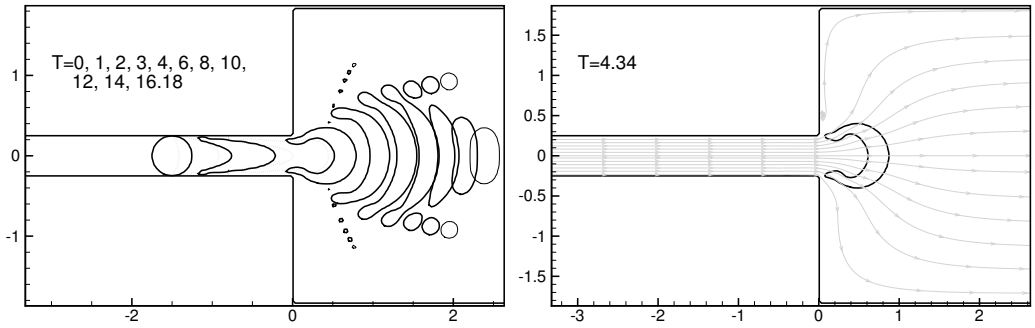

(b) $Ca = 0.882$

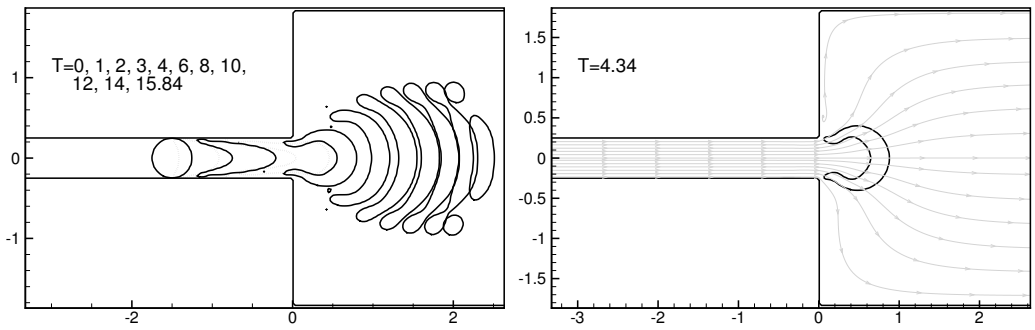

(c) $Ca = 0.980$

Figure 7.57: Continuation of Figure 7.56. For $Re = 14.7$.

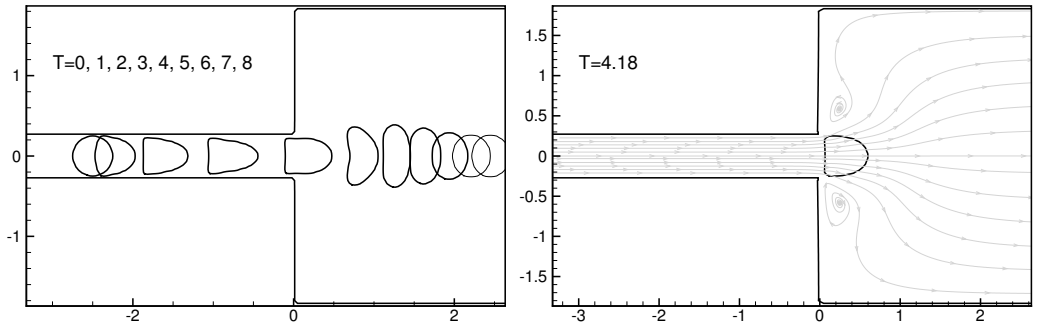

Figure 7.58: Continuation of Figure 7.56. For $Re = 38.2$, $Ca = 0.382$, $e = 6.\widehat{6}$, $\alpha = 1.\widehat{1}$, $x_o = 10a$.

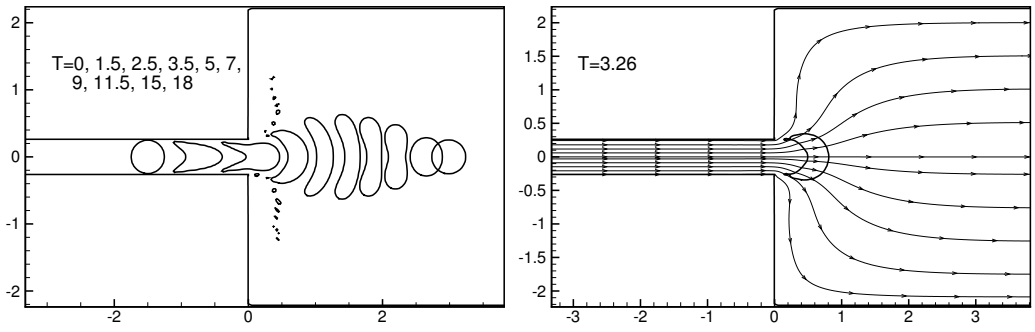

(a) $Ca = 0.716$

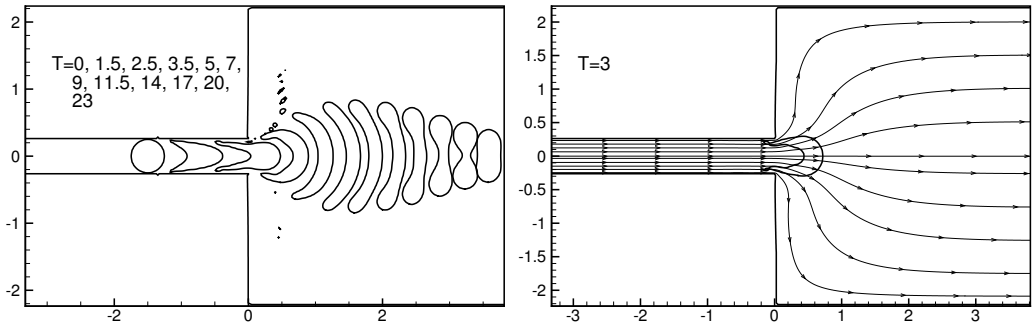

(b) $Ca = 0.832$

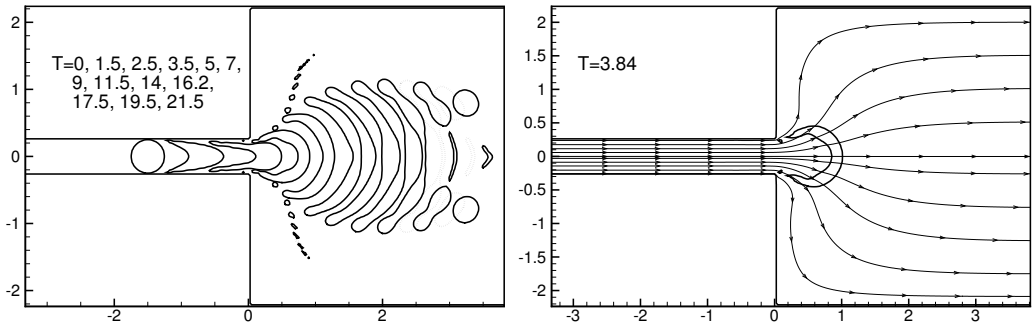

(c) $Ca = 1.073$

Figure 7.59: Evolution of a splitting drop in a bilateral sudden expansion for $e = 8.04\widehat{5}$, $\alpha = 1$, and $Re = 17.9$ and prescribed pressures.

7.4.2 Axisymmetric Sudden Expansion

Preliminary results in an axisymmetric sudden expansion showed that the drop can stretch as a flattened disk, instead of a banana shape, and then it forms an annular structure. This ring may break up due to capillary instability or collapse as a drop again. This study is only mentioned as another possibility to produce drop fragmentation. Considering the narrow range of Re and Ca observed in the previous section, finding such conditions in this case may require several simulations.

Chapter 8

Summary and Final Discussion

A volume-of-fluid method together with several fluxing algorithms (VOF-FCT, BDR-PLIC-VOF, DDR-PLIC-VOF) have been used to investigate the deformation and breakup of droplets in shearing and extensional flows, with and with out rigid particles. Because of numerical limitation, emphasis is done on the accuracy of the submodels: advection, plane reconstruction, fluxing of the volume fraction, interface curvature, surface-tension forces, rigidifying forces, among others. The accuracy in drop deformation is observed to be highly dependent on the curvature model, while the stability relies on the fluxing algorithm. Other aspects are mass conservation capabilities, and the DDR method is shown to conserve mass exactly, which not necessarily means that the transport of material from one cell to another is exact. Accuracy, stability and consistency are the requirements for a robust solver. We encounter that combining the HF model for normals and curvatures, together with the DDR-PLIC method and a first-to-second-order fluid flow solver is sufficient to analyze engineering problems involving drops. Part of the analysis involved the comparison of the Taylor deformation parameter and the drop half-length for a single drop. Such results are in good agreement with the values of other authors using VOF.

Drops in high confinement showed a slight increase in stability. It may be possible to increase the stability even more if the symmetry planes are brought immediately close to the drop. If the purpose is to reduce the requirements to produce breakup, localizing the boundaries far away is preferred. Typically, a distance of six times the drop radius in one direction is sufficient.

When the drop viscosity is within two times the viscosity of the medium, the critical capillary number remains similar to the uniform case. However, different types of daughter drops are observed. When the viscosity of the medium is ten times more viscous than the drop, the flow is considerably stable, requiring large capillary numbers to induce breakup. The cases with inertia showed an increase in deformation for

a given capillary number, but the drop is considerably more stable than the unconfined case due to the presence of the walls. Inertia also produces traversal oscillations. The maximum drop half-length increases exponentially in terms of the capillary number near critical conditions for a constant Reynolds, while it may asymptote for large Reynolds. The critical capillary number decreases monotonically with increasing Reynolds.

In the case of particulate flows, a drop can be punctured by the presence of rigid particles. Among several parameters, the capillary number determines the requirements of the particles in order to produce puncturing. For low capillary numbers and uniform properties, puncturing is not possible, but the requirements are reduced as the capillary number reaches the critical capillary number without particles (i.e ~ 0.5). The initial position of the particles is the second parameter of relevance under these conditions. Particles closer to the centerline produce larger deformation, but take longer to accelerate, while particles far away in the direction of the flow produce an enhanced effect and may take less time to pass over the drop. Even though the initial position of the particle can be optimized, increasing the particle size to at least three times the drop size is preferred because it produces large deformations and puncturing under low capillary conditions. Denser particles also increase the deformation, but the impact is less significant.

Particulate flows that where studied before considered suddenly started flows. In those cases, the initial angular velocity of the particles is the result of a rigidization process and enhanced lift forces may be present. This may increase drafting effect and thereby puncturing. The analysis presented here is more conservative because the angular velocity is the solution of the dynamics of the problem and the results are less prone to produce puncturing. Here, the particle-particle distance is used to determine the conditions for puncturing. Because the lubrication force is important in the gap, a criteria is made on whether puncturing is happening or not. Extrapolating the results to that criteria showed that large capillary numbers are required to produce collision effectively. However, it was also observed that our methods are incapable of analyzing the collision problem in detail mainly because the singularity that appears when the particles are within one cell distance from each other. A rugosity of at least two cells is required to account for elastic collisions, but such distance can be considerably large. This type of analysis required a multigrid approach and such method was not incorporated.

It was also reported that particles increase the drop deformation. Such effect is observed qualitatively and is remarkable for capillary numbers below the critical value. Several mechanism are described for supercritical cases as those flows are complex in nature.

The analysis presented here is referenced on a Reynolds and Capillary basis. This is the typical basis for unconfined flows without particles and therefore is preferred. Considering the amount of parameters, this study is only performed for limited cases. A general parameter that determines the possibility for puncturing

was not encountered.

This work can be extended to viscoelastic fluids.

Bibliography

Abmayr, S., Adachi, H., Adams, L.D., et al., 1995. Current Protocols in Molecular Biology. John Wiley & Sons.

Almeida-Rivera, C., Bongers, P., 2012. Modelling and simulation of extensional-flow units in emulsion formation. Computers & Chemical Engineering 37, 33 – 39.

Anderson, J.D., 1994. Computational fluid dynamics : the basics with applications. McGraw-Hill, New York.

Ardekani, A., Dabiri, S., Rangel, R., 2008. Collision of multi-particle and general shape objects in a viscous fluid. Journal of Computational Physics 227, 10094 – 10107.

Ashgriz, N., Poo, J., 1991. Flair: Flux line-segment model for advection and interface reconstruction. Journal of Computational Physics 93, 449–468.

Bailey, C., Cross, M., 1995. A finite volume procedure to solve elastic solid mechanics problems in three dimensions on an unstructured mesh. International Journal for Numerical Methods in Engineering 38, 1757–1776.

Barthès-Biesel, D., Acrivos, A., 1973. Deformation and burst of a liquid droplet freely suspended in a linear shear field. Journal of Fluid Mechanics 61, 1–22.

Basaran, O.A., 1992. Nonlinear oscillations of viscous liquid drops. Journal of Fluid Mechanics 241, 169–198.

Becker, L.E., McKinley, G.H., Rasmussen, H.K., Hassager, O., 1994. The unsteady motion of a sphere in a viscoelastic fluid. Journal of Rheology 38, 377–403.

Bird, R.B., Armstrong, R.C., Hassager, O., 1977. Dynamics of polymeric liquids. volume 2 of *Fluid mechanics*. 2 ed., J. Wiley, New York.

Bot, E., Hulsen, M., van den Brule, B., 1998. The motion of two spheres falling along their line of centres in a boger fluid. Journal of Non-Newtonian Fluid Mechanics 79, 191 – 212.

Brackbill, J.U., Kothe, D.B., Zemach, C., 1992. A continuum method for modeling surface tension. Journal of Computational Physics 100, 335–354.

de Bruijn, R., 1993. Tipstreaming of drops in simple shear flows. Chemical Engineering Science 48, 277 – 284.

Brust, M., Schaefer, C., Doerr, R., Pan, L., Garcia, M., Arratia, P.E., Wagner, C., 2013. Rheology of human blood plasma: Viscoelastic versus newtonian behavior. Phys. Rev. Lett. 110, 078305.

Chenadec, V.L., Pitsch, H., 2013. A 3d unsplit forward/backward volume-of-fluid approach and coupling to the level set method. Journal of Computational Physics 233, 10 – 33.

Cho, Y.I., Kensey, K.R., 1991. Effects of the non-Newtonian viscosity of blood on flows in a diseased arterial vessel. Part 1: Steady flows. Biorheology 28, 241–262.

Choi, Y.J., Hulsen, M.A., 2012. Alignment of particles in a confined shear flow of a viscoelastic fluid. Journal of Non-Newtonian Fluid Mechanics 175-176, 89 – 103.

Clift, R., Grace, J., Weber, M., 1978. Bubbles, Drops and Particles. Academic Press, New York.

Crank, J., Nicolson, P., 1996. A practical method for numerical evaluation of solutions of partial differential equations of the heat-conduction type. Advances in Computational Mathematics 6, 207–226.

Cristini, V., Blawzdziewicz, J., Loewenberg, M., 2001. An adaptive mesh algorithm for evolving surfaces: Simulations of drop breakup and coalescence. Journal of Computational Physics 168, 445 – 463.

Crochet, M.J., Walters, K., Davies, A.R., 1984. Numerical simulation of non-Newtonian flow / M.J. Crochet, A.R. Davies, K. Walters. Elsevier, Amsterdam ; New York :.

Cummins, S.J., Francois, M.M., Kothe, D.B., 2005. Estimating curvature from volume fractions. Computers & Structures 83, 425 – 434. frontier of Multi-Phase Flow Analysis and Fluid-Structure Frontier of Multi-Phase Flow Analysis and Fluid-Structure.

Cundall, P., Strack, O., 1979. A discrete numerical model for granular assemblies. GÃ©otechnique 29, 47–65.

D'Avino, G., Maffettone, P., Greco, F., Hulsen, M., 2010a. Viscoelasticity-induced migration of a rigid sphere in confined shear flow. Journal of Non-Newtonian Fluid Mechanics 165, 466 – 474.

D'Avino, G., Tuccillo, T., Maffettone, P., Greco, F., Hulsen, M., 2010b. Numerical simulations of particle migration in a viscoelastic fluid subjected to shear flow. Computers & Fluids 39, 709 – 721.

Dupont, J.B., Legendre, D., 2010. Numerical simulation of static and sliding drop with contact angle hysteresis. Journal of Computational Physics 229, 2453 – 2478.

Enright, D., Fedkiw, R., Ferziger, J., Mitchell, I., 2002. A hybrid particle level set method for improved interface capturing. J. Comput. Phys 183, 83–116.

Evans, E., Waugh, R., Melnik, L., 1976. Elastic area compressibility modulus of red cell membrane. Biophysical Journal 16, 585 – 595.

Fearn, R.M., Mullin, T., Cliffe, K.A., 1990. Nonlinear flow phenomena in a symmetric sudden expansion. Journal of Fluid Mechanics 211, 595–608.

Ferdowsi, P.A., Bussmann, M., 2008. Short note: Second-order accurate normals from height functions. J. Comput. Phys. 227, 9293–9302.

Ferziger, J.H., Peric, M., 1999. Computational Methods for Fluid Dynamics. Springer, Berlin.

Foo, J.J., Chan, V., Liu, K.K., 2006. Coupling bending and shear effects on liposome deformation. Journal of Biomechanics 39, 2338 – 2343.

Francois, M.M., Cummins, S.J., Dendy, E.D., Kothe, D.B., Sicilian, J.M., Williams, M.W., 2006. A balanced-force algorithm for continuous and sharp interfacial surface tension models within a volume tracking framework. Journal of Computational Physics 213, 141–173.

Gaskell, P.H., Lau, A.K.C., 1988. Curvature-compensated convective transport: SMART, A new boundedness- preserving transport algorithm. International Journal for Numerical Methods in Fluids 8, 617–641.

Ghia, U., Ghia, K., Shin, C., 1982. High-re solutions for incompressible flow using the navier-stokes equations and a multigrid method. Journal of Computational Physics 48, 387 – 411.

Grace, H.P., 1982. Dispersion phenomena in high viscosity immiscible fluid systems and application of static mixers as dispersion devices in such systems. Chemical Engineering Communications 14, 225–277.

Halow, J.S., Wills, G.B., 1970. Experimental observations of sphere migration in couette systems. Industrial & Engineering Chemistry Fundamentals 9, 603–607.

Hao, J., Pan, T.W., Glowinski, R., Joseph, D.D., 2009. A fictitious domain/distributed lagrange multiplier method for the particulate flow of oldroyd-b fluids: A positive definiteness preserving approach. Journal of Non-Newtonian Fluid Mechanics 156, 95 – 111.

Harvie, D.J., Fletcher, D.F., 2000. A new volume of fluid advection algorithm: The stream scheme. Journal of Computational Physics 162, 1 – 32.

Harvie, D.J.E., Fletcher, D.F., 2001. A new volume of fluid advection algorithm: the defined donating region scheme. International Journal for Numerical Methods in Fluids 35, 151–172.

Helmsen, J., Colella, P., Puckett, E., 1997. Non-convex profile evolution in two dimensions using volume of fluids. Technical Report LBNL-40693. Lawrence Berkeley National Laboratory.

Ho, B.P., Leal, L.G., 1974. Inertial migration of rigid spheres in two-dimensional unidirectional flows. Journal of Fluid Mechanics 65, 365–400.

Huang, P.Y., Feng, J., Hu, H.H., Joseph, D.D., 1997. Direct simulation of the motion of solid particles in couette and poiseuille flows of viscoelastic fluids. Journal of Fluid Mechanics 343, 73–94.

Huang, P.Y., Joseph, D.D., 2000. Effects of shear thinning on migration of neutrally buoyant particles in pressure driven flow of newtonian and viscoelastic fluids. Journal of Non-Newtonian Fluid Mechanics 90, 159 – 185.

Hulsen, M.A., Fattal, R., Kupferman, R., 2005. Flow of viscoelastic fluids past a cylinder at high weissenberg number: Stabilized simulations using matrix logarithms. Journal of Non-Newtonian Fluid Mechanics 127, 27 – 39.

Hwang, W.R., Hulsen, M.A., Meijer, H.E., 2004. Direct simulations of particle suspensions in a viscoelastic fluid in sliding bi-periodic frames. Journal of Non-Newtonian Fluid Mechanics 121, 15 – 33.

Jamet, D., Torres, D., Brackbill, J.U., 2002. On the Theory and Computation of Surface Tension: The Elimination of Parasitic Currents through Energy Conservation in the Second-Gradient Method. Journal of Computational Physics 182, 262–276.

Janssen, P.J.A., Anderson, P.D., 2007. Boundary-integral method for drop deformation between parallel plates. Physics of Fluids 19.

Joseph, D.D., 1990. Fluid Dynamics of Viscoelastic Liquids. Springer, Berlin.

Joseph, D.D., Funada, T., Wang, J., 2007. Potential flows of viscous and viscoelastic liquids. Cambridge University Press, Cambridge.

Kang, B., Mackey, M.A., El-Sayed, M.A., 2010. Nuclear targeting of gold nanoparticles in cancer cells induces DNA damage, causing cytokinesis arrest and apoptosis. J. Am. Chem. Soc. 132, 1517–1519.

Khodaparast, S., Borhani, N., Thome, J.R., 2014. Sudden expansions in circular microchannels: flow dynamics and pressure drop. Microfluidics and Nanofluidics 17, 561–572.

Kim, S.O., No, H.C., 1998. Second-order model for free surface convection and interface reconstruction. International Journal for Numerical Methods in Fluids 26, 79–100.

Ko, T., Patankar, N.A., Joseph, D.D., 2006. Lift and multiple equilibrium positions of a single particle in newtonian and oldroyd-b fluids. Computers & Fluids 35, 121 – 146.

Kothe, D., 1998. Perspective on eulerian finite volume methods for incompressible interfacial flows, in: Kuhlmann, H., Rath, H.J. (Eds.), Free Surface Flows. Springer Vienna. volume 391 of *International Centre for Mechanical Sciences*, pp. 267–331.

Kothe, D.B., Rider, W., Mosso, S.J., Brock, J.S., Hochstein, J.I., 1996. Volume tracking of interfaces having surface tension in two and three dimensions, in: 34th Aerospace Sciences Meeting and Exhibit, American Institute of Aeronautics and Astronautics, Reno, NV.

Lafaurie, B., Nardone, C., Scardovelli, R., Zaleski, S., Zanetti, G., 1994. Modelling merging and fragmentation in multiphase flows with {SURFER}. Journal of Computational Physics 113, 134 – 147.

LeVeque, R.J., 1996. High-resolution conservative algorithms for advection in incompressible flow. SIAM J. Numer. Anal. 33, 627–665.

Li, J., Renardy, Y.Y., Renardy, M., 2000. Numerical simulation of breakup of a viscous drop in simple shear flow through a volume-of-fluid method. Physics of Fluids (1994-present) 12, 269–282.

Lim, J., Lanni, C., Evarts, E.R., Lanni, F., Tilton, R.D., Majetich, S.A., 2011. Magnetophoresis of nanoparticles. ACS Nano 5, 217–226.

Liovic, P., Francois, M., Rudman, M., Manasseh, R., 2010. Efficient simulation of surface tension-dominated flows through enhanced interface geometry interrogation. Journal of Computational Physics 229, 7520–7544.

Liovic, P., Rudman, M., Liow, J.L., Lakehal, D., Kothe, D., 2006. A 3d unsplit-advection volume tracking algorithm with planarity-preserving interface reconstruction. Computers & Fluids 35, 1011 – 1032.

Liu, X.D., Fedkiw, R.P., Kang, M., 2000. A boundary condition capturing method for poisson's equation on irregular domains. Journal of Computational Physics 160, 151 – 178.

López, J., Hernández, J., 2010. On reducing interface curvature computation errors in the height function technique. Journal of Computational Physics 229, 4855 – 4868.

Lunsmann, W., Genieser, L., Armstrong, R., Brown, R., 1993. Finite element analysis of steady viscoelastic flow around a sphere in a tube: calculations with constant viscosity models. Journal of Non-Newtonian Fluid Mechanics 48, 63 – 99.

M., B., DeBlois, 1997. Linearizing convection terms in the navier-stokes equations. Computer Methods in Applied Mechanics and Engineering 143, 289 – 297.

Ménard, T., Tanguy, S., Berlemont, A., 2007. Coupling level set/vof/ghost fluid methods: Validation and application to 3d simulation of the primary break-up of a liquid jet. International Journal of Multiphase Flow 33, 510 – 524.

Miller, G., Colella, P., 2002. A conservative three-dimensional eulerian method for coupled solid-fluid shock capturing. Journal of Computational Physics 183, 26 – 82.

Minale, M., 2008. A phenomenological model for wall effects on the deformation of an ellipsoidal drop in viscous flow. Rheologica Acta 47, 667–675.

Mukherjee, S., Sarkar, K., 2009. Effects of viscosity ratio on deformation of a viscoelastic drop in a newtonian matrix under steady shear. Journal of Non-Newtonian Fluid Mechanics 160, 104 – 112.

Oliveira, P., Alves, M., Pinho, F., 2000. The flow of ucm and oldroyd-b fluids past a cylinder, ASME. Rheology and Fluid Mechanis of Nonlinear Materials.

Oliveira, P.J., 2003. Asymmetric flows of viscoelastic fluids in symmetric planar expansion geometries. Journal of Non-Newtonian Fluid Mechanics 114, 33 – 63.

Owens, R.G., Phillips, T.N., 2002. Computational Rheology. World Scientific Publishing Company.

Patankar, S.V., 1980. Numerical heat transfer and fluid flow. Hemisphere Pub. Corp., McGraw-Hill, Washington, New York.

Peskin, C.S., 1977. Numerical analysis of blood flow in the heart. Journal of Computational Physics 25, 220 – 252.

Pilliod, J.E., Puckett, E.G., 2004. Second-order accurate volume-of-fluid algorithms for tracking material interfaces. Journal of Computational Physics 199, 465 – 502.

Pilliod, Jr, J.E., 1992. An Analysis of Piecewise Linear Interface Reconstruction Algorithms for Volume-of-Fluid Methods. Master's thesis. University of California at Davis.

Puckett, E.G., 1991. A volume-of-fluid interface tracking algorithm with applications to computing shock wave refraction, in: Dwyer, H. (Ed.), Proceedings of the Fourth International Symposium on Computational Fluid Dynamics, Davis, CA. pp. 933–938.

Puckett, E.G., Almgren, A.S., Bell, J.B., Marcus, D.L., Rider, W.J., 1997. A high-order projection method for tracking fluid interfaces in variable density incompressible flows. Journal of Computational Physics 130, 269 – 282.

Raessi, M., Mostaghimi, J., Bussmann, M., 2007. Advecting normal vectors: A new method for calculating interface normals and curvatures when modeling two-phase flows. Journal of Computational Physics 226, 774 – 797.

Rajagopalan, D., Arigo, M., McKinley, G.H., 1996. The sedimentation of a sphere through an elastic fluid part 2. transient motion. Journal of Non-Newtonian Fluid Mechanics 65, 17 – 46.

Rajagopalan, D., Armstrong, R.C., Brown, R.A., 1993. Comparison of computational efficiency of flow simulations with multimode constitutive equations: integral and differential models. Journal of Non-Newtonian Fluid Mechanics 46, 243 – 273.

Ramanujan, S., Pozrikidis, C., 1998. Deformation of liquid capsules enclosed by elastic membranes in simple shear flow: large deformations and the effect of fluid viscosities. Journal of Fluid Mechanics 361, 117–143.

Renardy, Y., Cristini, V., Li, J., 2002. Drop fragment distributions under shear with inertia. International Journal of Multiphase Flow 28, 1125 – 1147.

Renardy, Y., Renardy, M., 2002. Prost: A parabolic reconstruction of surface tension for the volume-of-fluid method. Journal of Computational Physics 183, 400 – 421.

Rider, W.J., Kothe, D.B., 1998. Reconstructing volume tracking. Journal of Computational Physics 141, 112 – 152.

Rider, W.J., Kothe, D.B., Mosso, S.J., Cerutti, J.H., Hochstein, J.I., 1995. Accurate Solution Algorithms for Incompressible Multiphase Flows, in: 33rd Aerospace Sciences Meeting and Exhibit.

Rudman, M., 1997. Volume-tracking methods for interfacial flow calculations. International Journal for Numerical Methods in Fluids 24, 671–691.

Scardovelli, R., Zaleski, S., 1999. Direct numerical simulation of free-surface and interfacial flow. Annual Review of Fluid Mechanics 31, 567–603.

Shapira, M., Haber, S., 1990. Low reynolds number motion of a droplet in shear flow including wall effects. International Journal of Multiphase Flow 16, 305 – 321.

van Sint Annaland, M., Deen, N., Kuipers, J., 2005. Numerical simulation of gas bubbles behaviour using a three-dimensional volume of fluid method. Chemical Engineering Science 60, 2999 – 3011.

Skalak, R., Tozeren, A., Zarda, R., Chien, S., 1973. Strain energy function of red blood cell membranes. Biophysical Journal 13, 245 – 264.

Stone, H.A., 1994. Dynamics of drop deformation and breakup in viscous fluids. Annual Review of Fluid Mechanics 26, 65–102.

Sussman, M., 2003. A second order coupled level set and volume-of-fluid method for computing growth and collapse of vapor bubbles. Journal of Computational Physics 187, 110 – 136.

Sussman, M., Smereka, P., Osher, S., 1994. A level set approach for computing solutions to incompressible two-phase flow. Journal of Computational Physics 114, 146 – 159.

Tong, A.Y., Wang, Z., 2007. A numerical method for capillarity-dominant free surface flows. Journal of Computational Physics 221, 506 – 523.

Tryggvason, G., Bunner, B., Esmaeeli, A., Juric, D., Al-Rawahi, N., Tauber, W., Han, J., Nas, S., Jan, Y.J., 2001. A front-tracking method for the computations of multiphase flow. Journal of Computational Physics 169, 708 – 759.

Tsai, T.M., Miksis, M.J., 1994. Dynamics of a drop in a constricted capillary tube. Journal of Fluid Mechanics 274, 197–217.

Unverdi, S.O., Tryggvason, G., 1992. A front-tracking method for viscous, incompressible, multi-fluid flows. Journal of Computational Physics 100, 25 – 37.

van Doormaal, J.P., Raithby, G.D., 1984. Enhancements of the simple method for predicting incompressible fluid flows. Numerical Heat Transfer 7, 147–163.

Villone, M., D'Avino, G., Hulsen, M., Greco, F., Maffettone, P., 2011. Numerical simulations of particle migration in a viscoelastic fluid subjected to poiseuille flow. Computers & Fluids 42, 82 – 91.

Wahba, E., 2007. Iterative solvers and inflow boundary conditions for plane sudden expansion flows. Applied Mathematical Modelling 31, 2553 – 2563.

Wang, J., yuan Bai, R., Lewandowski, C., Galdi, G.P., Joseph, D.D., 2004. Sedimentation of cylindrical particles in a viscoelastic liquid: shape-tilting. China Particuology 2, 13 – 18.

Won, D., Kim, C., 2004. Alignment and aggregation of spherical particles in viscoelastic fluid under shear flow. Journal of Non-Newtonian Fluid Mechanics 117, 141 – 146.

Yabe, T., Chinda, K., Hiraishi, T., 2007. Computation of surface tension and contact angle and its application to water strider. Computers & Fluids 36, 184 – 190. challenges and Advances in Flow Simulation and Modeling.

Yoon, S., Walkley, M., Harlen, O., 2012. Two particle interactions in a confined viscoelastic fluid under shear. Journal of Non-Newtonian Fluid Mechanics 185-186, 39 – 48.

Yu, Z., Phan-Thien, N., Fan, Y., Tanner, R.I., 2002. Viscoelastic mobility problem of a system of particles. Journal of Non-Newtonian Fluid Mechanics 104, 87 – 124.

Zhang, Q., 2013. On a family of unsplit advection algorithms for volume-of-fluid methods. SIAM Journal on Numerical Analysis 51, 2822–2850.

Zheng, R., Phan-Thien, N., Tanner, R., 1990. On the flow past a sphere in a cylindrical tube: Limiting weissenberg number. Journal of Non-Newtonian Fluid Mechanics 36, 27 – 49.